

SEARCHING FOR NEW PHYSICS IN $b \rightarrow s\ell^+\ell^-$ TRANSITIONS AT THE LHCb EXPERIMENT

L. Pescatore

*Thesis submitted for the degree of
Doctor of Philosophy*



Particle Physics Group,
School of Physics and Astronomy,
University of Birmingham.

February 26, 2016

ABSTRACT

Flavour Changing Neutral Currents are transitions between different quarks with the same charge such as $b \rightarrow s$ processes. These are forbidden at tree level in the Standard Model but can happen through loop diagrams, which causes the branching ratio of this type of decays to be small, typically $\sim 10^{-6}$ or less. Particles beyond the SM can contribute in the loops enhancing the branching fractions of these decays, which are therefore very sensitive new physics. In this work two analysis of semileptonic $b \rightarrow s\ell^+\ell^-$ decays are presented. First $\Lambda_b^0 \rightarrow \Lambda\mu^+\mu^-$ decays are analysed to measure their branching fraction as a function of the dimuon invariant mass, q^2 . Furthermore, an angular analysis of these decays is performed for the first time. Secondly, $B^0 \rightarrow K^{*0}\ell^+\ell^-$ decays are analysed measuring the ratio between the muon, $B^0 \rightarrow K^{*0}\mu^+\mu^-$, and electron, $B^0 \rightarrow K^{*0}e^+e^-$, channels, which is interesting as it is largely free from uncertainties due to the knowledge of the hadronic matrix elements. This thesis is organised in the following way. Chapter 1 introduces the Standard Model and the concept of flavour and explains how rare decays can help us in the quest for physics beyond the SM. Chapter 2 describes the LHCb detector, which was used to collect the data analysed in this thesis. This chapter also includes studies performed to validate the hadronic physics in LHCb simulation software. Chapter 3 deals with the measurement of the differential branching fraction of the $\Lambda_b^0 \rightarrow \Lambda\mu^+\mu^-$ decay, while Chapter 4 describes an angular analysis of these decays. Finally, Chapter 5 reports the measurement of the $R_{K^{*0}}$ ratio between the decay rates of the $B^0 \rightarrow K^{*0}\mu^+\mu^-$ and $B^0 \rightarrow K^{*0}e^+e^-$ decays.

DECLARATION OF AUTHORS CONTRIBUTION

I am one of the main authors of the two analysis reported in Chapters 3, 4 and 5. For the analysis of the differential branching ratio of the $\Lambda_b^0 \rightarrow \Lambda\mu^+\mu^-$ decay I collaborated with Michal Kreps, who took care of implementing the decay model to re-weight the simulation and provided a few of the simulated samples. Furthermore, I want to thank him for the advice given throughout. The work in this part was also published and can be found at Ref. [1]. For the $R_{K^{*0}}$ analysis, described in Ch. 5, I actively participated in most stages of the analysis collaborating with Simone Bifani. In particular I took care of the production of various simulated samples, participated in the definition of the selection, in the yields extraction and I provided a fit and data-reduction framework. Finally, as a service work for the LHCb experiment, I developed the tools used to perform the studies described in Sections 2.11–2.13.

ACKNOWLEDGEMENTS

I thank everybody, evvvvvvvveverybody!

*A Lucia,
perché quando tutto perde di senso
tu sei il mio piccolo mondo felice.*

*Nec per se quemquam tempus sentire fatendumst
semotum ab rerum motu placidaque quiete.
(Lucretius, De rerum natura, vv. 462-463)*

Contents

1	Introduction	1
1.1	The electroweak interaction	4
1.2	Flavour and the CKM matrix	5
1.3	The puzzles of the SM	9
1.3.1	The flavour problem	10
1.4	Beyond the Standard Model	11
1.4.1	Flavour and BSM theories	12
1.5	Rare decays: a tool to search for new physics	13
1.5.1	Theoretical framework: the effective Hamiltonian	14
1.5.2	Operators	16
1.5.3	Phenomenology of $b \rightarrow s\ell^+\ell^-$ decays	18
1.5.4	Observables in $b \rightarrow s\ell^+\ell^-$ decays	19
1.6	Experimental status	20
1.6.1	Dimuon decays of b hadrons	20
1.6.2	Semileptonic $b \rightarrow s\ell^+\ell^-$ decays of b hadrons	22
1.6.3	Lepton Flavour Violation searches	23
2	The LHCb detector at the Large Hadron Collider	25
2.1	The Large Hadron Collider	25
2.2	The LHCb detector	27
2.3	The magnet	29
2.4	Tracking system	29
2.5	Calorimeters	32
2.5.1	Bremsstrahlung recovery for electrons	34
2.6	RICH	35
2.7	The muon system	36
2.8	Particle identification	37
2.8.1	PID calibration	39
2.9	Trigger and software	39
2.10	Constrained kinematic fits	41
2.11	Validation of hadronic processes in the simulation	42
2.11.1	Geometry and interaction probability	44
2.11.2	PDG prediction	45
2.11.3	Validation results	46
2.12	Material budget studies	49
2.13	Validation and material budget studies conclusions	50

3 Differential branching fraction of $\Lambda_b^0 \rightarrow \Lambda\mu^+\mu^-$	51
3.1 Analysis strategy and q^2 regions	53
3.2 Candidate types	54
3.3 Simulation	55
3.3.1 Decay Model	56
3.3.2 Kinematic re-weighting	56
3.3.3 Event type	58
3.4 Selection	59
3.4.1 Pre-selection	59
3.4.2 Neural Networks	60
3.4.3 MVA optimisation	64
3.4.4 Trigger	65
3.4.5 Background from specific decays	66
3.5 Yield extraction	68
3.5.1 Fit description	69
3.5.2 Fit results	73
3.6 Efficiency	79
3.6.1 Geometric acceptance	79
3.6.2 Reconstruction and neural network efficiencies	80
3.6.3 Trigger efficiency	80
3.6.4 PID efficiency	81
3.6.5 Relative efficiencies	82
3.7 Systematic uncertainties	85
3.7.1 Systematic uncertainty on the yields	85
3.7.2 Systematic uncertainties on the efficiency determination	87
3.7.2.1 Effect of new physics on the decay model	87
3.7.2.2 Simulation statistics	87
3.7.2.3 Production polarisation and decay structure	88
3.7.2.4 Λ_b^0 lifetime	89
3.7.2.5 Downstream candidates reconstruction efficiency	89
3.7.2.6 Data-simulation discrepancies	90
3.8 Differential branching ratio extraction	90
4 Angular analysis of $\Lambda_b^0 \rightarrow \Lambda\mu^+\mu^-$ decays	95
4.1 One-dimensional angular distributions	96
4.2 Multi-dimensional angular distributions	98
4.3 Angular resolution	100
4.4 Fit strategy	102
4.4.1 Feldman-cousins plug-in method	103
4.4.2 Modelling the angular distributions	104
4.4.3 Angular acceptance	105
4.4.4 Studies on a three-dimensional fit	107
4.5 Systematics uncertainties on angular observables	108
4.5.1 Angular correlations	108
4.5.2 Resolution	109
4.5.3 Efficiency description	110

4.5.4	Background parameterisation	112
4.5.5	Polarisation	112
4.6	J/ψ cross-check	113
4.7	Results	114
5	Testing lepton flavour universality with $R_{K^{*0}}$	118
5.1	Combining ratios	121
5.2	Experimental status	122
5.3	Analysis strategy	123
5.4	Dilepton invariant mass intervals	124
5.4.1	Control channels	125
5.5	Data samples and simulation	125
5.5.1	Data-simulation corrections	125
5.6	Selection	128
5.6.1	Trigger and Stripping	129
5.6.2	PID	132
5.6.3	Peaking backgrounds	134
5.6.3.1	Charmonium vetoes	134
5.6.3.2	ϕ veto	135
5.6.3.3	$B^+ \rightarrow K^+ \ell^+ \ell^-$ plus a random pion	136
5.6.3.4	Λ_b decays	136
5.6.3.5	$B^0 \rightarrow (D^- \rightarrow K e^- \bar{\nu}) e^+ \nu$	136
5.6.3.6	$B^0 \rightarrow K^{*0} (\gamma \rightarrow e^+ e^-)$	137
5.6.3.7	Other peaking backgrounds	138
5.6.4	Mis-reconstructed background	139
5.6.5	Bremsstrahlung corrected mass	139
5.6.6	Multivariate analysis	142
5.6.7	Optimisation	144
5.7	Selection summary	146
5.8	Mass fits	146
5.8.1	Muon channels	148
5.8.1.1	$B^0 \rightarrow K^{*0} (J/\psi \rightarrow \mu^+ \mu^-)$ PDF	148
5.8.1.2	$B^0 \rightarrow K^{*0} \mu^+ \mu^-$ PDF	150
5.8.1.3	Summary	152
5.8.2	Electron channels	152
5.8.2.1	Signal PDFs for the electron channels	153
5.8.2.2	Background PDFs for the electron channels	156
5.8.2.3	Summary of the fit to the electron samples	160
5.8.3	Event yields	162
5.9	Efficiency	165
5.9.1	Geometric efficiency	167
5.9.2	Reconstruction efficiency and bin migration	167
5.9.2.1	Bin migration	167
5.9.3	PID efficiency	169
5.9.4	Trigger efficiency	169
5.9.4.1	Electron triggers	170

5.9.4.2	TISTOS cross-check	172
5.9.5	Neural networks and BCM efficiencies	174
5.10	Systematic uncertainties	175
5.10.1	Choice of signal and background PDFs	175
5.10.2	Efficiency determinations	177
5.10.3	Bin migration	177
5.11	Result extraction	178
5.11.1	$R_{J/\psi}$ sanity check	179
5.11.2	$R_{K^{*0}}$	179
6	Conclusions	180
A	Decay models	193
A.1	$\Lambda_b^0 \rightarrow \Lambda \mu^+ \mu^-$ distribution	193
A.2	Bi-dimensional distribution parameters	196
A.3	$\Lambda_b^0 \rightarrow J/\psi \Lambda$ distribution	196
B	Data-simulation comparison	198
C	Systematic uncertainties on the efficiency calculation for the $\Lambda_b^0 \rightarrow \Lambda \mu^+ \mu^-$ branching fraction analysis.	201
D	Improved predictions for $\Lambda_b^0 \rightarrow \Lambda \mu^+ \mu^-$ observables.	204
E	Invariant mass fits to $B^0 \rightarrow K^{*0} \ell^+ \ell^-$ simulated candidates	207
F	Invariant mass fits to $B^0 \rightarrow K^{*0} e^+ e^-$ candidates divided in trigger categories	212

1

CHAPTER 1

2

3

Introduction

4

5 The Standard Model of particle physics (SM) is a Quantum Field Theory (QFT)
6 describing strong and electroweak (EW) interactions. It was formulated in its cur-
7 rent form in the mid-70s and has been an extremely successful predictive theory
8 since then. Almost all known phenomena from 1 eV up to several hundred GeV are
9 described well by the SM and experiments at the Large Hadron Collider (LHC)
10 are now probing the SM up to and above the TeV scale. As an example of the
11 level of accuracy of the SM, Tab. 1.1 reports the predicted and measured values of
12 the widths of the Z and W bosons [2]. Finally, in 2012 the Higgs boson, which is
13 one of the fundamental building blocks of the theory, was observed [3, 4] This is a
14 critical ingredient of the SM as it introduces a mechanism that produces particles'
15 masses [5]. Despite the success of the SM, experimentally well established effects,
16 like neutrino oscillations and the presence of dark matter, are outside the reach of
17 this theory. Furthermore, the model does not include the description of gravity,
18 which can be neglected at the EW energy scale. Therefore this motivates the search

for New Physics (NP).

Table 1.1: Predicted and measured values of the decay widths of the Z and W bosons [2].

Quantity	Predicted	Measured
Γ_Z	2.4960 ± 0.0002 GeV	2.4952 ± 0.0023 GeV
Γ_W	2.0915 ± 0.0005 GeV	2.085 ± 0.042 GeV

¹⁹

²⁰ The SM is based on the symmetry groups of strong, $SU(3)_C$, and electroweak,
²¹ $SU(2)_W \times U(1)_Y$, interactions. The subscripts C, W and Y stand for colour charge,
²² weak isospin and hyper-charge respectively. The Lagrangian describing the SM
²³ results from the application of the principle of invariance of the wave function under
²⁴ the unitary group transformations given by the product $SU(3)_C \otimes SU(2)_W \otimes U(1)_Y$,
²⁵ and leads to conservation laws such as the conservation of electric and strong charge.
²⁶ The model has then 26 free parameters, which have to be experimentally measured.

²⁷ Particles included in the SM can be grouped into a few categories depending on their
²⁸ properties and ability to interact with each other. The first distinction is between
²⁹ fermions, half-integer spin particles, and bosons, integer spin particles. Fermions
³⁰ constitute the basic building blocks of matter, while bosons are the mediators of
³¹ the interactions. Since the concept of bosonic mediators of interactions arises be-
³² cause of local gauge symmetry [6], they are called “gauge bosons”. The list of the

Table 1.2: Fundamental forces of nature together with their gauge bosons, relative strengths and range. Gravity is not included in the SM and the graviton is hypothetical at the current time.

Interaction	Mediator	Strength	Range (m)	Mediator mass
Strong	g	1	∞	0
EM	γ	10^{-3}	∞	0
Weak	Z^0, W^\pm	10^{-16}	10^{-18}	$W^\pm = 80.399 \text{ GeV}/c^2$ $Z^0 = 91.188 \text{ GeV}/c^2$
Gravity	g^0 (graviton?)	10^{-41}	∞	0

³²

³³ known interactions with their force carrier and properties is reported in Tab. 1.2.
³⁴ The matter of which we are made of is mainly composed of electrons and protons,
³⁵ which have spin 1/2; protons are in turn composed of u and d quarks, which again

³⁶ have spin 1/2. Among fermions one can then consider two smaller groups: quarks
³⁷ and leptons. Quarks carry colour charge and therefore can interact through the
³⁸ so-called strong interaction, while leptons, which do not carry colour charge, are
³⁹ insensitive to it. For each particle a corresponding anti-particle exists with opposite
⁴⁰ quantum numbers. Finally, fermions are divided into three families having similar
⁴¹ properties but different masses. This last classification embedded in the SM is also
⁴² called “flavour structure” and it will be the main tool used in this thesis; a more
⁴³ detailed description of it is given in the following sections. A schematic view of the
fundamental particles in the SM is shown in Fig. 1.1.

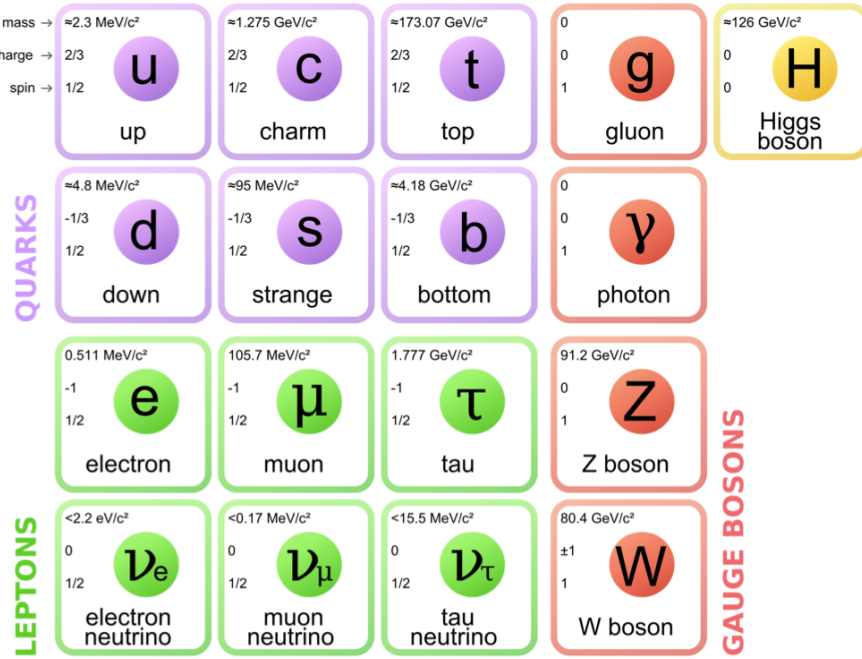


Figure 1.1: A scheme of the fundamental particles in the SM with their properties [7].

44

⁴⁵ Due to the asymptotic freedom of the strong interaction quarks cannot be observed
⁴⁶ alone but are always combined with other quarks to form color singlets [8]. Non-
⁴⁷ fundamental particles composed of quarks are called hadrons and are classified into
⁴⁸ two groups: mesons, where the color singlet is achieved by the combination of a
⁴⁹ quark and an antiquark ($q \bar{q}$), and baryons formed from three quarks ($q q q$) of
⁵⁰ different colours. Recently, in 2014 and 2015 evidence for new states, formed by
⁵¹ four and five quarks, was found [9, 10].

52 1.1 The electroweak interaction

53 The electromagnetic interaction is responsible for binding electrons and nuclei to-
54 gether to form atoms and its mediator is the photon. The weak interaction is respon-
55 sible for the β decay of nuclei and is mediated by the emission or absorption of W^\pm
56 and Z^0 bosons. Unlike the electromagnetic force, that affects only charged particles,
57 all known fermions interact through the weak interaction. The weak interaction is
58 also the only one that violates the parity symmetry, which states that interactions are
59 invariant under an inversion of spatial coordinates. This symmetry breaking arises
60 from the fact that only left-handed fermions interact through the weak interaction
61 as discovered by Wu in 1957 [11]. Similarly, the weak interaction is the only one that
62 also breaks the CP symmetry, which combines parity transformations and charge
63 conjugation. This is particularly interesting because all interactions are believed to
64 be invariant under the CPT transformation, which combines the CP transforma-
65 tion and time reversal. Hence, breaking CP the weak interaction implies that the
66 process is also not invariant under time reversal transformations. In 1968 Salam,
67 Glashow and Weinberg unified the weak and electromagnetic forces into a single
68 theory, where the coupling constants of the electromagnetic, e , and weak, g , interac-
69 tions are related through the weak mixing angle, θ_W by the relation $g \sin \theta_W = e$ [2].
70 The electroweak symmetry is spontaneously broken by the Higgs mechanism [12]
71 and this causes the W^\pm and Z bosons to become massive (see Tab. 1.2) and conse-
72 quently the weak force has a very short range. In fact, using Heisenberg's Principle
73 ($\Delta E \Delta t > \hbar$) together with Einstein's formula $\Delta E = mc^2$, which relates mass and
74 energy, and knowing that the maximum space that a particle can cover in a time
75 Δt is $r \sim c\Delta t$, qualitatively $r \sim \hbar/mc$. In this picture the carriers of the weak
76 force can travel $r \sim 2 \cdot 10^{-3}$ fm. In contrast, the photon must be massless in the
77 theory, which accounts for the long range of the electromagnetic force. The EW
78 interactions are divided into charged currents (CC) and neutral currents (NC). In
79 the first group, quarks and leptons interact with the W^\pm bosons, producing decays
80 such as $\mu^+(\mu^-) \rightarrow e^+ \nu_e \bar{\nu}_\mu (e^- \bar{\nu}_e \nu_\mu)$ and $n(\bar{n}) \rightarrow p e^- \bar{\nu}_e (\bar{p} e^+ \nu_e)$. The study of these
81 processes confirmed that only the left-handed (right-handed) component of fermions

82 (anti-fermions) takes part in weak processes. The CC interactions have a peculiar-
83 ity: they are the only interactions in the SM that violate flavour conservation at
84 tree level (see next section), while any other interaction not conserving flavour has
85 to proceed through higher order processes. The second group of EW interactions,
86 NC, corresponds to diagrams mediated by a photon or a Z boson interacting with
87 a fermion and its anti-fermion.

88 1.2 Flavour and the CKM matrix

89 “Flavour” in particle physics refers to the quark-lepton composition of a particle.
90 The introduction of flavour quantum numbers was motivated in order to explain why
91 some decays, although kinematically allowed, had never been observed. All leptons
92 are assigned a quantum number $L_\ell = 1$ (where $\ell = e, \mu, \tau$), which in the SM is
93 conserved by all interactions. This conservation is experimentally well established;
94 for example decays like $\mu^- \rightarrow e^- \gamma$ have never been observed. In the hadronic sector
95 particles carry flavour numbers described as:

- 96 • *Isospin*: $I_3 = 1/2$ for the up quark and $I_3 = -1/2$ for the down quark;
- 97 • *Strangeness*: $S = -(n_s - \bar{n}_s)$, where n_s and \bar{n}_s are the numbers of strange and
98 anti-strange quarks respectively;
- 99 • *charmness, bottomness, topness*: in analogy to strangeness they are respec-
100 tively defined as $C = -(n_c - \bar{n}_c)$, $B = -(n_b - \bar{n}_b)$, $T = -(n_t - \bar{n}_t)$.

101 As mentioned previously, in the SM the only interaction violating flavour conserva-
102 tion is the weak interaction when mediated by W^\pm bosons.

103 Measuring branching fractions of weak decays like $\pi \rightarrow \mu\nu_\mu$ and $K \rightarrow \mu\nu_\mu$, corre-
104 sponding respectively to $ud \rightarrow \mu\nu_\mu$ and $us \rightarrow \mu\nu_\mu$ processes, suggested the existence
105 of more than one coupling constant for different quarks. Nicola Cabibbo [2, 13], in
106 order to preserve the universality of weak interactions, suggested that the differences

¹⁰⁷ could arise from the fact that the doublets participating in the weak interactions are
¹⁰⁸ an admixture of the mass eigenstates. He therefore introduced the Cabibbo angle,
¹⁰⁹ θ_c , proposing that eigenstates participating to the weak interaction are rotated with
¹¹⁰ respect to the flavour eigenstates.

$$\begin{pmatrix} d_W \\ s_W \end{pmatrix} = \begin{pmatrix} \cos \theta_c & \sin \theta_c \\ -\sin \theta_c & \cos \theta_c \end{pmatrix} \begin{pmatrix} d \\ s \end{pmatrix} = \begin{pmatrix} \cos \theta_c \cdot d + \sin \theta_c \cdot s \\ \cos \theta_c \cdot s - \sin \theta_c \cdot d \end{pmatrix} \quad (1.1)$$

¹¹¹ In a six quark system one angle is not sufficient to describe a rotation but the mixing
¹¹² can be generalised using a 3×3 unitary matrix, called the CKM matrix, from the
¹¹³ names of Cabibbo, Kobayashi and Maskawa [13, 14]. The unitarity of the matrix
¹¹⁴ is required to preserve the universality of the weak interaction. Theoretically, a
¹¹⁵ $N \times N$ complex matrix depends on $2 \cdot N^2$ real parameters. Requiring unitarity
¹¹⁶ ($AA^\dagger = A(A^*)^T = I$), the number of independent parameters left is

$$(N-1)^2 = \underbrace{\frac{1}{2}N(N-1)}_{\text{Number of mixing angles}} + \underbrace{\frac{1}{2}(N-1)(N-2)}_{\text{Number of complex phases}} . \quad (1.2)$$

Therefore a 3×3 matrix depends then on 4 real parameters: three real constants and one imaginary phase. The imaginary phase generates the CP-violation which was observed in weak interactions. Figure 1.2 displays examples of CC processes together with the CKM elements associated with their vertices. Equation 1.6 reports the most

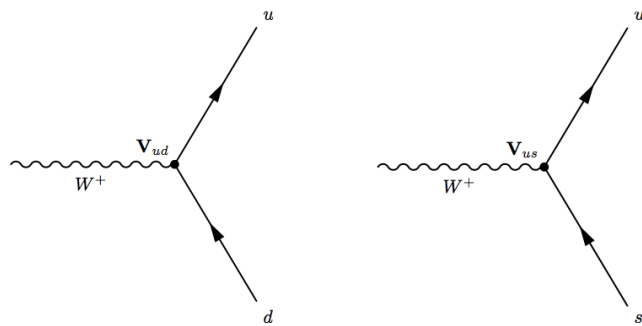


Figure 1.2: Feynman diagrams with CKM weights on weak interaction vertices

recent measured values of its elements [2] together with the widely used Wolfenstein parametrisation which highlights the hierarchical structure of the matrix. In fact

elements on the diagonal, corresponding to transitions between quarks of the same generation, are approximately 1 and become smaller and smaller going farther from the diagonal. In the formula ρ , A , and λ are the real constants and η the imaginary phase and Eq. 1.7 shows how they are related to the three mixing angles; terms further from the diagonal are proportional to higher powers of λ .

$$V_{CKM} = \begin{pmatrix} V_{ud} & V_{us} & V_{ub} \\ V_{cd} & V_{cs} & V_{cb} \\ V_{td} & V_{ts} & V_{tb} \end{pmatrix} = \quad (1.3)$$

$$= \begin{pmatrix} 0.97427 \pm 0.00015 & 0.22534 \pm 0.00065 & 0.00351^{+0.00015}_{-0.0014} \\ 0.22520 \pm 0.00065 & 0.97344 \pm 0.00016 & 0.00412^{+0.0011}_{-0.0005} \\ 0.00867^{+0.00029}_{-0.00031} & 0.0404^{+0.0011}_{-0.0005} & 0.999146^{+0.000021}_{-0.000046} \end{pmatrix} = \quad (1.4)$$

$$= \begin{pmatrix} 1 - \lambda^2/2 & \lambda & A\lambda^3(\rho - i\eta) \\ -\lambda & 1 - \lambda^2/2 & A\lambda^2 \\ A\lambda^3(1 - \rho - i\eta) & A\lambda^2 & 1 \end{pmatrix} + O(\lambda^4) \quad (1.5)$$

$$(1.6)$$

¹¹⁷

$$\begin{aligned} \lambda &= \sin(\theta_{12}) = \sin(\theta_c) \\ A\lambda^2 &= \sin(\theta_{23}) \\ A\lambda^3(\rho - i\eta) &= \sin(\theta_{13})e^{i\delta} \end{aligned} \quad (1.7)$$

¹¹⁸ The unitarity of the CKM matrix imposes constraints to its elements of the form:

$$\sum_i |V_{ik}|^2 = 1 \text{ and } \sum_k V_{ik}V_{jk}^* = 0. \quad (1.8)$$

- ¹¹⁹ These correspond to constraints on three complex numbers, which can be viewed
- ¹²⁰ as the sides of triangles in the (ρ, η) plane; these are called “unitarity triangles”.
- ¹²¹ The most commonly used unitarity triangle arises from $V_{ud}V_{ub}^* + V_{cd}V_{cb}^* + V_{td}V_{tb}^* = 0$.
- ¹²² Figure 1.3 shows a representation of such triangle together with a plot summarising
- ¹²³ the most up-to-date experimental constraints to its parameters [15]. Due to these
- ¹²⁴ unitarity constraints flavour-changing neutral currents are forbidden at tree level in

125 the SM.

126 The precise measurement of the parameters of the CKM matrix is a powerful sta-
127 bility test of the SM and sets a solid basis for new physics searches in the flavour
128 sector. One of the main goals of the LHCb experiment is to measure precisely the angle γ , which is currently the least constrained by measurements.

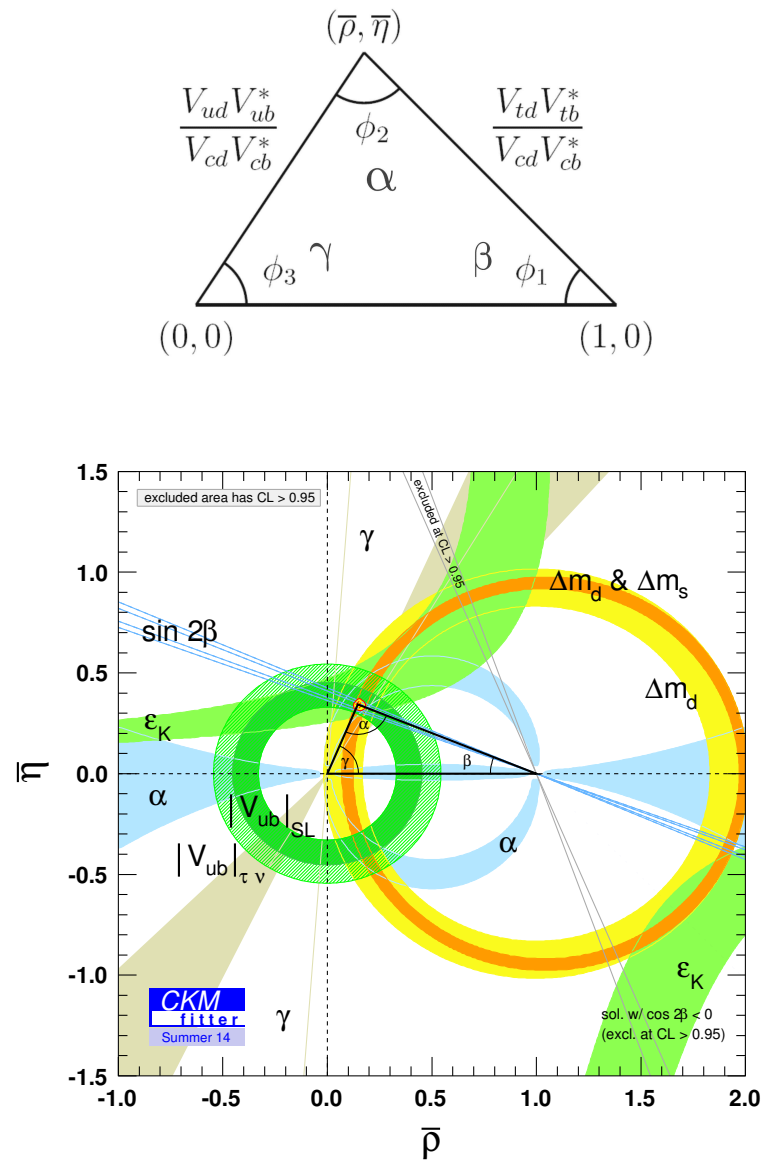


Figure 1.3: (top) A representation of the unitarity triangle and its parameters. (bottom) A summary of the most up-to-date measurements of the unitarity triangle parameters [15].

₁₃₀ 1.3 The puzzles of the SM

₁₃₁ Despite the experimental confirmation of many predictions of the SM, the theory has
₁₃₂ several limitations and is unable to account for some well established experimental
₁₃₃ facts:

- ₁₃₄ • *Dark matter*: experimental evidence tells us that the content of visible matter
₁₃₅ in the universe is not sufficient to account for the observed rotation of galaxies [16]. The most natural way to solve the problem is the hypothesis of a form
₁₃₆ of matter that interacts with the gravitational field but not with the other SM
₁₃₇ interactions.
- ₁₃₉ • *Matter-antimatter asymmetry*: a large asymmetry is observed between the
₁₄₀ quantity of matter and antimatter in the universe, $O(10^{-9})$. Assuming that
₁₄₁ both were equally created in the initial state of the universe, a condition such
₁₄₂ as the violation of the CP symmetry is necessary to account for the observed
₁₄₃ imbalance. However, the magnitude of CP violation predicted by the SM,
₁₄₄ $O(10^{-20})$, is unable to account for the observed imbalance [17].
- ₁₄₅ • *Gravity*: even though the gravitational force was the first to be discovered
₁₄₆ this is not included in the SM. When introducing gravity in the framework of
₁₄₇ QFT the theory diverges. On the other hand gravity becomes irrelevant for
₁₄₈ the small masses of particles and can be neglected to a good approximation at
₁₄₉ the EW energy scale. Many attempts have been made but there is not yet a
₁₅₀ consistent theoretical framework through which gravity can be introduced in
₁₅₁ the SM.
- ₁₅₂ • *Neutrino oscillation*: measurements of solar and atmospheric neutrinos, as
₁₅₃ well as neutrinos from nuclear reactors have established that neutrinos can
₁₅₄ change flavour while propagating in space. This is not predicted in the SM, in
₁₅₅ fact in the SM neutrinos are massless, while an oscillation requires a non-zero
₁₅₆ mass [18, 19, 20, 21].

- ¹⁵⁷ • *The hierarchy problem:* the mass of a scalar (spin 0) particle, such as the
¹⁵⁸ Higgs boson, suffers from quantum corrections due to the physics at high
¹⁵⁹ energy scales. As new physics can appear anywhere up to the Planck scale,
¹⁶⁰ $\sim 10^{19}$ GeV, at which gravity cannot be neglected any more, these corrections
¹⁶¹ can be very large and it would require a high level of fine-tuning for them to
¹⁶² cancel out and give such a small value as the one measured for the Higgs Mass,
¹⁶³ ~ 126 GeV/ c^2 [22, 3].
- ¹⁶⁴ In conclusion, even though the SM has been very successful in describing the prop-
¹⁶⁵ erties of the observed particles and their interactions so far, because of its many
¹⁶⁶ puzzles, it is believed only to be part of a more general theory or only to be valid
¹⁶⁷ up to a certain energy scale.

¹⁶⁸ 1.3.1 The flavour problem

¹⁶⁹ Flavour Changing Charged Currents (FCCC) that are mediated by the W^\pm bosons
¹⁷⁰ are the only sources of flavour changing interaction in the SM and, in particular, of
¹⁷¹ generation changing interactions, where a quark or a lepton of a family transforms
¹⁷² into one of another family. Another class of processes is the Flavour Changing
¹⁷³ Neutral Currents (FCNCs), e.g. transitions from a b quark with a charge of -1/3 to
¹⁷⁴ a s or d quark with the same charge. Examples of FCNC transitions in the quark
¹⁷⁵ and lepton sector are shown in Fig. 1.4. FCNCs are experimentally observed to
¹⁷⁶ be highly suppressed which derives from the unitarity of the CKM matrix, however
¹⁷⁷ there is no fundamental reason why there cannot be FCNCs at tree level. In fact the
¹⁷⁸ CKM matrix could be part of a larger matrix involving for example quark-lepton
¹⁷⁹ terms. This would introduce new sources of FCNCs but also allow for natural
¹⁸⁰ explanations of the equality of the proton and electron charges. On the other hand
¹⁸¹ the observation of neutrino oscillation proves that flavour is not always conserved
¹⁸² suggesting flavour structures beyond the SM. Furthermore, the values of the terms
¹⁸³ of the CKM matrix and the PMNS matrix [23, 24], which is the mixing-matrix
¹⁸⁴ equivalent to the CKM in the lepton sector, are not explained in the SM but have

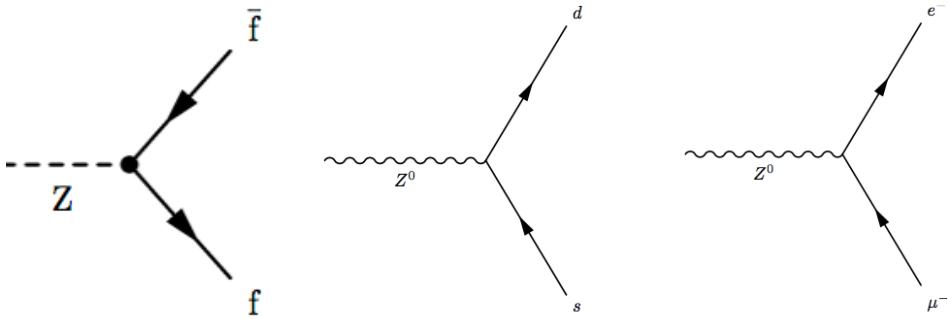


Figure 1.4: Feynman diagrams of (left) neutral current allowed in the SM, where f represents any fermion, and (center-right) FCNCs processes forbidden in the SM.

185 to be measured experimentally. These open problems motivate searches for flavour
186 symmetries and deeper motivations for flavour conservation.

187 1.4 Beyond the Standard Model

188 From the previous sections it is evident that, despite the great success of the SM,
189 there is a need to explore theories Beyond the SM (BSM). Among the most promis-
190 ing approaches there are those involving Super-Symmetry (SUSY) [25] and extra-
191 dimensions [26]. In SUSY new degrees of freedom are introduced to suppress the
192 diverging terms of the Higgs mass. This theory assumes that for each fermion there
193 is a corresponding boson and, since bosons and fermions contribute with opposite
194 sign to the mass term, these would naturally cancel out. Supersymmetry also pro-
195 vides a candidate for dark matter. In fact the lightest Super-Symmetric particle,
196 the neutralino, which in R-parity [27] conserving variants of the theory must be
197 stable, is a weakly interacting potentially heavy particle. The idea to introduce
198 extra-dimensions was triggered by the fact that, normally, gravity is not relevant
199 in particle physics but it would be natural if all forces had similar strength. By
200 adding extra dimensions to the normal three spatial dimensions, one can restore the
201 strength of gravity, as this could be dispersed by the wider space available. In all
202 these approaches constraints to masses and couplings must be imposed to maintain
203 compatibility with the SM at the electroweak scale and the existing experimental

²⁰⁴ observations.

²⁰⁵ 1.4.1 Flavour and BSM theories

²⁰⁶ Most BSM theories predict processes violating flavour conservation. Therefore, the
²⁰⁷ observation or non-observation of these processes can give important information
²⁰⁸ about new physics. BSM theories can be classified according to the amount of
²⁰⁹ flavour violation they introduce. The first class of models to consider is that with
²¹⁰ Minimal Flavour Violation (MFV). These are models in which the only sources of
²¹¹ flavour changing transitions are governed by the CKM matrix and the CKM phase
²¹² is the only source of CP violation. This definition is driven by the fact that usually
²¹³ a solution of the hierarchy problem is expected at the TeV scale, while the very
²¹⁴ small amount of flavour violation observed in measurements seems to indicate that
²¹⁵ the SM would remain valid up to much higher energy scales. It is therefore assumed
²¹⁶ that new physics must respect flavour symmetry principles, which also makes these
²¹⁷ types of models naturally compatible with the SM. Examples of such models include
²¹⁸ the MSSM with minimal flavour violation and the SM with one extra-dimension.
²¹⁹ Reviews of MFV models are presented in Refs. [28, 29]. A powerful test of MFV
²²⁰ is provided by the study of ratios between $b \rightarrow d$ and $b \rightarrow s$ transitions, because
²²¹ their hamiltonians share the same structure. One particularly important example
²²² is the ratio of B^0 and B_s^0 dimuon decay rates [30], as this is a purely leptonic decay
²²³ free from hadronic uncertainties. In the SM such ratios are approximately equal to
²²⁴ $|V_{td}/V_{ts}| \sim 1/25$, only modified by phase space and hadronic matrix elements, while
²²⁵ they can take very different values in non-MFV models.

²²⁶ In the quest for new physics an important role is also played by simplified models
²²⁷ as an intermediate model building step. Instead of constructing theories valid up to
²²⁸ the GUT scale one can consider simplified models, where the SM is extended by
²²⁹ the addition of a new sector with a limited number of parameters. Such models
²³⁰ are easier to constrain but can nevertheless point in the right direction to build
²³¹ more complete theories. The choice of the new sector to add can be driven by

the need to explain existing tensions between measurements and SM predictions or by theoretical prejudice. Two models especially relevant when studying rare decays, which are the main topic of this thesis, are Z' -penguins and leptoquarks. A Z' -penguin is a FCNC process involving a neutral field arising from an extra $U(1)$ gauge symmetry, for example $U(1)_{B-L}$, where B and L are the baryon and lepton numbers. As for the SM penguins, the Z' field contributes in loops causing modifications of the effective couplings with respect to the SM. A survey of Z' models can be found in Ref. [31]. Leptoquarks are bosonic particles that carry both quark and lepton flavour quantum numbers, which for simplicity are commonly assumed to be scalar particles. A tree level exchange of a leptoquark induces processes such as $b \rightarrow (s, d)\ell^+\ell^-$, and therefore can result in an enhancement of their decay rates with respect to the SM [32]. Leptoquarks would also provide a natural explanation for non-universal couplings to leptons.

1.5 Rare decays: a tool to search for new physics

In the Standard Model FCNC processes are forbidden at tree level but can occur through loop diagrams such as penguin or W box diagrams (see Fig. 1.5). The branching fractions of decays going through these processes are small, typically $\sim 10^{-6}$ or lower, and therefore they are called “rare decays”. Additional contributions to the virtual loops are not necessarily suppressed with respect to the SM component and this makes these decays very sensitive to new physics. This approach to new physics searches is interesting as new particles could be at high mass scales that are not accessible via direct production at colliders but their effect could be observed in loops. Radiative and penguin decays are particularly interesting because they are theoretically well understood, which allows precise comparisons with measurements. Furthermore, they provide a large quantity of observables that can be affected by new physics, not only decay rates, but also CP asymmetries and angular observables such as forward-backward asymmetries. The joint analysis of different observables can help to build a consistent picture and rule out specific models.

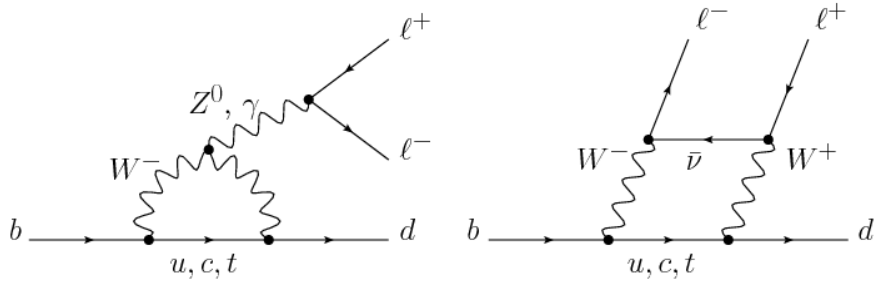


Figure 1.5: Loop Feynmann diagrams allowing $b \rightarrow d$ FCNC processes: penguin diagram (left) and W box (right).

²⁶⁰ 1.5.1 Theoretical framework: the effective Hamiltonian

²⁶¹ Rare decays of b hadrons are governed by an interplay between weak and strong
²⁶² interactions. The large masses of the W and Z bosons and top quark compared to
²⁶³ that of the b quark allow the construction of an effective theory that divides the
²⁶⁴ problem of calculating weak decay amplitudes into two parts: “short-distance” and
²⁶⁵ “long-distance” effects separated at an energy scale μ . The first part, dealing with
²⁶⁶ short distance physics, handles perturbative contributions due to energy scales above
²⁶⁷ the b mass. The second part typically deals with non-perturbative contributions.
²⁶⁸ A classic example of an effective theory is the Fermi theory of weak interactions
²⁶⁹ which describes the β decay in terms of a four-fermion interaction, where the short
 distance physics is hidden into a point-like vertex as illustrated in Fig. 1.6.

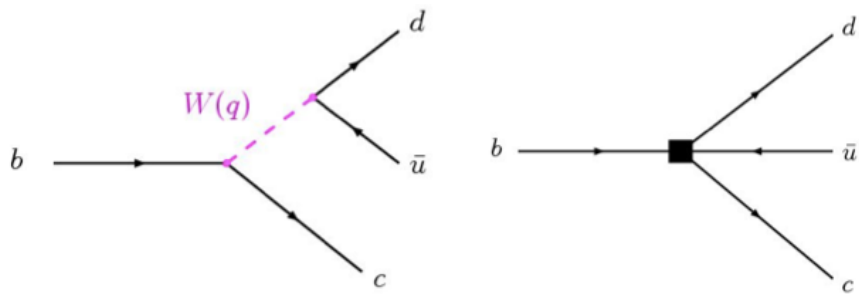


Figure 1.6: Example of a Fermi theory in which the full theory is divided between a short distance contribution, hidden in the vertex, and a long distance contribution.

²⁷⁰

²⁷¹ The effective hamiltonian [33] relevant to $b \rightarrow s/d\gamma$ and $b \rightarrow s/d\ell^+\ell^-$ transitions

272 can be written as:

$$\mathcal{H}_{eff} = \frac{-4G_F}{\sqrt{2}} \left[\lambda_q^t \sum C_i(\mu, M) \mathcal{O}_i(\mu) + \lambda_q^u \sum C_i(\mu, M) (\mathcal{O}_i(\mu) - \mathcal{O}_i^u(\mu)) \right], \quad (1.9)$$

273 where G_F denotes the Fermi coupling constant and the λ constants are the CKM
274 factors, $\lambda_q^t = V_{tb}V_{tq}^*$ and $\lambda_q^u = V_{ub}V_{uq}^*$. In $b \rightarrow s$ quark transitions, which are the main
275 topic of this thesis, the doubly Cabibbo-suppressed contributions can be neglected
276 as $\lambda_s^u \ll \lambda_s^t$. To obtain this formula the Operator Product Expansion (OPE) [34]
277 method is used, which implements a summation over all contributing operators
278 weighted by corresponding constants called Wilson coefficients. In this Hamiltonian
279 the long-distance contributions are described by the operators, \mathcal{O}_i , while the short-
280 distance physics is encoded in the Wilson Coefficients, C_i . Operators and coefficients
281 are evaluated at the renormalisation scale μ . Any particle that contributes to the
282 decay and has a mass greater than the scale μ will affect the value of at least one of
283 the Wilson coefficients, including SM particles as the top quark.

284 In order to describe SM processes the effective theory must be matched with the
285 SM by requiring the equality between each term in effective theory and the full the-
286 oretical calculation at a matching scale, typically the EW scale (μ_W). Then, using
287 the scale independence of the effective Hamiltonian, one can derive a renormalisa-
288 tion group equation for the Wilson Coefficients [35]. Taking into account only SM
289 contributions and using $\mu_W = m_b$, the Wilson Coefficients have values:

$$C_7^{SM} = -0.3, \quad C_9^{SM} = 4.2, \quad C_{10}^{SM} = -4.2 \quad (1.10)$$

290 and new physics contributions appear in the Wilson Coefficients in the form of
291 additive factors:

$$C_i = C_i^{NP} + C_i^{SM}. \quad (1.11)$$

292 The amplitudes of exclusive hadronic decays can be calculated as the expectation
293 values of the effective Hamiltonian. Given an initial state I and a final state F

²⁹⁴ (e.g. $I = B$ and $F = K^{*0}\mu^+\mu^-$) the decay amplitude can be calculated as

$$A(I \rightarrow F) = \langle I | \mathcal{H}_{eff} | F \rangle = \\ = \frac{G_F}{\sqrt{2}} \sum V_{CKM}^i \underbrace{C_i(\mu)}_{\substack{\text{Perturbative} \\ \text{Includes new physics}}} \cdot \underbrace{\langle I | \mathcal{O}_i(\mu) | F \rangle}_{\substack{\text{Non-perturbative} \\ \text{Known physics}}} , \quad (1.12)$$

²⁹⁵ where $\langle I | \mathcal{O}_i(\mu) | F \rangle$ are the hadronic matrix elements also called “form factors”.
²⁹⁶ These can be evaluated using non perturbative methods such as lattice calculations.
²⁹⁷ However, due to the limitations of these methods, they represent the dominant
²⁹⁸ source of uncertainty in theoretical calculations.

²⁹⁹ 1.5.2 Operators

³⁰⁰ Separating the left- and right-handed components the effective Hamiltonian is

$$\mathcal{H}_{eff} = \frac{4G_F}{\sqrt{2}} V_{tb} V_{ts}^* \frac{\alpha_e}{4\pi} \sum_{i=1}^{10} [C_i \mathcal{O}_i + C'_i \mathcal{O}'_i] . \quad (1.13)$$

³⁰¹ A complete basis is given by a set of 10 operators, where $\mathcal{O}_{1,2}$ are the tree level
³⁰² W operators; $\mathcal{O}_{3-6,8}$ are penguin diagrams mediated by gluons; and $\mathcal{O}_{7,9,10}$, which
³⁰³ are the operators that are relevant for radiative and leptonic penguin processes are
³⁰⁴ defined as [30]:

$$\begin{aligned} \mathcal{O}_7 &= \frac{m_b}{e} (\bar{s}\sigma^{\mu\nu} P_R b) F_{\mu\nu}, & \mathcal{O}'_7 &= \frac{m_b}{e} (\bar{s}\sigma^{\mu\nu} P_L b) F_{\mu\nu}, \\ \mathcal{O}_9 &= (\bar{s}\gamma_\mu P_L b)(\bar{\ell}\gamma^\mu \ell), & \mathcal{O}'_9 &= (\bar{s}\gamma_\mu P_R b)(\bar{\ell}\gamma^\mu \ell), \\ \mathcal{O}_{10} &= (\bar{s}\gamma_\mu P_L b)(\bar{\ell}\gamma^\mu \gamma_5 \ell), & \mathcal{O}'_{10} &= (\bar{s}\gamma_\mu P_R b)(\bar{\ell}\gamma^\mu \gamma_5 \ell), \end{aligned} \quad (1.14)$$

³⁰⁵ where $P_{L/R} = (1 \mp \gamma_5)/2$ denote the left- and right-handed chiral projections, T^a
³⁰⁶ are the QCD generators and $F_{\mu\nu}$ is the electromagnetic field tensor. The \mathcal{O}' op-
³⁰⁷ erators correspond to right-handed coupling obtained by swapping P_R and P_L in
³⁰⁸ the equations. In the SM, as well as in MFV models where the flavour violation is
³⁰⁹ entirely ruled by the CKM matrix, the C' Wilson Coefficients are suppressed by the

310 strange coupling, $C'_i \sim (m_s/m_b)C_i$. The operator \mathcal{O}_7 relates to penguin diagrams
311 that are mediated via a photon. It represents the dominant contribution to the ra-
312 diative $b \rightarrow s\gamma$ transition and contributes to $b \rightarrow s\ell^+\ell^-$ processes when the virtual
313 photon decays into a dilepton pair. The semileptonic \mathcal{O}_9 and \mathcal{O}_{10} correspond to
314 penguin diagrams mediated by a Z boson and W mediated box diagrams. These
315 are the dominant contributions in semileptonic $b \rightarrow s\ell^+\ell^-$ decays. The vertices
316 corresponding to the radiative and semileptonic operators are illustrated in Fig. 1.7

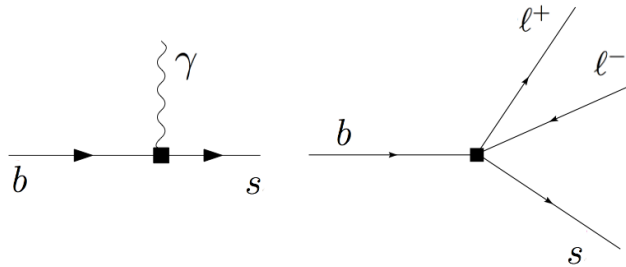


Figure 1.7: Interaction vertices corresponding to the radiative (left) and semileptonic (right) operators.

317

318 It is also common to express the semileptonic operators in a basis with left and right
319 projected leptons

$$\begin{aligned} \mathcal{O}_{LL} &= (\mathcal{O}_9 - \mathcal{O}_{10})/2 & \mathcal{O}_{LR} &= (\mathcal{O}_9 + \mathcal{O}_{10})/2 \\ \mathcal{O}_{RR} &= (\mathcal{O}'_9 - \mathcal{O}'_{10})/2 & \mathcal{O}'_{RL} &= (\mathcal{O}'_9 + \mathcal{O}_{10})/2 \end{aligned} \quad (1.15)$$

320 where the Wilson Coefficients are redefined as

$$\begin{aligned} C_{LL} &= C_9 - C_{10}, & C_{LR} &= C_9 + C_{10}, \\ C_{RR} &= C'_9 - C'_{10}, & C'_{RL} &= C'_9 + C_{10}. \end{aligned} \quad (1.16)$$

321 This basis is particularly useful in frameworks where BSM physics at a high mass
322 scale respects the $SU(2)_W$ part of the SM gauge symmetry group. Finally, in the
323 picture presented in this section all operators were considered as universal with
324 respect of the flavour of the involved leptons. However, BSM models often contain
325 sources of lepton universality violation leading to a split of the same operators

³²⁶ depending on the lepton considered: $C_i \rightarrow C_i^e, C_i^\mu, C_i^\tau$ and $\mathcal{O}_i \rightarrow \mathcal{O}_i^e, \mathcal{O}_i^\mu, \mathcal{O}_i^\tau$.

³²⁷ 1.5.3 Phenomenology of $b \rightarrow s\ell^+\ell^-$ decays

³²⁸ Semileptonic b hadron decays are characterised by two kinematic regimes which are
³²⁹ treated theoretically in different ways; Table 1.3 shows a scheme of the q^2 spec-
³³⁰ trum. The ‘high q^2 ’ is the region of low hadron recoil, $q^2 > 15 \text{ GeV}^2/c^4$, and is
³³¹ characterised by the energy of the hadron being less than the energy scale of QCD in-
³³² teractions within the meson, $\Lambda_{QCD} \sim 1 \text{ GeV}$. In this region theoretical calculations
³³³ of B meson decays can be simplified by working in the heavy quark limit, $m_b \rightarrow \infty$.
³³⁴ In this limit a Heavy Quark Effective Theory (HQET) [36] can be constructed in
³³⁵ which the heavy quark interacts only via ‘soft’ hadronic processes and an OPE in
³³⁶ $1/m_b$ is valid. The ‘low q^2 ’ region is where the light spectator quark is energetic
³³⁷ and cannot be neglected. Furthermore, the light quark interacts not only via ‘soft’
³³⁸ hadronic processes, as in HQET, but also via the so-called ‘collinear’ hadronic pro-
³³⁹ cesses. The boundary of this region can be set at $\sim 7 \text{ GeV}^2/c^4$ which corresponds
³⁴⁰ to the threshold for $c\bar{c}$ production, $(2m_c)^2$. In this region the hadronic interactions
³⁴¹ are handled by expanding in terms of the energy of the emitted energetic hadron,
³⁴² $1/E_h$, forming the so-called Soft-Collinear Effective Theory (SCET) [37]. In both
³⁴³ regions decay rates can be predicted using the different methods and the biggest un-
³⁴⁴ certainties come from the limited knowledge of hadronic transition matrix elements.
³⁴⁵ The intermediate region is characterised by the presence of charmonium resonances,
³⁴⁶ produced through tree level $b \rightarrow \bar{c}cs$ transitions and no precise theoretical calculation
³⁴⁷ is available [38].

Table 1.3: A scheme of the q^2 spectrum.

q^2	$E_{K^{*0}}$	Regime	Valid theory
$\sim 0 \text{ GeV}^2/c^4$	$\sim m_B$	Max. recoil	SCET
$< 6 \text{ GeV}^2/c^4$	$>> \Lambda_{QCD}$	Large recoil	
$q^2 \sim m_{J/\psi, \psi(2S)}^2$	$\sim 3 \text{ GeV}$	$c\bar{c}$ resonances	–
$q^2 > 15 \text{ GeV}^2/c^4$	$E_{K^{*0}} \sim \Lambda_{QCD}$	Low recoil	HQET
$q^2 = (m_B - m_K^{*0})^2$	$E_{K^{*0}} \sim 0$	Zero recoil	

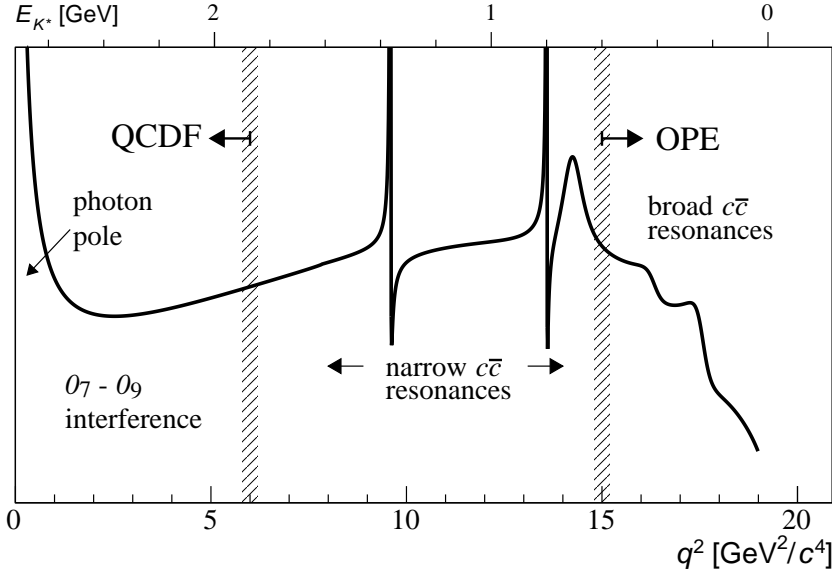


Figure 1.8: A typical q^2 spectrum of $b \rightarrow s\ell^+\ell^-$ process characterised by the photon pole at very low q^2 , charmonium resonances at central q^2 and broad resonances at high q^2 [30].

348 As can be seen in Fig. 1.8 the very low q^2 region is characterised by a peak due to
 349 the virtual photon contribution, associated with C_7 . In the region $1 - 6$ GeV^2/c^4 the
 350 interference between C_7 and C_9 becomes large, yielding sensitivity to new physics in
 351 C_9 . The $7 - 15$ GeV^2/c^4 interval is dominated by the charmonium resonances, J/ψ
 352 and $\psi(2S)$. Although these decays can be experimentally vetoed in principle char-
 353 monia affect the entire q^2 space. Finally, at high q^2 broad charmonium resonances
 354 can contribute, like those observed by LHCb in $B^+ \rightarrow K^+\mu^+\mu^-$ decays [39].

355 1.5.4 Observables in $b \rightarrow s\ell^+\ell^-$ decays

356 Rare decays and especially semileptonic $b \rightarrow s\ell^+\ell^-$ processes offer a number of ob-
 357 servables which can be used to study BSM models. The most direct effects appear
 358 in decay rates that can be enhanced by new physics but the precision on these
 359 measurements is often limited by uncertainties on the perturbative part of the cal-
 360 culations. Therefore, it is important to also look for different observables. One
 361 important class of observables are angular quantities that can often carry comple-

362 mentary information with respect to branching ratio measurements. The most basic
363 of these observable are forward-backward asymmetries that characterise the angular
364 distribution of final particles. For the $B^0 \rightarrow K^* \mu^+ \mu^-$ decay combinations of ob-
365 servables have been proposed that are independent of form factor uncertainties at
366 leading order order [30].

367 Another way to build safe observables is to construct ratios between similar decays,
368 in which uncertainties due to the hadronisation process cancel out. These observ-
369 ables include the R_H ratios, between B^0 decays into electrons and muons, that are
370 described in detail in Ch. 5. It is also interesting to compare decays which proceed
371 via the same fundamental process but where the spectator quark has a different
372 flavour. This is the case of $B^+ \rightarrow K^+ \mu^+ \mu^-$ and $B^0 \rightarrow K_s^0 \mu^+ \mu^-$ decays, which are
373 both $b \rightarrow s$ transitions where the spectator quark is an u quark in the first case
374 and a d quark in the second. The normalised difference of the branching fractions
375 of these decays is called isospin asymmetry.

376 1.6 Experimental status

377 To set the background for the analysis described in this thesis, this section reports a
378 brief review of recent results of new physics searches involving rare decays or lepton
379 flavour violation. Among these, results recently obtained by the LHCb experiment
380 show a series of anomalies with respect to the SM that have the potential to yield
381 to BSM scenarios.

382 1.6.1 Dimuon decays of b hadrons

Decays of B mesons into a pair of muons are two-body decays where the two muons
are back to back in the hadron rest frame. The simple signatures of these decays
makes them easy to study and the fact that they are unaffected by hadronic physics
in the final state makes predictions very clean and precise. Therefore these are

essential tests of the SM. The $B^0 \rightarrow \mu^+ \mu^-$ and $B_s^0 \rightarrow \mu^+ \mu^-$ decays are FCNCs that can only happen via loops and furthermore they are CKM-suppressed, which makes them particularly rare. In addition to that the decay of a pseudo-scalar B meson into two muons has a significant helicity suppression. The latest SM predictions for these decay rates are [40]:

$$\mathcal{B}(B_s^0 \rightarrow \mu^+ \mu^-) = (3.65 \pm 0.23) \times 10^{-9} \text{ and} \quad (1.17)$$

$$\mathcal{B}(B^0 \rightarrow \mu^+ \mu^-) = (1.06 \pm 0.09) \times 10^{-10}. \quad (1.18)$$

The uncertainties on these values are dominated by the knowledge of the decay constants and CKM-elements. BSM models can produce significant enhancement to these decay rates. Furthermore, the measurement of their ratio is a stringent test of the MFV hypothesis. A combination of the LHCb and CMS results measured the values [41]:

$$\mathcal{B}(B_s^0 \rightarrow \mu^+ \mu^-) = (2.8^{+0.7}_{-0.6}) \times 10^{-9} \text{ and} \quad (1.19)$$

$$\mathcal{B}(B^0 \rightarrow \mu^+ \mu^-) = (3.9^{+1.6}_{-1.4}) \times 10^{-10}. \quad (1.20)$$

Neither decay had been previously observed, while now the B_s^0 decay is observed

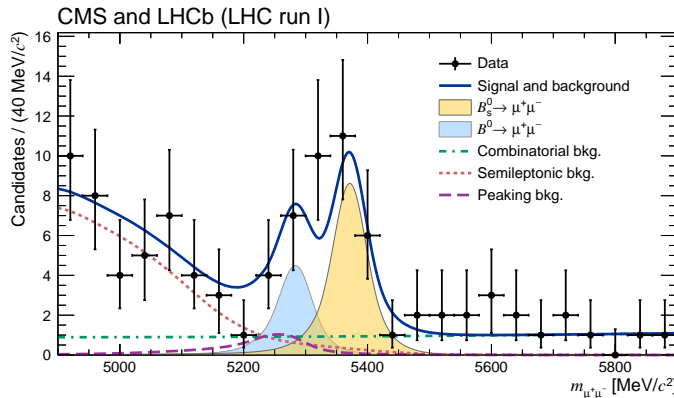


Figure 1.9: Dimuon invariant mass of B candidates showing peaks corresponding $B_s^0 \rightarrow \mu^+ \mu^-$ and $B^0 \rightarrow \mu^+ \mu^-$ decays [41].

³⁸⁶ 2σ and put strong constraints on the available parameter-space for BSM theories.
³⁸⁷ Figure 1.9 shows the fit the dimuon invariant mass of B meson candidates where
³⁸⁸ the peaks of the two decays are visible.

³⁸⁹ 1.6.2 Semileptonic $b \rightarrow s\ell^+\ell^-$ decays of b hadrons

³⁹⁰ At the LHC energies is possible to collect large data samples of semileptonic decays,
³⁹¹ especially those with muons in the final state. Many branching fractions of semilep-
³⁹² tonic B meson decays were recently measured at the LHCb experiment, including
³⁹³ $B \rightarrow K\mu^+\mu^-$, $B \rightarrow K^{*0}\mu^+\mu^-$ and $B_s^0 \rightarrow \phi\mu^+\mu^-$ [42, 43, 44]. Baryon decays were
³⁹⁴ also studied at LHCb: including the rare $\Lambda_b \rightarrow \Lambda\mu^+\mu^-$ decay [1], whose analysis is
³⁹⁵ described in this thesis. In contrast to purely leptonic decays, SM predictions for
³⁹⁶ semileptonic decays are affected by the knowledge of hadronic form factors, which
³⁹⁷ results in relatively large uncertainties, $\mathcal{O}(30\%)$. As a result measurements are now
³⁹⁸ typically more precise than predictions.

³⁹⁹ Among the measurements of angular observables that can be affected by new physics,
⁴⁰⁰ particular interest was risen by the measurement of a set of observables in $B \rightarrow$
⁴⁰¹ $K^{*0}\mu^+\mu^-$ decays, free from form factors uncertainties at leading order [45]. Most of
⁴⁰² the measurements are found to be in agreement with SM predictions with the excep-
⁴⁰³ tion of the P'_5 observable, shown in Fig. 1.10, which presents a local 3.7σ deviation.
⁴⁰⁴ Attempts to build a consistent picture point to a new physics contribution to the
⁴⁰⁵ Wilson Coefficient C_9 [46]. An angular analysis of $B^+ \rightarrow K^+\mu^+\mu^-$ decays was also
⁴⁰⁶ performed, where observables are found to be compatible with SM predictions [47].
⁴⁰⁷ Other observables for which the sensitivity to form factors effects is reduced are the
⁴⁰⁸ CP asymmetry between B and \bar{B} decays, \mathcal{A}_{CP} , and the isospin asymmetry between
⁴⁰⁹ B^0 and B^+ decays, \mathcal{A}_{CP} . Due to the small size of the corresponding CKM elements,
⁴¹⁰ CP asymmetries of $B^0 \rightarrow K^{(*)}\mu^+\mu^-$ decays are tiny in the SM, $O(10^{-3})$. In BSM
⁴¹¹ models new sources of CP violation can arise and therefore \mathcal{A}_{CP} measurements are
⁴¹² a powerful null test of the SM. The isospin asymmetry is not zero in the SM due
⁴¹³ to isospin breaking effects in the form factors. This is expected to be $\sim 1\%$ at low

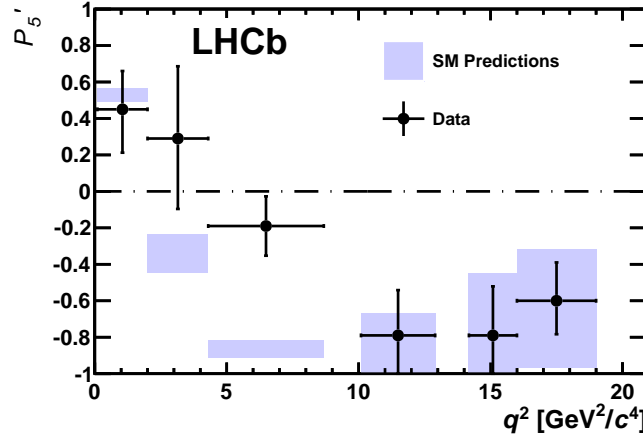


Figure 1.10: Measurement of the observable as a function of q^2 , showing a tension with SM predictions in the 2–6 GeV^2/c^4 region [45].

Asymmetry	$B^0 \rightarrow K^+ \mu^+ \mu^-$		$B^0 \rightarrow K^{*0} \mu^+ \mu^-$	
	$1.1\text{--}6 [\text{GeV}^2/\text{c}^4]$	$15.0\text{--}22.0 [\text{GeV}^2/\text{c}^4]$	$1.1\text{--}6 [\text{GeV}^2/\text{c}^4]$	$15.0\text{--}19.0 [\text{GeV}^2/\text{c}^4]$
\mathcal{A}_{CP}	0.004 ± 0.028	-0.005 ± 0.030	0.094 ± 0.047	-0.074 ± 0.044
\mathcal{A}_I	$-0.10^{+0.08}_{-0.09} \pm 0.02$	$-0.09 \pm 0.08 \pm 0.02$	$0.00^{+0.12}_{-0.10} \pm 0.02$	$0.06^{+0.10}_{-0.09} \pm 0.02$

Table 1.4: Measurement of CP and isospin asymmetry in $B^0 \rightarrow K^{*0} \mu^+ \mu^-$ decays from the LHCb experiment [30].

⁴¹⁴ q^2 and increase to $\sim 10\%$ as q^2 tends to zero. The LHCb experiment, using the
⁴¹⁵ full dataset collected in Run I, corresponding to an integrated luminosity of 3 fb^{-1}
⁴¹⁶ and $\sim 10^9$ B decays, measured both of these asymmetries to be consistent with
⁴¹⁷ zero [42, 48], as reported in Tab. 1.4. Recently, progress was also made measuring
⁴¹⁸ also electron channels. The branching fraction of the $B^0 \rightarrow K^{*0} e^+ e^-$ decay was
⁴¹⁹ measured to be $(3.1 \pm 1.3) \times 10^{-7}$ in the dilepton mass interval $30\text{--}1000 \text{ MeV}/c^2$ [49].
⁴²⁰ Furthermore, for the first time angular observables were measured for this decay
⁴²¹ and found to be consistent with SM predictions [50].

⁴²² 1.6.3 Lepton Flavour Violation searches

⁴²³ Several Lepton Flavour Violation (LFV) searches are linked to rare decays as they
⁴²⁴ involve small branching ratios in the SM that can be enhanced by BSM physics. Lepto-
⁴²⁵ n flavour conservation is experimentally well-established measuring the branching
⁴²⁶ ratios of decays of muons into electrons and no neutrinos, but has no strong the-

oretical explanation in the context of the SM. In fact it is already observed that flavour is not conserved in neutrino oscillations. The best-studied decays violating lepton flavour are rare muon decays including $\mu^+ \rightarrow e^+ \gamma$ and $\mu^+ \rightarrow e^+ e^- e^+$. Since muons can be abundantly produced and the final states are simple, these decays provide the best constraints to LFV. The present best upper limits are 1.2×10^{-11} for the radiative decay and 1.0×10^{-12} for $\mu^+ \rightarrow e^+ e^- e^+$ obtained respectively by the MEGA [51] and SINDRUM [52] experiments. Several LFV searches in the B sector have recently been performed at the LHCb experiment including decays such as $B^0 \rightarrow e\mu$ [53] and τ decays such as $\tau \rightarrow \mu^+ \mu^- \mu$ [54]. None of these searches has found evidence of new physics so far and therefore they set limits, constraining the parameter space available for BSM models. Figure 1.11 shows a summary of the best limits set at different times on LFV searches [55].

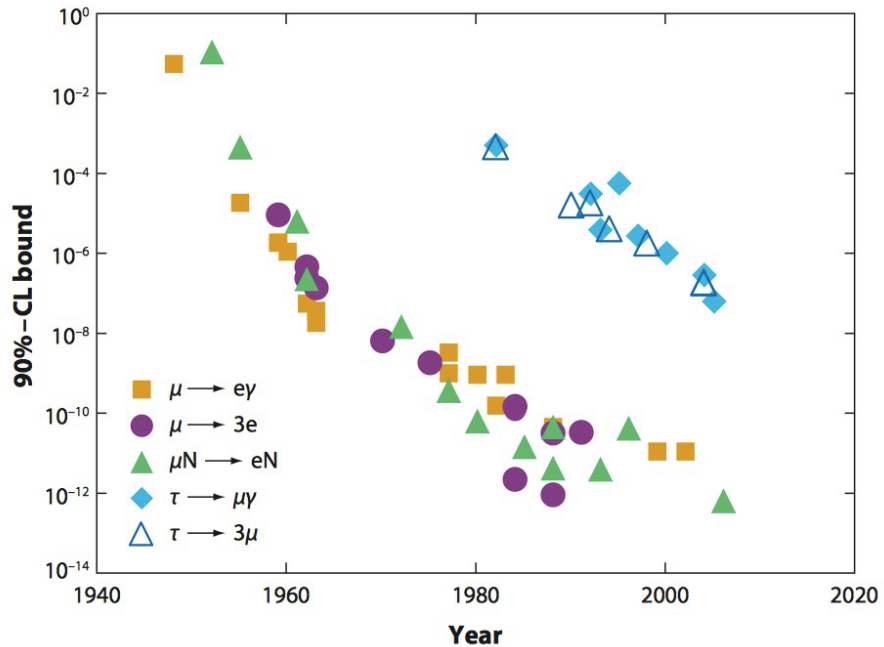


Figure 1.11: Summary of limits set in LFV searches as a function of time [55].

439

CHAPTER 2

440

441

The LHCb detector at the Large Hadron Collider

442

443

2.1 The Large Hadron Collider

444 The Large Hadron Collider (LHC) [56] is a synchrotron particle accelerator with a
445 circumference of 27 km located about 100 m underground at CERN in the surround-
446 ings of Geneva, Switzerland. Two proton beams circulate in opposite directions
447 around the ring and cross each other in four points, in which particle detectors are
448 placed. These include two general-purpose detectors, ATLAS and CMS, sitting on
449 opposites sides of the ring and two smaller detectors, ALICE and LHCb that are
450 designed to study specific topics (see Fig. 2.1).

451 Each beam consists of a series of proton bunches, up to a maximum of 2835. Each
452 bunch consists of about 10^{11} protons and the bunch spacing is such that the nominal
453 bunch crossing rate is 40 MHz. The beams are injected into pre-accelerators and
454 then pass into the LHC through the CERN acceleration system shown in Fig. 2.1.

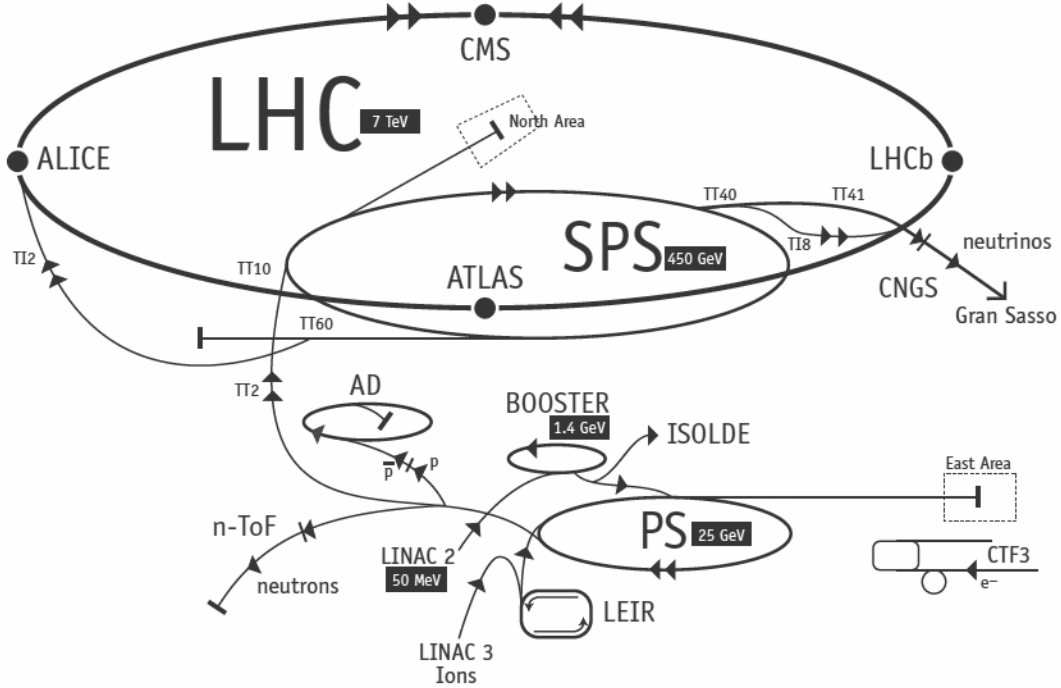


Figure 2.1: Scheme of CERN accelerators.

455 Protons are produced from hydrogen gas and are initially accelerated to an energy
 456 of 50 MeV in a linear accelerator (LINAC). Then they are injected into the Proton
 457 Synchrotron Booster (PSB), where they are boosted to an energy of 1.4 GeV, into
 458 the Proton Synchrotron (PS) to 25 GeV and into the Super Proton Synchrotron
 459 (SPS) to 450 GeV. Finally, protons enter into the LHC storage ring, where they are
 460 accelerated from injection energy to the final one by radio frequency (RF) cavities.
 461 The beams are steered around the ring by 8 T magnetic fields produced by 15 m
 462 long superconducting niobium-titanium dipole magnets and focused by quadrupole
 463 magnets. The LHC magnets use a design in which both proton beam pipes are
 464 contained in the same housing, allowing a common liquid helium cooling the system
 465 to be used. The LHC began colliding proton beams in “physics mode” in 2009 at
 466 a centre of mass energy of $\sqrt{s} = 900$ GeV and from April 2010 to November 2011
 467 accelerated beams at $\sqrt{s} = 7$ TeV (3.5 TeV per proton beam) with a maximum
 468 instantaneous luminosity of $3 \cdot 10^{33} \text{ cm}^{-2}\text{s}^{-1}$, while in 2012 the energy was increased
 469 to 8 TeV. The LHC maximum design energy is 14 TeV, and its design luminosity is
 470 $10^{34} \text{ cm}^{-2}\text{s}^{-1}$. After a long shut down to upgrade and maintain the machine, a new

471 run started in June 2015, in which protons are collided at a centre of mass energy
472 of $\sqrt{s} = 13$ TeV. At this energy the total proton-proton cross-section is expected to
473 be roughly 100 mb.

474 **2.2 The LHCb detector**

475 The LHCb detector [57] was designed to study decays of B and D mesons, mainly
476 looking for CP-violating processes. In 2011, running at a centre of mass energy of 7
477 TeV, the cross-section for $b\bar{b}$ production was measured to be $284 \pm 53 \mu b$ [58], while
478 it will be $\sim 500 \mu b$ at the current LHC energy, 13 TeV. At these high energies,
479 proton-proton interactions produce highly boosted virtual gluons which produce $b\bar{b}$
480 pairs at small angles, close to the beam pipe. For this reason the LHCb detector is
481 designed to have a very forward angular coverage. The detector is fully instrumented
482 from 10 mrad to 300 mrad, corresponding to an interval $2 < \eta < 5$, where η is the
483 “pseudorapidity”, a quantity defined as:

$$\eta = -\ln(\tan(\theta/2)), \quad (2.1)$$

484 where θ is the angle between a particle’s momentum and the beam direction ¹.

485 At LHCb’s collision point the luminosity can be adjusted by displacing the beams
486 from head on collisions while keeping the same crossing angle. This allows the exper-
487 iment to keep an approximately constant instantaneous luminosity, compensating
488 for the reduction in beam intensity due to extended operation periods. This also
489 means that the average number of interactions per bunch crossing can be regulated,
490 which is important because the detector efficiency, especially in detecting secondary
491 vertices, decreases for events with an high number of primary vertices (PV). Reduc-
492 ing the particle occupancy through the detector also keeps radiation damage to a

¹LHCb’s reference system has the z axis in the direction of the beam, the x axis directed to the centre of the accelerator and y is directed upward. Then we define θ as the angle with the beam direction and ϕ as the position around the beam in the xy plane, taking $\phi = 0$ on the x axis. The origin, $(x, y, z) = (0, 0, 0)$, corresponds to the centre of the interaction area.

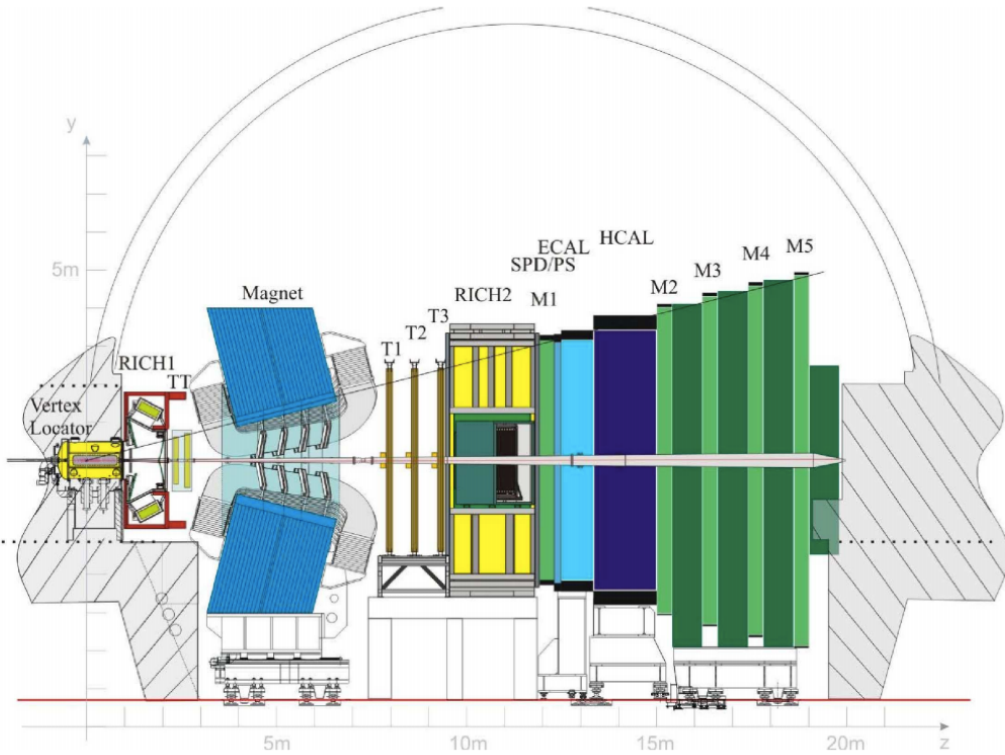


Figure 2.2: A side view of the LHCb detector [57].

minimum. Until the end of 201 the instantaneous luminosity was $3 \cdot 10^{32} \text{ cm}^{-2}\text{s}^{-1}$, corresponding to an average number of 1.5 PVs per bunch crossing and at the end of 2011 LHCb had collected an integrated luminosity of 1 fb^{-1} . In 2012 the luminosity was increased and a further 2 fb^{-1} of data were collected.

Experiments like BaBar at the Stanford Linear Accelerator (SLAC), Belle at KEK at J-PARC (Japan) and the Tevatron experiments at Fermilab have made measurements in heavy flavour physics which have so far been found to be consistent with the SM predictions. However, some of the deviations from the SM are expected to be very small. Therefore LHCb was designed to make the most precise measurements in heavy flavour physics to test the consistency of the SM and look for new physics.

The LHCb detector includes a high-precision tracking system consisting of a silicon-strip vertex detector surrounding the pp interaction region, and a larger silicon-strip and drift tubes detectors located on both sides of a dipole magnet with a bending power of about 4 Tm. Charged hadrons are identified using two Ring-Imaging

507 Cherenkov detectors (RICH) [59]. Photon, electron and hadron candidates are iden-
508 tified by a calorimeter system and muons by a system composed of alternating layers
509 of iron and multi-wire proportional chambers [60]. A schematic view of the detector
510 is shown in Fig. 2.2 and more details on each sub-detector are given in the following
511 sections.

512 2.3 The magnet

513 Charged particle trajectories are deflected horizontally in the magnetic field so that
514 their momentum can be measured from the radius of curvature. The LHCb dipole
515 magnet is composed of two coils supported by an iron yoke and is shaped to fit
516 the LHCb angular acceptance. Unlike the other LHC experiments, LHCb uses a
517 warm magnet which can be easily ramped allowing the field polarity to be inverted
518 periodically. When the polarity is flipped, particles of a given sign are bent in the
519 opposite direction. This method is used to limit systematic uncertainties that can
520 arise due to performance variations in different areas of the detector and average
521 out using data taken in both polarities. A current of 5.85 kA flows in the magnet
522 generating an integrated magnetic field of 4 Tm for 10 m long tracks. In order to
523 achieve the required momentum precision the magnetic field must be mapped with
524 a 10^{-4} precision. For this reason a grid of 60 sensors is positioned inside the magnet
525 and provides real time magnetic field maps.

526 2.4 Tracking system

527 B mesons have lifetimes of approximately 1.5 ps. At the LHC energies, this means
528 they travel about 1 cm before decaying to form a displaced vertex. To study specific
529 decays, it is therefore important to be able to separate the particles produced at the
530 primary pp vertex and at the B decay secondary vertex (SV). The tracking system
531 consists of the Vertex Locator (VeLo), and 4 tracking stations: the Tracker Turicensis

532 (TT), which are located before the magnet and the T1, T2 and T3 stations, located
 533 after of the magnet. The latter three stations are in turn formed by two subsystems:
 534 the Inner Tracker (IT) close to the beam-line, where the particle density is greatest,
 535 and the Outer Tracker (OT) covering the rest of the acceptance.

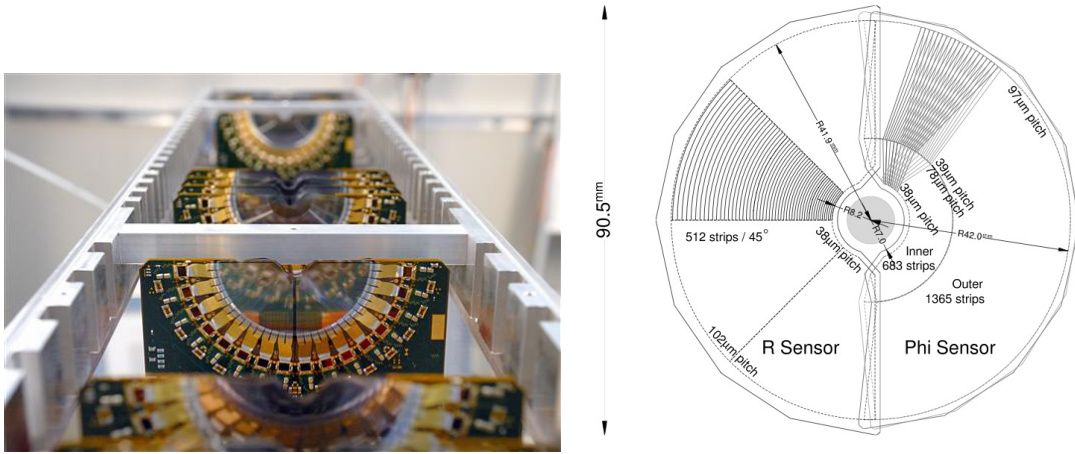


Figure 2.3: On the left VeLo sensors mounted in line and on the right a schematic view of one sensor [57].

536

537 The VeLo accurately measures positions of tracks close to the interaction point
 538 which is essential to reconstruct production and decay vertices of bottom and charm
 539 hadrons. The VeLo is composed by 21 silicon modules that surround the beam axis
 540 and are positioned from $z = -18$ cm to $+80$ cm. The sensitive region of the VeLo
 541 starts at an inner diameter of only 8 mm from the beam axis and it is able to
 542 detect particles within a pseudorapidity range $1.6 < \eta < 4.9$. The VeLo is housed
 543 in its own vacuum vessel of thin aluminium foil, which protects the vacuum of the
 544 beam pipe from any outgassing. The silicon layers composing the VeLo consist of
 545 two modules each including two types of sensors: the ϕ -sensor, which measures the
 546 azimuthal position around the beam, and the R-sensor, which measures the radial
 547 distance from the beam axis. A sketch of the VeLo sensors is shown in Fig. 2.3. The
 548 sensors are $300 \mu\text{m}$ thick and to ensure that they cover the full azimuthal angle the
 549 right-side module is placed 1.5 cm behind the left-side module on the z -axis and

550 they overlap. There are two modules which cover the backward direction and are
 551 used as a veto for multiple interactions; this is called the pileup system.

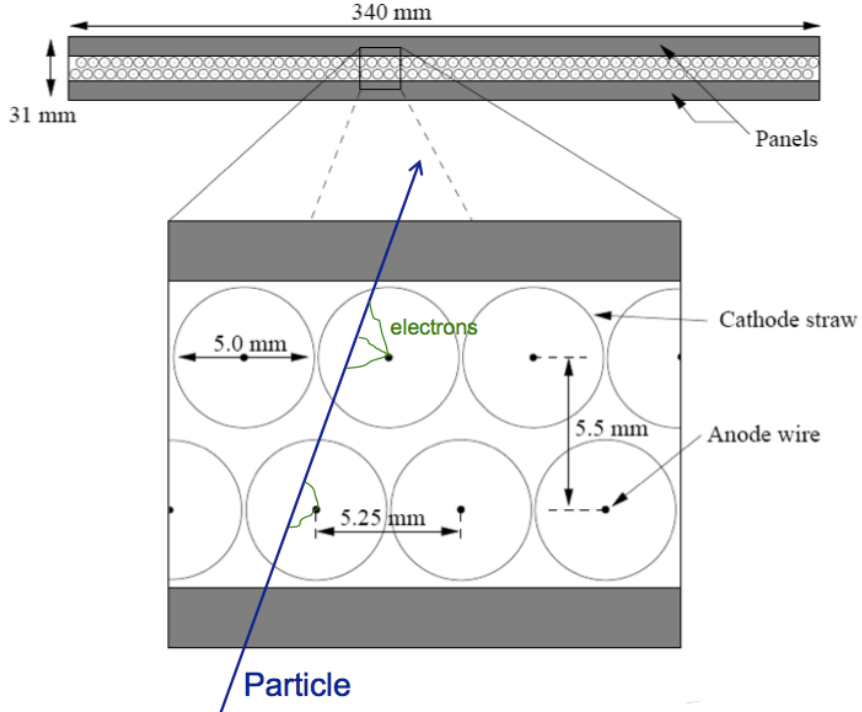


Figure 2.4: Sketch of the straw tubes which constitute the Outer Tracker layers [57].

552

553 The IT and TT both use silicon strips and together constitute the Silicon Tracker
 554 (ST). Straw tubes are instead used in the OT, of which a sketch is shown in Fig. 2.4.
 555 The IT requires a higher inner granularity because of the greater flux of particles
 556 close to the beam pipe. In fact, it covers only 1.3% of the total area of IT plus
 557 OT but it contains about 20% of the tracks. Each ST station has four detection
 558 layers: the first and last are vertical, measuring the track position in x , while the
 559 second and third layers are rotated by an angle of +5 and -5 degrees, which allows
 560 the measurement of the y coordinate. The TT is placed upstream of the magnet to
 561 allow the reconstruction of tracks from low-momentum particles, which are bent out
 562 of the downstream acceptance. Overall the tracking system provides a measurement
 563 of momentum, p , with a relative uncertainty that varies from 0.4% at 5 GeV/ c to
 564 1.0% at 200 GeV/ c . The impact parameter (IP), namely the minimum distance of a

track to a primary vertex, is measured with a resolution of $(15 + 29/p_T) \mu\text{m}$, where p_T is the component of the momentum transverse to the beam, in GeV/c . The z -axis position of a PV reconstructed with 35–40 tracks can be measured with a precision of roughly $50\text{--}60 \mu\text{m}$. The decay products of B mesons tend to have high IP values because the B decay imparts transverse momentum to them. Therefore, accurate IP and vertex displacement measurements allow LHCb to distinguish effectively between B meson decays and background processes.

2.5 Calorimeters

In general the main purpose of a calorimeter system is to determine the energy of particles but in LHCb it is mostly used to help the identification electrons and hadrons. Sampling calorimeters, as those used in LHCb, are composed of layers of absorber and active material. Particles interact with the absorber layers and produce a cascade of secondaries, that multiply quickly and are detected by the active part, which is usually composed of scintillating layers. The light produced is detected by photo-multipliers (PMTs) and it is approximately proportional to the energy of the deposited particles. Calibration is then used to translate the signal into an energy measurement. The LHCb’s calorimeter system consists of the Scintillator Pad Detector (SPD), the Pre-Shower Detector (PS) as well as the Electromagnetic Calorimeter (ECAL) and the Hadronic Calorimeter (HCAL). A sketch of the LHCb calorimeters is shown in Fig. 2.5. The SPD/PS cells are read out with PMTs located outside the LHCb acceptance, while the ECAL and HCAL have individual PMTs located on the modules. All four detectors are segmented, which allows the energy deposits to be associated to the tracks detected by the tracking system. The segmentation of the cells varies according to the distance from the beam pipe due to the different track density.

The most difficult identification in LHCb is that of electrons. The rejection of a high background of charged pions is achieved using a longitudinal segmentation of the

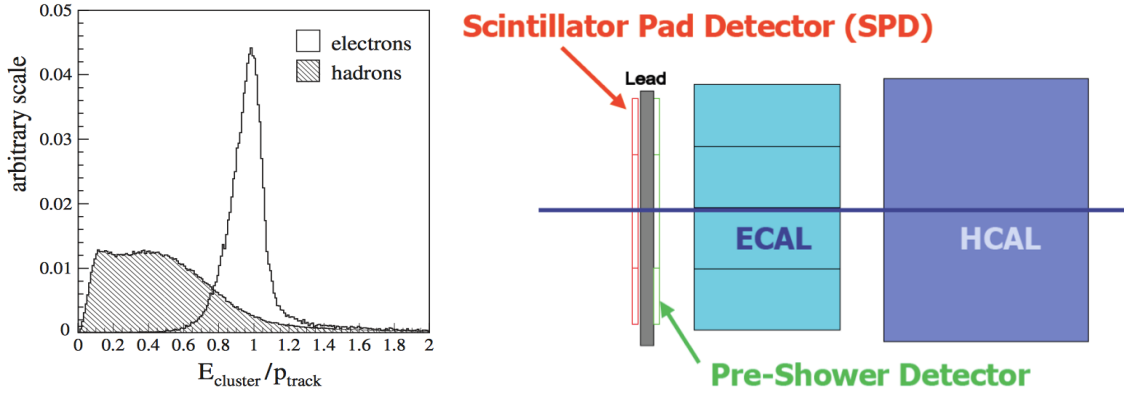


Figure 2.5: (left) The ratio of the energy deposited in the ECAL and the particle momentum, which allows the separation between electrons and hadrons [57]. (right) A schematic of the calorimeter system.

592 electromagnetic calorimeter which is provided by the PS detector added in front of
 593 the main electromagnetic calorimeter, ECAL. Electrons also have to be distinguished
 594 from high energy π^0 s and photons. For this purpose the SPD calorimeter, detecting
 595 charged particles, is located in front of the PS and ECAL detectors. Figure 2.5
 596 illustrates how the ratio between the energy detected in the ECAL and a particle's
 597 momentum allows the separation of electrons and hadrons.

598 The ECAL is formed by 66 lead layers (2 mm thick) separated by 4 mm thick plastic
 599 scintillator layers. In order to obtain the highest energy resolution the showers
 600 from high energy photons must be fully absorbed. For this reason the ECAL has a
 601 thickness of 25 radiation lengths and its resolution is measured to be $\sigma_{\text{ECAL}}(E)/E =$
 602 $10\%/\sqrt{E(\text{GeV})} + 1\%$ [57], which results in a mass resolution of $\sim 70 \text{ MeV}/c^2$ for
 603 B mesons and $\sim 8 \text{ MeV}/c^2$ for π^0 . The HCAL is mainly used for triggering and
 604 it is similar to the ECAL but with 4 mm thick scintillator layers and 16 mm thick
 605 absorber layers. The trigger requirements on the HCAL resolution do not depend
 606 on the containment of the hadron showers as much as for the ECAL, therefore, due
 607 to space limits, its thickness is only 5.6 interaction lengths and its resolution is given
 608 by $\sigma_{\text{HCAL}}(E)/E = 69\%/\sqrt{E(\text{GeV})} + 9\%$.

⁶⁰⁹ 2.5.1 Bremsstrahlung recovery for electrons

⁶¹⁰ Bremsstrahlung is an electromagnetic radiation produced by charged particles that
⁶¹¹ undergo an acceleration. Typically electrons produce Bremsstrahlung when de-
⁶¹² flected by atomic nuclei. The probability of emitting bremsstrahlung radiation is
⁶¹³ proportional to the inverse of the squared mass of the particle ($1/m^2$) and therefore
it is most relevant for electrons. At LHC energies, if electrons radiate after the mag-

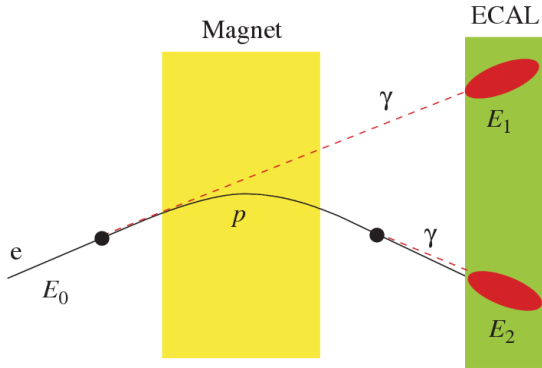


Figure 2.6: Schematic view of the bremsstrahlung recovery [57].

⁶¹⁴

⁶¹⁵ net, the photon will hit the same calorimeter cell as the electron and the energy will
⁶¹⁶ be automatically recovered, as illustrated in Fig. 2.6. However, if the photon is emit-
⁶¹⁷ ted before the magnet, the electron will be deflected by the magnetic field whereas
⁶¹⁸ the photon will continue on its initial trajectory, with its energy being deposited in
⁶¹⁹ a different part of the calorimeter. Missing this energy results in a poorer recon-
⁶²⁰ structed invariant mass resolution, so it is desirable to recover these bremsstrahlung
⁶²¹ photons. A tool for bremsstrahlung recovery is available in the LHCb analysis soft-
⁶²² ware. This tool looks for other clusters in the calorimeter and, reconstructing the
⁶²³ trajectory of the electron, checks if they may be associated with photons emitted.
⁶²⁴ The photon energy is then added to the electron and its momentum is recalculated.
⁶²⁵ For more information see Ref. [61].

626 2.6 RICH

627 The two RICH detectors are a special feature of LHCb, as it is the only experiment
 628 at LHC using them. These detectors take advantage of the Cherenkov radiation
 629 produced by particles passing through a medium with speed higher than the speed
 630 of light in the medium. The Cherenkov light, as shown in Fig. 2.7, is produced in
 631 cones with a specific opening angle depending on the velocity of the particle. The
 632 relation between the angle and the particle velocity can be written as

$$\cos \theta = \frac{1}{\beta n}, \quad (2.2)$$

where $\beta = v/c$ and n is the refraction index of the medium.

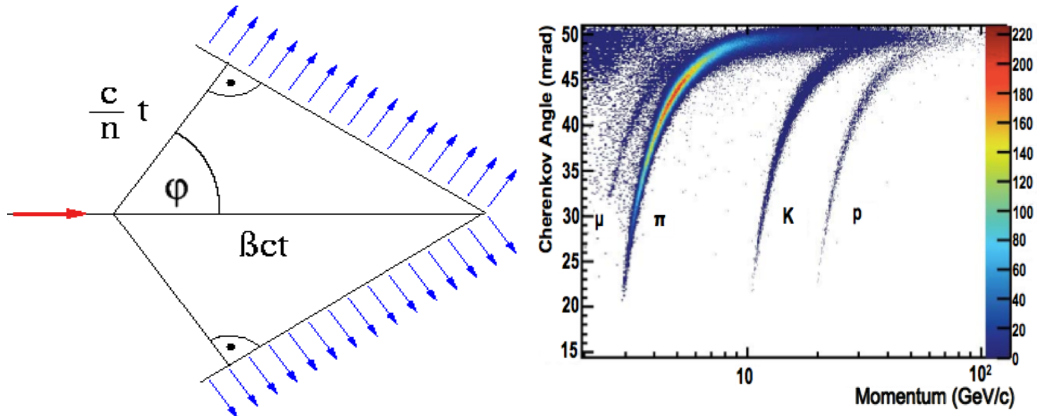


Figure 2.7: (left) A sketch of Cherenkov light emission and on the right the Cherenkov angle versus the particle momentum, where one can see that the study of the Cherenkov angle allows distinguish particles identities. (right) Measured Cherenkov angle as a function of particle momentum [57].

633

634 RICH 1 is located before the magnet in order to cover a larger angular accep-
 635 tance. Its purpose is to ensure particle identification over the momentum range
 636 $1 < p < 70 \text{ GeV}/c$. It uses two radiators: C_4F_{10} that covers the momentum range
 637 $5 - 70 \text{ GeV}/c$ and silica aerogel which covers $1 - 10 \text{ GeV}/c$. RICH 2 is positioned
 638 after the magnet and tracking stations and it identifies higher momentum particles
 639 from approximately $20 \text{ GeV}/c$ up to beyond $100 \text{ GeV}/c$ using CF_4 as a radiator.
 640 The Cherenkov light produced when charged particles travel through the radiators,

is reflected and focussed using mirrors, which are tilted so that the ring image is reflected onto arrays of PMTs. The radius of the ring can be used to measure the opening angle of the Cherenkov cone because of the known geometry. The photo-detectors are located outside of the LHCb acceptance in order to reduce the amount of material that the particles have to traverse. Pattern recognition algorithms are then used to reconstruct the Cherenkov rings.

2.7 The muon system

It is essential for many of the key physics analyses in LHCb to be able to identify muons in decay final states. Muons are the most penetrating particles that can be detected at LHC experiments, so the muon chambers are the farthest sub-detectors from the interaction point. The muon system consists of five stations (M1 - M5), the first one being located before the calorimeters in order to improve p_T measurements. The remaining four stations are behind the HCAL and are separated from each other and interleaved with 80 cm thick iron blocks, which absorb hadrons, electrons and photons to ensure that only muons reach the final muon station. A schematic of the muon system is shown in Fig. 2.8. Only muons with a minimum momentum of 10 GeV/c traverse all of the five stations and, for positive identification of a muon, the trigger requires a signal in each of them. Each station has a detection efficiency of at least 95% and the detectors also provide position measurements. Since there is a larger particle flux close to the beam pipe, the stations are divided into four concentric rectangular regions (R1-R4) with increasing cell size, which results in a similar occupancy over the four regions. All of the muon stations use Multi Wire Proportional Chambers (MWPC) except for the inner region of M1, where the particle flux is too high. In this region triple-GEM (Gas Electron Multiplier) detectors are used because of their better ageing properties as they have to withstand a rate up to 500 kHz cm⁻² of charged particles. These detectors consist of three gas electron multiplier foils sandwiched between anode and cathode.

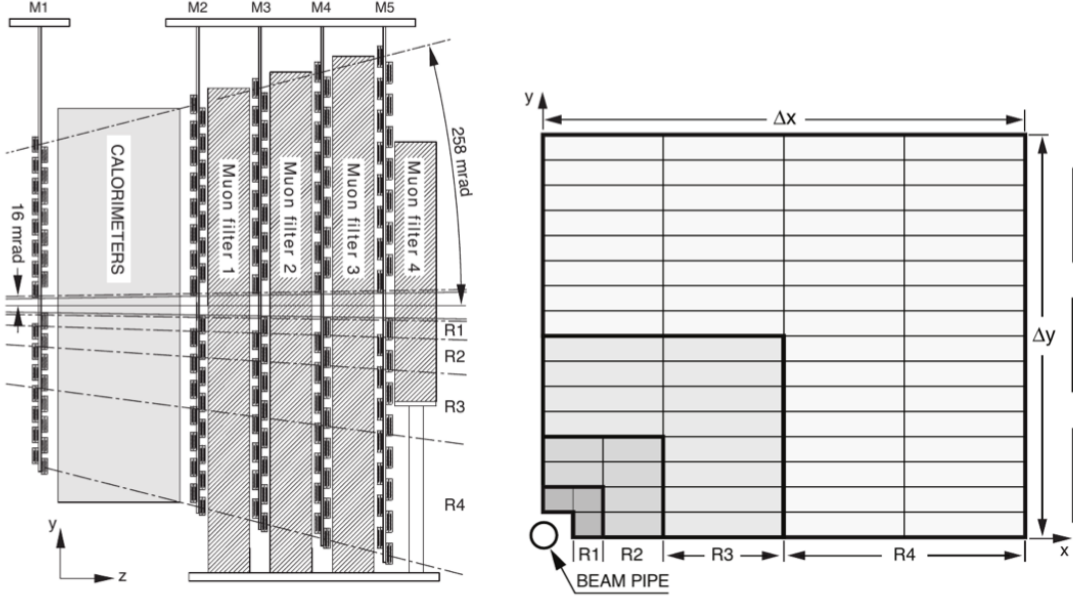


Figure 2.8: The LHCb muon system [57].

668 2.8 Particle identification

669 Particle identification (PID) is an important feature in LHCb and it is performed in
 670 various ways. The electromagnetic calorimeters can distinguish between pions and
 671 electron, the muon chambers identify muons and the RICH detectors can be used
 672 to identify heavier charged particles such as protons and kaons.

673 The RICH assigns an ID to a track calculating the global likelihood for the observed
 674 distribution of hits being consistent with the expected distribution from various
 675 ID hypotheses. The algorithm iterates through each track and recalculates the
 676 likelihood when the track PID hypothesis is changed to that of an electron, muon,
 677 kaon or proton. For electrons and muons additional information from the calorimeter
 678 and muon systems is also used. The hypothesis which maximises the likelihood is
 679 assigned to the track.

680 To quantify the quality of the ID the pion hypothesis is used as a reference point
 681 and the probability of a specific ID is given in terms of Log-Likelihood difference
 682 between the given ID hypothesis and the pion one. This variable is called Delta

683 Log-Likelihood (DLL) and denoted with ‘‘PID’’. For example:

$$\text{PID}_K = \text{DLL}_{K-\pi} = \log(\mathcal{L}_K) - \log(\mathcal{L}_\pi) \quad (2.3)$$

684 quantifies the probability of a particle being a kaon rather than a pion. Figure 2.9
 685 shows the efficiency for correctly identifying and mis-identifying kaons and protons as
 686 a function of the measured momentum of the particle. For kaons the efficiency drops
 687 at momenta below 10 GeV, where they fall below threshold for the gas radiators.
 688 The DLL cuts enable LHCb physics analyses to distinguish between kinematically
 689 similar decays with different final states, such as B^0 and B_s^0 mesons decaying into
 690 two hadrons. Figure 2.10 illustrates the power of particle identification, showing
 691 how the application of DLL cuts can be used to isolate $B^0 \rightarrow \pi^+\pi^-$ decays from
 other two-body B decays. The identification of muons is particularly important in

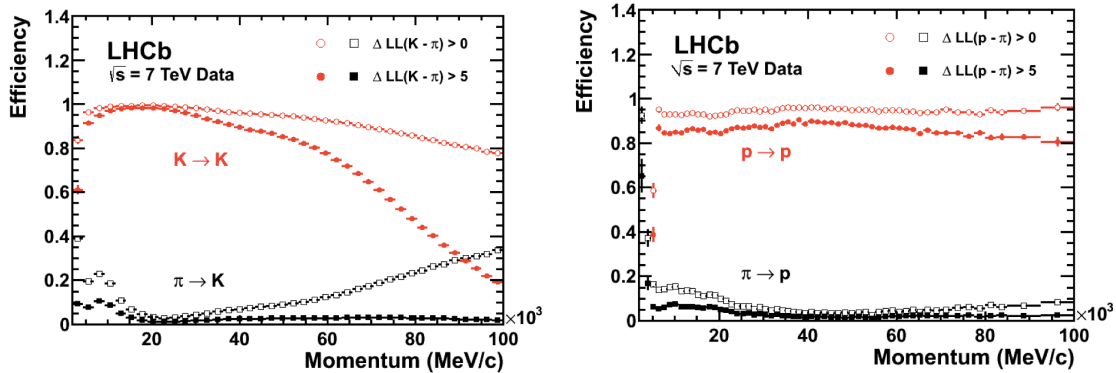


Figure 2.9: Particle Identification performances for kaons (left) and protons (right) as a function of the measured momentum of the particles [57].

692

693 LHCb and it is quantified using two variables: the $\text{DLL}\mu$ and the `isMuon` variable.
 694 The latter is a boolean variable determined by defining a ‘field of interest’ around
 695 a track trajectory extrapolated through the muon chambers. The variable is set to
 696 true if hits in multiple muon stations are found in the field of interest.

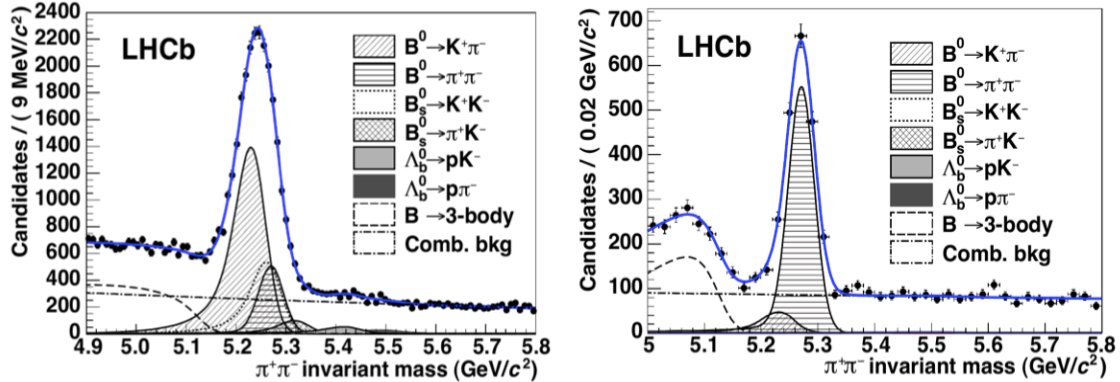


Figure 2.10: Invariant mass peak of the $B^0 \rightarrow \pi^+\pi^-$ decay before (left) and after (right) the application of PID requirements [62].

697 2.8.1 PID calibration

698 In order to be able to calculate detection efficiencies, a “data-driven” method was
 699 developed. The calibration software is referred to as `PIDCalib` package [62]. This
 700 tool uses decays where final particles can be identified thanks to their kinematic
 701 properties. For example the $K_s^0 \rightarrow \pi^+\pi^-$ decay has a clear signature with a displaced
 702 vertex and can be easily singled out from other decays and used to test pion ID
 703 efficiency. The narrow peaks of the $J/\psi \rightarrow \mu^+\mu^-$ and $J/\psi \rightarrow e^+e^-$ decays allow
 704 muon and electron efficiencies to be calibrated. A “tag-and-probe” method is used
 705 in this case, where only one of the two leptonic tracks is reconstructed requiring
 706 the correct identity and the other one is used to probe the PID efficiency. Finally,
 707 $\phi \rightarrow KK$ samples and $D^{*+} \rightarrow D(\rightarrow K^-\pi^+)\pi^+$ decays, where the D^{*+} is used to tag
 708 the decay, are used to test the kaon efficiency. In all cases the residual background
 709 is subtracted using the $s\mathcal{P}$ lot technique [63].

710 2.9 Trigger and software

711 The LHCb trigger system [64] consists of a hardware stage, L0, based on information
 712 from the calorimeters and muon system, followed by a software stage, the High-
 713 Level Trigger (HLT), which applies a full reconstruction of the events. To increase

⁷¹⁴ performance, the HLT is further split into two stages, HLT1 and HLT2. The HLT1
⁷¹⁵ phase happens in real time and saves data in local disks while the HLT2 phase uses
⁷¹⁶ the resources available during periods with no beam. The event selected by the
⁷¹⁷ HLT2 stage are then saved for offline analysis. Figure 2.11 shows a scheme of the
⁷¹⁸ trigger system. The bunch crossing frequency is 40 MHz, which corresponds to an
⁷¹⁹ instantaneous luminosity of $2 \cdot 10^{32} \text{ cm}^{-2}\text{s}^{-1}$ for LHCb. About 15% of the total
⁷²⁰ number of $b\bar{b}$ pairs produced will contain at least one B meson with all of its decay
⁷²¹ products within the detector acceptance. This rate needs to be reduced to about
2 kHz at which the events can be written to disk.

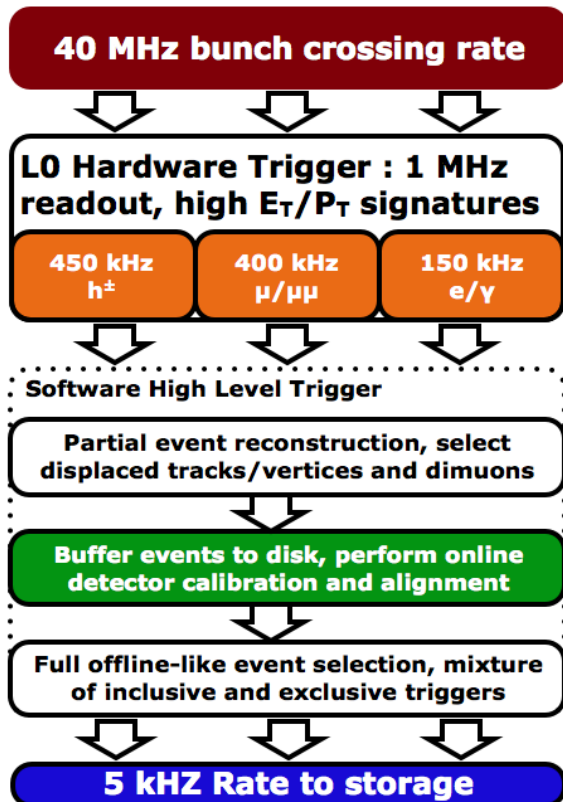


Figure 2.11: Scheme of the LHCb trigger system [57].

⁷²²

⁷²³ The L0 trigger reduces the rate of visible interactions from 10 MHz to 1 MHz.
⁷²⁴ Due to the heavy mass of B mesons, they often produce particles with high en-
⁷²⁵ ergy and momentum. Therefore the trigger selects events with large E_T deposits in
⁷²⁶ the calorimeter or high p_T muons. The event is classified as L0Muon if it was trig-
⁷²⁷ gered due to information from the muon detector, while the information from the

728 calorimeters is used to divide the events into five categories: `L0Photon`, `L0Electron`,
729 `L0LocalPion`, `L0GlobalPion`, `L0Hadron`. The PS detector information is converted
730 to a photon flag (`PS && !SPD`) or an electron flag (`PS && SPD`). The “local” label of
731 the `L0Pion` trigger refers to π^0 reconstructed through their $\gamma\gamma$ decay, where the two
732 photons fall in the same ECAL element, they are labelled “global” otherwise. The
733 first four calorimeter triggers require energy clusters in the ECAL, while `L0Hadron`
734 requires clusters also in the HCAL. The HLT1 uses information from the VELO
735 and trackers performing a partial reconstruction of the event and reduces the rate
736 to 2 kHz by adding requirements of the IP and χ^2 of tracks. Finally, the HLT2
737 involves a full reconstruction of the event and includes many “lines” designed to
738 select specific decay structures.

739 LHCb also developed an extended simulation software in order to reconstruct ef-
740 ficiencies and signal shapes. In the simulation, pp collisions are generated using
741 PYTHIA8 [65, 66] with a specific LHCb configuration [67]. Decays of hadronic par-
742 ticles are described by EVTGEN [68], and final state radiation is generated using
743 PHOTOS [69]. Finally, the interaction of the generated particles with the detec-
744 tor and its response are implemented using the GEANT4 toolkit [70] as described
745 in Ref. [71]. For this analysis in this thesis, the ROOT framework [72] is used to
746 analyse data and the RooFit package to perform maximum likelihood fits. A multi-
747 variate analysis is also performed based on the NeuroBayes package [73, 74], which
748 provides a framework for neural network training.

749 2.10 Constrained kinematic fits

750 The resolution of key variables, such as the measured invariant mass of decaying
751 particles, can be improved by imposing constraints on the measured quantities to
752 remove redundant degrees of freedom. The four-momentum conservation can be
753 ensured at each vertex and the origin and decay vertices of a particle are related via
754 the momentum of the particle. Furthermore, additional constraints can be imposed

due to a particular decay hypothesis such as the known invariant masses of final and intermediate particles. In order to do this the `DecayTreeFitter` tool was developed by the BaBar experiment and later used by LHCb [75]. The algorithm takes a complete decay chain and parametrises it in terms of vertex positions, decay lengths and momentum parameters. These parameters are then fit simultaneously, taking into account the relevant constraints, including the information from photons. Figure 2.12 illustrates the effect of the application of the kinematical fit on the 4-body invariant mass of the final daughters of the $\Lambda_b^0 \rightarrow J/\psi \Lambda$ decay. The resolution in this case improves by over a factor of 2. Furthermore, the χ^2 from the kinematic fit can be used to quantify the compatibility with a specific decay structure, which helps to separate candidates where random particles from the event have been added to the decay tree, or where one or more particles is not reconstructed or mis-identified.

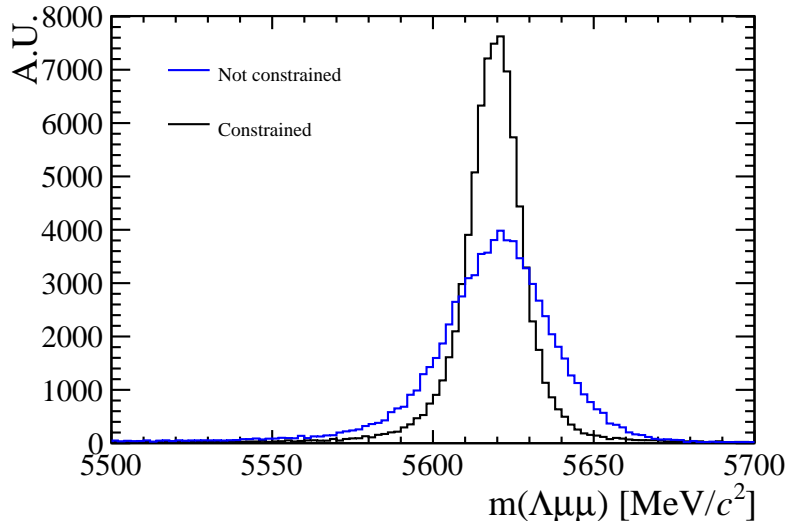


Figure 2.12: Invariant mass of the final daughters of simulated $\Lambda_b^0 \rightarrow J/\psi \Lambda$ decays calculated with and without constraints using the `DecayTreeFitter` tool.

766

2.11 Validation of hadronic processes in the simulation

768 Particle-antiparticle asymmetries are of major interest for LHCb and detection ef-
769 ficiencies are usually obtained from simulation. It is therefore important, in order

770 to limit systematic uncertainties, to have a model that parametrises correctly the
771 cross-sections of particles and antiparticles or at least their ratio.

772 The LHCb simulation software propagates particles through the detector using the
773 GEANT4 toolkit [57]. This offers a variety of models for physics processes over a
774 wide range of energies for both electromagnetic and strong interactions. Given a
775 combination of projectile, target and energy there can be several models applicable
776 with different reliability and computational costs. GEANT4 provides a number of
777 pre-packaged physics lists each representing complete and consistent sets of models
778 chosen to be appropriate for a given use case. In LHCb mainly two hadronic physics
779 lists are considered:

780 • **LHEP** (Low and High Energy Parametrisation): based on a parametrised
781 modelling of all hadronic interactions for all particles. This list combines
782 the High Energy Parametrised model (HEP) and the low energy one (LEP).
783 There is a sharp switch from the low to the high energy model at 25 GeV.
784 The modelling of elastic scattering off a nucleus and of nuclear capture also
785 proceeds via parametrised models.

786 • **FTFP_BERT**: includes the following models:

- 787 – Bertini cascade model (BERT) [76], which simulates the intra-nuclear cas-
788 cade, followed by pre-equilibrium and evaporation phases of the residual
789 nucleus, for protons, neutrons, pions and kaons interaction with nuclei
790 at kinetic energies below 9.9 GeV. The Bertini model produces more
791 secondary neutrons and protons than the LEP model, yielding a better
792 agreement with experiment data.
- 793 – FTFP model, which implements high energy inelastic scattering of hadrons
794 by nuclei using the FRITIOF model [77]. The change between the two
795 models happens with a linear shift from BERT to FTF that starts at 4
796 GeV and ends at 5 GeV.

797 Figure 2.13 summarises the composition of the different models.

798

799 When two models overlap in an energy interval the choice of the model for each
 800 interaction is made using a random number: the probability to select each model
 801 varies linearly from 0 to 100% over the overlap range. Because of the differences of
 802 the two models in the overlap region, unphysical discontinuities can be produced as
 803 a function of energy.

804 2.11.1 Geometry and interaction probability

805 The results presented in the following sections are produced using the version v45r0
 806 of the full LHCb framework for simulation, Gauss [71], interfaced to GEANT4
 807 v95r2p1. A simple geometry setup is used in order to be able to calculate in a
 808 clean way the interaction cross-sections in a specific material. This is constituted
 809 by a series of rectangular boxes filled with the most relevant materials for LHCb:
 810 Aluminium, Silicon and Beryllium. For each material three boxes are defined with
 811 different thicknesses (1mm, 10mm, 50mm). These values are chosen to be indicative
 812 of the amount of material present in the LHCb detector.

813 The simplest quantity available to extract the cross-section is the interaction prob-
 814 ability (P_{int}), defined as:

$$P_{int} = \frac{N_{int}}{N_{tot}}, \quad (2.4)$$

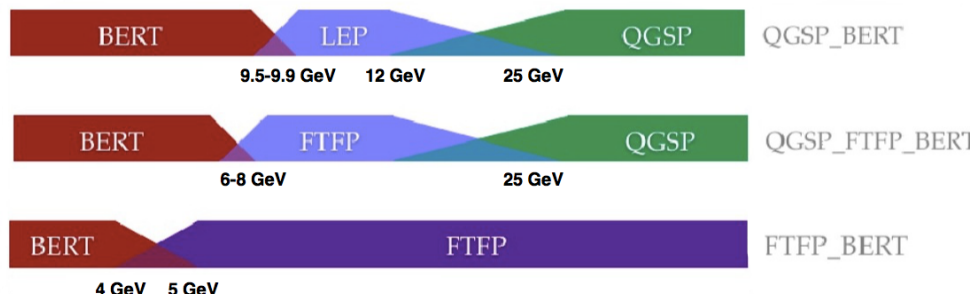


Figure 2.13: Diagram of LHEP, FTFP_BERT and QGSP_BERT models composition as a function of energy.

815 where N_{int} is the number of particles which interacted in the material and N_{tot} is
816 the number of generated particles. As GEANT4 provides an ID for the end process
817 of a particle (e.g. 121 for inelastic interaction, 111 for elastic, 201 for decay) it
818 is possible to distinguish the inelastic and elastic probabilities of interaction and
819 therefore cross-sections.

820 To compare simulation and data the cross-section and P_{int} are linked by the following
821 formula valid for thin layers:

$$\sigma_{int} = \frac{A}{\rho N_A \Delta x} \cdot P_{int}, \quad (2.5)$$

822 where ρ is the density of the material and A is its mass number, Δx is the thickness
823 of the considered layer and N_A is the Avogadro number.

824 2.11.2 PDG prediction

In the Review of Particle Physics [2] cross-sections of protons and neutrons are parametrised as:

$$\sigma_{tot}^{ab} = Z^{ab} + B^{ab} \log^2(s/s_M) + Y_1^{ab}(s_M/s)^{\eta_1} - Y_2^{ab}(s_M/s)^{\eta_2}, \quad (2.6)$$

$$\sigma_{tot}^{\bar{a}\bar{b}} = Z^{ab} + B^{ab} \log^2(s/s_M) + Y_1^{ab}(s_M/s)^{\eta_1} + Y_2^{ab}(s_M/s)^{\eta_2}, \quad (2.7)$$

825 where $s_M = (m_a + m_b + M)^2$ and $B^{ab} = \lambda \pi (\frac{\hbar c}{M})^2$. Some of the constants in these
826 equations are universal and valid for any kind of collision: $M = 2.15$, $\eta_1 = 0.462$, η_2
827 = 0.551, $\lambda = 1$ (for p, n and γ) and 1.63 (for d). The other ones are characteristic
828 of each type of collision and are listed in Tab. 2.11.2. In these formulae the particle-
829 antiparticle asymmetry arises from the last term which has opposite sign in the
830 two equations. This term becomes less and less important with increasing energies.
831 Therefore a net asymmetry is found at low energies, while the cross-sections tend
832 to a common point at high energy and continue increasing logarithmically.

2.11.3 Validation results

This section reports particle and antiparticle cross-sections and their ratios compared, where available, with predictions and with data from the COMPASS experiment [78]. Figure 2.14 shows the probability of interaction for protons and anti-protons in 1mm of Aluminium using the FTFP_BERT and LHEP models compared with COMPASS data and Fig. 2.15 shows the ratios of $\sigma_{\bar{p}}^{tot}/\sigma_p^{tot}$ together with the PDG prediction. A difference of 40% is found between the two considered models for 1 GeV incoming anti-protons. This difference becomes negligible at higher energies. The discrepancies between the two physics lists for kaons and pions are of a few percents (2–3%) and usually constant with the energy. From the comparison with data and PDG predictions it can be qualitatively concluded that the FTFP_BERT model gives a better description of hadronic interactions at low energies, while both models give good results at high energy, above ~ 10 GeV. The tool developed for this studies is not limited to cross-sections but can also give information on other simulated quantities. As an example, Fig. 2.11.3 shows a comparison between the types of particles generated in inelastic collisions of protons and anti-protons onto Aluminium using different models. Physics lists can give very different results, for example the LHEP model does not produce photons in inelastic collisions. However, it is difficult to use these quantities for validation as there is no data available for comparison.

854

Proj / Targ	Z^{ab}	Y_1^{ab}	Y_2^{ab}
$\bar{p},p / p$	34.71	12.72	7.35
π^\pm / p	19.02	9.22	1.75
K^\pm / p	16.56	4.02	3.39
K^\pm / n	16.49	3.44	1.82
$\bar{p},p / n$	35.00	12.19	6.62

Table 2.1: Values for the constants Z^{ab} , Y_1^{ab} and Y_2^{ab} [2], which parametrise hadronic cross-sections.

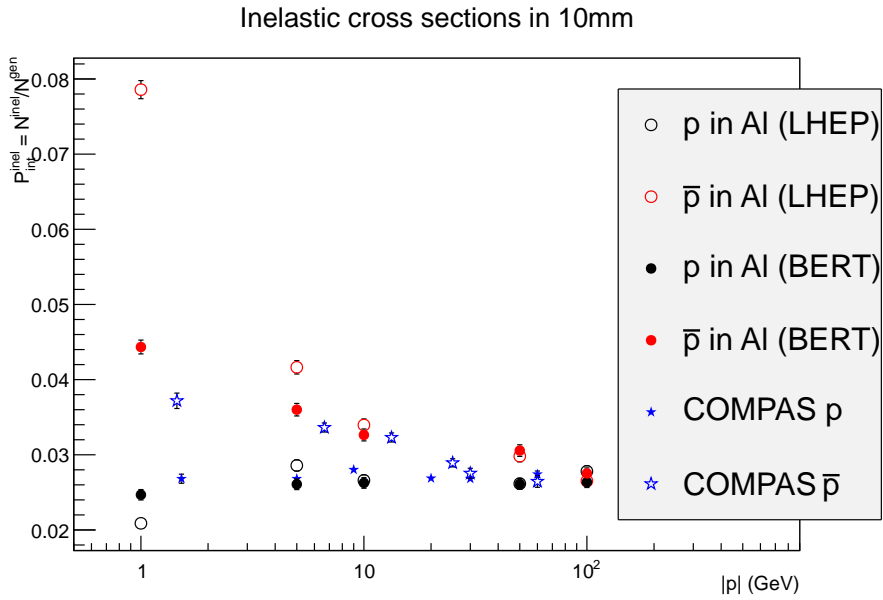


Figure 2.14: Probability of interaction for protons and anti-protons in Aluminium as a function of the projectile momentum. Two physics lists are used to generate events that can be compared with data from the COMPASS experiment.

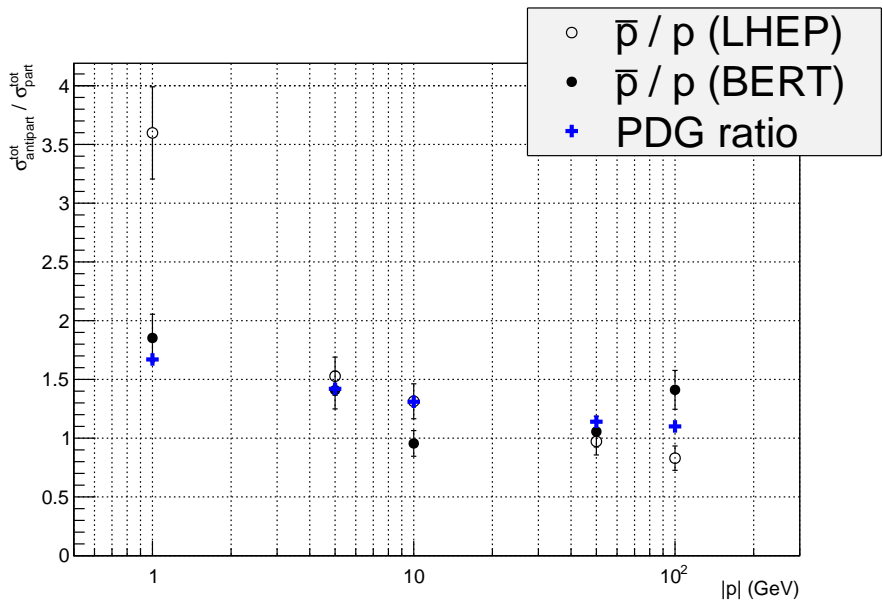


Figure 2.15: Ratio of antiproton over proton total interaction cross-section as a function of energy compared with PDG predictions.

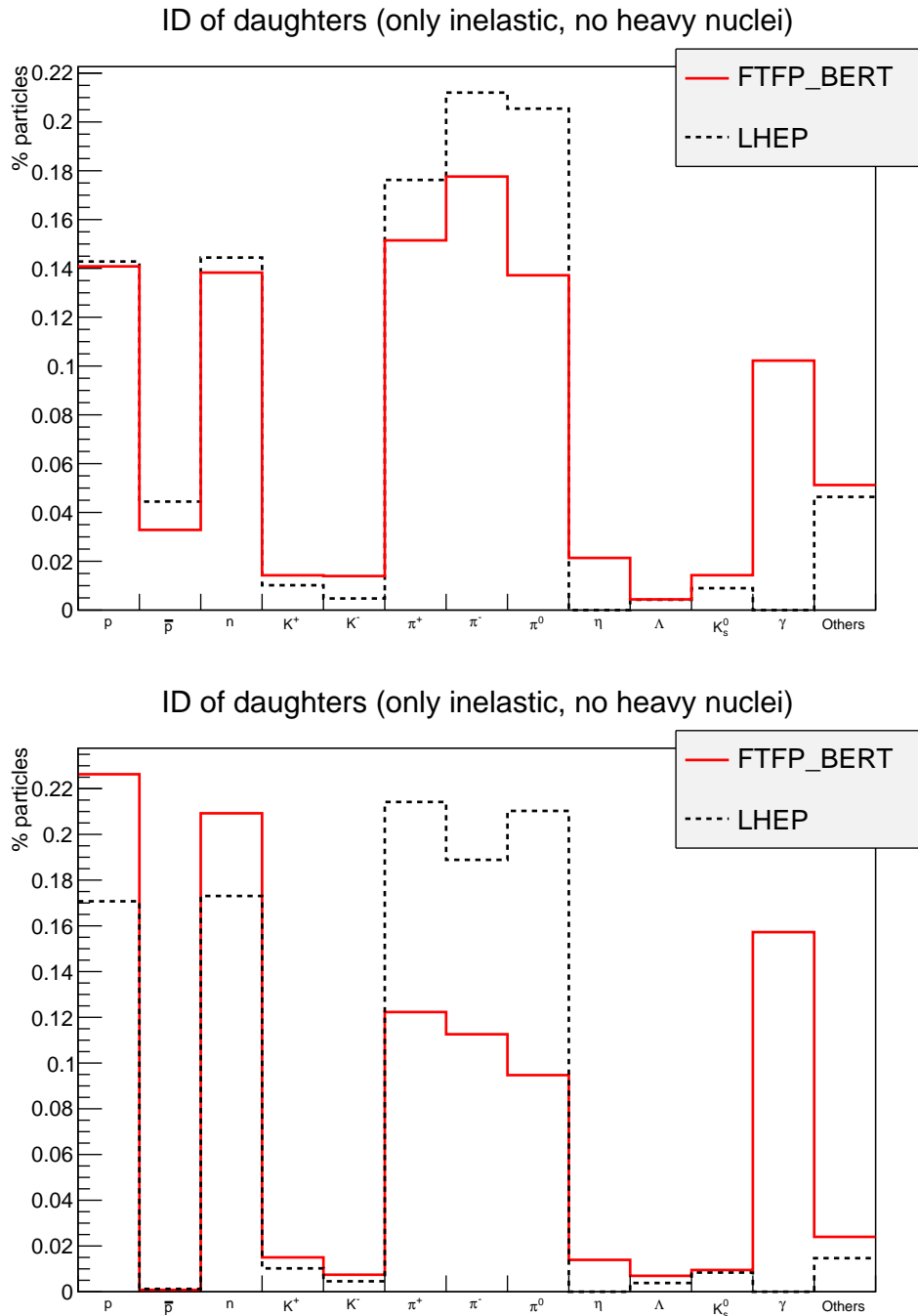


Figure 2.16: Composition of secondary particles produced in 100 GeV protons (top) and anti-protons (bottom) collisions in 1 mm Aluminium.

855 2.12 Material budget studies

856 It is important for many analysis to quantify the amount of material present in the
 857 detector, for example to estimate the amount of multiple scattering. In GEANT4
 858 particles are propagated in steps through the detector and for each step the frame-
 859 work analyses the geometry to understand in what material the particle is and
 860 modifies its trajectory accordingly. A tool was developed where neutrinos are used
 861 as probes to scan the detector summing the radiation length seen at each step up
 862 to a certain point.

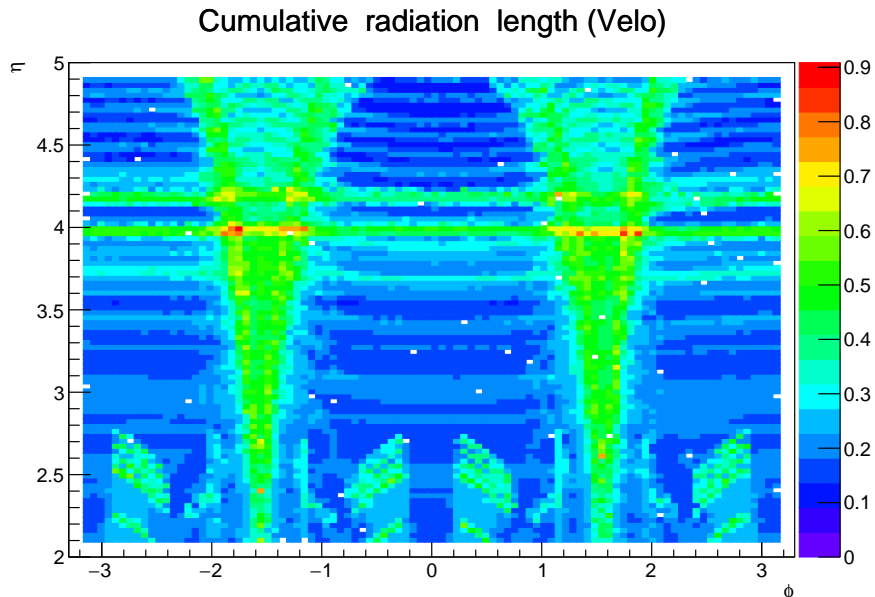


Figure 2.17: Map of cumulative radiation length traversed by a particle starting from the interaction point up to the end of the VeLo.

863 Neutrinos are used as they do not bend in magnetic field and do not interact with
 864 the detector to any appreciable extent. Thin air planes are inserted after each
 865 sub-detector. When these are traversed by the neutrinos, the information about
 866 the accumulated radiation and interaction length is saved. In this way it is
 867 possible to obtain maps of the detector, such as the one shown in Fig. 2.17. Using
 868 the tool developed for this study it is also possible to obtain the cumulative
 869 radiation and interaction lengths as a function of the position along the beam axis
 870 and the pseudorapidity. As an example Fig. 2.18 shows the average radiation

length as a function of the distance from the interaction point. Furthermore, it is possible to displace the primary vertex from its position, normally set at the origin, in order to study how this translates into the amount of material traversed.

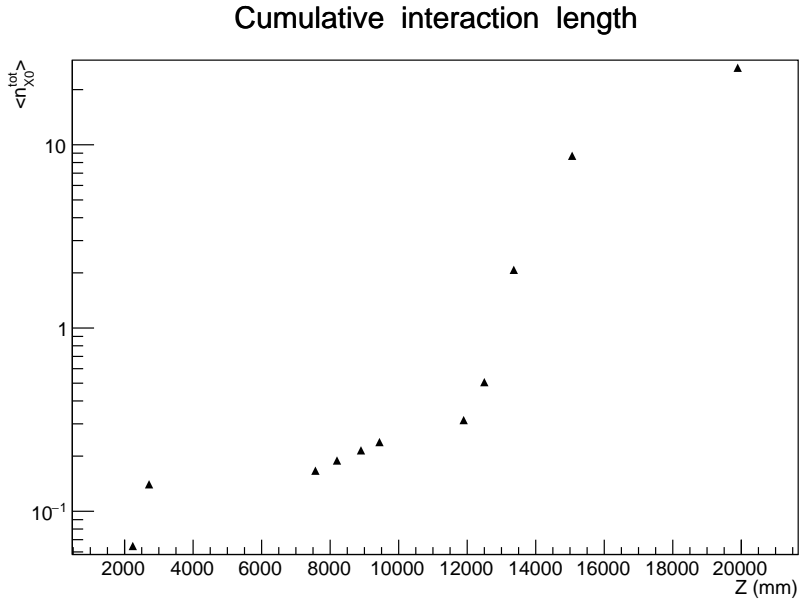


Figure 2.18: Average cumulative radiation length as a function of the horizontal distance from the interaction point. Each considered point corresponds to the end of a sub-detector: VeLo, RICH1, RICH2, tracking stations, ECAL and HCAL and muon detector.

2.13 Validation and material budget studies conclusions

The studies outlined in the previous two sections are based on tools which are now officially part of the LHCb simulation framework. These tools were used to validate the framework when passing from GEANT4 version 95 to version 96 and will continue to be used in the future. In particular a patch was provided by the GEANT4 team including improved kaon cross section. And it was verified these go in the right direction. Furthermore, the tools can be used by analyses sensitive to the quality of the simulation of particle and antiparticles cross section in order to study systematic effects and uncertainties.

883

CHAPTER 3

884

885

Differential branching fraction of $\Lambda_b^0 \rightarrow \Lambda\mu^+\mu^-$

886

887 The rare $\Lambda_b^0 \rightarrow \Lambda\mu^+\mu^-$ decay is a FCNC process governed by the $b \rightarrow s\mu^+\mu^-$
888 quark level transition. In the SM this decay proceeds only through loop diagrams
889 (electroweak penguin and W box) as discussed in Sec. 1.5, and therefore it is highly
890 sensitive to new particles entering the loops. Interest in Λ_b^0 baryon decays arises
891 from two important facts. First of all, the Λ_b^0 has non-zero initial spin, which allows
892 us to extract information about the helicity structure of the underlying Hamiltonian
893 that cannot be obtained from the meson decays [79, 80]. Secondly, the Λ_b^0 baryon
894 can be considered to a first approximation as being composed of a heavy quark and a
895 light di-quark, therefore the hadronic physics differs significantly from similar meson
896 decays. This provides the possibility to better understand and test the hadronic
897 physics in the theory, which could yield improved understanding that would also be
898 relevant for the meson case.

899 With respect to B^0 decays going though the same transitions, such as $B^0 \rightarrow K^{*0}\mu^+\mu^-$,
900 Λ_b^0 decays can provide independent confirmations of the results as they involve the

same operators but different hadronic matrix elements. Furthermore, Λ baryons decays weakly, which results in complementary constraints with respect to B^0 decays. Finally, the narrow width approximation, used in theoretical calculations, is fully applicable in the Λ_b^0 case, which has $\Gamma_{\Lambda_b^0} \sim 2.5 \cdot 10^{-6}$ eV. This is not the case for $B^0 \rightarrow K^{*0} \mu^+ \mu^-$ decays because the contribution from the non-resonant channel $B^0 \rightarrow K \pi \mu^+ \mu^-$ is unconstrained.

The theory of the $\Lambda_b^0 \rightarrow \Lambda \mu^+ \mu^-$ decays was widely considered both in the context of the SM and in different new physics scenarios [81, 82, 83, 84, 85, 86, 87, 88, 89, 90, 91]. All authors start from the same effective Hamiltonian outlined in Sec. 1.5.1. However, form factors, describing hadronic physics are not as well-developed as for the meson case because there are fewer experimental constraints. This leads to a relatively large spread in predicted branching fractions. For these reasons an interesting quantity to study is the differential branching fraction as a function of q^2 . This still suffers from the limited knowledge of form factors but, as different approaches to form factors calculations are applicable in different q^2 regions, it allows a more meaningful comparison with theory.

Experimentally, the $\Lambda_b^0 \rightarrow \Lambda \mu^+ \mu^-$ decay was observed for the first time in 2011 by the CDF collaboration [92], with a signal yield of 24 ± 5 events, and later updated in preliminary form using their full statistics [93]. CDF observed the signal only in the q^2 region above the square of the $\psi(2S)$ mass. The latter measurement using their full statistics yields $\mathcal{B}(\Lambda_b^0 \rightarrow \Lambda \mu^+ \mu^-) = [1.95 \pm 0.34(\text{stat}) \pm 0.61(\text{syst})] \times 10^{-6}$. Recently, the decay was also observed at LHCb [94] with a yield of 78 ± 12 signal events using 1 fb^{-1} of integrated luminosity collected in 2011. The signal was also found only in the high q^2 region, above $m_{\psi(2S)}^2$. The LHCb result for the branching fraction relative to the $J/\psi \Lambda$ decay, which is used as a normalisation channel, is

$$\frac{\mathcal{B}(\Lambda_b^0 \rightarrow \Lambda \mu^+ \mu^-)}{\mathcal{B}(\Lambda_b^0 \rightarrow J/\psi \Lambda)} = [1.54 \pm 0.30 \text{ (stat)} \pm 0.20 \text{ (syst)} \pm 0.02 \text{ (norm)}] \times 10^{-3}$$

and for absolute branching fraction,

$$\mathcal{B}(\Lambda_b^0 \rightarrow \Lambda\mu^+\mu^-) = [0.96 \pm 0.16 \text{ (stat)} \pm 0.13 \text{ (syst)} \pm 0.21 \text{ (norm)}] \times 10^{-6}.$$

917 This chapter describes the measurement of the differential branching fraction of the
918 $\Lambda_b^0 \rightarrow \Lambda\mu^+\mu^-$ decay using 3 fb^{-1} of pp collisions collected by the LHCb experiment
919 in 2011 and 2012.

920 3.1 Analysis strategy and q^2 regions

921 A typical q^2 spectrum of $b \rightarrow s\ell^+\ell^-$ decays was shown in Fig. 1.8. This is charac-
922 terised by the presence of the photon pole at low q^2 and the narrow peaks of the
923 J/ψ and $\psi(2S)$ resonances at intermediate values of q^2 . In the analysis, $\Lambda_b^0 \rightarrow J/\psi\Lambda$
924 decays, in which the J/ψ decays into two muons and therefore has the same final
925 state as the signal, are used as the normalisation channel. The rare and normal-
926 isation channels are naturally distinguished by the q^2 intervals in which they are
927 reconstructed. The Λ decay mode into a pion and a proton, $\Lambda \rightarrow p\pi$, is always used
928 to reconstruct the decays. The intervals in which the rare channel is studied are:

- 929 • $0.1 < q^2 < 8 \text{ GeV}^2/c^4$, where the signal is unobserved and the selection is
930 optimised to observe the signal. The upper bound of this interval is chosen
931 to be sufficiently far from the J/ψ radiative tail at low masses and reduce its
932 contamination into the rare sample;
- 933 • $11 < q^2 < 12.5 \text{ GeV}^2/c^4$, between two charmonium resonances, and
- 934 • $q^2 > 15 \text{ GeV}^2/c^4$, above $\psi(2S)$.

935 The first interval is referred to as “low q^2 ” region, below the J/ψ resonance ($q^2 < 8$
936 GeV^2/c^4), and the other two as “high q^2 ” regions, above the J/ψ resonance ($q^2 > 11$
937 GeV^2/c^4). The above regions are then sub-divided into smaller intervals, as the

938 available statistics allows, which results in $\sim 2 \text{ GeV}^2/c^4$ wide bins. The binning
939 used is the following:

$$[0.1, 2.0, 4.0, 6.0, 8.0], J/\psi, [11.0, 12.5], \psi(2S), [15.0, 16.0, 18.0, 20.0]. \quad (3.1)$$

940 In addition the result is also provided in two integrated regions:

- 941 • 1.1-6.0 GeV^2/c^4 : this interval is theoretically clean since it is far from the
942 photon pole, which dominates at low q^2 values, reducing the sensitivity to new
943 physics contributions. The lower bound of this interval is chosen to exclude
944 the possible contribution from the ϕ resonance, which appears at \sim
945 1 GeV^2/c^4 . The upper bound of the interval is chosen to exclude completely
946 a small contribution from the J/ψ resonance that leaks below 8 GeV^2/c^4 .
- 947 • 15.0-20.0 GeV^2/c^4 : this interval is the one that is expected to contain most
948 of the rare decays and it is used as a natural cross check that the analysis is
949 stable when performed in smaller bins.

950 3.2 Candidate types

951 This analysis deals with Λ baryons, which have a lifetime of $(2.632 \pm 0.020) \times 10^{-10}$ s [2].
952 These are considered long-lived particles in particle physics terms and can travel sev-
953 eral metres into the detector generating well distinguished secondary vertices. In
954 LHCb, Λ baryons can be reconstructed from tracks either with or without hits in
955 the VeLo (see Sec. 2.4) and therefore two candidates types are defined as follows:

- 956 • **Downstream candidates**: built from tracks without hits in the VeLo, “down-
957 stream tracks”, also denoted as “DD”.
- 958 • **Long candidates**: built from tracks which have hits in the VeLo, “long
959 tracks”. These candidates, also denoted as “LL”, are characterised by a better

960 momentum resolution than downstream tracks thanks to the longer lever arm
 961 available to their tracks.

962 Figure 3.1 shows the two types of candidates used in the analysis, together with
 963 other possible track types in LHCb, which are not used in this analysis. As the long
 964 and downstream candidate categories are characterised by different resolutions and
 965 kinematic properties, the analysis is performed separately on the two samples and
 966 the results are then combined.

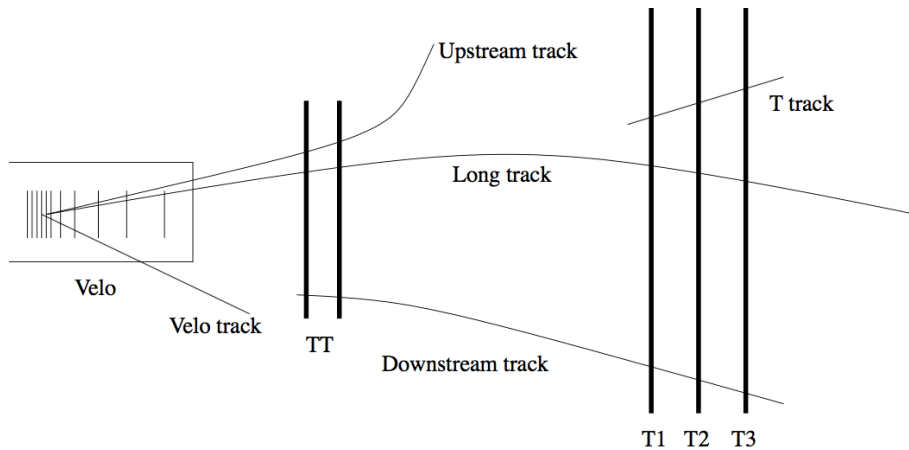


Figure 3.1: Representation of possible track types in LHCb. Candidates built from “long” and “downstream” tracks are used in this analysis [57].

967 3.3 Simulation

968 Samples of simulated events are needed in order to train the multivariate classifier
 969 (see Sec. 3.4.2), calculate the selection efficiency and study possible backgrounds;
 970 in particular for this analysis samples of ~ 2 millions $\Lambda_b^0 \rightarrow J/\psi \Lambda$ and ~ 5 millions
 971 $\Lambda_b^0 \rightarrow \Lambda\mu^+\mu^-$ simulated events are used. Samples of simulated $B^0 \rightarrow J/\psi K_s^0$,
 972 $B^0 \rightarrow K_s^0\mu^+\mu^-$ and $B^+ \rightarrow \mu^+\mu^-K^{*+}$ events are also used to study backgrounds
 973 from these decays. The events are generated using PYTHIA8; hadronic particles are
 974 decayed using EVTGEN and GEANT4 is used to simulate the interaction of final
 975 state particles with the detector. Simulated events are then reconstructed by the
 976 same reconstruction software that is used for real data. The L0 hardware trigger

is emulated in the simulation, while for the software stage, HLT (see Sec. 2.9), the same code can be used as for data. Events are simulated using both 2011 and 2012 beam and detector conditions, in the same proportion as recorded data. While the simulation gives a generally good description of data, some discrepancies remain. It is important that the simulation gives an accurate description of the data, in particular for the extraction of efficiencies. The next sections therefore describe corrections applied to the simulation in order to provide a better description of data. In Appendix B data distributions are compared with simulated ones for variables relevant to this analysis.

3.3.1 Decay Model

Little is known about the decay structure of Λ_b^0 decays and therefore the simulation software generates events according to the phase space given by the available kinematics. To include a reasonably realistic q^2 dependence, the simulation is weighted using decay amplitudes based on the predictions in Ref. [95]. Equations in this paper are for the case of unpolarised Λ_b^0 production and for this analysis those are extended to include polarisation. Details about the models used are given in Appendix A.1. The value of the Λ_b^0 production polarisation, P_b , used in the calculations is $P_b = 0.06$ as measured by LHCb [96]. Figure 3.2 shows the phase space q^2 distribution and the one obtained by re-weighting the events. The latter can be qualitatively compared to the q^2 spectrum of a generic $b \rightarrow s\ell^+\ell^-$ decay shown in Fig. 1.8. For the normalisation mode, the decay model used is described in Appendix A.3, with amplitude magnitudes and production polarisation taken from the measurements in Ref. [96]. Phases are not yet measured and are therefore set to zero.

3.3.2 Kinematic re-weighting

Small data-simulation differences are found in the kinematic properties of the mother particle, Λ_b^0 , which also affect the final state particles. The simulation is re-weighted

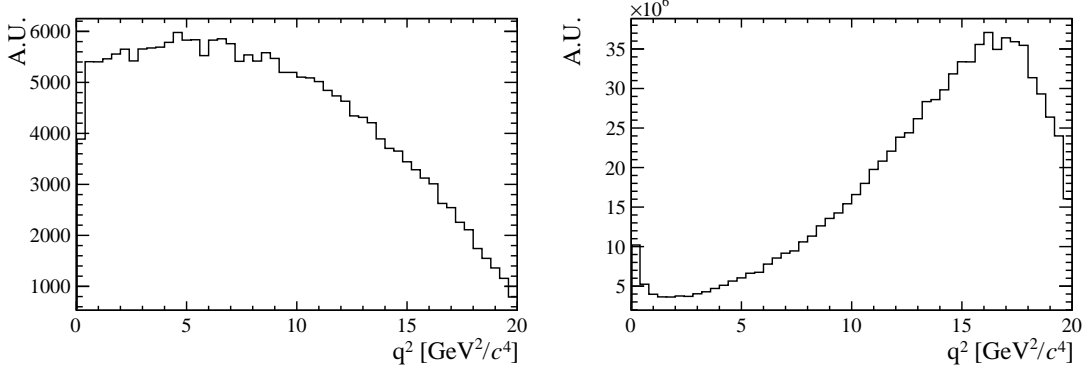


Figure 3.2: The q^2 spectrum of $\Lambda_b^0 \rightarrow \Lambda\mu^+\mu^-$ simulates events according to the phase space of the decay (left) and re-weighted using the decay amplitudes (right).

1003 by comparing the momentum and transverse momentum of Λ_b^0 baryons in real and
 1004 simulated $\Lambda_b^0 \rightarrow J/\psi \Lambda$ candidates that satisfy the pre-selection (see Sec. 3.4). To
 1005 do this a high purity data sample is obtained by selecting a narrow invariant mass
 1006 interval around the J/ψ and Λ_b^0 peaks; this contains about $4 \cdot 10^5$ candidates. The
 1007 Λ_b^0 invariant mass distribution is then fitted to estimate the number of background
 1008 decays under the peak. The background fraction, $f_b = B/(S + B)$, is then used to
 1009 subtract statistically the background from the kinematical distributions as described
 1010 by the equation:

$$S(p, p_T) = T(p, p_T) - f_b \cdot B(p, p_T), \quad (3.2)$$

1011 where $S(p, p_T)$ is the distribution of pure signal events, which we want to obtain,
 1012 $T(p, p_T)$ is the total distribution of signal plus background, namely the distribution
 1013 of all events in the signal interval, $5605 < m(p\pi\mu^+\mu^-) < 5635 \text{ MeV}/c^2$, and $B(p, p_T)$
 1014 is the pure background distribution obtained using events from the upper sideband,
 1015 $m(p\pi\mu^+\mu^-) > 5800 \text{ MeV}/c^2$.

1016 After the signal distributions have been obtained from data, they are compared
 1017 with $\Lambda_b^0 \rightarrow J/\psi \Lambda$ simulated events and a weight, $w(p_{\Lambda_b^0}, p_{T\Lambda_b^0})$ is defined by taking
 1018 the ratio of the two dimensional (p, p_T) distributions. The result is shown in Fig. 3.3,
 1019 while Appendix B reports distributions of sideband subtracted data in the signal and
 1020 sideband regions together with weighted and unweighted simulated events. In these
 1021 plots the momentum and p_T distributions of Λ_b^0 baryons match by construction. The
 1022 re-weighting also improves the agreement between the kinematical distributions of

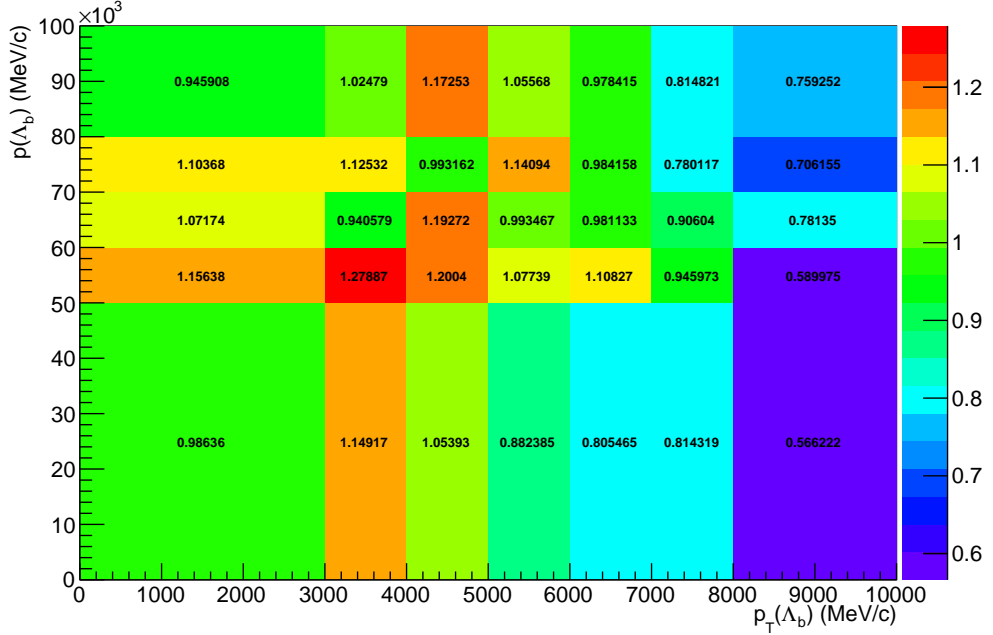


Figure 3.3: Weights used for the kinematical re-weighting as a function of the momentum and transverse momentum of Λ_b^0 .

1023 all final particles. Small differences remain due to the finite binning used for the
 1024 weights calculation. Quality variables, such as the χ^2 of tracks and vertices, show
 1025 little dependence on the kinematics and are relatively unaffected by the weighting
 1026 procedure.

1027 3.3.3 Event type

1028 There is not complete agreement on the fraction of Λ baryons reconstructed from
 1029 long tracks and downstream tracks in data and simulation. For $\Lambda_b^0 \rightarrow J/\psi \Lambda$ decays
 1030 passing the full selection, $\sim 70\%$ of candidates are reconstructed from downstream
 1031 tracks in data, compared with $\sim 75\%$ in the simulation. The fraction of downstream
 1032 and long tracks also varies as a function of q^2 and the biggest differences are found
 1033 at low values of q^2 . In order to deal with these differences all efficiencies are obtained
 1034 separately for downstream and long candidates and the analysis is carried out sep-
 1035 arately for the two categories; results are then combined to ensure the best use of
 1036 the available information. It is therefore not necessary to correct the simulation to

1037 reproduce the correct fraction of events in each category.

1038 3.4 Selection

1039 This section described the requirements applied to reconstruct $\Lambda_b^0 \rightarrow \Lambda\mu^+\mu^-$ and
1040 $\Lambda_b^0 \rightarrow J/\psi\Lambda$ candidates. The selection procedure is divided into two steps: a pre-
1041 selection, where cuts are applied in order to be able to work with manageable
1042 datasets and a multivariate analysis (MVA) which combines information from several
1043 variables. As a first step good quality tracks are selected by imposing requirements
1044 on their basic kinematic properties, such as the p_T of the final particles, and quality
1045 requirements, such as the track χ^2 . The selection then forms a dimuon candidate
1046 from two oppositely charged muons. In events containing a dimuon candidate, two
1047 oppositely charged tracks are combined and retained as a Λ candidate if they form
1048 a good quality vertex which is well separated from all primary vertices. Finally,
1049 the dimuon and Λ candidates are combined to form Λ_b^0 baryons with requirements
1050 placed on the properties of this combination.

1051 3.4.1 Pre-selection

1052 The full list of pre-selection cuts is reported in Tab. 3.1. In the table χ_{IP}^2 is defined
1053 as the projected distance from a vertex divided by its uncertainty, for example the
1054 $\chi_{IP}^2(primary) > n$ requirement on Λ_b^0 means that the Λ_b^0 vertex must be at least \sqrt{n}
1055 standard deviations away from the primary vertex. Another quantity, found to be
1056 particularly powerful at removing combinatorial background, is a pointing variable
1057 called DIRA defined as the cosine of the angle between the direction of a particle's
1058 momentum and the flight direction from its mother vertex. Requiring a DIRA close
1059 to unity corresponds to the selection of particles with well-defined origin vertices.
1060 A graphical representation of the χ_{IP}^2 and DIRA variables are shown in Fig. 3.4.
1061 The variable χ_{FD}^2 represents the flight distance of a particle from its origin vertex

1062 divided by the corresponding uncertainty. The χ^2_{trk}/ndf and χ^2_{vtx}/ndf quantities
 1063 are the χ^2 from the fit to tracks and vertices, which are used to quantify their
 1064 quality. The `GhostProb` quantity describes the probability of a track being fake. By
 1065 construction, cutting at a value of k , removes $(1 - k) \cdot 100\%$ of fake tracks. The
 1066 `hasRich`, `hasCalo` and `isMuon` variables are binary indicators that the information
 1067 from the RICH, calorimeter and muon detectors is available for the track. Loose
 1068 PID requirements on the proton are also applied in the pre-selection. Details about
 1069 PID quality estimators are given in Sec. 2.8. A large mass window around the Λ_b^0
 1070 peak is used to allow a fit to the sideband to be performed and to use sideband
 1071 candidates to train a multivariate classifier. Rare candidates are selected by the
 1072 q^2 region requirements described in Sec. 3.1, while resonant candidates are further
 1073 constrained to have dimuon invariant masses in a 100 MeV/ c^2 interval around the
 1074 known J/ψ mass [2].

1075 3.4.2 Neural Networks

1076 The final selection is performed using a neural network (NN) classifier based on the
 1077 NeuroBayes package [73, 74]. The input to the neural network consists of 14 variables
 1078 carrying information about the kinematics of the decay, the quality of tracks and
 1079 vertices and the PID of the muons. The list of the 10 most significant inputs is
 1080 reported in Tab. 3.2, together with information about the importance of each input.

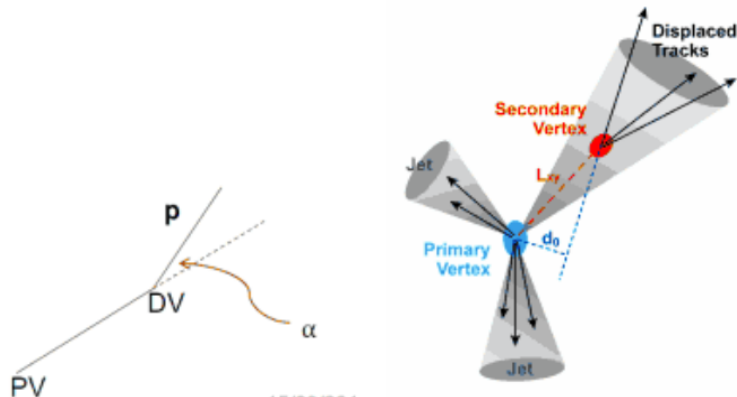


Figure 3.4: Graphical representation of the DIRA (left) and χ^2_{IP} (right) variables.

Particle	Requirement
Λ_b^0	$4.6 < m(p\pi\mu\mu) < 7.0 \text{ GeV}/c^2$ $\text{DIRA} > 0.9999$ $\chi_{\text{IP}}^2 < 16.0$ $\chi_{\text{FD}}^2 > 121.0$ $\chi_{\text{vtx}}^2/\text{ndf} < 8.0$
Λ	$\chi_{\text{vtx}}^2/\text{ndf} < 30.0(25.0)$ Decay time $> 2 \text{ ps}$ $ m(p\pi) - m_A^{\text{PDG}} < 35(64) \text{ GeV}/c$
p/π	$p > 2 \text{ GeV}/c$ $p_T > 250 \text{ MeV}/c$ $\chi_{\text{IP}}^2 > 9(4)$
p (only long cand.)	hasRICH $\text{PID}_p > -5$
μ	isMuon $\chi_{\text{trk}}^2/\text{ndf} < 5$ $\text{GhostProb} < 0.4$ $\text{PID}_\mu > -3$ $\chi_{\text{IP}}^2 > 9.0$
Dimuon	$\chi_{\text{vtx}}^2/\text{ndf} < 12.0$ $m(\mu\mu) < 7.1 \text{ GeV}/c^2$

Table 3.1: Summary of pre-selection requirements. Where two values are given, the main one applies to long candidates and the one in parenthesis to downstream candidates.

1081 Variables related to Λ and its daughters are considered as different inputs depending
1082 on the candidate type (long or downstream). This effectively corresponds to making
1083 a separate training for the two categories.

1084 The NN is trained using representative samples of signal and background. A sample
1085 of simulated $\Lambda_b^0 \rightarrow \Lambda\mu^+\mu^-$ events is used as a proxy for the signal, while for the
1086 background a representative sample is given by candidates in the upper $m(p\pi\mu\mu)$
1087 invariant mass sideband. Only the upper sideband, $m(p\pi\mu\mu) > 6 \text{ GeV}/c^2$, is used
1088 since it contains only combinatorial background, while the lower sideband may con-
1089 tain partially reconstructed and misreconstructed candidates. In the q^2 spectrum
1090 of background samples the J/ψ and $\psi(2S)$ peaks are still present indicating that
1091 charmonium resonances are often combined with other random tracks. These can-
1092 didates do not give a good description of purely combinatorial background and, in
1093 order to avoid biases, they are removed from the training sample by rejecting events

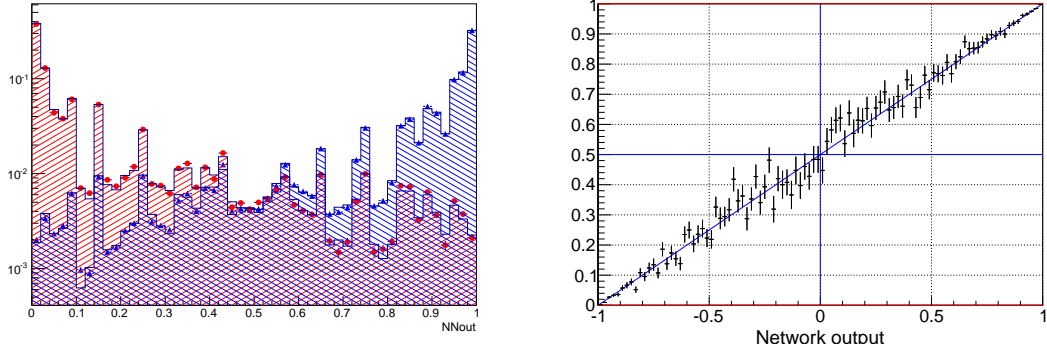


Figure 3.5: (left) Neural network output distribution for training (points) and test (stripes) samples, for signal and background events. (right) Purity as a function of neural network output.

in a $100 \text{ MeV}/c^2$ interval around the nominal J/ψ and $\psi(2S)$ masses [2]. A total of 30000 total events is used for the training from each sample. This corresponds $\sim 50\%$ of the available sideband data sample and $\sim 20\%$ of the simulated sample. The full simulated sample is not used as the same sample will also be used to study efficiencies. For reproducibility the events are sampled uniformly.

The single most important variable used for downstream candidates is the transverse momentum of Λ , which allows to reject random combination of tracks as these have preferentially low p_T . For long candidates instead the best variable is the χ^2 from a kinematic fit that constrains the decay products of the Λ_b^0 , the Λ and the dimuon, to originate from their respective vertices performed using the `DecayTreeFitter` tool (see Sec. 2.10). Other variables that contribute significantly are the χ_{IP}^2 of Λ_b^0 , Λ and muons, the separation between the Λ_b^0 and Λ vertices and, finally, the muon PID.

Figure 3.5 shows distributions of neural network output for the signal and background samples and purity, $P = N_{\text{sig}}/N_{\text{bkg}}$, as a function of the neural network output. The distributions from test samples are also overlaid in order to check for overtraining. The distributions follow the same shape but with different fluctuations indicating no significant overtraining. In general it can be concluded that the neural network is able to separate signal from background and the training converged properly. It can happen that too much information is given to the classifier,

Table 3.2: Summary of the 10 most significant inputs to the neural network in order of importance. Column “adds” gives the significance added by a given input when it is added to the list of those ranked above. Column “only this” provides the power of a given input alone and “loss” shows how much information is lost when removing only a given input.

Input	adds	only this	loss
$\Lambda_{\text{DD}} p_T$	143.11	143.11	29.20
χ^2_{DTF}	77.81	134.00	51.10
$\min(\chi^2_{\text{IP}} \mu)$	61.31	113.62	29.76
$\chi^2_{\text{IP}} \Lambda_b^0$	52.94	113.23	40.98
$\chi^2_{\text{IP}} \pi_{\text{LL}}$	20.29	60.72	12.82
$\min(\text{PID } \mu)$	17.91	59.11	13.44
$\tau_{\Lambda_b^0}$	16.24	35.36	11.24
$\Lambda_b^0 \text{ DIRA}$	12.28	73.96	9.98
$\Lambda_{\text{DD}} \text{ flight distance}$	9.47	86.75	11.24
$\chi^2_{\text{IP}} \Lambda_{\text{DD}}$	10.58	59.84	8.88

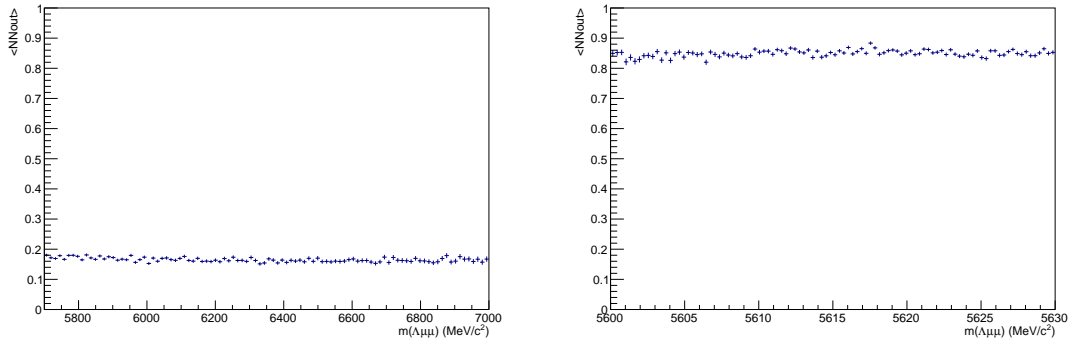


Figure 3.6: Average value of NN output as a function of Λ_b^0 mass for data sideband (left) and simulated signal (right) events.

which becomes able to calculate the invariant mass of the candidates from the input variables. This can generate fake peaks and it is therefore important to check for correlations between the 4-body invariant mass and the NN output. Figure 3.6 reports the average neural network output as a function of the 4-body $m(p\pi\mu\mu)$ invariant mass for data and simulation. The distributions are flat indicating that no significant correlation is present.

1120 3.4.3 MVA optimisation

1121 In the high q^2 region, where the signal is already observed, the requirement on
1122 the neural network output is chosen maximising the significance, $N_S/\sqrt{N_S + N_B}$,
1123 where N_S and N_B are the numbers of expected signal and background candidates
1124 respectively. N_S is derived from simulation but, as an arbitrary number of events can
1125 be generated, it needs to be normalised. To do this, the invariant mass distribution
1126 of real $\Lambda_b^0 \rightarrow J/\psi \Lambda$ candidates is fit after pre-selection (including all requirements
1127 but MVA). This is possible as the peak of the resonant channel is already well visible
1128 before the MVA cut. The resonant yield is then scaled by the ratio of between the
1129 $\Lambda_b^0 \rightarrow \Lambda \mu^+ \mu^-$ and $\Lambda_b^0 \rightarrow J/\psi \Lambda$ branching fractions as measured by LHCb on 2011
1130 data

$$\mathcal{B}(\Lambda_b^0 \rightarrow \Lambda \mu^+ \mu^-)/\mathcal{B}(\Lambda_b^0 \rightarrow J/\psi \Lambda) = 1.54 \times 10^{-3} \quad (3.3)$$

1131 and by the $J/\psi \rightarrow \mu^+ \mu^-$ branching fraction. In summary:

$$N_S = N_{J/\psi} \cdot \frac{\mathcal{B}(\Lambda_b^0 \rightarrow \Lambda \mu^+ \mu^-)}{\mathcal{B}(\Lambda_b^0 \rightarrow J/\psi \Lambda) \cdot \mathcal{B}(J/\psi \rightarrow \mu^+ \mu^-)}. \quad (3.4)$$

1132 The number of expected background events instead is derived fitting the data side-
1133 band with an exponential and extrapolating under the signal region.

1134 In the low q^2 region, where the signal is unobserved, the so called ‘‘Punzi figure-of-
1135 merit’’, $N_S/(n_\sigma/2 + \sqrt{N_B})$, is maximised [97]. This figure-of-merit is considered to be
1136 optimal for discovery and the parameter n_σ corresponds to the number of expected
1137 standard deviations of significance, in this analysis $n_\sigma = 3$ is used. Moreover,
1138 the Punzi shape does not depend on the relative normalisation between signal and
1139 background, which is important since the signal is still unobserved at low q^2 and the
1140 existing predictions vary significantly for this region. The dependence of the figure-
1141 of-merit for both q^2 regions is shown in Fig. 3.7, and curves of signal efficiency versus
1142 background rejection are shown in Fig. 3.8.

1143 For final selection the neural network output is required to be larger than 0.76
1144 for candidates in the high q^2 region and 0.97 for the low q^2 ones. Using these

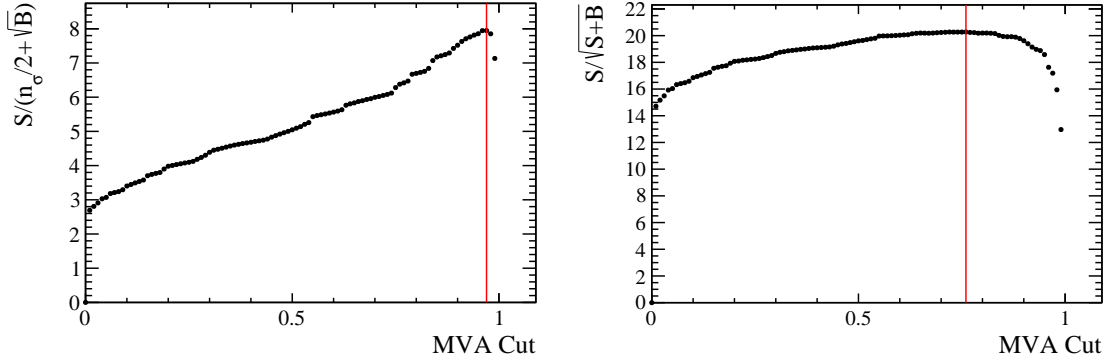


Figure 3.7: Dependence of the figure-of-merits on the neural network output requirement for the low q^2 (left) and high q^2 (right) regions. The vertical lines correspond to the chosen cuts.

1145 requirements the neural network retains approximately 96% (66 %) of downstream
 1146 candidates and 97 % (82 %) of long candidates for the high (low) q^2 selection,
 1147 with respect to the pre-selected samples. After full selection $\sim 0.5\%$ of the events
 1148 contain multiple candidates which are randomly rejected keeping only one candidate
 1149 per event. To normalise the branching ratio measurement J/ψ events are selected
 1150 using the low and high q^2 requirements to normalise respectively low and high q^2
 1151 intervals.

1152 3.4.4 Trigger

1153 Finally, specific trigger lines are selected, corresponding to events triggered by muons
 1154 which formed the reconstructed candidate. This is denoted as Trigger On Signal
 1155 (TOS). The trigger lines used in the analysis are listed in Tab. 3.3. The logical *or*
 1156 of the lines on the same lever is required and the logical *and* of those on different
 1157 levels. The L0Muon trigger requires hits in the muon detector and triggers if a muon
 1158 with $p_T > 1.5$ GeV/ c is identified. L0Dimuon imposes the same requirement on the
 1159 sum of the transverse momenta of two tracks. The Hlt1TrackAllL0 performs a
 1160 partial reconstruction of the events and applies basic requirements on the IP, χ^2
 1161 and p_T of tracks; it triggers if the L0 decision is confirmed. Hlt1TrackMuon applies
 1162 looser requirements but in addition requires the isMuon variable (see Sec. 2.8) to be

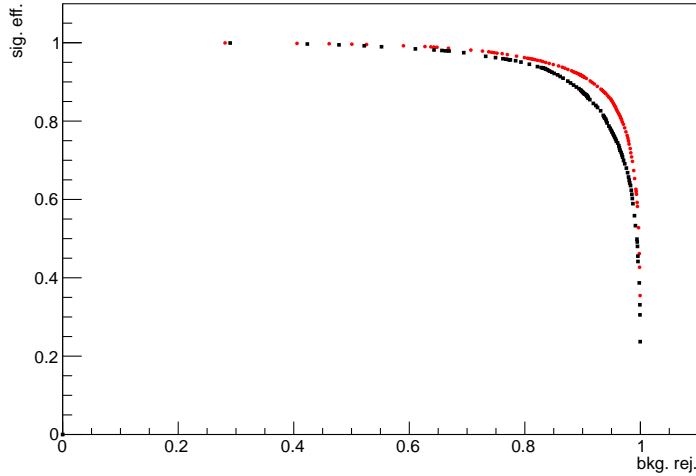


Figure 3.8: Receiver operating characteristic (ROC) curves for low q^2 (black) and high q^2 (red). They show the signal efficiency versus the background rejection. The optimal points on these curves are the closest ones to (1,1).

1163 true to limit the yield. Finally, at the Hlt2 level, a complete reconstruction is done
 1164 and a multivariate analysis is used to identify decay structures. One of the main
 1165 variables used at this stage is the Distance Of Closest Approach (DOCA), which is required to be less than 0.2 mm to form a 2-body object.

Table 3.3: Summary of trigger lines which candidates have to pass at various trigger levels. Trigger is always required to be due to tracks of the candidate itself.

Trigger Level	Lines
L0	LOMuon
	LODiMuon
Hlt1	Hlt1TrackAllL0
	Hlt1TrackMuon
Hlt2	Hlt2Topo [2-4] BodyBBDT
	Hlt2TopoMu [2-4] BodyBBDT
	Hlt2SingleMuon
	Hlt2DiMuonDetached

1166

1167 3.4.5 Background from specific decays

1168 Candidates from other decays can be reconstructed as the decays of interest if par-
 1169 ticles are not reconstructed or mis-identified. A survey of possible backgrounds

concluded that the only physics background to take into account comes from mis-reconstructed decays of B^0 to K_s^0 with two muons in the final state, whether via J/ψ or not, where the K_s^0 is reconstructed as a Λ with a $p \rightarrow \pi$ identity swap. The lack of background from other decays is mainly due to the particular topology of the Λ decay, which is long-lived and decays at a displaced vertex. To study the effect of misreconstructed $B^0 \rightarrow J/\psi K_s^0$ and $B^0 \rightarrow K_s^0 \mu^+ \mu^-$ decays simulated samples are used. On data the $B^0 \rightarrow J/\psi K_s^0$ contribution is clearly visible in the resonant channel mass distribution. This background is not suppressed with specific cuts in this analysis as its mass shape is sufficiently distinct from the Λ_b^0 signal and its contribution can be reliably modelled in the mass fits (see Sec. 3.5.1). For the rare case a rough estimate of the K_s^0 background size is obtained using the yield in the resonant channel rescaled by the measured ratio between the rare and resonant branching fractions. Details are given in Sec. 3.5.1 and numbers of events predicted are reported in Tab. 3.4. This contribution, although close to negligible is again considered in the fit. A possible pollution due to $B^+ \rightarrow \mu^+ \mu^- K^{*+}$ decays, where the K^{*+} further decays into $K_s^0 \pi$ is also investigated using a dedicated simulated sample and found to be negligible. Finally, $\Lambda_b^0 \rightarrow J/\psi \Lambda$ events radiating photons from the final state, can escape the J/ψ veto and be reconstructed in the rare channel sample. Analysing simulated events it was found that the only contribution is in the closest q^2 interval to the J/ψ tail, $6 < q^2 < 8$ GeV $^2/c^4$. In this interval 1.3% of the $\Lambda_b^0 \rightarrow J/\psi \Lambda$ candidates are reconstructed but only 0.06% fall into the 4-body invariant mass window used for the fits. This corresponds to ~ 6 events, 4 of which in the downstream category. Given the low yield and that these events do not peak under the signal but show a decaying distribution at the edge of the fit mass window, this background is considered as absorbed in the combinatorial background. Figure 3.9 shows the invariant mass distribution of simulated $\Lambda_b^0 \rightarrow J/\psi \Lambda$ events falling into the rare q^2 region and the distribution of simulated $B^+ \rightarrow \mu^+ \mu^- K^{*+}$ events mis-reconstructed as $\Lambda_b^0 \rightarrow J/\psi \Lambda$ decays.

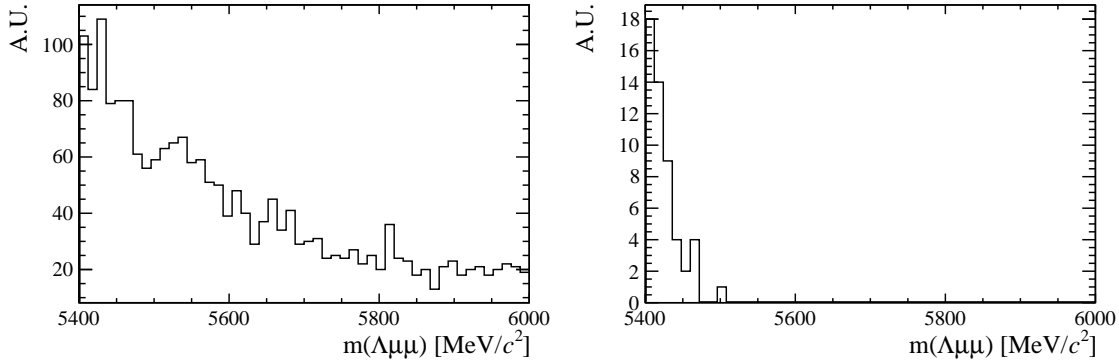


Figure 3.9: Invariant mass distributions of simulated $B^+ \rightarrow \mu^+ \mu^- K^{*+}$ (left) and $\Lambda_b^0 \rightarrow J/\psi \Lambda$ (right) candidates passing the full selection. Only $\Lambda_b^0 \rightarrow J/\psi \Lambda$ candidates reconstructed in $q^2 < 8 \text{ GeV}^2/c^4$ are selected. Distributions are shown in the invariant mass range relevant for the analysis (see Sec. 3.5.1).

1198 3.5 Yield extraction

1199 Extended unbinned maximum likelihood fits are used to extract the yields of the
1200 rare and resonant channels. The likelihood has the form:

$$\mathcal{L} = e^{-(N_S + N_C + N_B)} \times \prod_{i=1}^N [N_S P_S(m_i) + N_C P_C(m_i) + N_B P_B(m_i)] \quad (3.5)$$

1201 where N_S , N_C and N_B are respectively the numbers of signal, combinatorial and
1202 K_s^0 background events and the $P_i(m_i)$ are the corresponding probability density
1203 functions (PDF). The fit variable is the 4-body $m(p\pi\mu\mu)$ invariant mass obtained
1204 from a kinematical fit of the full decay chain in which each particle is constrained
1205 to point to its assigned origin vertex and the invariant mass of the $p\pi$ system is
1206 constrained to be equal to the world average for the Λ baryon mass. In the resonant
1207 case a further constrain is used on the dimuon mass to be equal to the known J/ψ
1208 mass. This method allows to improve the mass resolution giving better defined
1209 peaks and therefore a more stable fit. For brevity, in the following these variables
1210 are simply referred to as “invariant mass”.

₁₂₁₁ 3.5.1 Fit description

₁₂₁₂ The fit is performed through the following steps:

- ₁₂₁₃ • simulated distributions are fit to extract initial parameters;
- ₁₂₁₄ • the resonant data sample is fitted;
- ₁₂₁₅ • the rare sample is fitted fixing some parameters to those obtained in the previous cases.

₁₂₁₇ In the first step simulated $\Lambda_b^0 \rightarrow J/\psi \Lambda$ distributions are fitted using the signal PDF
₁₂₁₈ alone. This is done separately for long and downstream candidates. Figure 3.10
₁₂₁₉ shows distributions of candidates selected in the resonant sample with the fit function
₁₂₂₀ overlaid. The signal is described as the sum of two Crystal Ball functions (CB)
₁₂₂₁ with common mean (m_0) and tail slope (n). This is also known as Double Crystal
₁₂₂₂ Ball (DCB) function. A single Crystal Ball [98] is a probability density function
₁₂₂₃ commonly used to model processes involving energy loss. In particular it is used to
₁₂₂₄ describe resonances' peaks with radiative tails. This function consists of a Gaussian
₁₂₂₅ core and a power-law tail below a certain threshold and has form

$$C(x; \alpha, n, \bar{x}, \sigma) = N \cdot \begin{cases} \exp\left(-\frac{(x-\bar{x})^2}{2\sigma}\right) & \text{if } \frac{(x-\bar{x})}{\sigma} > \alpha, \\ A \left(B - \frac{(x-\bar{x})}{\sigma}\right)^{-n} & \text{if } \frac{(x-\bar{x})}{\sigma} < \alpha, \end{cases} \quad (3.6)$$

₁₂₂₆ where for normalisation and continuity

$$\begin{aligned} A &= \left(\frac{c}{|\alpha|}\right)^n \cdot \exp\left(-\frac{\alpha^2}{2}\right), \\ B &= \frac{n}{|\alpha|} - |\alpha|. \end{aligned} \quad (3.7)$$

₁₂₂₇ The full PDF for the resonant channel is therefore:

$$P_S(m; m_0, \alpha_1, \alpha_2, f, n) = f \text{CB}(m; m_0, \sigma_1, \alpha_1, n) + (1-f) \text{CB}(m; m_0, \sigma_2, \alpha_2, n), \quad (3.8)$$

₁₂₂₈ where f is the relative fraction of candidates falling into the first CB function.

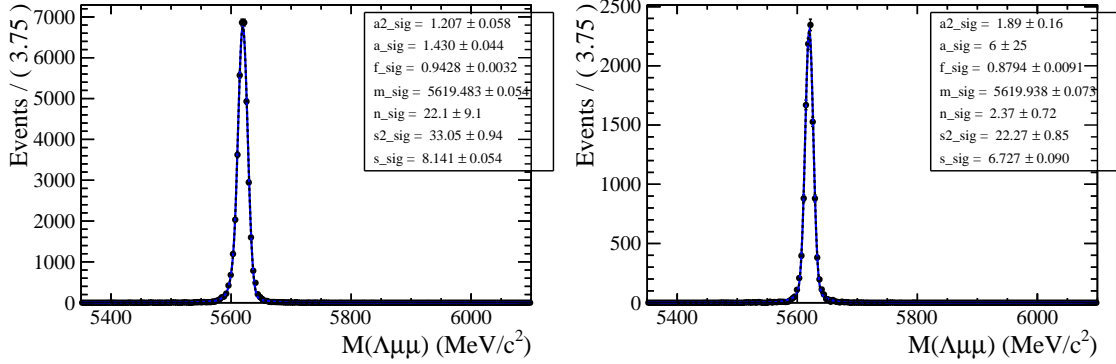


Figure 3.10: Invariant mass distribution of $\Lambda_b^0 \rightarrow \Lambda J/\psi$ downstream (left) long (right) candidates. The points show simulated data and the blue line is the signal fit function.

- 1229 In a second step the fit to the resonant channel data sample is performed. For this fit
 1230 the tail slope parameter, “ n ”, which is highly correlated with α_1 and α_2 , is fixed to
 1231 the value found in the fit to simulated data. In this fit two background components
 1232 are modelled: the combinatorial background, parameterized with an exponential
 1233 and the background from $B^0 \rightarrow J/\psi K_s^0$ decays. The shape used to describe the
 1234 K_s^0 background is obtained from a $B^0 \rightarrow J/\psi K_s^0$ simulated sample to which the
 1235 full selection is applied. The invariant distribution of these events is fit with a DCB
 1236 function, which is then used to model the K_s^0 background in the $\Lambda_b^0 \rightarrow J/\psi \Lambda$ fit. The
 1237 fit to the simulated $B^0 \rightarrow J/\psi K_s^0$ events is reported in Fig. 3.11. When the K_s^0 shape
 1238 is introduced in the fit to the data all its parameters are fixed. This is particularly
 1239 important when fitting long candidates, where the K_s^0 peak is less evident, which
 1240 does not allow to constrain many parameters. On the other hand, in order to take
 1241 into account possible data-simulation differences, an horizontal shift is added and
 1242 left floating (by adding a constant to the central value of the DCB, $m_0 \rightarrow m_0 + m'$).
 1243 In summary, the free parameters in the fit to the resonant $\Lambda_b^0 \rightarrow J/\psi \Lambda$ sample are
 1244 the yields of the signal and the combinatorial and K_s^0 backgrounds, the slope of the
 1245 exponential and the horizontal shift of the K_s^0 shape. Note that all parameters of
 1246 the fit to the long and downstream samples are independent.
 1247 Finally, the rare $\Lambda_b^0 \rightarrow \Lambda\mu^+\mu^-$ data sample is fit. In this case the fit to the long
 1248 and downstream samples is performed simultaneously to obtain a more stable con-

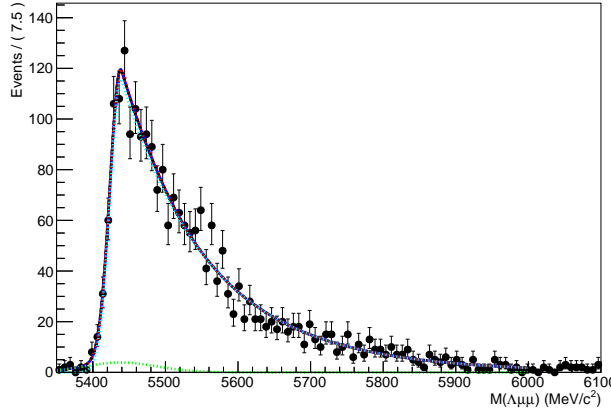


Figure 3.11: Invariant mass distribution of simulated $B^0 \rightarrow J/\psi K_s^0$ events after full selection fitted a Double Crystal Ball function.

vergence. In this fit the signal is modelled with the same shape used in the resonant case as there is no physical reason why they should be different. This method is also useful to limit systematic uncertainties as the result will be given as a ratio between rare and resonant quantities. However, the low statistics for the rare sample does not allow to constrain many parameters. Therefore, all parameters of the signal shape are fixed to the ones derived from the fit to the normalisation channel. However, to account for possible differences, arising from a different resolution in different q^2 regions, a scale factor is multiplied to the widths of the two gaussian cores of the signal DCB: $\sigma_1 \rightarrow c \cdot \sigma_1$ and $\sigma_2 \rightarrow c \cdot \sigma_2$, where the two scale factors are the same. This factors are fixed in the fit to data by fitting rare $\Lambda_b^0 \rightarrow \Lambda\mu^+\mu^-$ simulated events in each q^2 bin and comparing the widths with the ones found on the fit to the resonant simulated sample, namely

$$c = \sigma_{\mu^+\mu^-}^{MC} / \sigma_{J/\psi}^{MC}. \quad (3.9)$$

Values obtained are ~ 1.9 for downstream candidates and ~ 2.3 for long candidates, corresponding to the fact that in the resonant case a further constrain on the dimuon mass is used, which improves the resolution by a factor of ~ 2 . The dependence of the scaling factor on q^2 is found to be small. For the fits on the long and downstream samples the parameters are always fixed to the corresponding J/ψ fit; in this analysis

Table 3.4: Predicted numbers of $B^0 \rightarrow K_s^0 \mu^+ \mu^-$ events in each considered q^2 interval.

q^2 interval [GeV $^2/c^4$]	Downstream	Long
0.1–2.0	0.9	0.1
2.0–4.0	0.9	0.1
4.0–6.0	0.8	0.1
6.0–8.0	1.1	0.1
11.0–12.5	1.9	0.2
15.0–16.0	1.1	0.1
16.0–18.0	2.0	0.2
18.0–20.0	1.1	0.1
1.1–6.0	2.1	0.1
15.0–20.0	4.2	0.5

1266 shape parameters are never shared between the two candidate categories.

1267 Also in the rare case the modelled background components are the combinatorial
1268 background, described with an exponential function and the K_s^0 background. The
1269 slope of the background is visibly different depending on the q^2 interval. This is
1270 partly due to the fact that at high q^2 the combinatorial changes slope because of
1271 a kinematical limit at low 4-body masses imposed by the q^2 requirements. The
1272 exponential slopes are therefore left as independent parameters in each q^2 interval.
1273 The background component from $B^0 \rightarrow K_s^0 \mu^+ \mu^-$ decays is modelled using the same
1274 shapes used for the resonant channel. However, in this case the horizontal shift is
1275 fixed to what found for the resonant channel. The expected amount of misrecon-
1276 structed $B^0 \rightarrow K_s^0 \mu^+ \mu^-$ events is small and does not allow to determine reliably the
1277 yield. Therefore this is fixed to the yield of $B^0 \rightarrow J/\psi K_s^0$ decays rescaled by the
1278 expected ratio of branching fractions between the resonant and rare channels. The
1279 q^2 distribution of $B^0 \rightarrow K_s^0 \mu^+ \mu^-$ simulated events is used to predict the yield as a
1280 function of q^2 . Table 3.4 reports the number of predicted $B^0 \rightarrow K_s^0 \mu^+ \mu^-$ events in
1281 each q^2 interval obtained with the following formula:

$$N_{K_s^0 \mu^+ \mu^-}(q^2) = N_{J/\psi K_s^0} \frac{B(B^0 \rightarrow K_s^0 \mu^+ \mu^-)}{B(B^0 \rightarrow K_s^0 J/\psi)} \cdot \frac{1}{\epsilon_{rel}} \cdot B(J/\psi \rightarrow \mu^+ \mu^-) \frac{N(q^2)_{MC}}{N_{MC}^{tot}} \quad (3.10)$$

1282 where $N(q^2)_{MC}$ is the number of simulated rare candidates falling in a q^2 interval
1283 after full selection and N_{MC}^{tot} is the total number of simulated events.

As the fit on the rare sample is performed simultaneously on long and downstream candidates, their two yields are not free to vary separately but are parameterised as a function of the common branching fraction using the following formula:

$$N(\Lambda\mu^+\mu^-)_k = \left[\frac{d\mathcal{B}(\Lambda\mu^+\mu^-)/dq^2}{\mathcal{B}(J/\psi\Lambda)} \right] \cdot N(J/\psi\Lambda)_k \cdot \varepsilon_k^{rel} \cdot \frac{\Delta q^2}{\mathcal{B}(J/\psi \rightarrow \mu^+\mu^-)}, \quad (3.11)$$

where $k = (\text{LL}, \text{DD})$, Δq^2 is the width of the q^2 interval and the only free parameter is the relative branching fraction ratio of the rare over J/ψ channels. For the branching fraction of the $J/\psi \rightarrow \mu^+\mu^-$ decay the value reported in the PDG book, $(5.93 \pm 0.06) \cdot 10^{-2}$ [2] is used and ε^{rel} corresponds to the relative efficiency between the rare and resonant channels obtained in Sec. 3.6. In this formula the efficiencies and the normalisation yield appear as constants, namely $N(\Lambda\mu^+\mu^-)_k = C_k \cdot \mathcal{B}^{rel}$.

3.5.2 Fit results

Figures 3.12 and 3.13 show fitted invariant mass distributions for the normalisation channel, selected with the high q^2 and low q^2 requirements respectively. Table 3.5 reports the measured yields of $\Lambda_b^0 \rightarrow J/\psi\Lambda$ candidates found using the low and high q^2 selections. Values for the signal shape parameters are shown on Fig. 3.12. Fits to the rare $\Lambda_b^0 \rightarrow \Lambda\mu^+\mu^-$ samples are shown in Fig. 3.14 for the integrated $15 < q^2 < 20$ and $1.1 < q^2 < 6.0 \text{ GeV}^2/c^4$ q^2 intervals, while fitted invariant mass distribution in all other considered q^2 intervals are in Figs. 3.15 and 3.16 for downstream and long candidates respectively. The yields of rare candidates obtained from the fit are listed in Tab. 3.6 together with their significances. Most candidates are found in the downstream sample, which comprises $\sim 80\%$ of the total yield. Note that, since the fit is simultaneous to the two candidate categories, their yields are not parameters free to float independently in the fit but are correlated via the branching ratio. The statistical significance of the observed signal yields is evaluated as $\sqrt{2\Delta \ln \mathcal{L}}$, where $\Delta \ln \mathcal{L}$ is the change in the logarithm of the likelihood function when the signal component is excluded from the fit, relative to the nominal fit in which it is present.

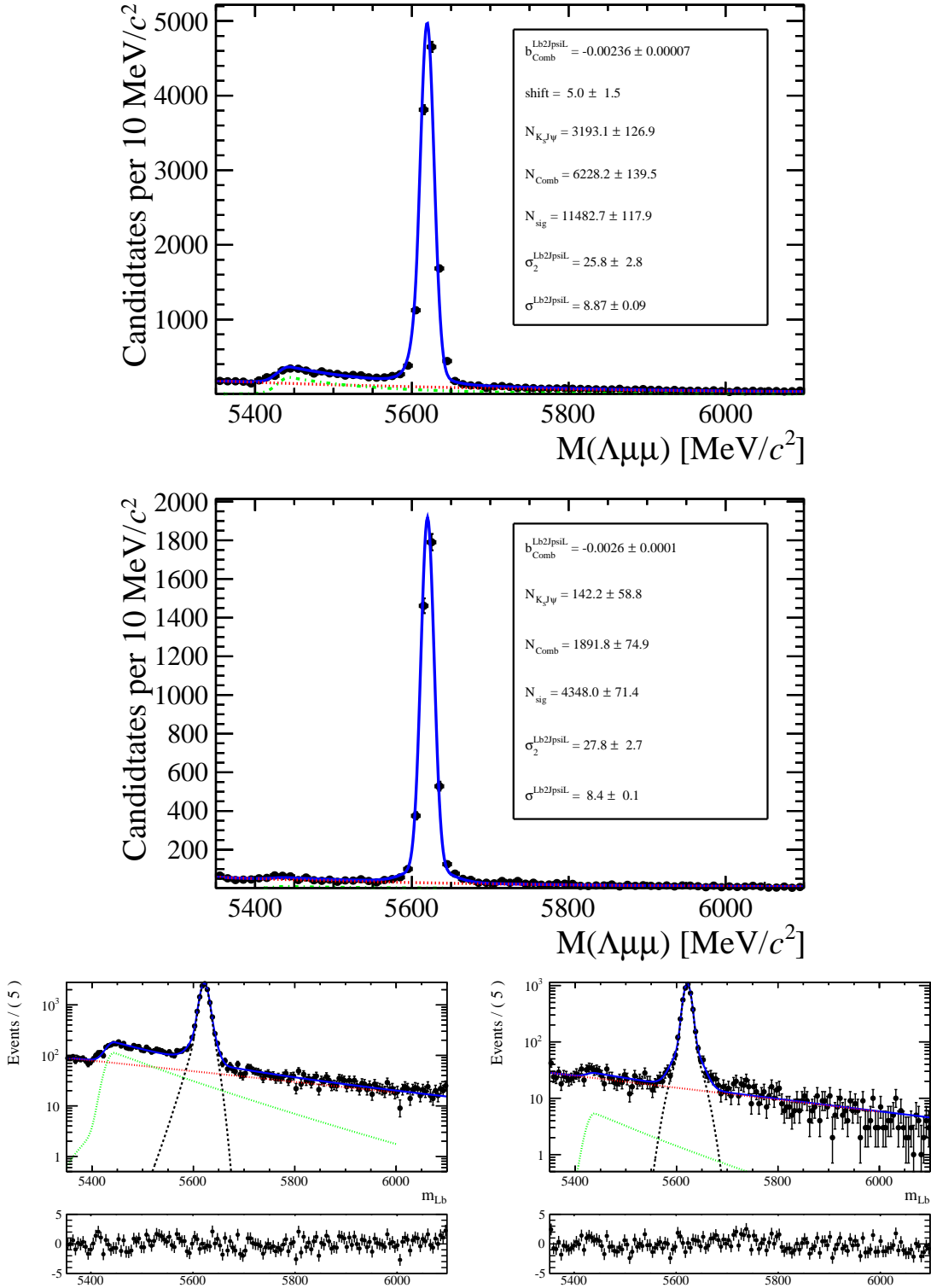


Figure 3.12: Invariant mass distributions of $\Lambda_b^0 \rightarrow J/\psi \Lambda$ downstream (top) and long (middle) candidates selected with high q^2 requirements. Bottom plots are the same as the upper ones but shown in logarithmic scale. Black points show data. The blue solid line represents the total fit function, the black dashed line the signal, the red dashed line the combinatorial background and the green dashed line the $B^0 \rightarrow K_s^0 \mu^+ \mu^-$ background.

Table 3.5: Number of $\Lambda_b^0 \rightarrow J/\psi \Lambda$ candidates in the long and downstream categories found using the for low- and high- q^2 requirements. Uncertainties shown are statistical only.

Selection	Long	Downstream
high- q^2	4313 ± 70	11497 ± 123
low- q^2	3363 ± 59	7225 ± 89

Table 3.6: Signal yields (N_S) obtained from the mass fit to $\Lambda_b^0 \rightarrow \Lambda\mu^+\mu^-$ candidates in each q^2 interval together with their statistical significances. The $8 - 11$ and $12.5 - 15$ GeV^2/c^4 q^2 intervals are excluded from the study as they are dominated by decays via charmonium resonances.

q^2 interval [GeV^2/c^4]	DD	LL	Tot. yield	Significance
0.1 – 2.0	6.9 ± 2.2	9.1 ± 3.0	16.0 ± 5.3	4.4
2.0 – 4.0	1.8 ± 1.7	3.0 ± 2.8	4.8 ± 4.7	1.2
4.0 – 6.0	0.4 ± 0.9	0.6 ± 1.4	0.9 ± 2.3	0.5
6.0 – 8.0	4.3 ± 2.0	7.2 ± 3.3	11.4 ± 5.3	2.7
11.0 – 12.5	14.6 ± 2.9	42.8 ± 8.5	60 ± 12	6.5
15.0 – 16.0	13.5 ± 2.2	43.5 ± 7.2	57 ± 9	8.7
16.0 – 18.0	28.6 ± 3.3	88.8 ± 10.1	118 ± 13	13
18.0 – 20.0	22.4 ± 2.6	78.0 ± 8.9	100 ± 11	14
1.1 – 6.0	3.6 ± 2.4	5.7 ± 3.8	9.4 ± 6.3	1.7
15.0 – 20.0	64.6 ± 4.7	209.6 ± 15.3	276 ± 20	21

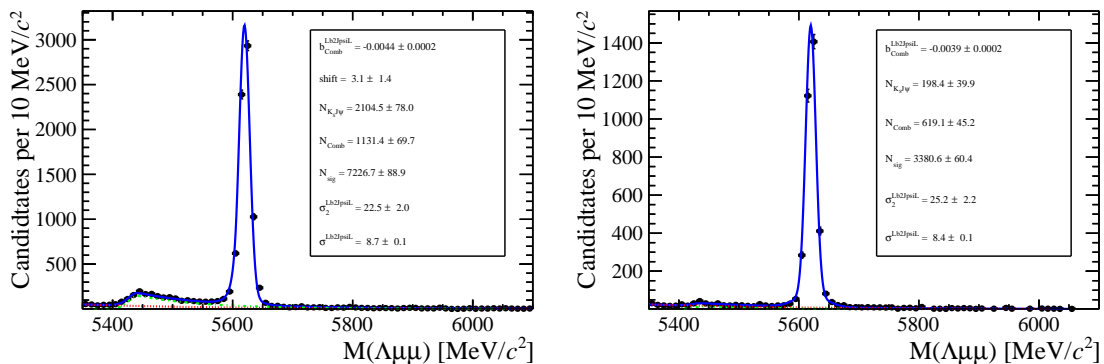


Figure 3.13: Invariant mass distribution of $\Lambda_b^0 \rightarrow J/\psi \Lambda$ for downstream (left) and long (right) candidates selected with low q^2 requirements.

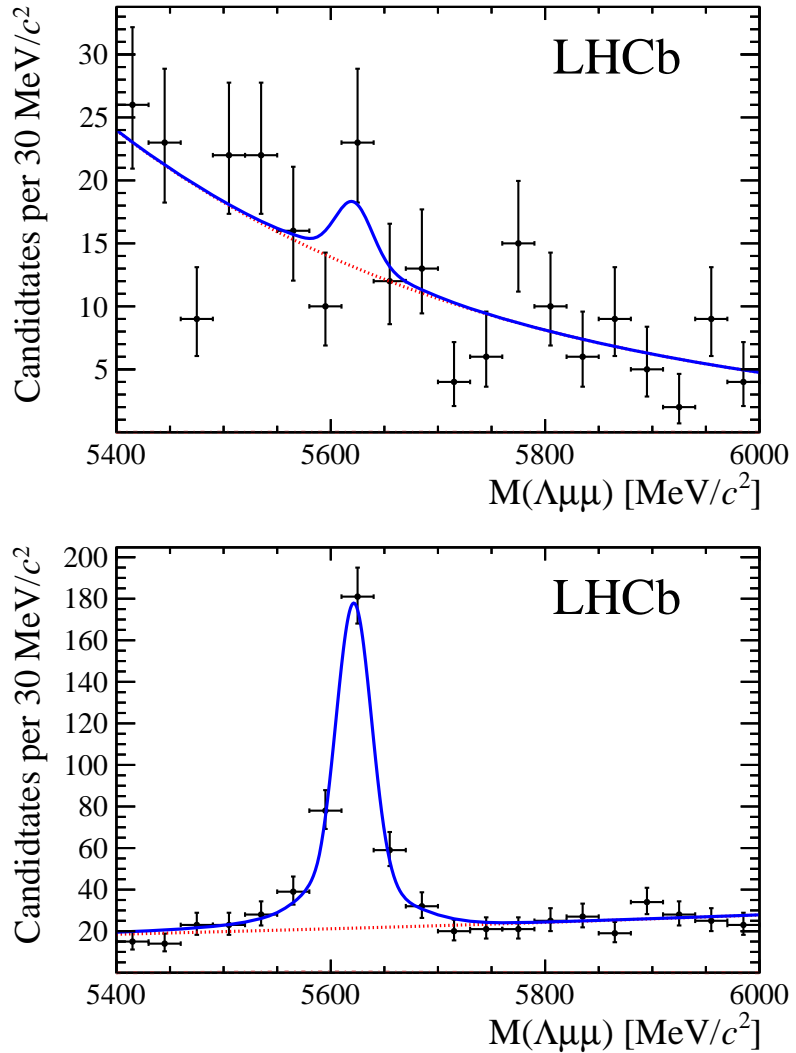


Figure 3.14: Invariant mass distributions of $\Lambda_b^0 \rightarrow \Lambda\mu^+\mu^-$ candidates in the integrated $0.1\text{--}6.0 \text{ GeV}^2/c^4$ (top) and $15\text{--}20 \text{ GeV}^2/c^4$ (bottom) q^2 intervals. Points show data combining downstream and long candidates together. The blue solid line represents the total fit function and the dashed red line the combinatorial background.

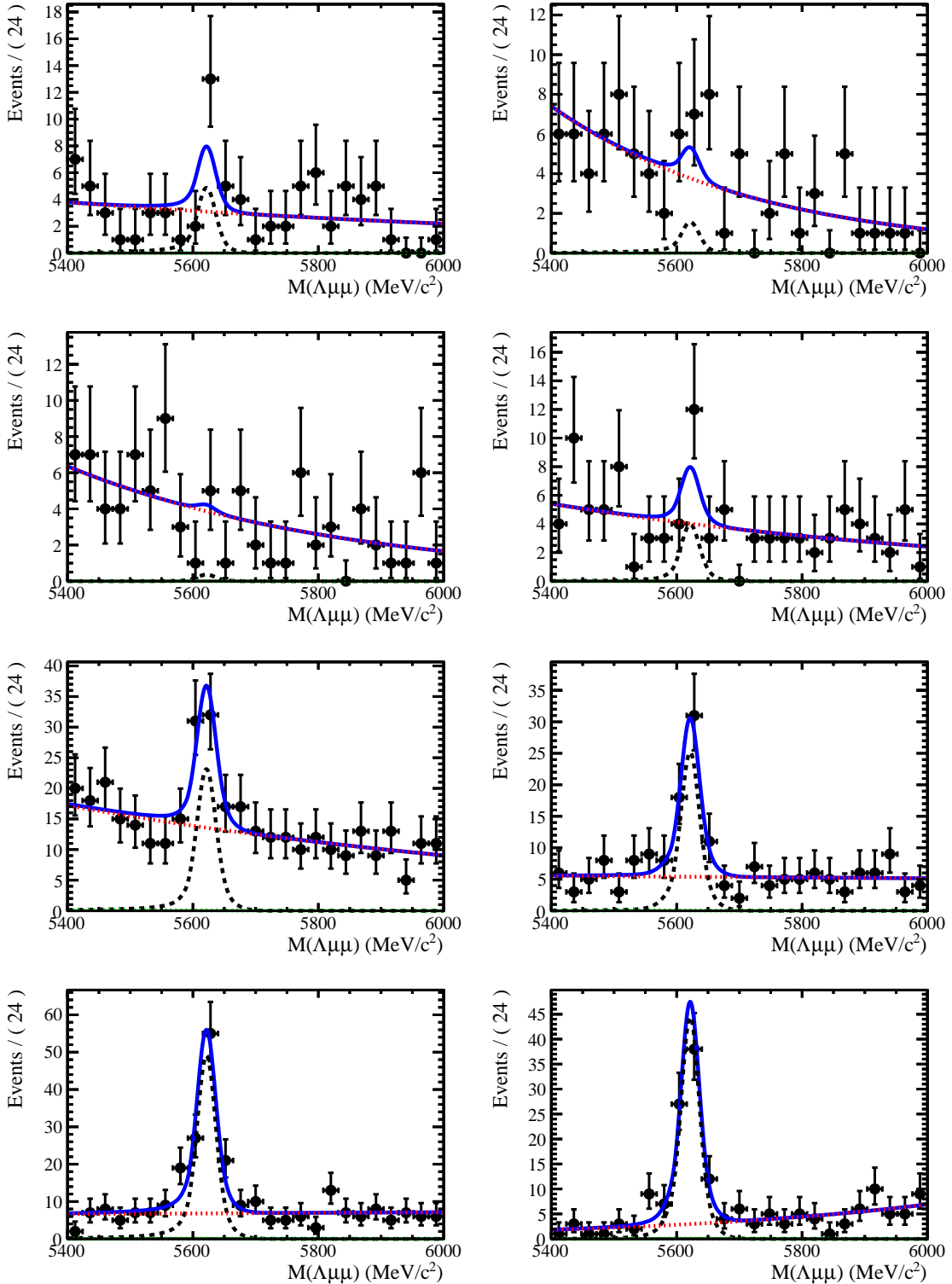


Figure 3.15: Invariant mass distributions of rare $\Lambda_b^0 \rightarrow \Lambda\mu^+\mu^-$ candidates in the considered q^2 bins for downstream candidates.

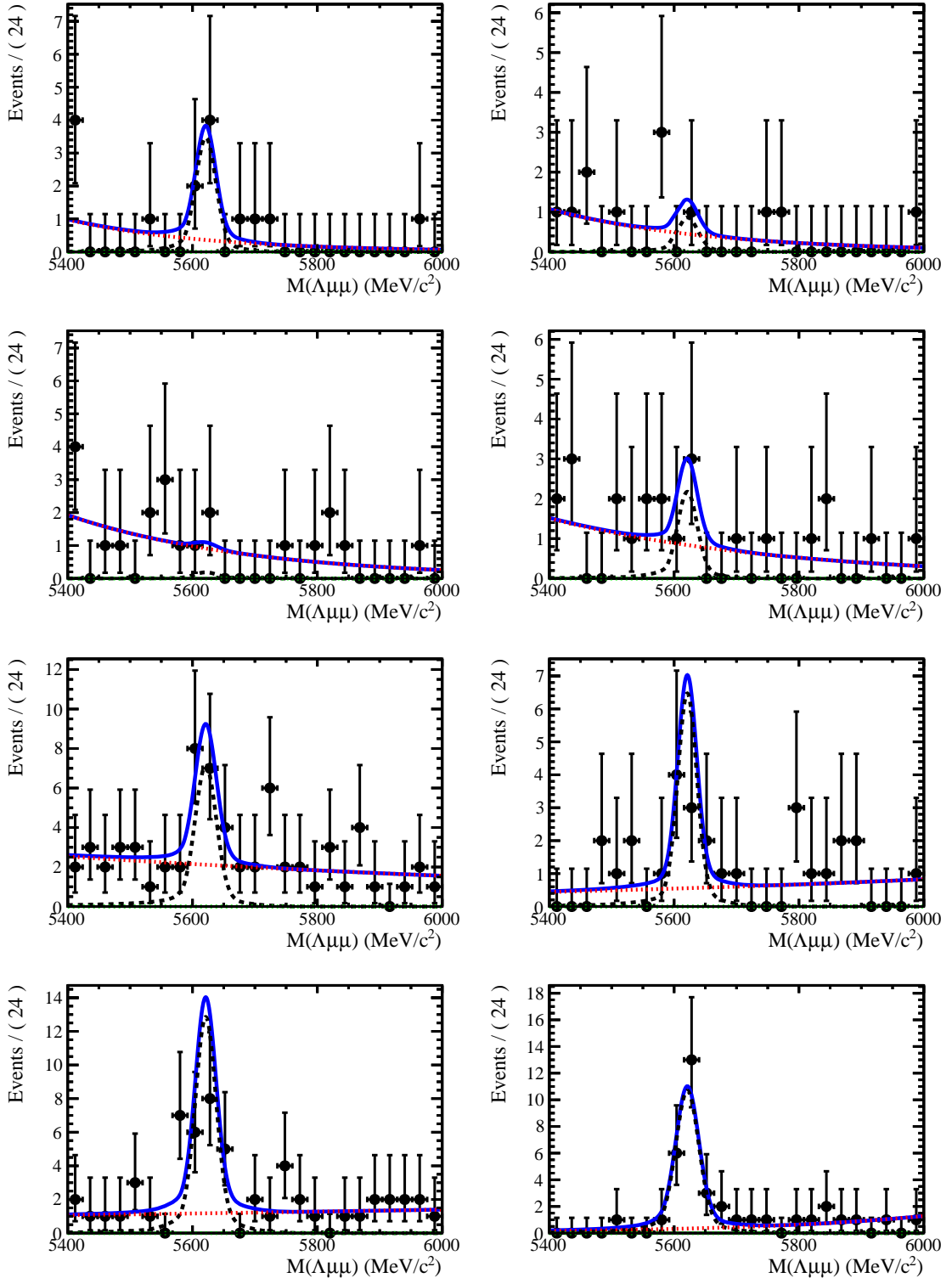


Figure 3.16: Invariant mass distributions of rare $\Lambda_b^0 \rightarrow \Lambda\mu^+\mu^-$ candidates in the considered q^2 bins for long candidates.

₁₃₀₉ **3.6 Efficiency**

₁₃₁₀ The selection efficiency is calculated for each decay according to the formula

$$\varepsilon^{tot} = \varepsilon(Geom)\varepsilon(Det|Geom)\varepsilon(Reco|Det)\epsilon(MVA|Reco)\varepsilon(Trig|MVA). \quad (3.12)$$

₁₃₁₁ In this expression the first term gives the efficiency to have final state particles
₁₃₁₂ in the LHCb acceptance. The second term handles the possibility of Λ escaping
₁₃₁₃ the detector or interacting with it and therefore never decaying into $p\pi$; this term
₁₃₁₄ is referred to as “detection” efficiency. The third term carries information about
₁₃₁₅ the reconstruction and pre-selection efficiencies, which are kept together given that
₁₃₁₆ boundaries between them are completely artificial. The fourth part deals with the
₁₃₁₇ efficiency of the Neural Network for those events which passed the pre-selection.
₁₃₁₈ Finally, the last term handles the trigger efficiency for events which are accepted
₁₃₁₉ by the full selection. Most of the efficiency components are evaluated using the
₁₃₂₀ simulated samples described in Sec. 3.3. Only the efficiency of the PID requirement
₁₃₂₁ for the proton (see Tab. 3.1) is separately derived with a data–driven method because
₁₃₂₂ the simulation does not provide a good description of PID variables. For complete
₁₃₂₃ information, all absolute efficiencies for the two decays $\Lambda_b^0 \rightarrow \Lambda\mu^+\mu^-$ and $\Lambda_b^0 \rightarrow J/\psi\Lambda$
₁₃₂₄ are separately listed in the next subsections. However, for the analysis itself only
₁₃₂₅ the relative efficiency, $\varepsilon(\Lambda_b^0 \rightarrow \Lambda\mu^+\mu^-)/\varepsilon(\Lambda_b^0 \rightarrow J/\psi\Lambda)$, is used.

₁₃₂₆ **3.6.1 Geometric acceptance**

₁₃₂₇ In order to save disk space and time only events are simulated in which the final
₁₃₂₈ muons are in the detector acceptance and therefore can be reconstructed. This corre-
₁₃₂₉ sponds to a requirement for each of the muons to be in an interval $10 < \theta < 400$ mrad,
₁₃₃₀ where θ is the angle between the muon momentum and the beam line. The efficiency
₁₃₃₁ of this requirement is obtained by using a separate simulated sample, where events
₁₃₃₂ are generated in the full space. The geometric efficiency varies between 18% at
₁₃₃₃ high- q^2 and 20% at low- q^2 ; Fig. 3.17 shows the dependence of this efficiency as a

1334 function of q^2 .

1335 3.6.2 Reconstruction and neural network efficiencies

1336 The efficiency to reconstruct the decays together with the pre-selection requirements
1337 is evaluated from simulated data. The reconstruction efficiency is subdivided in “De-
1338 tection” and “Reconstruction and pre-selection” efficiencies. In fact, since Λ is a long
1339 lived particle, there is a non-negligible probability that it interacts in the detector or
1340 escapes from it and therefore never decays in proton and pion. The reconstruction
1341 efficiency includes the efficiency of for the tracks to produce observable signatures
1342 and the efficiency for candidates to pass the pre-selection requirements. This compo-
1343 nent does not include the efficiency of the PID cut that appears in Tab. 3.1, which
1344 is kept separate because PID variables are not well described by the simulation.
1345 The detection efficiency varies between 88% at high- q^2 and 20% at low- q^2 while the
1346 reconstruction efficiency for downstream candidates is almost flat at 6.6% and for
1347 long candidates it varies from 1.6% at high- q^2 to 2.0% at low- q^2 . Fig. 3.17 shows the
1348 dependence of these efficiencies as a function of q^2 . The NN selection efficiency is
1349 again evaluated from simulated samples and it is observed to vary from 58% to 84%
1350 for downstream candidates and from 77% to 92% for log candidates. Fig. 3.17 shows
1351 the dependence of this efficiency as a function of q^2 . The sudden jump in efficiency
1352 at $\sim 9 \text{ GeV}/c^2$ is due to the fact that a different figure-of-merit is used to optimise
1353 the NN cut in the low and high q^2 regions, which results in different efficiencies.

1354 3.6.3 Trigger efficiency

1355 The trigger efficiency is again calculated using a simulated sample and it varies
1356 between 61% and 84% for downstream candidates and from 65% to 85% for long
1357 candidates. Fig. 3.17 shows the dependence of this efficiency as a function of q^2 .
1358 Using the resonant channel it is possible to crosscheck on data the efficiency obtained
1359 using the simulation. In LHCb triggered events can fall in two categories: events

1360 triggered by a track which is part of a signal candidate, Trigger On Signal (TOS),
1361 or by other tracks in the event, Trigger Independent of Signal (TIS). As the TIS and
1362 TOS categories are not exclusive the TIS sample provides a control sample which
1363 can be used to obtain the efficiency for TOS trigger. This is calculated with the
1364 formula:

$$\varepsilon_{\text{TOS}} = \frac{\text{TIS and TOS}}{\text{TIS}}. \quad (3.13)$$

1365 As data contains background the numbers of signal candidates in the “TIS” and
1366 “TIS && TOS” categories are not just determined by counting events but from a fit
1367 to the 4-body invariant mass, $m(p\pi\mu\mu)$. This procedure takes the name of TISTOS
1368 method. Using the data–driven method an efficiency of $(70 \pm 5)\%$ is obtained, while
1369 this is calculated to be $(73.33 \pm 0.02)\%$ using the simulation. Results are therefore
1370 compatible within 1σ .

1371 3.6.4 PID efficiency

1372 For long tracks a PID requirement on protons ($\text{PID}_p > -5$) is applied. The simula-
1373 tion is known not to describe particle ID variables well and therefore a data-driven
1374 method is used to obtain this efficiency component. This is done using the `PIDCalib`
1375 package (see Sec. 2.8.1), which uses as calibrations samples decays where particles
1376 can be identified due to their kinematic properties. In the case of protons a sample
1377 of Λ particles is used, where the proton can be identified because it always has the
1378 highest momentum. The package allows to divide the phase space in bins of variables
1379 relevant for PID performances; in this analysis momentum and pseudorapidity are
1380 used. Using the calibration sample the efficiency is derived in each two-dimensional
1381 bin. Finally, to take into account that the decay channel under study could have
1382 different kinematical distributions than the calibration sample these efficiency tables
1383 are used to re-weight the simulation. The PID efficiency varies from 97.3% at low- q^2
1384 to 98.2% at high- q^2 .

Table 3.7: Absolute efficiency values for $\Lambda_b^0 \rightarrow J/\psi \Lambda$. Uncertainties are statistical only.

Efficiency	Downstream	Long
$\varepsilon(PID)$	0.1818 ± 0.0003	
$\varepsilon(Det)$	0.9017 ± 0.0003	
$\varepsilon(Reco)$	0.0724 ± 0.0004	0.0203 ± 0.0002
$\varepsilon(PID)$	–	97.89 ± 0.005
$\varepsilon(MVA)$	0.882 ± 0.002	0.942 ± 0.002
$\varepsilon(Trig)$	0.697 ± 0.003	0.734 ± 0.005
Full Selection	0.0445 ± 0.0003	0.0140 ± 0.0002
Total	0.00729 ± 0.00005	0.00230 ± 0.00003

1385 3.6.5 Relative efficiencies

1386 In the previous sections absolute efficiencies values were given for the rare channel
 1387 in different q^2 intervals. Figure 3.17 contains a summary of those values in these
 1388 tables in graphical form. This section reports the corresponding relative efficiencies
 1389 with respect to the $\Lambda_b^0 \rightarrow J/\psi \Lambda$ channel, which will be used to correct the yields and
 1390 obtain the differential branching fraction. Table 3.7 reports the absolute efficiency
 1391 values for the J/ψ channel used to derive the relative efficiencies. Relative geometric,
 1392 detection and PID efficiencies are listed in Tab. 3.8, while Tabs. 3.10 and 3.9 report
 1393 relative reconstruction, trigger and NN efficiencies separately for downstream and
 1394 long candidates. Since the latter three components are obtained from the same sim-
 1395 ulated sample their statistical errors are correlated. Therefore the total of the three
 1396 is also reported as a single efficiency and labeled “Full Selection”. Finally, Tab. 3.13
 1397 reports the total of all relative efficiencies, which will be then used to correct the
 1398 raw yields and calculate the differential branching fraction. Uncertainties reflect
 1399 the statistics of both rare and resonant samples, while systematic uncertainties are
 1400 discussed in next sections.

Table 3.8: Relative geometric, detection and PID relative efficiencies between $\Lambda_b^0 \rightarrow \Lambda\mu^+\mu^-$ and $\Lambda_b^0 \rightarrow J/\psi\Lambda$ decays. Uncertainties reflect the statistics of both samples.

q^2 [GeV $^2/c^4$]	Geometric	Detection	PID
0.1 – 2.0	1.2976 ± 0.0050	0.9751 ± 0.0006	0.99418 ± 0.00013
2.0 – 4.0	1.1541 ± 0.0043	0.9814 ± 0.0005	0.99523 ± 0.00013
4.0 – 6.0	1.1043 ± 0.0044	0.9872 ± 0.0006	0.99699 ± 0.00012
6.0 – 8.0	1.0778 ± 0.0045	0.9939 ± 0.0006	0.99805 ± 0.00011
11.0 – 12.5	1.0431 ± 0.0058	1.0074 ± 0.0007	1.00151 ± 0.00010
15.0 – 16.0	1.0426 ± 0.0084	1.0188 ± 0.0010	1.00431 ± 0.00008
16.0 – 18.0	1.0296 ± 0.0068	1.0255 ± 0.0008	1.00215 ± 0.00008
18.0 – 20.0	1.0288 ± 0.0087	1.0333 ± 0.0010	1.00226 ± 0.00005
1.1 – 6.0	1.1396 ± 0.0031	0.9835 ± 0.0004	0.99589 ± 0.00009
15.0 – 20.0	1.0320 ± 0.0048	1.0269 ± 0.0006	1.00281 ± 0.00006

Table 3.9: Relative efficiencies between $\Lambda_b^0 \rightarrow \Lambda\mu^+\mu^-$ and $\Lambda_b^0 \rightarrow J/\psi\Lambda$ decays for long events. Uncertainties reflect the statistics of both samples.

q^2 [GeV $^2/c^4$]	Recostrucion	MVA	Trigger	Full Selection
0.1 – 2.0	0.96 ± 0.02	0.863 ± 0.012	0.79 ± 0.02	0.65 ± 0.02
2.0 – 4.0	0.97 ± 0.02	0.803 ± 0.012	0.89 ± 0.02	0.69 ± 0.02
4.0 – 6.0	1.04 ± 0.02	0.824 ± 0.012	0.92 ± 0.02	0.79 ± 0.02
6.0 – 8.0	1.05 ± 0.02	0.825 ± 0.012	0.96 ± 0.02	0.84 ± 0.02
11.0 – 12.5	1.10 ± 0.03	1.002 ± 0.008	1.01 ± 0.02	1.10 ± 0.03
15.0 – 16.0	0.89 ± 0.03	0.987 ± 0.013	1.13 ± 0.02	0.98 ± 0.04
16.0 – 18.0	0.84 ± 0.03	0.985 ± 0.010	1.17 ± 0.02	0.97 ± 0.03
18.0 – 20.0	0.67 ± 0.03	0.944 ± 0.017	1.18 ± 0.02	0.75 ± 0.04
1.1 – 6.0	1.00 ± 0.02	0.820 ± 0.008	0.89 ± 0.01	0.73 ± 0.02
15.0 – 20.0	0.78 ± 0.02	0.973 ± 0.008	1.16 ± 0.01	0.89 ± 0.02

Table 3.10: Relative efficiencies between $\Lambda_b^0 \rightarrow \Lambda\mu^+\mu^-$ and $\Lambda_b^0 \rightarrow J/\psi\Lambda$ decays for downstream events. Uncertainties reflect the statistics of both samples.

q^2 [GeV $^2/c^4$]	Reconstruction	MVA	Trigger	Full Selection
0.1 – 2.0	0.721 ± 0.009	0.706 ± 0.010	0.805 ± 0.011	0.410 ± 0.009
2.0 – 4.0	0.920 ± 0.010	0.661 ± 0.008	0.870 ± 0.010	0.529 ± 0.010
4.0 – 6.0	0.997 ± 0.010	0.662 ± 0.008	0.895 ± 0.010	0.590 ± 0.011
6.0 – 8.0	1.050 ± 0.011	0.665 ± 0.008	0.960 ± 0.010	0.671 ± 0.012
11.0 – 12.5	1.112 ± 0.014	1.007 ± 0.006	1.069 ± 0.009	1.197 ± 0.019
15.0 – 16.0	1.019 ± 0.018	1.000 ± 0.009	1.175 ± 0.012	1.197 ± 0.026
16.0 – 18.0	0.968 ± 0.014	0.961 ± 0.008	1.200 ± 0.010	1.115 ± 0.020
18.0 – 20.0	0.832 ± 0.016	0.943 ± 0.010	1.231 ± 0.012	0.966 ± 0.023
1.1 – 6.0	0.950 ± 0.007	0.663 ± 0.005	0.876 ± 0.007	0.551 ± 0.007
15.0 – 20.0	0.929 ± 0.010	0.963 ± 0.005	1.204 ± 0.007	1.077 ± 0.014

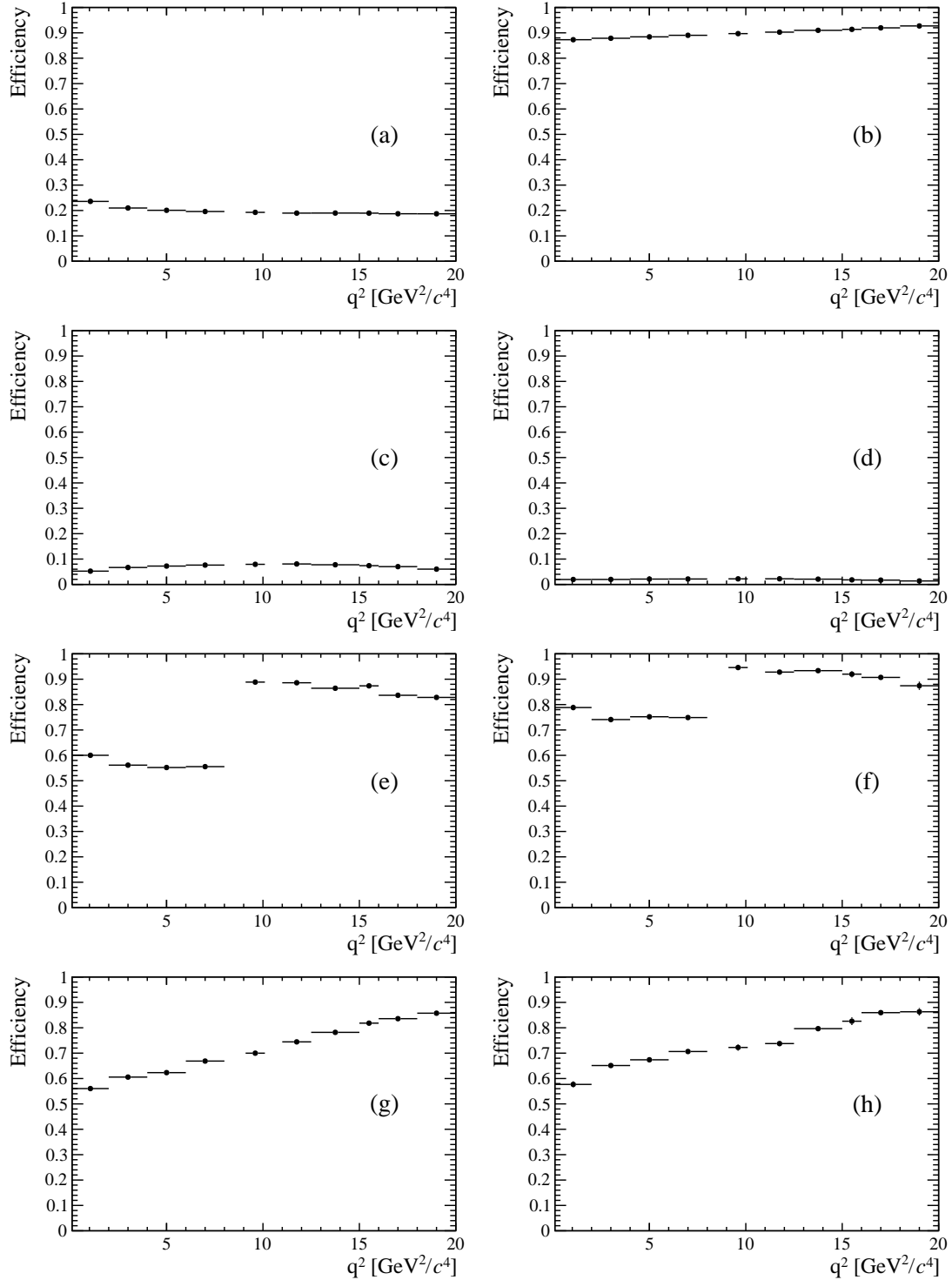


Figure 3.17: Absolute efficiencies as a function of q^2 : geometric efficiency (a), detection efficiency (b), reconstruction efficiency for DD (c) and LL (d) candidates, NN efficiency for DD (e) and LL (f) and trigger efficiency for DD (g) and LL (h).

¹⁴⁰¹ **3.7 Systematic uncertainties**

¹⁴⁰² This section describes the main considered sources of systematic uncertainty.

¹⁴⁰³ **3.7.1 Systematic uncertainty on the yields**

¹⁴⁰⁴ The choice of specific PDFs to model the invariant mass distribution could result in
¹⁴⁰⁵ a bias. To asses the effect of the signal PDF choice as a first step a number of models
¹⁴⁰⁶ are tried on the $\Lambda_b^0 \rightarrow J/\psi \Lambda$ data sample to understand which ones are plausible.
¹⁴⁰⁷ Table 3.11 reports the χ^2 and relative probabilities obtained using different models
¹⁴⁰⁸ including: the default model (a DCB function), a simple Gaussian function, a single
¹⁴⁰⁹ Crystal Ball function and the sum of two Gaussians. The only two models that give
¹⁴¹⁰ a reasonable p-value are the default DCB and the sum of two Gaussian functions
¹⁴¹¹ (DG). In a second step simulated experiments are generated and fit with the two
¹⁴¹² chosen models. Events are generated according to a density function given by the
¹⁴¹³ default model fitted on data separately for each q^2 interval. In this way, for each
¹⁴¹⁴ q^2 interval, a specific shape is reproduced including the background level and slope.
¹⁴¹⁵ Furthermore, a number of events comparable to the one found in data is generated.
¹⁴¹⁶ For each experiment a normalised bias is calculated as

$$b = \left(\frac{N_{\ell\ell}^{DCB}}{N_{J/\psi}^{DCB}} - \frac{N_{\ell\ell}^{DG}}{N_{J/\psi}^{DG}} \right) / \frac{N_{\ell\ell}^{DCB}}{N_{J/\psi}^{DCB}} \quad (3.14)$$

¹⁴¹⁷ where $N_{\ell\ell}^{model}$ and $N_{J/\psi}^{model}$ are the numbers of rare and resonant candidates observed
¹⁴¹⁸ using a specific model. The average bias over 1000 pseudo-experiments is taken as
¹⁴¹⁹ systematic uncertainty. Note that in each case the rare and normalisation channels
¹⁴²⁰ are fit with the same signal model and, while for the default case the rare parameters
¹⁴²¹ are fixed to what found for the resonant channel, they are left free to vary in the
¹⁴²² second model in order to asses at the same time the systematic due to the parameters
¹⁴²³ constraints.

Table 3.11: χ^2 , NDF, p-values and number of signal events obtained fitting $\Lambda_b^0 \rightarrow J/\psi \Lambda$ data using different models.

Model	χ^2/ndf	NDF	p-value	N_{evts}
DCB (default)	1.0	187	0.51	9965.4
Gauss	1.8	193	~ 0	9615.7
Double Gauss	1.1	191	0.45	9882.4
CB	1.5	191	~ 0	9802.4

1424

1425 For the background PDF systematic the rare channel is re-fit leaving the yield of
 1426 the K_s^0 component free to vary; this is instead fixed to the predicted value in the
 1427 default fit. The same procedure as for the signal PDF is applied. Results are re-
 1428 ported in Tab. 3.12. The most affected q^2 interval is the one in the middle of the
 1429 charmonium resonances, where a combination of lower statistics and higher back-
 1430 ground leaves more freedom to the signal shape. Finally, a background component
 1431 for $B^+ \rightarrow K^{*+}(K_s^0\pi^+)\mu^+\mu^-$ decays is added to the fit, modelled using the distri-
 1432 bution of simulated events after full selection. No significant bias is found for this
 1433 component.

q^2 [GeV $^2/c^4$]	Sig. PDF bias (%)	Bkg. PDF bias (%)	Tot. sys. (%)
0.1 – 2.0	3.2	1.1	3.4
2.0 – 4.0	2.9	2.4	3.8
4.0 – 6.0	4.6	4.8	6.6
6.0 – 8.0	1.2	1.7	2.0
11.0 – 12.5	2.6	1.8	3.2
15.0 – 16.0	1.3	2.5	2.8
16.0 – 18.0	0.6	1.3	1.4
18.0 – 20.0	1.7	1.8	2.5
1.1 – 6.0	0.1	4.2	4.2
15.0 – 20.0	1.0	0.2	1.1

Table 3.12: Values of systematic uncertainties due to the choice of signal and background shapes in bins of q^2 .

1434

¹⁴³⁵ 3.7.2 Systematic uncertainties on the efficiency determination

¹⁴³⁶ Systematic uncertainties in the efficiency determination are due to the limited knowl-
¹⁴³⁷ edge of the decay properties such as the Λ_b^0 lifetime and production polarisation. The
¹⁴³⁸ uncertainties are directly calculated on the relative efficiencies as these are the ones
¹⁴³⁹ that are actually used in the analysis. It should be noted that not all sources con-
¹⁴⁴⁰ tribute to each part of the efficiency. For brevity, this section only reports estimates
¹⁴⁴¹ of the systematic uncertainties obtained while the full information is contained in
¹⁴⁴² Appendix C.

¹⁴⁴³ 3.7.2.1 Effect of new physics on the decay model

¹⁴⁴⁴ New physics could affect the decay model by adding contributions to the C_7 and
¹⁴⁴⁵ C_9 Wilson Coefficients. This would result in a modification of the q^2 spectrum
¹⁴⁴⁶ and therefore of the efficiency. To asses this systematic the Wilson Coefficients are
¹⁴⁴⁷ modified by adding a new physics component ($C_i \rightarrow C_i + C_i^{\text{NP}}$). Figure 3.18 shows q^2
¹⁴⁴⁸ spectra obtained weighting the simulation for a model embedding the default and 3
¹⁴⁴⁹ modified sets of Wilson Coefficients. The used values, reported on top of each plot,
¹⁴⁵⁰ are inspired to maintain compatibility with the recent LHCb result about the P'_5
¹⁴⁵¹ observable [46]. The biggest effect is observed in the very low q^2 , below 2 GeV^2/c^4 ,
¹⁴⁵² where the efficiency can change up to 7%, while it changes 3-4 % between 3 and
¹⁴⁵³ 4 GeV^2/c^4 and 2-3 % in the rest of the spectrum. As this analysis is performed under
¹⁴⁵⁴ the hypothesis that the decays are described by a the SM, these values are given in
¹⁴⁵⁵ order to provide the full information but are not added as systematic uncertainties.

¹⁴⁵⁶ 3.7.2.2 Simulation statistics

¹⁴⁵⁷ The limited statistics of the simulated samples used to determine efficiencies is
¹⁴⁵⁸ considered as a source of systematic uncertainty. While it is not the dominant
¹⁴⁵⁹ source, its size does not allow to completely neglect it. When reporting relative

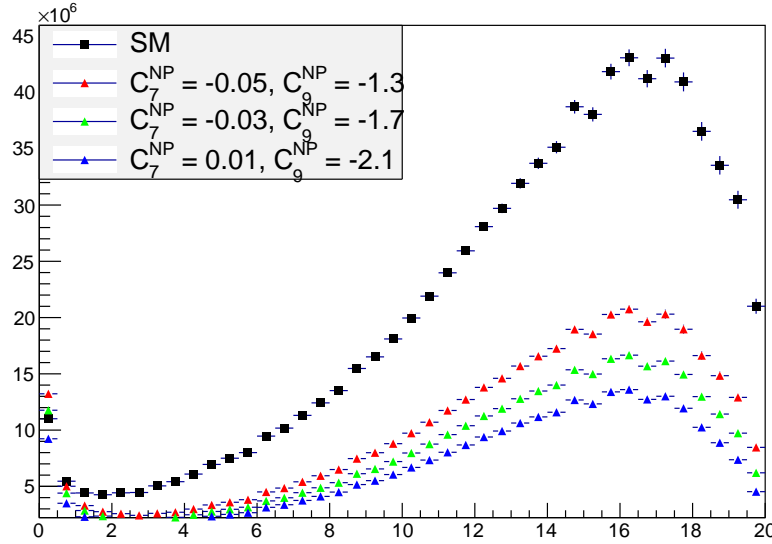


Figure 3.18: The q^2 spectrum of $\Lambda_b^0 \rightarrow \Lambda \mu^+ \mu^-$ events weighted with models embedding different sets of Wilson Coefficients. The black distribution corresponds to the weighting used to calculate efficiencies.

1460 efficiency values the statistical uncertainty due to the rare and resonant channels is
1461 always considered.

1462 3.7.2.3 Production polarisation and decay structure

1463 One of the main unknown, which affects the determination of the efficiencies, is
1464 the angular structure of the decays. And, connected to it, also the production
1465 polarisation, which is a parameter of the model. To assess the systematic uncertainty
1466 due to the knowledge of the production polarisation for $\Lambda_b^0 \rightarrow \Lambda \mu^+ \mu^-$ decays the
1467 polarisation parameter in the model is varied within one standard deviation from
1468 the central value of the most recent LHCb measurement, $P_b = 0.06 \pm 0.09$ [96]. The
1469 full observed difference is taken as systematic uncertainty. To assess the systematic
1470 uncertainty due to the decay structure an alternative set of form factors is used based
1471 on lattice QCD calculation [99]. Details of this are explained in Appendix A.1. The
1472 two models are compared and the full difference is taken as systematic uncertainty.
1473 In total this results in an uncertainty of $\sim 1.3\%$ for long candidates and $\sim 0.6\%$

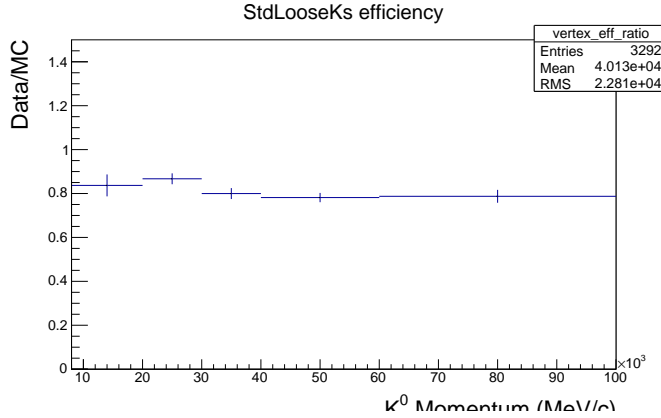


Figure 3.19: Ratio of reconstruction efficiency in Data and MC found using K_S events [101].

1474 for downstream candidates, mostly coming from the knowledge of the production
 1475 polarisation.

1476 3.7.2.4 Λ_b^0 lifetime

1477 The Λ_b^0 lifetime is known with limited precision. For evaluation of the efficiencies the
 1478 world average value, 1.482 ps^{-1} [100] is used. To evaluate the systematic uncertainty,
 1479 this is varied within one standard deviation from the measured value. Only the
 1480 case where both signal and normalisation channel are varied in same direction are
 1481 considered. The larger difference with the default lifetime case is taken as systematic
 1482 uncertainty, which is found to range from $\sim 0.4\%$ at low q^2 to $\sim 0.1\%$ at high q^2 .

1483 3.7.2.5 Downstream candidates reconstruction efficiency

1484 Other analysis in LHCb using particles reconstructed with downstream tracks showed
 1485 that the efficiency for these candidates is not well simulated. For example, Fig. 3.19
 1486 shows the ratio between the reconstruction efficiency for downstream candidates in
 1487 data and simulation found analysing K_S^0 events [101]. This effect is not yet fully
 1488 understood and is currently under study. It seems to be mainly due to a poor sim-
 1489 ulation of the vertexing efficiency for downstream tracks. This effect is dealt with

in two steps. Firstly, the analysis is performed separately for downstream and long candidates. Since efficiencies are also calculated separately, the effect mostly cancels in the ratio between the rare and resonant channels. In a second step a systematic uncertainty is assigned for downstream candidates only re-weighting the simulation by the efficiency ratio between data and simulation found for K_S as a function of momentum (see Fig. 3.19). The efficiencies obtained using the weighted and unweighted simulation are compared and the full difference is taken as systematic uncertainty. As the discrepancy shows little dependence on momentum, dependencies due to the different momentum distributions of Λ and K_S^0 are assumed to be negligible. This results in an extra 0.4% systematic uncertainty at low q^2 and 1.2% at high q^2 , only for downstream candidates.

3.7.2.6 Data-simulation discrepancies

The simulation used to calculate the efficiency is re-weighted as described in Sec. 3.3.2. The influence of this procedure on the efficiency determination is checked by comparing values obtained with and without re-weighting. The effect is negligible with respect to other systematics considered.

3.8 Differential branching ratio extraction

In this section the differential branching fraction of the $\Lambda_b^0 \rightarrow \Lambda\mu^+\mu^-$ decay is calculated relative to the $\Lambda_b^0 \rightarrow J/\psi\Lambda$ channel as a function of q^2 . The values are directly obtained from the fit to the rare sample by parameterising the downstream and long yields with the following formula:

$$N(\Lambda\mu^+\mu^-)_k = \left[\frac{d\mathcal{B}(\Lambda\mu^+\mu^-)/dq^2}{\mathcal{B}(J/\psi\Lambda)} \right] \cdot N(J/\psi\Lambda)_k \cdot \varepsilon_k^{\text{rel}} \cdot \frac{\Delta q^2}{\mathcal{B}(J/\psi \rightarrow \mu^+\mu^-)}, \quad (3.15)$$

where $k = (\text{LL}, \text{DD})$, Δq^2 is the width of the q^2 interval, $\mathcal{B}(J/\psi \rightarrow \mu^+\mu^-) = (5.93 \pm 0.06) \cdot 10^{-2}$ [2] and the only free parameter is the relative branching fraction ratio.

Table 3.13: Absolute values of the total relative efficiency and the absolute value of the uncorrelated uncertainty (σ_{uncorr}^k), together with relative values of the correlated uncertainty (σ_{corr}).

q^2 [GeV $^2/c^4$]	Eff. (DD)	σ_{uncorr}^{DD}	Eff. (LL)	σ_{uncorr}^{LL}	σ_{corr}
0.1 – 2.0	0.694	0.058	1.136	0.066	1.0%
2.0 – 4.0	0.693	0.027	0.907	0.047	2.7%
4.0 – 6.0	0.699	0.018	0.964	0.044	2.7%
6.0 – 8.0	0.733	0.020	0.953	0.048	2.7%
11.0 – 12.5	1.254	0.032	1.140	0.057	3.4%
15.0 – 16.0	1.260	0.035	1.035	0.060	3.0%
16.0 – 18.0	1.163	0.029	0.997	0.048	1.7%
18.0 – 20.0	1.023	0.027	0.782	0.040	2.7%
1.1 – 6.0	0.696	0.032	0.950	0.058	1.0%
15.0 – 20.0	1.132	0.014	0.927	0.031	1.4%

1513 Table 3.13 summarises the total relative efficiencies, ε^{rel} , for downstream and long
 1514 candidates together with their correlated and uncorrelated uncertainties, where the
 1515 correlation is intended between the downstream and long samples. On the table
 1516 the uncorrelated uncertainty corresponds to the total systematic uncertainty on the
 1517 efficiency determination. The correlated uncertainty is given in percent form since
 1518 it can be applied to either downstream, long candidates or their combination. This
 1519 includes the PDF systematic described in Sec. 3.7.1 and the systematic due to the
 1520 uncertainty on the $J/\psi \rightarrow \mu^+\mu^-$ branching fraction.

1521 Figure 3.20 shows the branching fraction obtained by fitting the downstream and
 1522 long samples independently, while the combined result, obtained fitting both sam-
 1523 ples simultaneously, is shown in Fig. 3.21. Values are also listed in Tab. 3.14, where
 1524 the statistical uncertainty on the rare channel and the total systematic uncertainty
 1525 are shown separately. The statistical uncertainty is calculated using the MINOS ap-
 1526 plication of the MINUIT package [102], which provides an asymmetric interval. The
 1527 normalisation and systematic uncertainties are evaluated by pushing the efficiencies
 1528 and normalisation yields up and down by one standard deviation and re-performing
 1529 the fit. The different efficiencies used translate into a different branching fraction and
 1530 the full difference with respect to the default fit is taken as systematic uncertainty
 1531 in each direction.

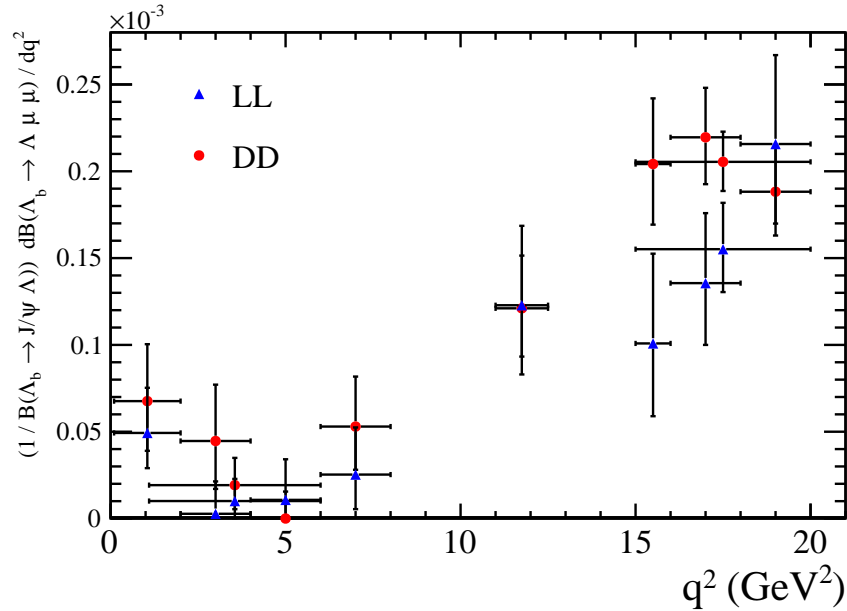


Figure 3.20: Measured values of the $\Lambda_b^0 \rightarrow \Lambda \mu^+ \mu^-$ branching fraction relative to the $\Lambda_b^0 \rightarrow J/\psi \Lambda$ decay as a function of q^2 obtained fitting the downstream and long samples independently. Error bars represent the total statistical and systematic uncertainty.

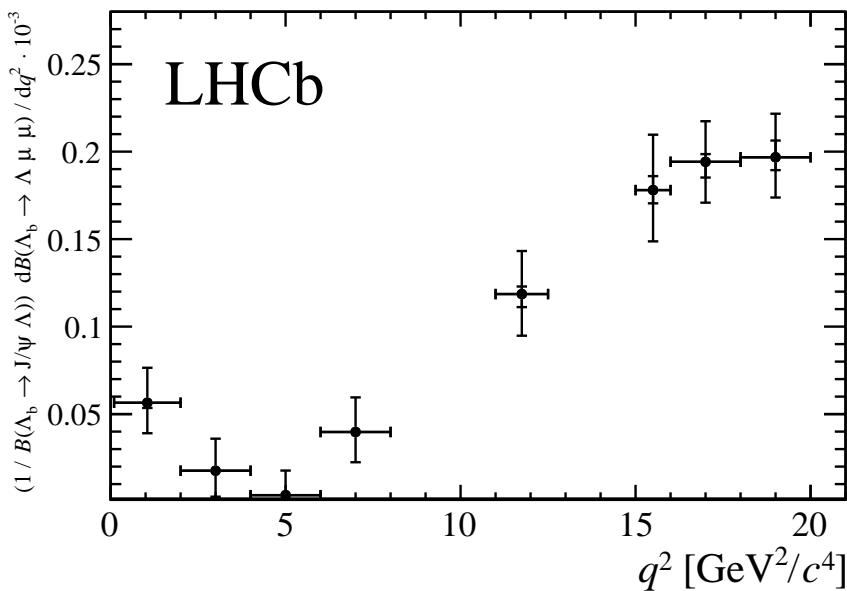


Figure 3.21: Branching fraction of the $\Lambda_b^0 \rightarrow \Lambda \mu^+ \mu^-$ decay normalised to the $\Lambda_b^0 \rightarrow J/\psi \Lambda$ mode. The inner error bar represents the systematic uncertainty and the outer error bar includes the statistical uncertainty.

Table 3.14: Differential branching fraction of the $\Lambda_b^0 \rightarrow \Lambda\mu^+\mu^-$ decay relative to $\Lambda_b^0 \rightarrow J/\psi\Lambda$ decays, where the uncertainties are statistical and systematic, respectively.

q^2 interval [GeV^2/c^4]	$\frac{d\mathcal{B}(\Lambda_b^0 \rightarrow \Lambda\mu^+\mu^-)/dq^2}{\mathcal{B}(\Lambda_b^0 \rightarrow J/\psi\Lambda)} \cdot 10^{-3}[(\text{GeV}^2/c^4)^{-1}]$		
0.1 – 2.0	0.56	+0.20 –0.17	+0.03 –0.03
2.0 – 4.0	0.18	+0.18 –0.15	+0.01 –0.01
4.0 – 6.0	0.04	+0.14 –0.04	+0.01 –0.01
6.0 – 8.0	0.40	+0.20 –0.17	+0.01 –0.02
11.0 – 12.5	1.19	+0.24 –0.23	+0.04 –0.07
15.0 – 16.0	1.78	+0.31 –0.28	+0.08 –0.08
16.0 – 18.0	1.94	+0.23 –0.22	+0.04 –0.09
18.0 – 20.0	1.97	+0.23 –0.22	+0.10 –0.07
1.1–6.0	0.14	+0.10 –0.09	+0.01 –0.01
15.0–20.0	1.90	+0.14 –0.14	+0.04 –0.06

Finally, values for the absolute branching fraction of the $\Lambda_b^0 \rightarrow \Lambda\mu^+\mu^-$ decay are obtained by multiplying the relative branching fraction by the absolute branching fraction of the normalisation channel, $\mathcal{B}(\Lambda_b^0 \rightarrow J/\psi\Lambda) = (6.3 \pm 1.3) \times 10^{-4}$ [2]. Values are shown in Fig. 3.22 and summarised in Tab. 3.15, where the uncertainty due to the knowledge of the normalisation channel (norm), which is correlated across q^2 , is shown separately. The SM predictions on the plot are obtained from Ref. [99].

Evidence for the signal is found for the first time in the q^2 region between the charmonium resonances and in the interval $0.1 < q^2 < 2.0 \text{ GeV}^2/c^4$, where an increased yield is expected due to the proximity of the photon pole. The uncertainty on the absolute branching fraction is dominated by the precision with which the branching fraction of the normalisation channel is known, while the uncertainty on the relative branching fraction is dominated by the size of the available data sample. The data are consistent with the theoretical predictions in the high- q^2 region but lie below the predictions in the low- q^2 region.

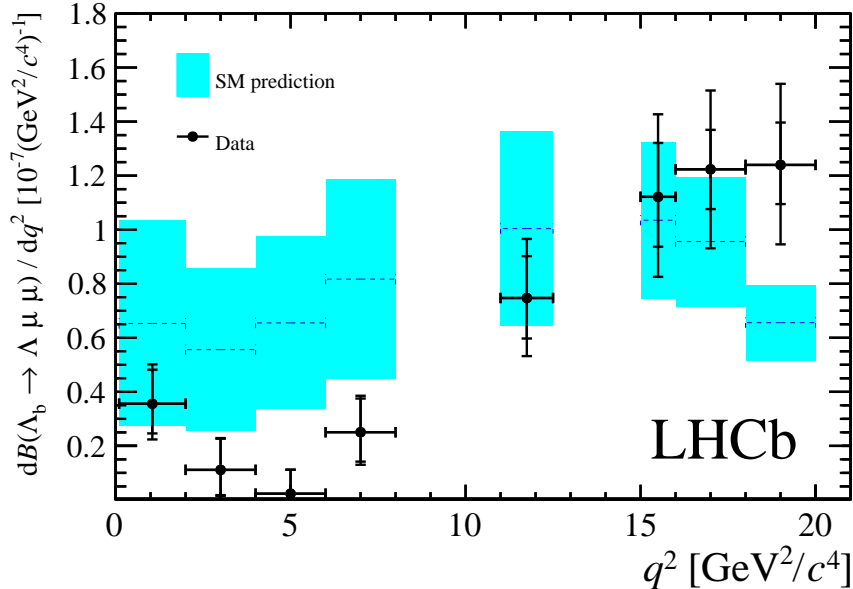


Figure 3.22: Measured $\Lambda_b^0 \rightarrow \Lambda \mu^+ \mu^-$ branching fraction as a function of q^2 with the SM predictions [99] superimposed. The inner error bars on data points represent the total uncertainty on the relative branching fraction (statistical and systematic); the outer error bar also includes the uncertainties from the branching fraction of the normalisation mode.

Table 3.15: Measured differential branching fraction of the $\Lambda_b^0 \rightarrow \Lambda \mu^+ \mu^-$ decay, where the uncertainties are statistical, systematic and due to the uncertainty on the normalisation mode, $\Lambda_b^0 \rightarrow J/\psi \Lambda$, respectively.

q^2 interval [GeV $^2/c^4$]	$d\mathcal{B}(\Lambda_b^0 \rightarrow \Lambda \mu^+ \mu^-)/dq^2 \cdot 10^{-7}[(\text{GeV}^2/c^4)^{-1}]$			
0.1 – 2.0	0.36	$+0.12$	$+0.02$	± 0.07
2.0 – 4.0	0.11	$+0.12$	$+0.01$	± 0.02
4.0 – 6.0	0.02	$+0.09$	$+0.01$	± 0.01
6.0 – 8.0	0.25	$+0.12$	$+0.01$	± 0.05
11.0 – 12.5	0.75	$+0.15$	$+0.03$	± 0.15
15.0 – 16.0	1.12	$+0.19$	$+0.05$	± 0.23
16.0 – 18.0	1.22	$+0.14$	$+0.03$	± 0.25
18.0 – 20.0	1.24	$+0.14$	$+0.06$	± 0.26
1.1 – 6.0	0.09	$+0.06$	$+0.01$	± 0.02
15.0 – 20.0	1.20	$+0.09$	$+0.02$	± 0.25

CHAPTER 4

Angular analysis of $\Lambda_b^0 \rightarrow \Lambda\mu^+\mu^-$ decays

Neglecting Λ_b^0 production polarisation, the $\Lambda_b^0 \rightarrow \Lambda\mu^+\mu^-$ decay angular distributions can be described as a function of three angles and q^2 . The first two angles are the ones which are relevant for the analysis in this chapter and are defined in Fig. 4.1, where θ_ℓ is the angle between the positive (negative) muon direction and the dimuon system direction in the Λ_b^0 ($\bar{\Lambda}_b^0$) rest frame, and θ_h is defined as the angle between the proton and the Λ baryon directions, also in the Λ_b^0 rest frame. The third angle is the angle between the dimuon and Λ decay planes, which is integrated over in this analysis. This chapter describes a measurement of two forward-backward asymmetries in the leptonic (A_{FB}^ℓ) and in the hadronic (A_{FB}^h) systems. These forward-backward asymmetries are defined as

$$A_{FB}^i(q^2) = \frac{\int_0^1 \frac{d^2\Gamma}{dq^2 d\cos\theta_i} d\cos\theta_i - \int_{-1}^0 \frac{d^2\Gamma}{dq^2 d\cos\theta_i} d\cos\theta_i}{d\Gamma/dq^2}, \quad (4.1)$$

1550 where $d^2\Gamma/dq^2 d\cos\theta_i$ is the two-dimensional differential rate and $d\Gamma/dq^2$ is rate
 1551 integrated over the angles.

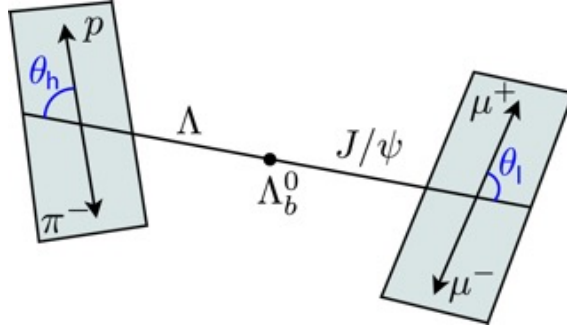


Figure 4.1: Graphical representation of the angles for the $\Lambda_b^0 \rightarrow \Lambda\mu^+\mu^-$ decay.

1552 The A_{FB}^ℓ observable was also measured by LHCb in $B^0 \rightarrow K^{*0}\mu^+\mu^-$ decays which
 1553 are going through the same quark level transition as $\Lambda_b^0 \rightarrow \Lambda\mu^+\mu^-$ decays. Instead
 1554 the hadronic asymmetry, A_{FB}^h , is interesting only in the Λ_b^0 case as it is zero by
 1555 definition in B^0 decays, where K^{*0} decays strongly.

1556 4.1 One-dimensional angular distributions

1557 This section describes the derivation of the functional form of the differential distri-
 1558 butions as a function of $\cos\theta_\ell$ and $\cos\theta_h$, which are used to measure the observables.
 1559 The content of this section is based on the calculations in Ref. [95].

1560 For unpolarised Λ_b^0 production, integrating over the three angles the differential
 1561 branching fraction is given in Eq. 11 of Ref. [95] as

$$\frac{d\Gamma(\Lambda_b \rightarrow \Lambda \ell^+ \ell^-)}{dq^2} = \frac{v^2}{2} \cdot \left(U^{V+A} + L^{V+A} \right) + \frac{2m_\ell^2}{q^2} \cdot \frac{3}{2} \cdot \left(U^V + L^V + S^A \right), \quad (4.2)$$

1562 and the lepton helicity angle differential distribution, given in Eq. 15, has the form

$$\begin{aligned} \frac{d\Gamma(\Lambda_b \rightarrow \Lambda \ell^+ \ell^-)}{dq^2 d\cos\theta_\ell} &= v^2 \cdot \left[\frac{3}{8} (1 + \cos^2\theta_\ell) \cdot \frac{1}{2} U^{V+A} + \frac{3}{4} \sin^2\theta_\ell \cdot \frac{1}{2} L^{V+A} \right] \\ &- v \cdot \frac{3}{4} \cos\theta_\ell \cdot P^{VA} + \frac{2m_\ell^2}{q^2} \cdot \frac{3}{4} \cdot \left[U^V + L^V + S^A \right]. \end{aligned} \quad (4.3)$$

In these formulas m_ℓ is the mass of the lepton and $v = \sqrt{1 - 4m_\ell^2/q^2}$; U denotes the unpolarised-transverse contributions, L the longitudinal contributions and S the scalar contribution. The apices V and A represent respectively vector and axial-vector currents, with $X^{V+A} = X^V + X^A$. The authors of Ref. [95] define then the lepton-side forward-backward asymmetry as

$$A_{\text{FB}}^\ell(q^2) = -\frac{3}{2} \frac{v \cdot P^{VA}}{v^2 \cdot (U^{V+A} + L^{V+A}) + \frac{2m_\ell^2}{q^2} \cdot 3 \cdot (U^V + L^V + S^A)}. \quad (4.4)$$

For this analysis the massless leptons limit, $m_\ell \rightarrow 0$, is used, which is a good approximation except at very low q^2 . Combining the previous equations ad taking the massless limit the differential rates simplify to

$$\frac{d\Gamma}{dq^2} = \frac{v^2}{2} \cdot (U^{V+A} + L^{V+A}) \quad (4.5)$$

and

$$\frac{d\Gamma}{dq^2 d \cos \theta_\ell} = \frac{v^2}{2} \left[\frac{3}{8} (1 + \cos^2 \theta_\ell) U^{V+A} + A_{\text{FB}}^\ell \cos \theta_\ell (U^{V+A} + L^{V+A}) + \frac{3}{4} \sin^2 \theta_\ell (L^{V+A}) \right]. \quad (4.6)$$

Equations 4.5 and 4.6 can be then combined to achieve the form

$$\begin{aligned} \frac{d\Gamma}{dq^2 d \cos \theta_\ell} &= \frac{d\Gamma}{dq^2} \left[\frac{3}{8} (1 + \cos^2 \theta_\ell) \frac{U^{V+A}}{U^{V+A} + L^{V+A}} + A_{\text{FB}}^\ell \cos \theta_\ell + \right. \\ &\quad \left. \frac{3}{4} \sin^2 \theta_\ell \frac{L^{V+A}}{U^{V+A} + L^{V+A}} \right]. \end{aligned} \quad (4.7)$$

The amplitude combination in the last term can be viewed as ratio between longitudinal and sum of longitudinal and unpolarised transverse contributions and therefore one can define the longitudinal fraction

$$f_L = \frac{L^{V+A}}{U^{V+A} + L^{V+A}}, \quad (4.8)$$

which leads to the functional form used in the analysis

$$\frac{d\Gamma}{dq^2 d \cos \theta_\ell} = \frac{d\Gamma}{dq^2} \left[\frac{3}{8} (1 + \cos^2 \theta_\ell) (1 - f_L) + A_{FB}^\ell \cos \theta_\ell + \frac{3}{4} \sin^2 \theta_\ell f_L \right]. \quad (4.9)$$

¹⁵⁷⁴ Using the same steps the proton helicity distribution is given in Ref. [95] as

$$\frac{d\Gamma(\Lambda_b \rightarrow \Lambda(\rightarrow p\pi^-)\ell^+\ell^-)}{dq^2 d \cos \theta_h} = \text{Br}(\Lambda \rightarrow p\pi^-) \frac{d\Gamma(\Lambda_b \rightarrow \Lambda \ell^+\ell^-)}{dq^2} \left(\frac{1}{2} + A_{FB}^h \cos \theta_h \right), \quad (4.10)$$

¹⁵⁷⁵ and A_{FB}^h is defined as

$$A_{FB}^h = \frac{1}{2} \alpha_\Lambda P_z^\Lambda(q^2), \quad (4.11)$$

¹⁵⁷⁶ where $P_z^\Lambda(q^2)$ is the polarisation of the daughter baryon, Λ , and $\alpha_\Lambda = 0.642 \pm 0.013$ [2]

¹⁵⁷⁷ is the Λ decay asymmetry parameter.

¹⁵⁷⁸ These expressions assume that Λ_b^0 is produced unpolarised, which is in agreement
¹⁵⁷⁹ with the recent LHCb measurement [103]. Possible effects due to a non zero pro-
¹⁵⁸⁰ duction polarisation are investigated as systematic uncertainties (see Sec. 4.5.5).

¹⁵⁸¹ 4.2 Multi-dimensional angular distributions

To incorporate effects of production polarisation this was introduced in the equations. In the modified version an angle θ is defined as the angle between the Λ direction in the Λ_b^0 rest frame with respect to $\hat{n} = \hat{p}_{inc} \times \hat{p}_{\Lambda_b^0}$, where \hat{p}_{inc} represents the direction of the incoming proton. This angle is sensitive to the production polarisation through the spin-density matrix. Integrating over all the angles but θ_ℓ results in the same distribution as in the unpolarised case (Eq. 4.3). Therefore, in the case of uniform efficiency, the lepton side forward-backward asymmetry, A_{FB}^ℓ , is unaffected by the production polarisation. To be able to estimate the effect of the production polarisation in the case of non-uniform efficiency, the differential distribution in θ and θ_ℓ is also derived, which in the massless leptons limit becomes (up

to a constant multiplicative factor)

$$\frac{d\Gamma(\Lambda_b \rightarrow \Lambda \ell^+ \ell^-)}{dq^2 d\cos\theta d\cos\theta_\ell} = \frac{d\Gamma}{dq^2} \left\{ \frac{3}{8} (1 + \cos^2\theta_\ell) (1 - f_L) + A_{FB}^\ell \cos\theta_\ell + \frac{3}{4} \sin^2\theta_\ell f_L + P_b \cos\theta \left[-\frac{3}{4} \sin^2\theta_\ell O_{Lp} + \frac{3}{8} (1 + \cos^2\theta_\ell) O_P \right. \right. \\ \left. \left. - \frac{3}{8} \cos\theta_\ell O_{UVA} \right] \right\}, \quad (4.12)$$

where three more observables are defined

$$O_{Lp} = \frac{L_P^V + L_P^A}{U^{V+A} + L^{V+A}}, \\ O_P = \frac{P^V + P^A}{U^{V+A} + L^{V+A}}, \\ O_{UVA} = \frac{U^{VA}}{U^{V+A} + L^{V+A}}.$$

- 1582 In the massless leptons approximation two of these quantities are related to the
1583 hadron side forward-backward asymmetry as

$$\frac{1}{2} \alpha_\Lambda (O_P + O_{Lp}) = A_{FB}^h. \quad (4.13)$$

Following the same steps as for the lepton case, after integrating over all the angles but θ_h one finds that the hadron side, A_{FB}^h , is also unaffected by the production polarisation in case of uniform efficiency. The differential distribution in θ and θ_h has the form

$$\frac{d\Gamma(\Lambda_b \rightarrow \Lambda \ell^+ \ell^-)}{dq^2 d(\cos\theta) d(\cos\theta_h)} = \frac{d\Gamma}{dq^2} [1 + 2A_{FB}^h \cos\theta_h + P_b (O_P - O_{Lp}) \cos\theta \\ + \alpha_\Lambda P_b (1 - 2f_L) \cos\theta \cos\theta_h]. \quad (4.14)$$

- 1584 In order to use these distributions, expectations for the three additional observables,
1585 which do not enter one-dimensional distributions, are needed. Expectations are
1586 calculated using form factors and numerical inputs from Ref. [95] and are listed in
1587 Appendix A.1 in Tab. A.1.

For completeness, the differential distribution in $\cos \theta_\ell$ and $\cos \theta_h$ has the form

$$\begin{aligned} \frac{d\Gamma(\Lambda_b \rightarrow \Lambda \ell^+ \ell^-)}{dq^2 d\cos \theta_h d\cos \theta_\ell} = & \frac{3}{8} + \frac{6}{16} \cos^2 \theta_\ell (1 - f_L) - \frac{3}{16} \cos^2 \theta_\ell f_L + A_{FB}^l \cos \theta_\ell + \\ & \left(\frac{3}{2} A_{FB}^h - \frac{3}{8} \alpha_A O_P \right) \cos \theta_h - \frac{3}{2} A_{FB}^h \cos^2 \theta_\ell \cos \theta_h - \frac{3}{16} f_L + \\ & \frac{9}{16} f_L \sin^2 \theta_\ell + \frac{9}{8} \alpha_A \cos^2 \theta_\ell \cos \theta_h O_P - \\ & \frac{3}{2} \alpha_A \cos \theta_\ell \cos \theta_h O_{UVA}. \end{aligned} \quad (4.15)$$

1588 4.3 Angular resolution

1589 This section describes a study of the angular resolution done in order to achieve
 1590 a better understanding of detector and reconstruction effects. This will be then
 1591 used to study systematic uncertainties (see Sec. 4.5.5). The study is performed by
 1592 analysing simulated events and comparing generated and reconstructed quantities.
 1593 Figure 4.2 shows plots of the difference between true and measured angular observ-
 1594 ables ($\cos \theta_\ell$ and $\cos \theta_h$) as a function of the observable itself. These are centred at
 1595 zero indicating no bias in the measurement. Figure 4.3 shows the angular resolution
 in two-dimensional bins of q^2 and angular observables. In Fig. 4.2 the same differ-

Table 4.1: Average angular resolutions integrated over the full interval and the full available q^2 .

Observable	Downstream	Long
$\cos \theta_\ell$	0.015	0.010
$\cos \theta_h$	0.066	0.014

1596
 1597 ence is shown also as a function of q^2 revealing again no bias. The spread of these
 1598 distributions around the central value can be takes as an estimate of the angular
 1599 resolution. Taking vertical slices of the plots in Fig. 4.2 one obtains approximately
 1600 gaussian distributions centred at zero. These are fit with a single gaussian and its
 1601 width is interpreted as the angular resolution. Table 4.1 reports the average resolu-
 1602 tions for the two angular observables separately for long and downstream candidates.
 1603 As expected candidates built from long tracks are characterised by a better angular

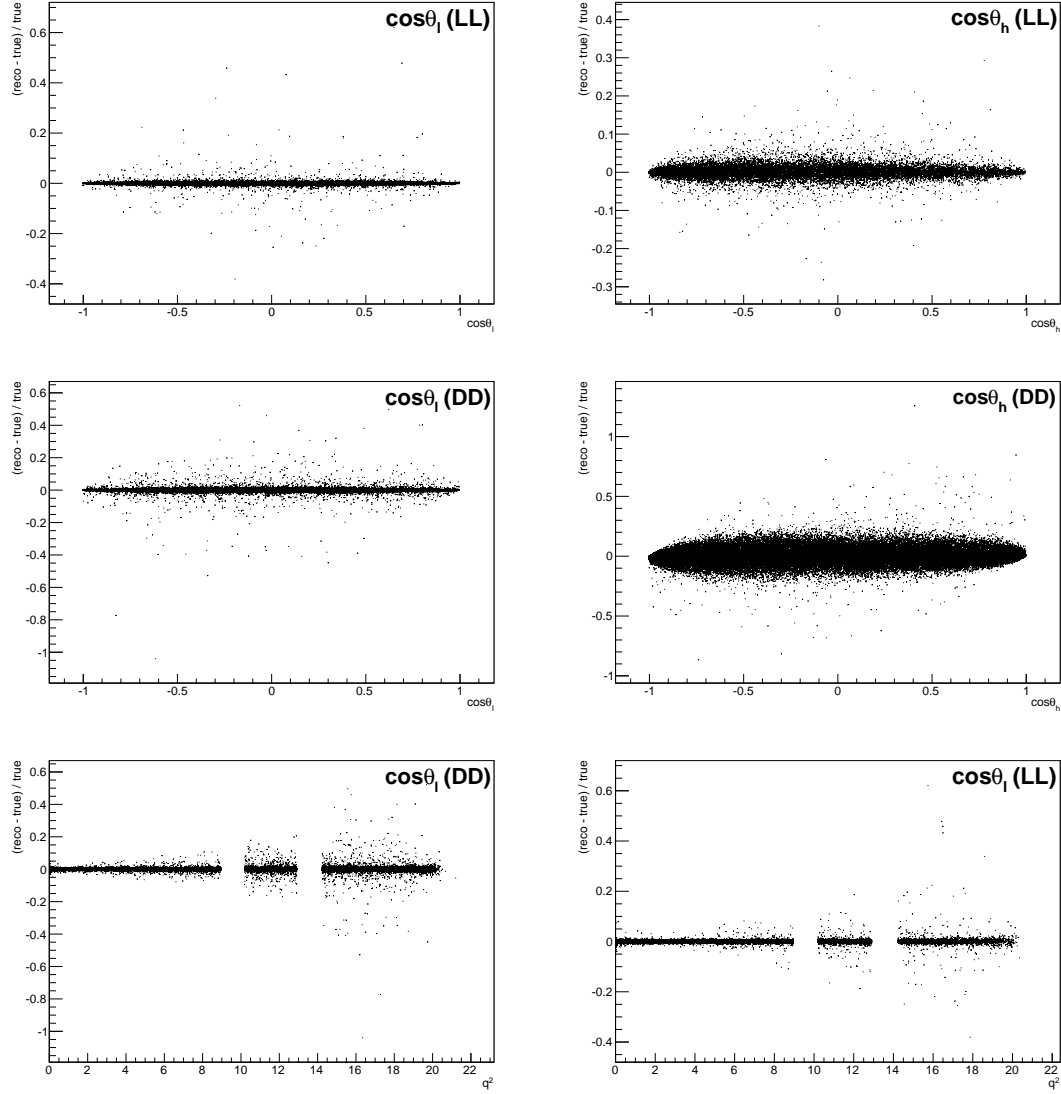


Figure 4.2: Difference of between generated and reconstructed angular observables as a function of the observables themselves for long (top) and downstream (bottom) candidates and as a function of q^2 for long (bottom left) and downstream (bottom right) candidates. As the plots are made using fully selected rare samples the bottom plots present empty bands corresponding to the charmonium vetoes.

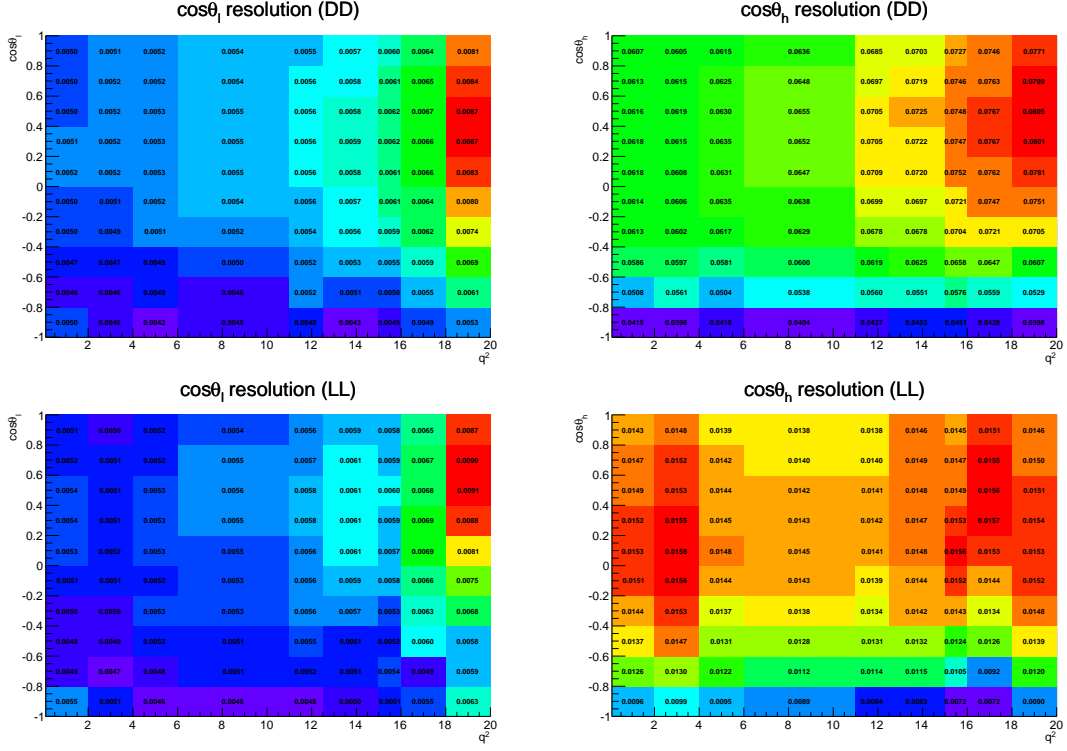


Figure 4.3: Angular resolution for $\cos \theta_\ell$ (left plots) and $\cos \theta_h$ (right plots) as a function of the angular observables and q^2 for downstream (upper plots) and long (lower plots) candidates. White bands correspond to the J/ψ and $\psi(2S)$ resonances which are excluded from the study.

resolution due to a better momentum and vertex resolution.

4.4 Fit strategy

There are physical limits to the values of the parameters of interests: A_{FB}^h is limited in the $[-0.5, 0.5]$ interval and for the f_L and A_{FB}^ℓ parameters the physical region, given by $|A_{\text{FB}}^\ell| < 3/4(f_L - 1)$, is the triangle shown in Fig. 4.4. If the measured value is close to the border the fit does not always converge. Therefore a “brute force” fitting technique is applied. For this purpose fit parameters are divided into two categories: parameters of interest (PoIs), A_{FB}^ℓ , A_{FB}^h and f_L and all other parameters, which are referred to as “nuisances”. The value of the Log-Likelihood ($\log \mathcal{L}$) of the fit model with respect to data is evaluated in a grid of points in the PoIs allowed area to find the function minimum. A first coarse scan finds a candidate minimum and then the

procedure is reiterated two more times in finer intervals around it. For each point all the nuisances are fitted using a maximum likelihood fit. Using this method the best fit point is therefore constrained inside the physical region. If the minimum of the log-likelihood is found to be outside it, the closest point on the boundary is chosen as the best fit.

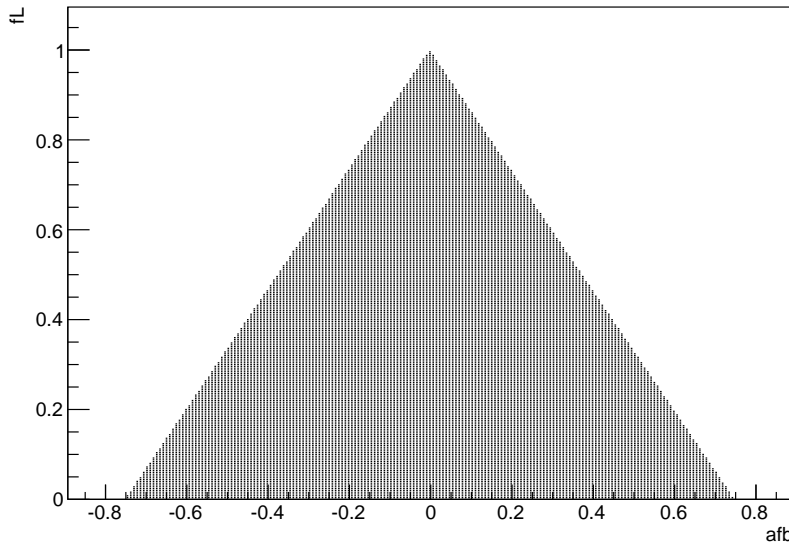


Figure 4.4: The physical (A_{FB}^{ℓ}, f_L) parameter space. The dark region corresponds to points where the PDF is positive in the whole $[-1, 1]$ interval.

1620 4.4.1 Feldman-cousins plug-in method

Physical boundaries of the parameter space could result in a wrong estimation of the uncertainties, especially if the measured value is close to the border. To deal with this effect in this analysis the likelihood-ordering method [104] is used to estimate uncertainties and nuisance parameters are accounted for using the plug-in method [105]. This is a unified method to calculate confidence intervals and upper/lower limits, based on simulated experiments and has the advantage of having a well defined frequentist coverage.

The method is constituted by the following steps:

-
- 1629 1. fit real data distributions with all parameters free;
- 1630 2. fit real data fixing the PoIs to a value of choice while keeping nuisance param-
- 1631 eters free;
- 1632 3. generate simulated samples following the distribution given by the fit model,
- 1633 where all nuisance parameters are taken from the fit in point 2 and PoIs are
- 1634 fixed to the same value used in point 2;
- 1635 4. repeat the two fits made on data (points 1 and 2) on each simulated sample:
- 1636 fit with all parameters free and with fixed PoIs;
- 1637 5. extract the value of the Log-Likelihoods at the minimum for all cases;
- 1638 6. calculate the percentage of simulated experiments in which the free-to-fixed
- 1639 likelihood ratio is bigger than in data: $\log \mathcal{L}_{fixed} / \log \mathcal{L}_{free} > (\log \mathcal{L}_{fixed} / \log \mathcal{L}_{free})_{data}$;
- 1640 7. repeat the procedure for many values of the PoIs scanning around the best fit
- 1641 point.
- 1642 The confidence interval at $k\%$ is given by the points where the free-to-fixed likelihood
- 1643 ratio is bigger in data than simulation for $(1 - k)\%$ of times. As an example, Fig. 4.5
- 1644 shows the p-values obtained with the plug-in method for A_{FB}^h and f_L . A two-
- 1645 dimensional region can also be scanned giving a grid of p-values, which translates
- 1646 into two-dimensional confidence regions.

1647 4.4.2 Modelling the angular distributions

- 1648 The observables are extracted from fits to one-dimensional angular distributions.
- 1649 The PDFs used to model the data are defined as

$$P^k(\cos \theta_{\ell/h}) = (1 - f_b)P_S(\cos \theta_{\ell/h}) \times \varepsilon^k(\cos \theta_{\ell/h}) + f_b P_B^k(\cos \theta_{\ell/h}), \quad (4.16)$$

1650 where $k = (\text{LL}, \text{DD})$. The signal function is composed by a theoretical shape (P_S)

1651 given by Eq. 4.10 and 4.9, which is multiplied by an acceptance function ε described

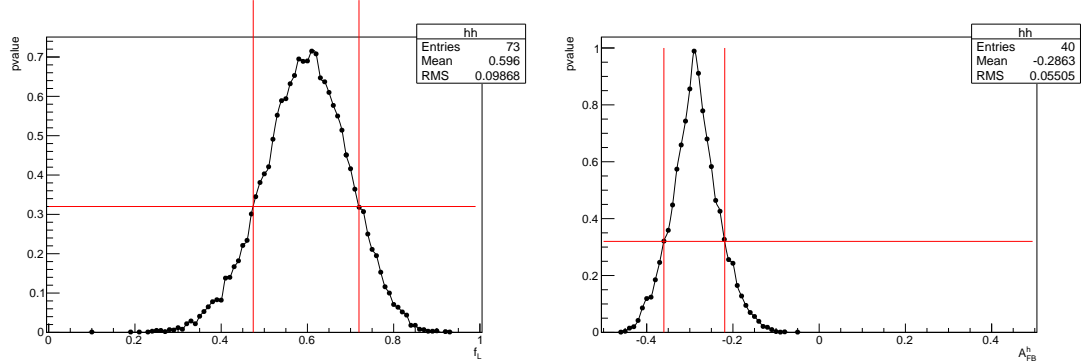


Figure 4.5: Dependence of the p-value from the values of the angular observables f_L (left) and A_{FB}^h (right) in simulated experiments. The red lines mark the points at p-value 32% corresponding to a 68% CL.

in Sec. 4.4.3. The background function, P_B , is parameterised with a linear function times the efficiency shape: $P_B^k(\cos\theta_{\ell/h}) = (cx + q) \times \varepsilon^k(\cos\theta_{\ell/h})$. The free parameter of this model is fixed by fitting candidates in the sideband which contains only background. Finally, f_b is the background fraction: $f_b = B/(S + B)$. To limit systematic effects due to the background parameterisation the fit is performed in a restricted mass region around the Λ_b^0 mass peak dominated by the signal: $5580 < m(\Lambda\mu^+\mu^-) < 5660$ MeV/ c^2 (“signal region”). The background fraction, f_b , is obtained by looking at the 4-body $m(p\pi\mu\mu)$ invariant mass distribution in a wider interval and fitting it to extract the fraction of background in the signal region. In the fit to the angular distributions this is then gaussian constrained to the obtained value. Figure 4.6 shows the background distributions in the sideband, $m(p\pi\mu^+\mu^-) > 5700$ MeV/ c^2 , for the high q^2 integrated interval with overlaid the background function. Note that a different acceptance shape is used for downstream and long events and for each q^2 interval. In summary the only free fit parameter in each of the final fits to data is the forward-backward asymmetry (and f_L in the leptonic case).

4.4.3 Angular acceptance

Selection requirements on the minimum momentum of the muons may distort the $\cos\theta_\ell$ distribution by removing candidates with extreme values of $\cos\theta_\ell$. Similarly,

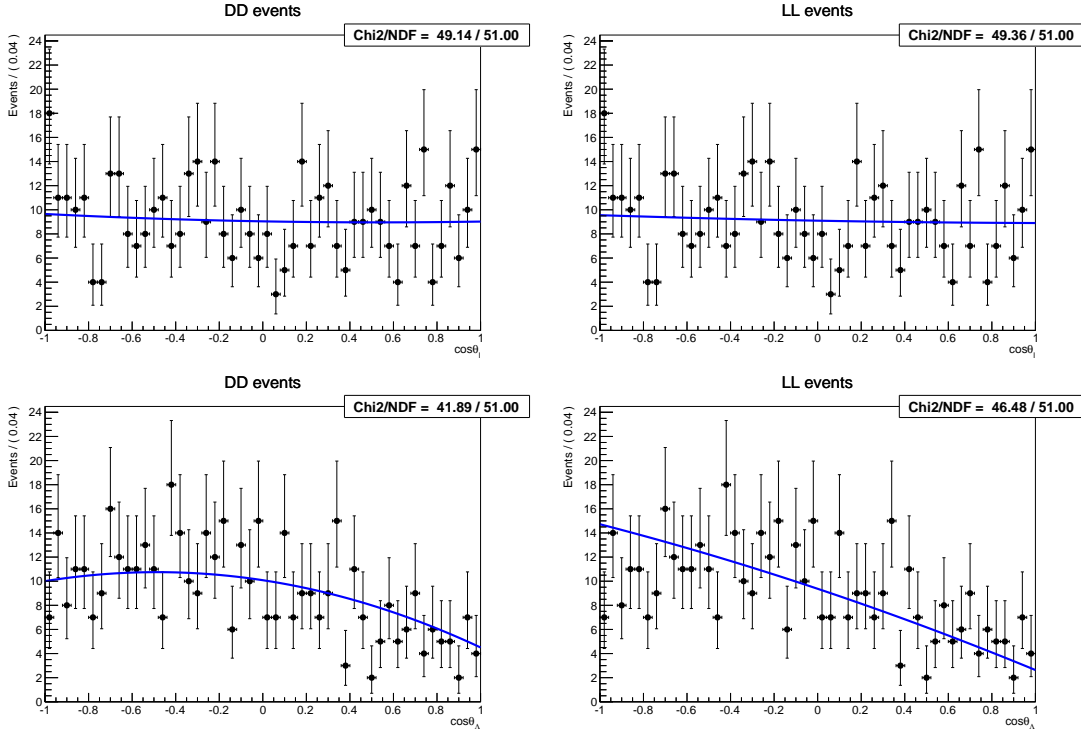


Figure 4.6: Background distribution as a function of $\cos\theta_\ell$ (top) and $\cos\theta_h$ (bottom) for downstream (left) and long (right) candidates in the $15\text{--}20 \text{ GeV}^2/c^4 q^2$ interval.

the impact parameter requirements affect $\cos\theta_h$ as very forward hadrons tend to have smaller impact parameter values. While in principle one could take this into account by an additional weight, to minimise the distortion of the uncertainties estimate, the efficiency function is incorporated in the fit model. The angular efficiency is parametrised using a second-order polynomial and determined separately for downstream and long candidates by fitting simulated events, using an independent set of parameters obtained for each q^2 interval. These parameters are then fixed for the fits to data. Using polynomial functions allows to calculate the PDF normalisation analytically. Figure 4.7 shows the acceptance as a function of $\cos\theta_h$ and $\cos\theta_\ell$ for the $15.0\text{--}20.0$ integrated q^2 interval obtained using a $\Lambda_b^0 \rightarrow \Lambda\mu^+\mu^-$ simulated sample. For the lepton side, even though the efficiency is symmetric by construction, all parameters are left free to float, namely it is not constrained to be symmetric.

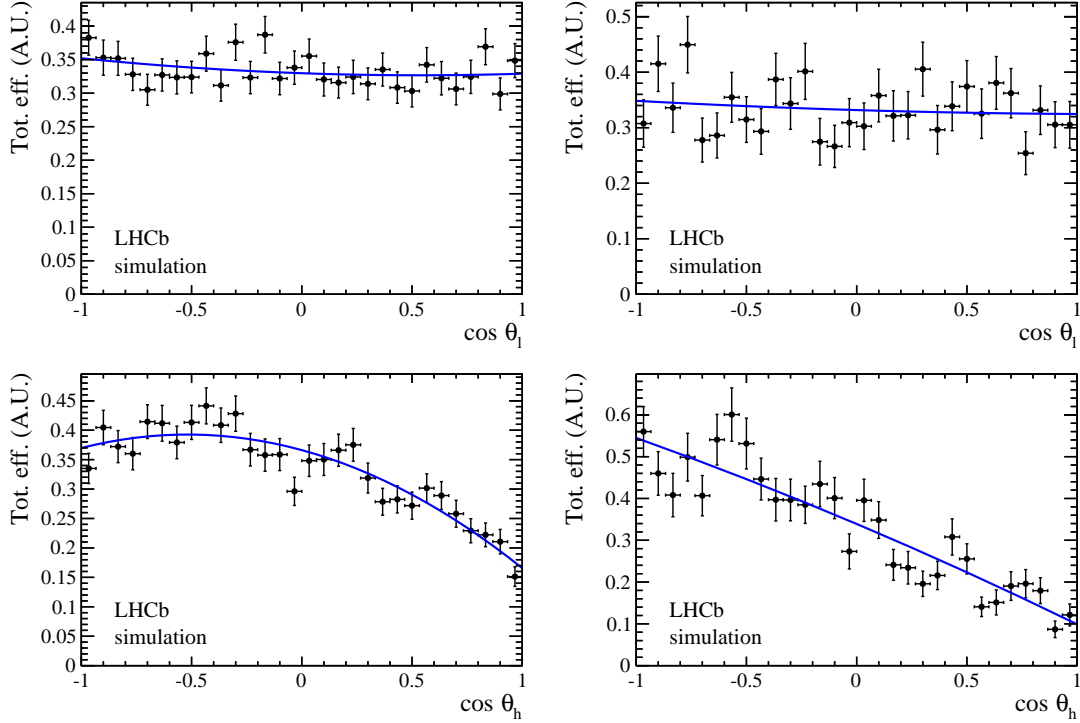


Figure 4.7: Efficiency as a function of $\cos \theta_\ell$ (top) and $\cos \theta_h$ (bottom) for downstream (left) and long (right) candidates in the $15\text{--}20 \text{ GeV}^2/c^4 q^2$ interval.

1684 4.4.4 Studies on a three-dimensional fit

1685 One other way of extracting the angular observables would be to fit at the same
1686 time both angles and also the invariant mass distribution in order to have a better
1687 handle on the level of background. In this case one can use more of the information
1688 available. On the other hand it is necessary to use a larger mass window including
1689 more background and this method involves more parameters to fit. In the 1D case
1690 the free parameters are the two parameters of interest (A_{FB}^ℓ and f_L) for the lepton
1691 case and one (A_{FB}^h) for the hadron one. For the 3D case in addition to the three
1692 PoIs there are two background fractions and the two exponential slopes for the
1693 invariant mass background. Furthermore, to take correctly into account correlations
1694 three more observables enter the fit (see Eq. 4.12). As an high number of free
1695 parameters is difficult to constrain with the very limited statistics available, pseudo-
1696 experiments are used to check which method gives the best sensitivity. Events are
1697 generated in a 3D $(\cos \theta_\ell, \cos \theta_h, m_{p\pi\mu\mu})$ space. The generated values of the PoIs

are $A_{\text{FB}}^\ell = 0$, $f_L = 0.7$ and $A_{\text{FB}}^h = -0.37$, which are data-like values inspired to a preliminary measurement in the highest statistics interval. The overall statistics and the fraction of background events in the mass window are generated to be data-like using information from the preliminary fit to data. Each pseudo-experiment is fitted with both methods and Fig. 4.8 reports distributions of parameters of interest obtained from the fit in the 1D and 3D cases. The RMS of these distributions can be taken as a measure of the sensitivity of each method. Table 4.2 lists the RMSs obtained from both methods; for all parameters of interest the 1D fit method gives a smaller RMS, hence a better sensitivity.

Table 4.2: RMS values for toy experiments on the extraction of the three parameters of interests with the 1D or 3D fitting methods.

q^2 [GeV $^2/c^4$]	Fit type	A_{FB}^h	A_{FB}^ℓ	f_L
15.0–20.0	1D	0.070	0.055	0.099
	3D	0.092	0.095	0.153
11.0–12.5	1D	0.142	0.128	0.198
	3D	0.249	0.254	0.303

1706

4.5 Systematics uncertainties on angular observables

1708 The following section describes the five main sources of systematic uncertainties
 1709 that are considered for the angular observables measurement and, finally, results
 1710 are reported in Sec. 4.7. Results are derived only for q^2 intervals where the signal
 1711 significance, shown in Tab. 3.6, is above 3 standard deviations. This includes all
 1712 q^2 intervals above the J/ψ resonance and the lowest q^2 interval, where an increased
 1713 yield is due to the presence of the photon pole.

4.5.1 Angular correlations

1715 The angular acceptance is non-flat as a function of $\cos \theta_\ell$ and $\cos \theta_h$. Therefore, while
 1716 integrating the full angular distribution, terms that cancel with perfect efficiency

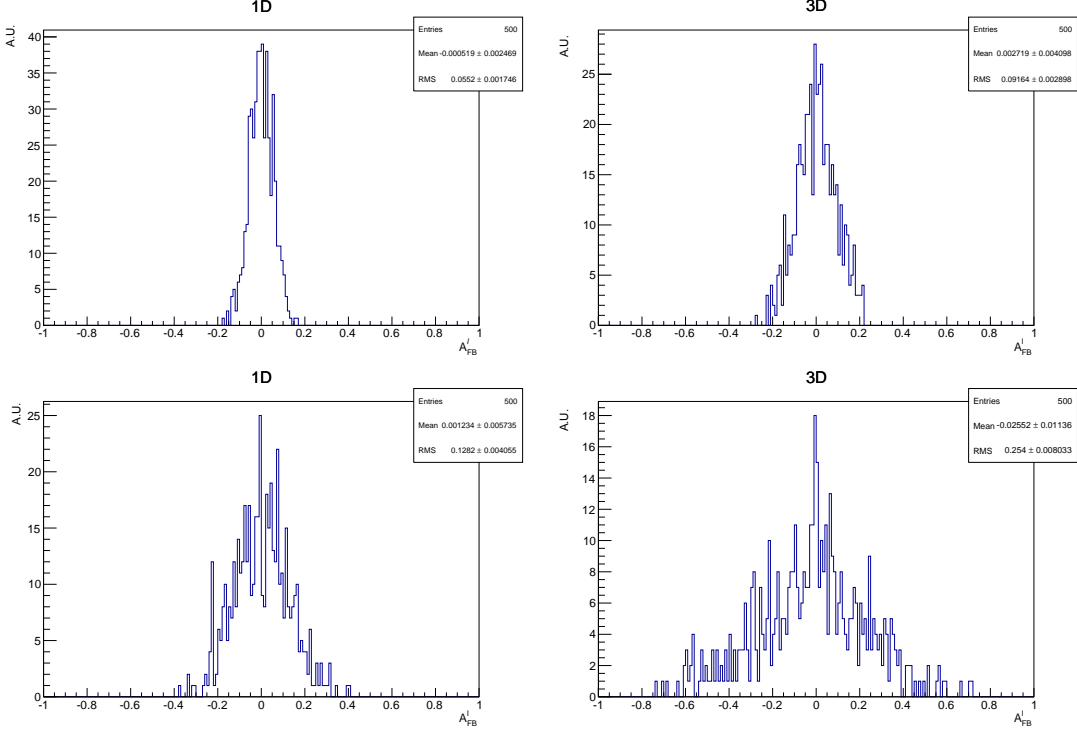


Figure 4.8: Values of the A_{FB}^l parameter observed over pseudo-experiments with input $A_{FB}^l = 0$ using the 1D fit method (left) and the 3D one (right). Events are generated with parameters and statistics corresponding to what is observed in the highest statistics interval (top), 15–20 GeV^2/c^4 , and in the lowest statistics one, 11–12.5 GeV^2/c^4 .

may remain and generate a bias in the final result. In order to deal with this effect simulated events are generated in a two-dimensional $(\cos\theta_\ell, \cos\theta_h)$ space according to the theoretical distribution described by Eq. 4.15 multiplied by the two-dimensional efficiency function obtained from simulation. Then, one-dimensional projections are taken and fit using the default one-dimensional efficiency functions. Figure 4.9 shows the distribution of observed deviations from the generated value, $\Delta x = x_{true} - x_{measured}$. Since the mean of these distributions is non-zero by more than 3σ , they are taken as a systematic uncertainties.

4.5.2 Resolution

The angular resolution could bias the observables measurement generating an asymmetric migration of events. This is especially important in the $\cos\theta_h$ case, because

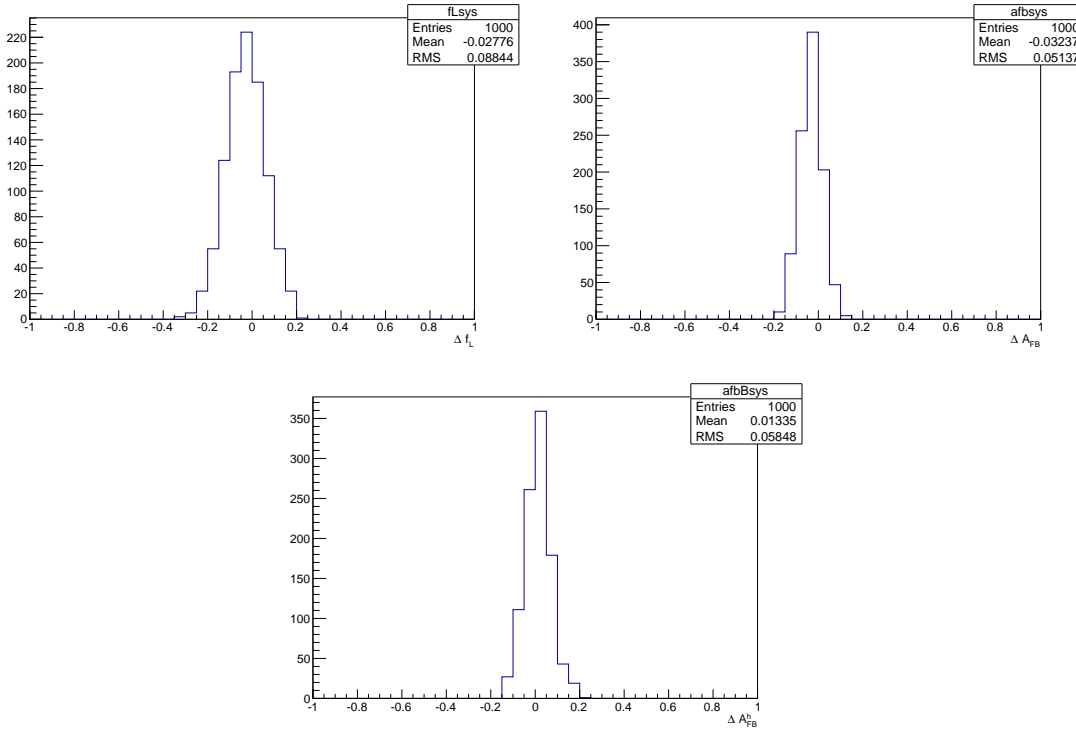


Figure 4.9: Deviations of the observables' values obtained fitting simulated events generated with a 2D distribution multiplied by a 2D efficiency and fitting 1D projections with respect to generated values. For f_L (top left), A_{FB}^ℓ (top right) and A_{FB}^h (bottom).

it has worse resolution and a considerably asymmetric distribution. Simulated experiments are used to asses this systematic. Events are generated according to the measured distributions including efficiencies. The generated events are then smeared by the angular resolution (gaussian smearing). To be conservative the case with biggest angular resolution, downstream candidates, is always used. Finally, the smeared and not-smeared distributions are fit with the same PDF. The average deviation from the default values are reported in Tab. 4.3 as a function of q^2 and assigned as systematic uncertainties.

4.5.3 Efficiency description

An imprecise determination of the reconstruction and selection efficiency can introduce an extra oddity and therefore bias the measurement. To asses this effect

Table 4.3: Values of simulated $\cos\theta_\ell$ and $\cos\theta_\Lambda$ resolutions and systematic uncertainties on angular observables due to the finite resolution in bins of q^2 .

q^2 [GeV $^2/c^4$]	σ_ℓ	σ_Λ	$\Delta A_{\text{FB}}^\ell$	Δf_L	ΔA_{FB}^h
0.1 – 2.0	0.0051	0.061	0.0011	-0.0022	-0.007
11.0 – 12.5	0.0055	0.067	0.0016	-0.0051	-0.013
15.0 – 16.0	0.0059	0.070	0.0006	-0.0054	-0.010
16.0 – 18.0	0.0064	0.070	0.0014	-0.0077	-0.010
18.0 – 20.0	0.0081	0.074	0.0014	-0.0062	-0.010
15.0 – 20.0	0.0066	0.072	0.0013	-0.0076	-0.011

¹⁷³⁹ the kinematic re-weighting described in Sec. 3.3.2 is removed from the simulation
¹⁷⁴⁰ and the efficiency is determined again. Simulated events are then fit using the same
¹⁷⁴¹ theoretical PDF but multiplied by the efficiency function obtained with and without
¹⁷⁴² kinematical weights. As in the previous cases the average bias is taken as systematic
¹⁷⁴³ uncertainty; results are shown in Tab. 4.4. Furthermore, the effect of the limited
simulated statistics is taken into account and added to the systematic uncertainty.

Table 4.4: Values systematic uncertainties due to limited knowledge of the efficiency function on the three angular observables in bins of q^2

q^2 [GeV $^2/c^4$]	A_{FB}^ℓ	f_L	A_{FB}^h
0.1 – 2.0	0.0020	0.0440	0.0093
11.0 – 12.5	0.0069	0.0027	0.0069
15.0 – 16.0	0.0018	0.0046	0.0109
16.0 – 18.0	0.0012	0.0043	0.0159
18.0 – 20.0	0.0030	0.0017	0.0148
15.0 – 20.0	0.0002	0.0046	0.0138

Table 4.5: Values of systematic uncertainties due to the statistics of the simulated samples on the three angular observables in bins of q^2 .

q^2 [GeV $^2/c^4$]	A_{FB}^ℓ	f_L	A_{FB}^h
0.1 – 2.0	0.00151	0.00170	0.00213
11.0 – 12.5	0.00121	0.00154	0.00196
15.0 – 16.0	0.00004	0.00017	0.00103
16.0 – 18.0	0.00065	0.00246	0.00417
18.0 – 20.0	0.00023	0.00372	0.00162
15.0 – 20.0	0.00039	0.00091	0.00137

¹⁷⁴⁵ 4.5.4 Background parameterisation

¹⁷⁴⁶ There is a certain degree of arbitrariness in the choice of a parameterisation for the
¹⁷⁴⁷ background, especially for q^2 intervals with low statistics. To assess possible biases
¹⁷⁴⁸ due to the PDF choice, simulated experiments are generated using the shapes from
¹⁷⁴⁹ data fits and the same statistics as observed in data for each q^2 interval. Each
¹⁷⁵⁰ pseudo-experiment is fit with two models: the default one, a “line times efficiency”
¹⁷⁵¹ function and the efficiency function alone, corresponding to the assumption that
¹⁷⁵² background distributions are originally flat and only modified by the interaction
¹⁷⁵³ with the detector. The average bias with respect to the default model is taken as
¹⁷⁵⁴ systematic uncertainty; results are reported in Tab. 4.6.

Table 4.6: Values of systematic uncertainties due to the choice of background parameterisation in bins of q^2 .

q^2 [GeV $^2/c^4$]	A_{FB}^ℓ	f_L	A_{FB}^h
0.1 – 2.0	0.003	0.049	0.053
11.0 – 12.5	0.045	0.034	0.035
15.0 – 16.0	0.010	0.038	0.026
16.0 – 18.0	0.026	0.036	0.022
18.0 – 20.0	0.011	0.031	0.025
15.0 – 20.0	0.007	0.014	0.017

¹⁷⁵⁵

¹⁷⁵⁶ 4.5.5 Polarisation

¹⁷⁵⁷ To study the effect of a non-zero Λ_b^0 production polarisation simulated events are
¹⁷⁵⁸ generated using the distributions given by Eqs. 4.12 and 4.14 as a function of the
¹⁷⁵⁹ angle under study ($\cos \theta_\ell$ or $\cos \theta_h$) and $\cos \theta$, defined in Sec. 4.2, which is sensitive to
¹⁷⁶⁰ polarisation. Similarly to the procedure used for the branching ratio measurement,
¹⁷⁶¹ events are generated using values of the polarisation corresponding to $\pm\sigma$ from the
¹⁷⁶² LHCb measurement [96]. In the theoretical functions $\cos \theta$ is always odd therefore
¹⁷⁶³ with perfect efficiency it always drops out by integrating over $\cos \theta$. Therefore

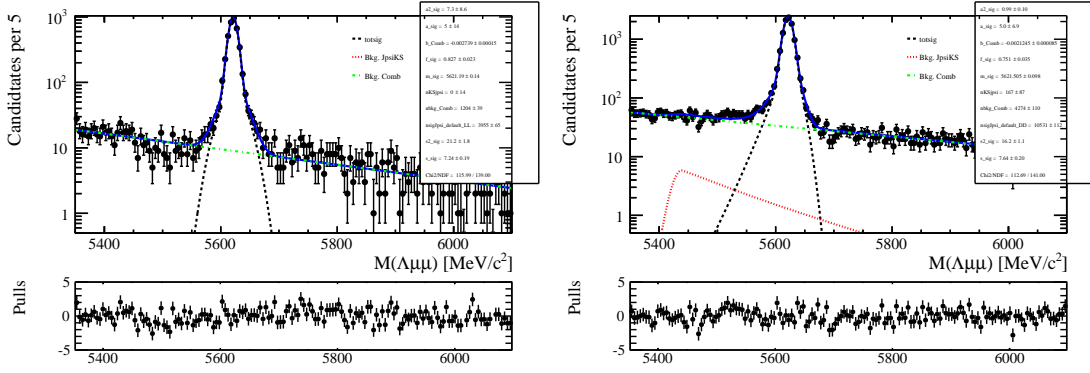


Figure 4.10: Invariant mass distribution of $\Lambda_b^0 \rightarrow J/\psi \Lambda$ long (left) and downstream (right) candidates with an extra proton PID cut to remove K_s^0 background.

¹⁷⁶⁴ the generated distributions are also multiplied by the two-dimensional efficiency
¹⁷⁶⁵ function. No significant bias is found.

¹⁷⁶⁶ 4.6 J/ψ cross-check

¹⁷⁶⁷ To cross-check the fitting procedure this is applied on the high statistics $\Lambda_b^0 \rightarrow J/\psi \Lambda$
¹⁷⁶⁸ sample. For this purpose events are selected with an additional requirement on the
¹⁷⁶⁹ proton PID, $\text{PID}_p > 10$. This is needed to reduce the $B^0 \rightarrow K_s^0 J/\psi$ background,
¹⁷⁷⁰ which is particularly important for the hadronic side fit, since the K_s^0 events are
¹⁷⁷¹ not distributed in a flat way in the $\cos\theta_h$ variable and would therefore bias the
¹⁷⁷² fit. Figure 4.10 shows the invariant mass distributions after this requirement is
¹⁷⁷³ applies, which can be compared with the ones in Fig. 3.12. After the PID cut there
¹⁷⁷⁴ are 0.2% of K_s^0 events left in the downstream sample and a fraction compatible
¹⁷⁷⁵ with zero in the long sample. The signal model used for this fit is the same
¹⁷⁷⁶ used for the rare case and described in Sec. 4.4.2. For the background instead the
¹⁷⁷⁷ higher statistics allows to leave more freedom to the fit. Therefore a second-order
¹⁷⁷⁸ Chebyschev polynomial is used, where the two parameters are free to vary. As for
¹⁷⁷⁹ the rare case the background fractions are gaussian-constrained to what found from
¹⁷⁸⁰ the invariant mass fit. Figures 4.11 and 4.12 show fitted angular distributions for
¹⁷⁸¹ the J/ψ channel. The measured values of the observables are $A_{\text{FB}}^\ell = -0.002^{+0.011}_{-0.011}$,
¹⁷⁸² $A_{\text{FB}}^h = -0.402^{+0.010}_{-0.009}$ and $f_L = 0.485^{+0.019}_{-0.020}$, where the uncertainties are 68% Feldman

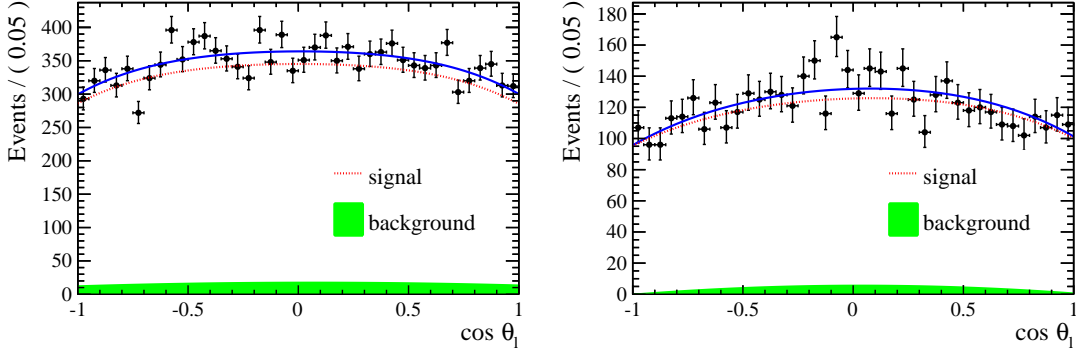


Figure 4.11: Fitted angular distribution as a function of $\cos \theta_\ell$ for $\Lambda_b^0 \rightarrow J/\psi \Lambda$ candidates reconstructed using downstream (left) and long (right) tracks.

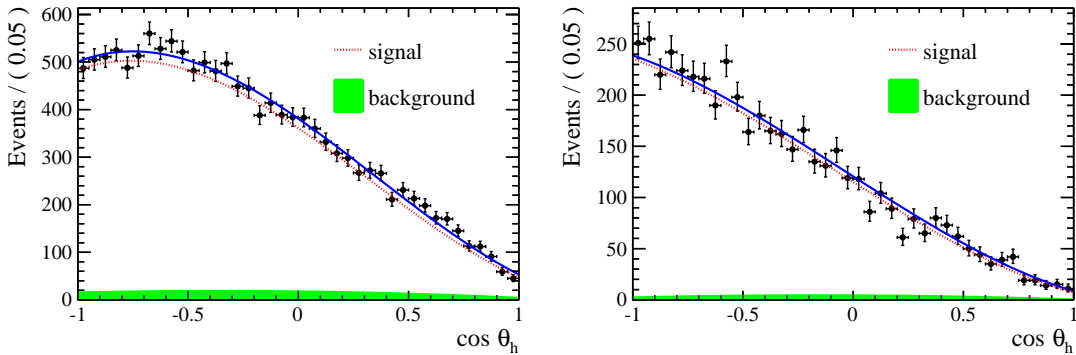


Figure 4.12: Fitted angular distribution as a function of $\cos \theta_h$ for $\Lambda_b^0 \rightarrow J/\psi \Lambda$ candidates reconstructed using downstream (left) and long (right) tracks.

1783 Cousins confidence intervals. The lepton side asymmetry as expected is measured
1784 to be zero.

1785 4.7 Results

1786 Figures 4.13 and 4.14 show fits to the angular distributions for the 15-20 $\text{GeV}^2/c^4 q^2$
1787 interval and Tab. 4.7 reports measured values of A_{FB}^ℓ , A_{FB}^h and f_L . The asymmetries
1788 are also shown in Fig. 4.15 together with SM predictions obtained from Ref. [99].
1789 The statistical uncertainties on these tables are obtained using the likelihood-ratio
1790 ordering method described in Sec. 4.4.1, where only one of the two observables is
1791 treated as the PoI at a time. The statistical uncertainties on A_{FB}^ℓ and f_L are also
1792 reported in Fig. 4.16 as two-dimensional 68 % confidence level (CL) regions, where

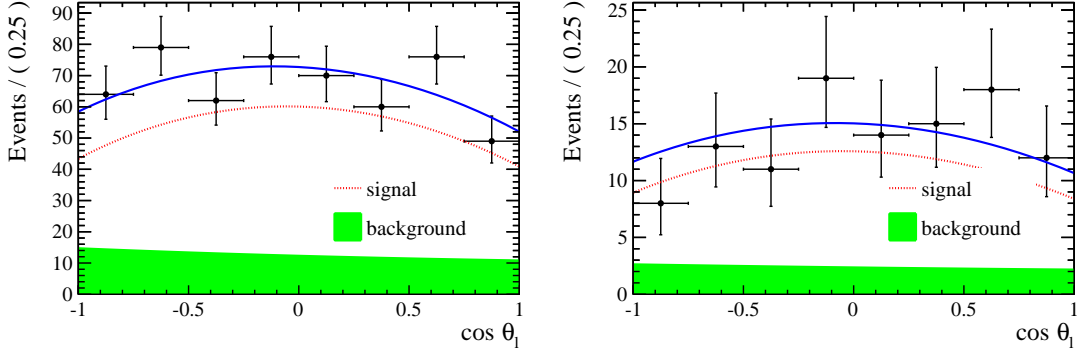


Figure 4.13: Fitted angular distributions as a function of $\cos \theta_\ell$ for downstream (left) and long (right) candidates in the $15\text{--}20 \text{ GeV}^2/c^4 q^2$ interval.

1793 the likelihood-ratio ordering method is applied by varying both observables and
1794 therefore taking correlations into account. Total systematic uncertainties correspond
1795 to the square root sum of the single considered sources.

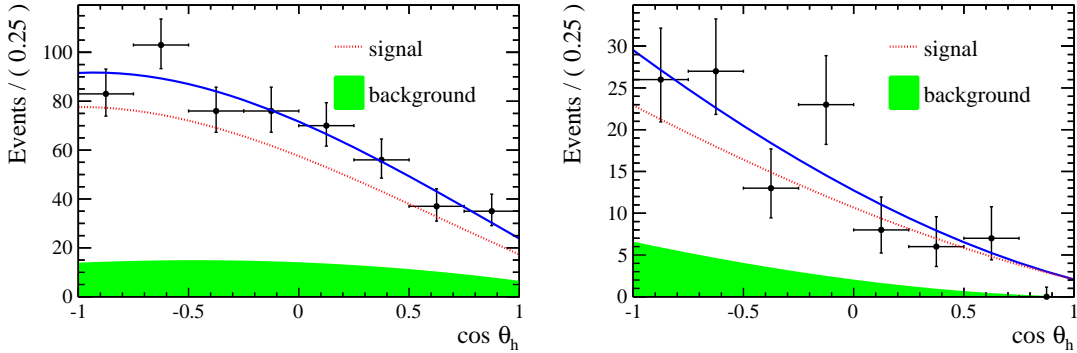


Figure 4.14: Fitted angular distributions as a function of $\cos \theta_h$ for downstream (left) and long (right) candidates in the $15\text{--}20 \text{ GeV}^2/c^4 q^2$ interval.

Table 4.7: Measured values of leptonic and hadronic angular observables, where the first uncertainties are statistical and the second systematic.

q^2 interval [GeV^2/c^4]	A_{FB}^ℓ	f_L	A_{FB}^h
0.1 – 2.0	$0.37^{+0.37}_{-0.48} \pm 0.03$	$0.56^{+0.23}_{-0.56} \pm 0.08$	$-0.12^{+0.31}_{-0.28} \pm 0.15$
11.0 – 12.5	$0.01^{+0.19}_{-0.18} \pm 0.06$	$0.40^{+0.37}_{-0.36} \pm 0.06$	$-0.50^{+0.10}_{-0.00} \pm 0.04$
15.0 – 16.0	$-0.10^{+0.18}_{-0.16} \pm 0.03$	$0.49^{+0.30}_{-0.30} \pm 0.05$	$-0.19^{+0.14}_{-0.16} \pm 0.03$
16.0 – 18.0	$-0.07^{+0.13}_{-0.12} \pm 0.04$	$0.68^{+0.15}_{-0.21} \pm 0.05$	$-0.44^{+0.10}_{-0.05} \pm 0.03$
18.0 – 20.0	$0.01^{+0.15}_{-0.14} \pm 0.04$	$0.62^{+0.24}_{-0.27} \pm 0.04$	$-0.13^{+0.09}_{-0.12} \pm 0.03$
15.0 – 20.0	$-0.05^{+0.09}_{-0.09} \pm 0.03$	$0.61^{+0.11}_{-0.14} \pm 0.03$	$-0.29^{+0.07}_{-0.07} \pm 0.03$

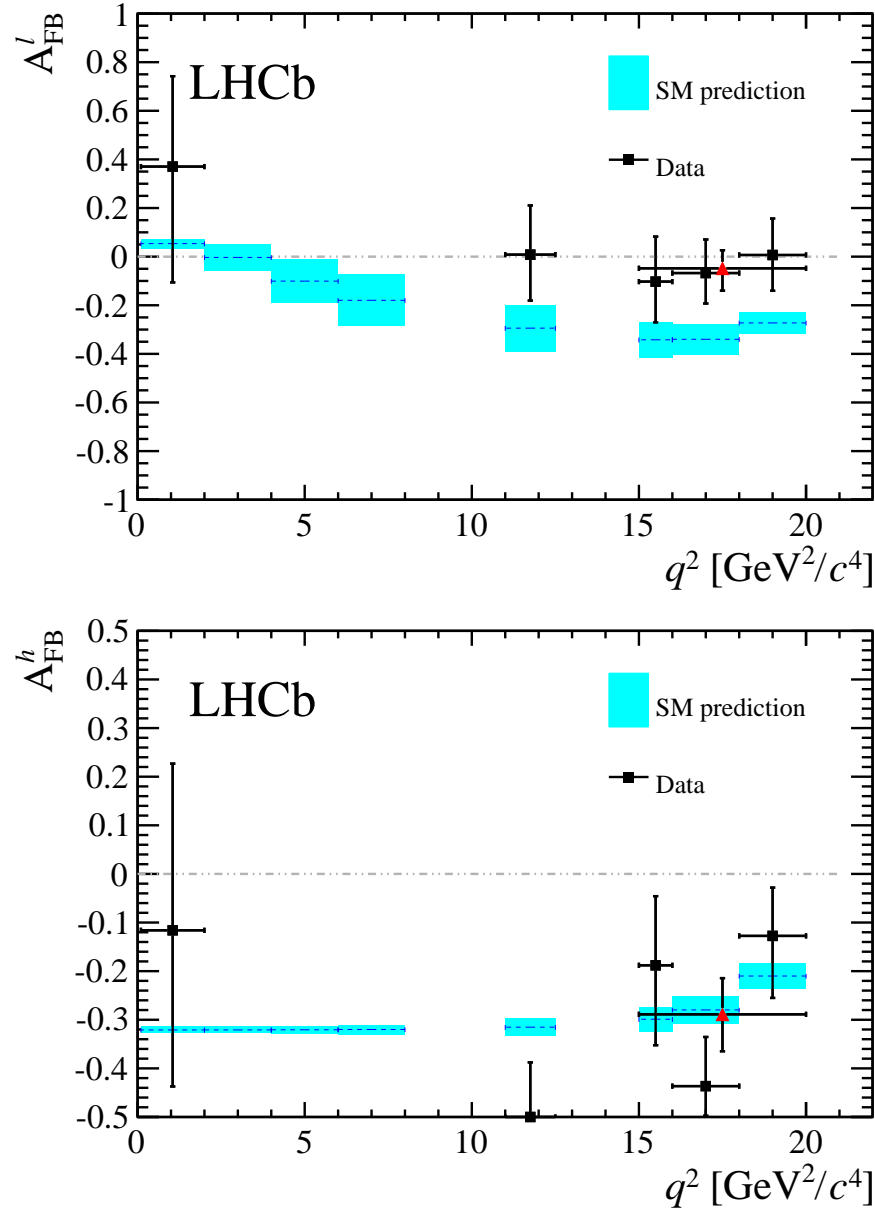


Figure 4.15: Measured values of the leptonic (top) and the hadronic (bottom) forward-backward asymmetries in bins of q^2 . Data points are only shown for q^2 intervals where a statistically significant signal yield is found, see text for details. The (red) triangle represents the values for the $15 < q^2 < 20$ GeV^2/c^4 interval. Standard Model predictions are obtained from Ref. [106].

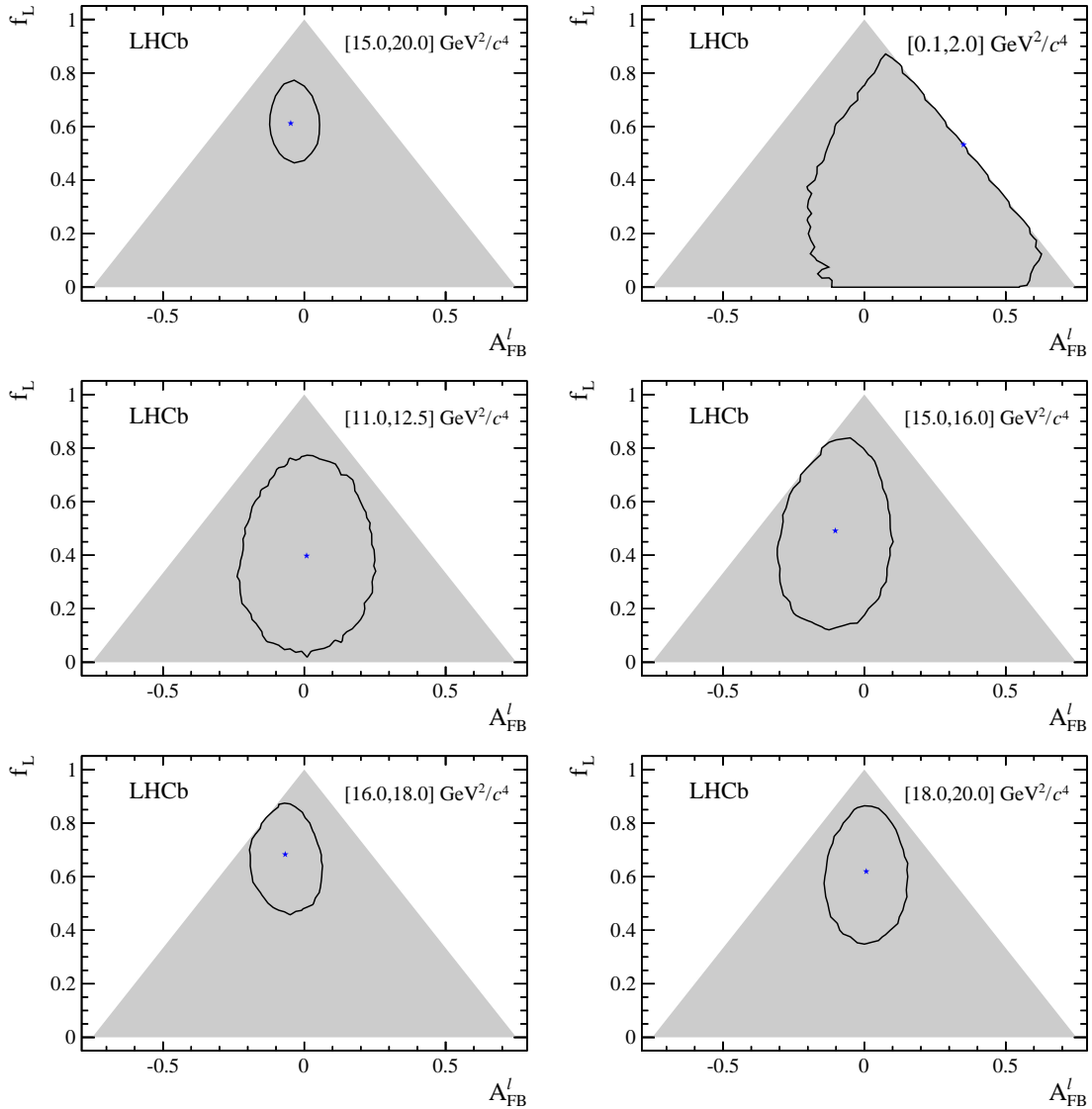


Figure 4.16: Two-dimensional 68 % CL regions (black) as a function of A_{FB}^l and f_L . The shaded areas represent the regions in which the PDF is positive over the complete $\cos \theta_\ell$ range. The best fit points are indicated by the (blue) stars.

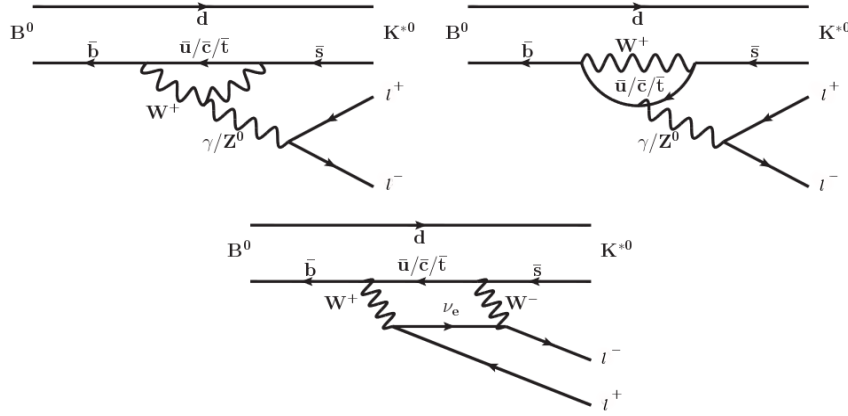
CHAPTER 5

Testing lepton flavour universality with $R_{K^{*0}}$

1800 Lepton Flavour Universality (LFU) is the equality of the weak coupling constants
 1801 for all leptons. FCNC processes, which are forbidden in the SM at tree level and
 1802 happen only at loop level, are an ideal laboratory to study LFU as new physics in
 1803 the loops could break the flavour symmetry.

1804 In this work $b \rightarrow s\mu^+\mu^- (e^+e^-)$ decays are studied to test LFU between electrons and
 1805 muons using penguin decays. In particular, the B^0 meson semileptonic decays $B^0 \rightarrow$
 1806 $K^{*0}\ell^+\ell^-$ are considered. Figure 5.1 shows the possible Feynman diagrams producing
 1807 such decays while Fig. 5.2 illustrates how these Feynman diagrams may include new
 1808 particles. A series of recent LHCb measurements [30] points to a tension with SM
 1809 predictions, which make these processes very interesting to better understand the
 1810 nature of the discrepancy.

1811 In order to exploit the sensitivity of loop diagrams, in 2004 Hiller and Kruger pro-
 1812 posed the measurement of the R_H ratio [107], defined in Eq. 5.1, where H can be an

Figure 5.1: Loop diagrams of the $B^0 \rightarrow K^{(*)0} \ell^+ \ell^-$ process.

₁₈₁₃ inclusive state containing an s quark (X_s) or an s -quark resonance like K or K^{*0} .

$$R_H = \frac{\int_{4m_\mu^2}^{m_b} \frac{d\mathcal{B}(B^0 \rightarrow H \mu^+ \mu^-)}{dq^2} dq^2}{\int_{4m_\mu^2}^{m_b} \frac{d\mathcal{B}(B^0 \rightarrow H e^+ e^-)}{dq^2} dq^2} \quad (5.1)$$

₁₈₁₄ In this quantity the differential branching ratio is integrated over the squared dilepton invariant mass, q^2 , from $q_{min}^2 = 4m_\mu^2$, which is the threshold for the $\mu\mu$ process,
₁₈₁₅ up to $q_{max}^2 = m_b^2$.

₁₈₁₇ The advantage of using ratios of branching fractions as observables is that, in the
₁₈₁₈ theoretical prediction, hadronic uncertainties cancel out. Furthermore, experimen-
₁₈₁₉ tally, some of the systematic uncertainties on the ratios are reduced giving a better
₁₈₂₀ measurement. For example, what is measured is the number of $\mu\mu$ and ee decays
₁₈₂₁ happening in a certain period of time. Then, the luminosity, \mathcal{L} , is used to obtain
₁₈₂₂ a cross section, σ , using $R = \mathcal{L}\sigma$, where R is the rate at which the decays occur.
₁₈₂₃ The luminosity measurement is usually a source of systematic uncertainty, but it
₁₈₂₄ appears on both sides of the ratio and therefore cancels out.

Since the SM does not distinguish between lepton flavours, the predicted value of the ratio is $R_H = 1$, under the assumption of massless leptons. Taking into account effects of order m_μ^2/m_b^2 Hiller and Kruger calculate that in the SM and in the full q^2

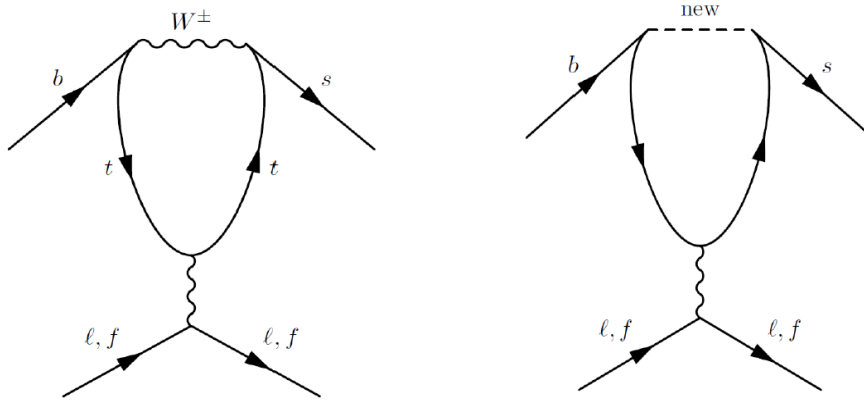


Figure 5.2: Example of penguin diagrams, on the left involving SM particles and on the right involving new possible particles.

range [107]:

$$R_{X_s} = 0.987 \pm 0.006, \quad (5.2)$$

$$R_K = 1.0000 \pm 0.0001, \quad (5.3)$$

$$R_{K^{*0}} = 0.991 \pm 0.002; \quad (5.4)$$

$$(5.5)$$

1825 under the assumptions that:

- 1826 • right-handed currents are negligible;
- 1827 • (pseudo-)scalar couplings are proportional to the lepton mass;
- 1828 • there are no CP-violating phases beyond the SM.

1829 The measurement of the R_H ratios is of particular interest after the recent measurement of the branching ratio of the $B_s^0 \rightarrow \mu^+ \mu^-$ decay [41], where no evidence of 1831 new physics was found. In fact the quantities $(R_H - 1)$ and $\mathcal{B}(B_s^0 \rightarrow \mu^+ \mu^-)$ remain 1832 proportional with

$$\frac{R_H - 1}{\mathcal{B}(B_s^0 \rightarrow \mu^+ \mu^-)} \sim 2 \cdot 10^{-5}. \quad (5.6)$$

1833 A joint measurement of these two quantities can give much information and constrain 1834 MFV models. If $R_H = 1$ and $\mathcal{B}(B_s^0 \rightarrow \mu^+ \mu^-)$ is close to the SM prediction as it is

measured to be this will allow to put strong constraints on extensions of the SM. If instead $R_H > 1$ and the equation above is not verified, this would mean that one of the assumptions listed above are not verified, which can happen in some extensions of the SM as Super-Symmetric models with broken R-parity. A series of recent LHCb measurements [30] shows tensions with SM predictions, which makes it interesting to further investigate these processes.

5.1 Combining ratios

The full power of the R_H ratios in understanding new physics scenarios comes from their combinations. In Ref. [108] Hiller and Schmaltz propose the measurement of the double ratios, $X_H = R_H/R_K$, which not only can test LFU but also allow to disentangle the kind of new physics that lies behind. These ratios are in fact sensitive to FCNCs of right-handed currents. Furthermore, in Ref. [108] the study is extended to B_s^0 decays such as $B_s^0 \rightarrow \phi\ell^+\ell^-$ or $B_s^0 \rightarrow \eta\ell^+\ell^-$.

Parity and Lorentz invariance require that the Wilson Coefficients with left-handed chirality (C) and their right-handed counterparts (C') appear in the decay amplitude of exclusive decays in determined combinations, e.g.

$$\begin{aligned} C + C' : & K, K_{\perp}^*, \dots \\ C - C' : & K_0(1430), K_{0,\parallel}^*, \dots \end{aligned} \tag{5.7}$$

where the labels for the K^* meson represent its longitudinal (0), parallel (\parallel) and perpendicular (\perp) transversity components. The C contributions are universal to all decays and therefore X_H double ratios are sensitive to right-handed currents. In fact the R_H ratios can be expressed in terms of their deviation from unity as

$$\begin{aligned} R_K &\simeq 1 + \Delta_+, \\ R_{K_0(1430)} &\simeq 1 + \Delta_-, \\ R_K^* &\simeq 1 + p(\Delta_- - \Delta_+) + \Delta_+, \end{aligned} \tag{5.8}$$

where the Δ_{\pm} quantities are combinations of Wilson coefficients described in Eq. 10 of Ref. [108] and the parameter p is the polarisation of K^* that in Ref. [108] is determined to be close to 1 simplifying the formula to $R_{K^*} \simeq 1 + \Delta_-$. In particular one can observe the following correlations:

- $R_K < 1$, as it is measured to be, and $X_{K^*} > 1$ points to dominant BSM contributions into C_{LR} (see definition in Sec. 1.5.2);
- a SM like $R_K \sim 1$ together with $X_{K^*} \neq 1$ requires BSM with $C_{LL} + C_{RL} \simeq 0$;
- $R_K \neq 1$ and $X_{K^*} \simeq 1$ corresponds to new physics in C_{LL} .

5.2 Experimental status

The R_K and $R_{K^{*0}}$ ratios have already been measured at the B-factories [109, 110], and the R_K ratio has been recently measured also at LHCb [111] in the $1 < q^2 < 6$ GeV $^2/c^4$ q^2 interval, which represents the most precise measurement to date. This measurement manifests a 2.6σ deviation from the SM prediction. The current experimental status is summarised in Tab. 5.1. By profiting of the large dataset collected during Run-I, the LHCb experiment is expected to reduce the uncertainty on $R_{K^{*0}}$ by at least a factor of 2 with respect to the B-factories.

Table 5.1: Experimental status of the $R_{K^{(*)}}$ measurements.

Ratio	Belle	BaBar	LHCb
R_K	$1.06 \pm 0.48 \pm 0.05$	$1.38^{+0.39+0.06}_{-0.41-0.07}$	$0.745^{+0.090}_{-0.074} \pm 0.036$
$R_{K^{*0}}$	$0.93 \pm 0.46 \pm 0.12$	$0.98^{+0.30+0.08}_{-0.31-0.08}$	—

¹⁸⁷² **5.3 Analysis strategy**

¹⁸⁷³ The aim of the analysis in this chapter is to measure the $R_{K^{*0}}$ ratio using pp collision
¹⁸⁷⁴ data collected by the LHCb detector in 2011 and 2012, corresponding to 3 fb^{-1} of
¹⁸⁷⁵ integrated luminosity. The $B^0 \rightarrow K^{*0}\mu^+\mu^-$ and $B^0 \rightarrow K^{*0}e^+e^-$, “rare channels”,
¹⁸⁷⁶ are reconstructed via the K^{*0} decay into a kaon and a pion with opposite charges.

¹⁸⁷⁷ The analysis has to separate signal candidates from background candidates which
¹⁸⁷⁸ have similar observed properties. The selection presented in Sec. 5.6 aims to max-
¹⁸⁷⁹ imise the yield while minimising the background contamination. Two types of back-
¹⁸⁸⁰ grounds are identified: “peaking background” and “combinatorial background”. The
¹⁸⁸¹ first comes from the mis-reconstruction of other decays or from partially recon-
¹⁸⁸² structed events. This type of background, because its specific kinematic properties,
¹⁸⁸³ usually peaks in some variable, such as the invariant mass of all final particles.
¹⁸⁸⁴ Therefore these candidates can be removed using specific cuts. The combinatorial
¹⁸⁸⁵ background instead comes from the random combination of particles and can be
¹⁸⁸⁶ lowered selecting events with good-quality tracks and vertices.

¹⁸⁸⁷ To further reduce the systematic uncertainties the measurement is performed as the
¹⁸⁸⁸ double ratio

$$R_{K^{*0}} = \frac{N_{B^0 \rightarrow K^{*0}\mu^+\mu^-}}{N_{B^0 \rightarrow K^{*0}J/\psi \rightarrow \mu^+\mu^-}} \cdot \frac{N_{B^0 \rightarrow K^{*0}J/\psi \rightarrow e^+e^-}}{N_{B^0 \rightarrow K^{*0}e^+e^-}} \cdot \frac{\varepsilon_{B^0 \rightarrow K^{*0}J/\psi \rightarrow \mu^+\mu^-}}{\varepsilon_{B^0 \rightarrow K^{*0}\mu^+\mu^-}} \cdot \frac{\varepsilon_{B^0 \rightarrow K^{*0}e^+e^-}}{\varepsilon_{B^0 \rightarrow K^{*0}J/\psi \rightarrow e^+e^-}}, \quad (5.9)$$

¹⁸⁸⁹ where decays reaching the same final states as the rare channels via a J/ψ resonance,
¹⁸⁹⁰ $B^0 \rightarrow K^{*0}(J/\psi \rightarrow \ell^+\ell^-)$, also referred to as “charmonium” or “resonant” channels,
¹⁸⁹¹ are used as control samples. These decays are distinguished from the rare channels
¹⁸⁹² using the invariant mass of the dilepton pair.

¹⁸⁹³ As new physics is expected not to affect charmonium resonances the ratio of the J/ψ
¹⁸⁹⁴ channels is 1 and therefore $R'_{K^{*0}} = R_{K^{*0}} \times R_{J/\psi} = R_{K^{*0}}$. On the other hand using
¹⁸⁹⁵ the relative efficiencies between the rare and resonant channels allows to cancel out
¹⁸⁹⁶ many effects resulting in a better control of systematic uncertainties. For brevity,

1897 the rare channels will also be denoted as “ $\ell\ell$ ”, or specifically “ ee ” and “ $\mu\mu$ ”, and
1898 the resonant channels as “ $J/\psi(\ell\ell)$ ”, or “ $J/\psi(ee)$ ” and “ $J/\psi(\mu\mu)$ ”.

1899 5.4 Dilepton invariant mass intervals

1900 Three q^2 intervals are considered in this work:

- 1901 • the “low- q^2 ” region between 0.0004 and $1.1 \text{ GeV}^2/c^4$, where the $b \rightarrow s\ell^+\ell^-$
1902 process is dominated by the photon pole;
- 1903 • the “central- q^2 ” region, $[1.1, 6.0] \text{ GeV}^2/c^4$;
- 1904 • the “high- q^2 ” region, above $15 \text{ GeV}^2/c^4$.

1905 The central- q^2 region is the most interesting place to look for new physics. In fact,
1906 at low q^2 , below $1 \text{ GeV}^2/c^4$ the photon pole dominates leaving little space for new
1907 physics to be found 1.5.3. The choice of the lower limit of the low- q^2 bin is driven by
1908 the need to reject the background due to the $B^0 \rightarrow K^{*0}\gamma$ decay where the photon
1909 converts into electrons in the material. The lower bound of the central interval is
1910 set at $1.1 \text{ GeV}^2/c^4$, in order to exclude the contribution from $\phi \rightarrow \ell^+\ell^-$ decays, that
1911 can dilute new physics effects. The upper bound of the central interval is chosen
1912 to be sufficiently far away from the J/ψ radiative tail, where predictions cannot be
1913 cleanly obtained. The $6\text{--}15 \text{ GeV}^2/c^4$ region is characterised by the presence of the
1914 narrow peaks of the J/ψ and $\psi(2S)$ resonances. The lower bound of the high- q^2
1915 region, where the signal in the electron channel is still unobserved, is chosen to
1916 be sufficiently far from the $\psi(2S)$ resonance. Rare and normalisation channels are
1917 selected depending on the q^2 interval they fall into (for details see Sec. 5.6).

¹⁹¹⁸ 5.4.1 Control channels

¹⁹¹⁹ Beyond the normalisation channels, $B^0 \rightarrow K^{*0}(J/\psi \rightarrow e^+e^-/\mu^+\mu^-)$, extra-control
¹⁹²⁰ channels are used to perform cross-checks and better constrain some of the back-
¹⁹²¹ ground components in the electron fit. In particular, $B^0 \rightarrow K^{*0}(\gamma \rightarrow e^+e^-)$, also
¹⁹²² denoted as “ $\gamma(ee)$ ”, and $B^0 \rightarrow K^{*0}(\psi(2S) \rightarrow e^+e^-)$, also denoted as “ $\psi(2S)(ee)$ ”.
¹⁹²³ All the normalisation and control channels are distinguished depending on the q^2
¹⁹²⁴ interval they fall into (for details see Sec. 5.6).

¹⁹²⁵ 5.5 Data samples and simulation

¹⁹²⁶ Simulated samples are used to study the background properties, determine efficien-
¹⁹²⁷ cies and to train the multivariate analysis. The hard interactions are generated with
¹⁹²⁸ Pythia8 hadronic particles are decayed using EvtGen and, finally, propagated into
¹⁹²⁹ the detector using Geant4 and reconstructed with the same software used for data.
¹⁹³⁰ Samples are generated with both 2011 and 2012, magnet up and down conditions
¹⁹³¹ and are combined in the right proportions, according to the luminosity registered on
¹⁹³² data. The next section describes the corrections applied to the simulation to obtain
¹⁹³³ a better description of data.

¹⁹³⁴ 5.5.1 Data-simulation corrections

¹⁹³⁵ Since the multivariate classifier training (see Sec. 5.6.6) and the calculation of most
¹⁹³⁶ of the efficiency components (see Sec. 5.9) are obtained from the study of simulated
¹⁹³⁷ events it is important to verify that the simulation provides a reliable reproduction
¹⁹³⁸ the data. In particular it is important to match data and Monte Carlo in the
¹⁹³⁹ kinematics of the final particles and the occupancy of the detector. The kinematics
¹⁹⁴⁰ of the decays is characterised by the transverse momentum spectrum of the B^0 .
¹⁹⁴¹ Discrepancies in this distribution cause also the spectra of the final particles to

1942 differ from data and affect the efficiency determination as its value often depends
 1943 on the momentum of the final particles. The occupancy of the detector is relevant
 1944 as it is correlated to the invariant mass shape of the signal because of the addition
 1945 of energy clusters in the electromagnetic calorimeter, which affects the electron's
 1946 momenta especially when bremsstrahlung photons emitted before the magnet. The
 1947 hit multiplicity in the SPD detector is a proxy for the detector occupancy.

1948 Since it is important that these quantities are well modelled, the simulation is
 1949 reweighted so that the distributions in data and simulation match for these vari-
 1950 ables. The weight is calculated using resonant $B^0 \rightarrow K^{*0}(J/\psi \rightarrow \ell^+\ell^-)$ candidates,
 1951 for which the signal peak is already visible in data after pre-selection (see Sec. 5.6).
 1952 However, the data still includes a high level of background and distributions cannot
 1953 be directly compared. The $s\mathcal{P}$ lot technique [63] is used to statistically subtract the
 1954 background from data and obtain pure signal distributions using the invariant mass
 1955 as control variable. Figure 5.3 shows fits to the 4-body invariant mass of candidates
 1956 after pre-selection. Data and simulation are then compared and the ratio between
 1957 the two distributions is used to re-weight the simulation. The discrepancy in the
 1958 SPD hits multiplicity is solved as a first step and then the B^0 transverse momentum
 1959 distributions are compared between data and simulation reweighted for the SPD
 1960 multiplicity only. Distributions of B^0 transverse momentum and SPD multiplicity
 1961 are reported in Fig. 5.4 and ratios of these distribution, which are used to re-weight
 1962 the simulation, are reported in Fig. 5.5. The weights for the SPD multiplicity are
 1963 calculated separately for 2011 and 2012 events, because distributions are signifi-
 1964 cantly different in the two years. The binnings for these distributions are chosen
 1965 to have approximately the same number of events in each bin to limit fluctuations.
 1966 Further corrections are made by re-weighting the simulation for PID efficiency using
 1967 the PIDCalib package as described in Sec. 5.9.3 and, finally, ee samples are also
 1968 reweighted for L0 trigger efficiency as described in Sec. 5.9.4. Weights are always
 1969 applied throughout unless specified.

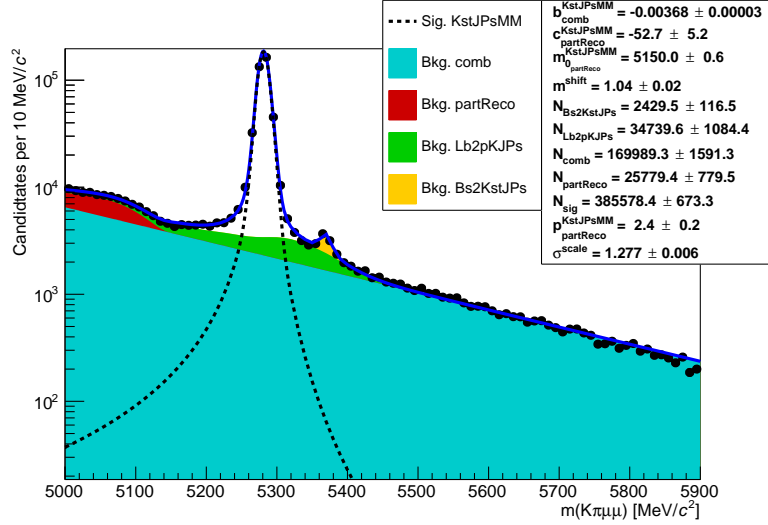


Figure 5.3: Fitted 4-body invariant mass distributions of muonic resonant candidates.

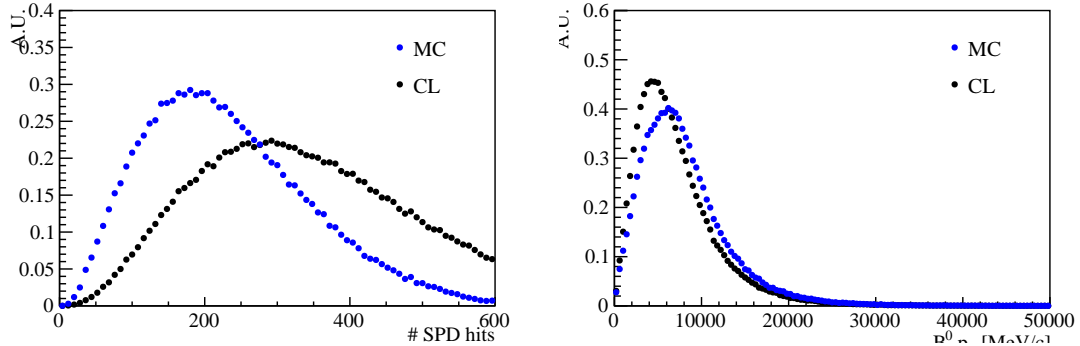


Figure 5.4: Distributions of number of SPD hits (left) and B^0 transverse momentum (right) in data and MC.

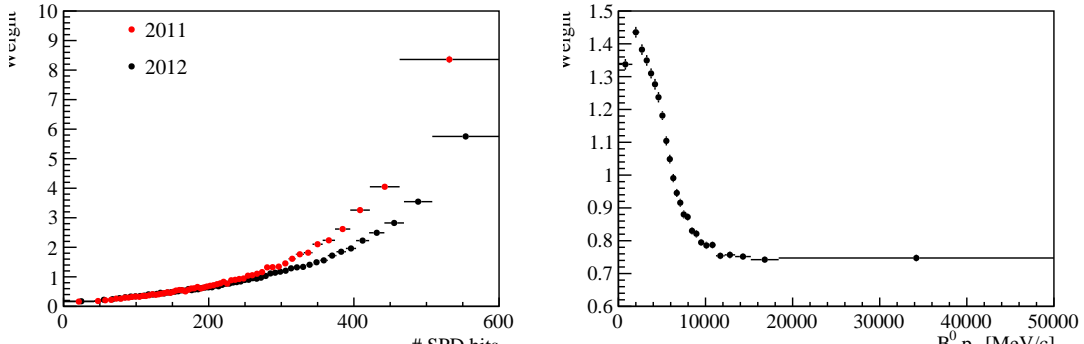


Figure 5.5: Ratios of simulated over real data distributions used to correct the Monte Carlo as a function of the number of SPD hits (left) and the B^0 transverse momentum (right).

1970 5.6 Selection

1971 The selection process, described in this section, is divided into several steps:

- 1972 • first of all candidates have to fall into the detector acceptance, produce hits and
1973 be selected on the basis of quality features, such as χ^2 of tracks and vertices
1974 and basic kinematic cuts. This stage is called “stripping”. Furthermore, it
1975 is required that the events are triggered by specific trigger lines and cuts are
1976 applied to remove backgrounds from specific decays. All these first three steps
1977 are referred to as “pre-selection”;
- 1978 • secondly, particle identification requirements are applied to remove part of
1979 misreconstructed background and clear the way for the last step;
- 1980 • in the final step a neural network is used to remove combinatorial background.
1981 Furthermore, for the electron channels, which are more challenging, the kine-
1982 matic structure of the decays is also used to improve the samples purity.

1983 To identify the $B^0 \rightarrow K^{*0}(J/\psi \rightarrow \mu^+\mu^-)$ candidates a dilepton mass interval of
1984 100 MeV/ c^2 around the nominal J/ψ peak [2] is selected. On the other hand it
1985 is not possible to use a narrow interval around $J/\psi(ee)$ mass peak as the invari-
1986 ant mass distribution is characterised by a long radiative tail at low masses due
1987 to bremsstrahlung radiation. Furthermore, a requirement in q^2 distorts the 4-body
1988 $m(K\pi ee)$ mass distribution which is not advisable as is important to be able to fit
1989 a wide mass range to constrain the backgrounds. For these reasons the interval to
1990 select $B^0 \rightarrow K^{*0}(J/\psi \rightarrow e^+e^-)$ candidates is chosen to go as low as possible without
1991 overlapping with the rare channel interval. Candidates are therefore identified as
1992 $J/\psi(ee)$ if they fall in the q^2 interval $6 < q^2 < 11$ GeV $^2/c^4$. Similarly, candidates
1993 are identified as $\psi(2S)(ee)$ if they fall into $11 < q^2 < 15$ GeV $^2/c^4$ and $\gamma(ee)$ if they
1994 fall into $q^2 < 0.004$ GeV $^2/c^4$. Table 5.2 summarises the requirements to distinguish
1995 sample from different channels. Figure 5.6 shows two-dimensional distributions of q^2
1996 versus the 4-body invariant mass for candidates passing the full selection. Horizontal

Table 5.2: Summary of the channel categories.

Type	Sample	q^2
$\mu\mu$	$B^0 \rightarrow K^{*0}\mu^+\mu^-$ (low)	$0.0004 < q^2 < 1.1 \text{ GeV}^2/c^4$
	$B^0 \rightarrow K^{*0}\mu^+\mu^-$ (central)	$1.1 < q^2 < 6 \text{ GeV}^2/c^4$
	$B^0 \rightarrow K^{*0}\mu^+\mu^-$ (high)	$q^2 > 15 \text{ GeV}^2/c^4$
	$B^0 \rightarrow K^{*0}(J/\psi \rightarrow \mu^+\mu^-)$ ($m(K\pi\mu\mu)$)	$ m_{\text{mm}} - m_{J/\psi}^{\text{PDG}} < 100 \text{ MeV}/c^2$
ee	$B^0 \rightarrow K^{*0}e^+e^-$ (low)	$0.0004 < q^2 < 1.1 \text{ GeV}^2/c^4$
	$B^0 \rightarrow K^{*0}e^+e^-$ (central)	$1.1 < q^2 < 6 \text{ GeV}^2/c^4$
	$B^0 \rightarrow K^{*0}e^+e^-$ (high)	$q^2 > 15 \text{ GeV}^2/c^4$
	$B^0 \rightarrow K^{*0}(J/\psi \rightarrow e^+e^-)$ ($m(K\pi ee)$)	$6 < q^2 < 11 \text{ GeV}^2/c^4$
Control samples		
	$B^0 \rightarrow K^{*0}(\gamma \rightarrow e^+e^-)$ ($m(K\pi ee)$)	$q^2 < 0.0004 \text{ GeV}^2/c^4$
	$B^0 \rightarrow K^{*0}(J/\psi \rightarrow e^+e^-)$ ($m(K\pi ee)$)	$6 < q^2 < 11 \text{ GeV}^2/c^4$
	$B^0 \rightarrow K^{*0}(\psi(2S) \rightarrow e^+e^-)$ ($m(K\pi ee)$)	$11 < q^2 < 15 \text{ GeV}^2/c^4$

¹⁹⁹⁷ bands can be clearly seen at q^2 values corresponding to the J/ψ and $\psi(2S)$ resonances. On the plot for muons it is also evident a vertical band which corresponds
¹⁹⁹⁸ to rare decay of interest.

²⁰⁰⁰ 5.6.1 Trigger and Stripping

²⁰⁰¹ Events are triggered for the $\mu\mu$ and the ee channels by the trigger lines reported
²⁰⁰² in Tab. 5.3, where the logical *and* of L0, HLT1 and HLT2 lines is required and the
²⁰⁰³ logical *or* of the lines on the same level. The candidates are required to be triggered-
²⁰⁰⁴ on-signal (TOS) for most of the stages, namely it is required for the particle which
²⁰⁰⁵ triggered to be one of the particles used to build the signal candidates. Only for
²⁰⁰⁶ **L0Global**, used in the electron case, we require a trigger-independent-of-signal (TIS),
²⁰⁰⁷ this is aimed to collect all the possible statistics for the electron channels, which are
²⁰⁰⁸ the most challenging. The **L0Muon** trigger requires hits in the muon detector, while
²⁰⁰⁹ **L0Electron** and **L0Hadron** use information from the calorimeters; **HLT1TrackAllL0**
²⁰¹⁰ adds information from the trackers and triggers if the L0 decision is confirmed;
²⁰¹¹ finally, **HLT2Topo[2,3]BodyBBBDT** uses a full reconstruction of the event and a neural
²⁰¹² network trained on events with a specific topology in order to detect specific decay

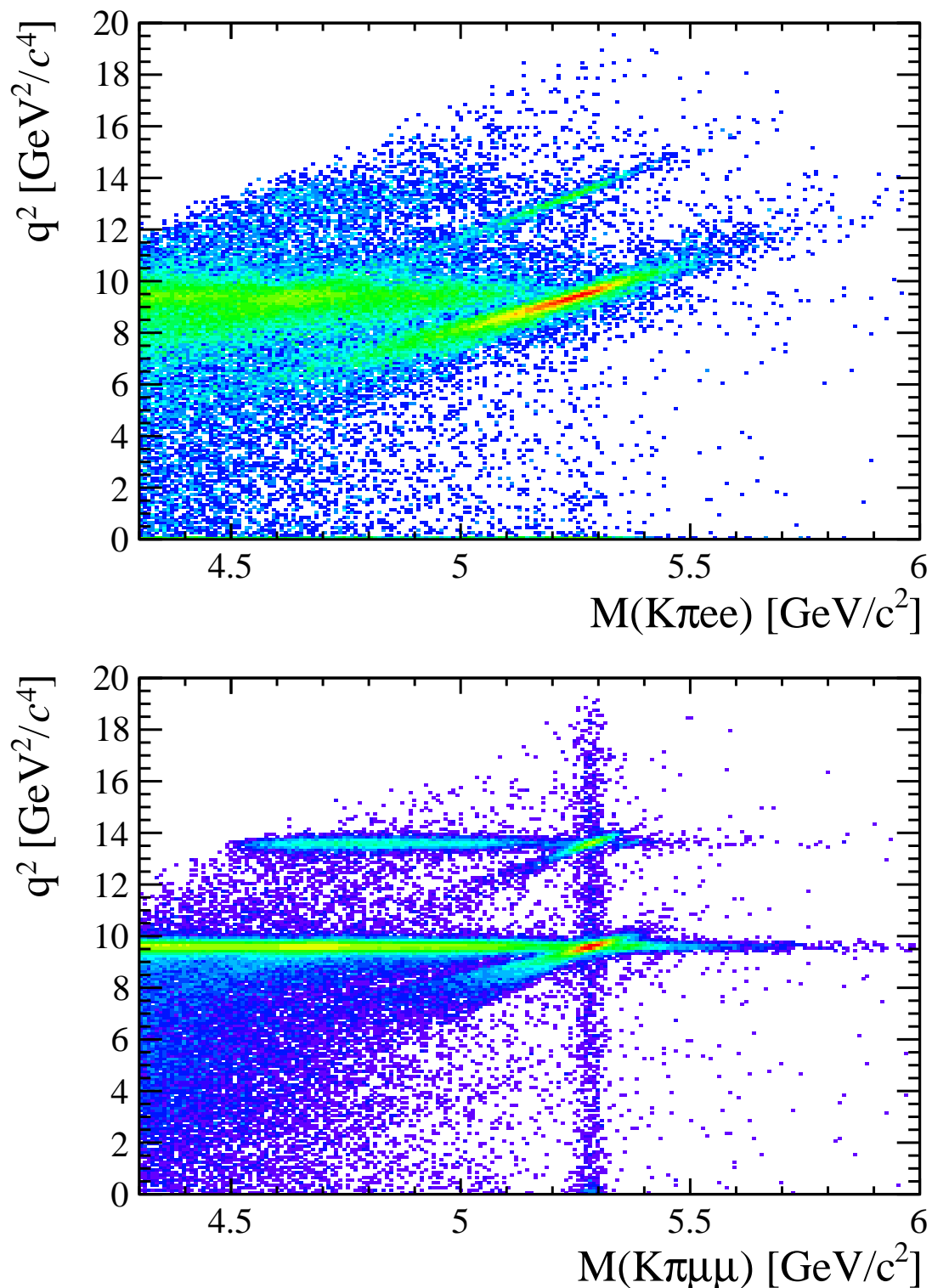


Figure 5.6: Two-dimensional distributions of q^2 versus 4-body $m(K\pi\ell\ell)$ invariant mass for the electron (top) and muonic (bottom) channels in 2012 data.

2013 structures.

Table 5.3: Summary of the trigger lines used to select the $\mu\mu$ and the ee channels. Where not explicitly indicated, the lines are required to be TOS.

$\mu\mu$ candidates	ee candidates
L0Muon	L0Electron L0Hadron L0Global (TIS)
Hlt1TrackAllL0	Hlt1TrackAllL0
Hlt1TrackMuon	
Hlt2Topo[2,4]BodyBBDT Hlt2TopoMu[2,4]BodyBBDT Hlt2DiMuonDetachedDecision	Hlt2Topo[2,4]BodyBBDT Hlt2TopoE[2,4]BodyBBDT

2014 For the electron channels the L0 lines have different properties, therefore the analysis
2015 is performed separately for three categories of events, depending on the L0 trigger
2016 that fired them. These categories are defined to be exclusive in the following way:

- 2017 • **L0E**: events triggered by at least one of the electrons in the signal candidate
2018 (`L0Electron_TOS`);
- 2019 • **L0H**: events triggered by at least one of the hadrons in the signal candidate
2020 and not by L0Electron (`L0Hadron_TOS && !L0Electron_TOS`);
- 2021 • **L0I**: events triggered by particles not in the signal candidate and not by the
2022 previous cases (`L0_TIS && !(L0Electron_TOS || L0Hadron_TOS)`).

2023 The majority of the selected events falls in the L0E category, while the L0H category
2024 is more efficient at low q^2 were the K^{*0} has more momentum. Because L0I is defined
2025 to be independent of the signal candidate, the corresponding signal efficiency is the
2026 same in the rare and resonant cases and cancels out in their ratio.

2027 Candidates are then required to pass the kinematic and quality cuts summarised
2028 in Tab. 5.4. The meaning of the variables in the table was already explained in
2029 Sec. 3.4. Loose PID cuts are applied in preselection to limit the size of the samples,
2030 while tighter cuts are applied in a second stage. A large mass window is kept

Table 5.4: Summary of stripping requirements.

Particle	Requirements
π	$\chi^2_{\text{IP}}(\text{primary}) > 9$
K	$\text{PID}_K > -5$ $\chi^2_{\text{IP}}(\text{primary}) > 9$ hasRICH
K^{*0}	$p_T > 500 \text{ MeV}/c$ $ m - m_{K^{*0}}^{\text{PDG}} < 300 \text{ MeV}/c^2$ $\chi^2_{\text{IP}}(\text{primary}) > 9$ Origin vertex $\chi^2/\text{ndf} < 25$
μ	$p_T > 300 \text{ MeV}/c$ $\chi^2_{\text{IP}}(\text{primary}) > 9$ isMuon
e	$p_T > 300 \text{ MeV}/c$ $\chi^2_{\text{IP}}(\text{primary}) > 9$ hasCalo $PID_e > 0$
$\ell\ell$	$m < 5500 \text{ MeV}/c^2$ End vertex $\chi^2/\text{ndf} < 9$ Origin vertex χ^2 separation > 16
B^0	DIRA > 0.9995 End vertex $\chi^2/\text{ndf} < 9$ $\chi^2_{\text{IP}}(\text{primary}) < 25$ Primary vertex χ^2 separation > 100

around the B^0 peak in order to be able to use the sideband to train the multivariate analysis and to constrain the backgrounds. Track and vertex quality cuts are also applied using the $\chi^2_{\text{track}}/\text{ndf}$, `GhostProb`, and $\chi^2_{\text{vtx}}/\text{ndf}$ variables. The `GhostProb` quantity describes the probability of a track being fake. By construction cutting at 0.4 removes $(1 - 0.4) \cdot 100 = 60\%$ of fake tracks. For details about the definition of the variables used see Ref. [112].

5.6.2 PID

After preselection there still are high levels of misreconstructed background. In particular, as the ID of kaons and pions are not constrained, the samples still contain both ID combinations for most candidates, therefore tighter PID cuts are applied.

In the LHCb analysis framework the particle identification probability can be quantified using the “`ProbNN`” variables [113]. These variables are the output of a neural network which takes as input information from the calorimeters, the RICH detectors the muon system and the tracking system. Unlike the DLL variables (see Sec. 2.8) the `ProbNN` are bound from 0 to 1 and can be therefore directly be interpreted as probabilities. For example `ProbNNk` is the probability for a reconstructed particle to be a kaon. Figure 5.7 shows distributions of the correct ID variables in the

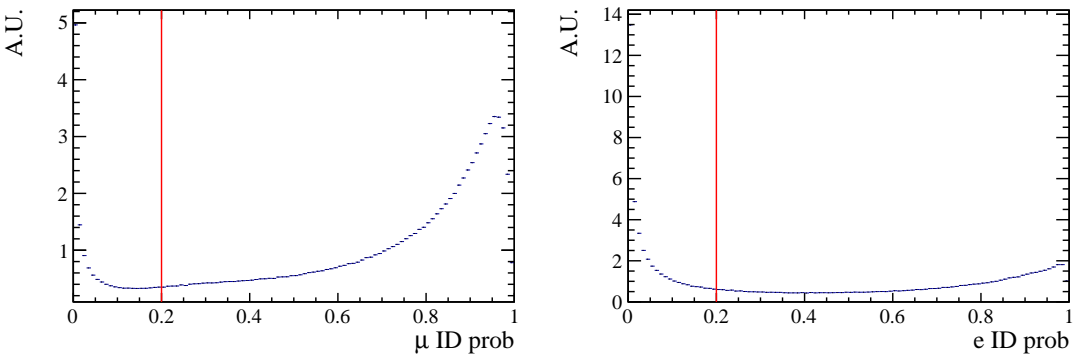


Figure 5.7: Correct ID probability distributions for muons (left) and electron (right) in 2012 data.

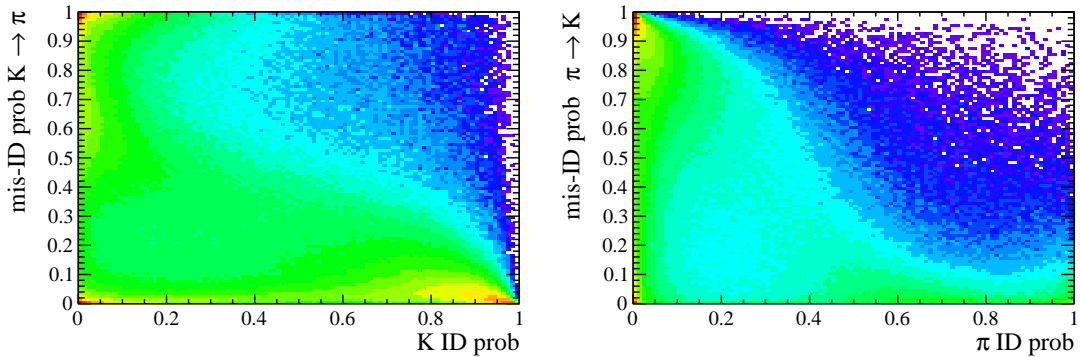


Figure 5.8: On the horizontal axis of these plots is shown the correct ID probabilities for kaons (left) and pions (right), while the vertical axis show the mis-ID probability.

2048 2012 data sample while Fig. 5.8 shows in a two-dimensional plane the probability
 2049 of correct identification and mis-identification of kaons and pions. These plots are
 2050 characterised by clear peak at maximal ID probability and minimal mis-ID probabil-
 2051 ity, corresponding to particles to which a well defined identification can be assigned.
 2052 In order to maximise the power of the PID requirements probabilities of correct ID
 2053 and mis-ID are combined using the following cuts:

$$\begin{aligned} \pi &\rightarrow \text{ProbNNpi} \times (1 - \text{ProbNNk}) \times (1 - \text{ProbNNp}) > 0.1 \\ K &\rightarrow \text{ProbNNk} \times (1 - \text{ProbNNp}) > 0.05 \\ \mu &\rightarrow \min(\text{ProbNNmu}, \text{ProbNNmu}) > 0.2 \\ e &\rightarrow \min(\text{ProbNNe}, \text{ProbNNe}) > 0.2 \end{aligned}$$

2054 In the first formula, for example, `ProbNNpi` is the probability of correctly identifying
2055 the pion as a pion, while `ProbNNk` is the probability of mistaking it for a kaon. Therefore by maximising the quantity “`ProbNNpi` \times (1 - `ProbNNk`)”, one can maximise
2056 the correct ID probability and minimise at the same time the mis-ID probability.
2057
2058

2059 5.6.3 Peaking backgrounds

2060 Backgrounds due to specific decays usually peak in some variable because of their
2061 distinctive kinematic properties and therefore they can be removed without sig-
2062 nificant signal efficiency loss. The following sections describe the main sources of
2063 peaking background. The same cuts are applied to the muon and electron channels,
2064 unless specified.

2065 5.6.3.1 Charmonium vetoes

2066 Charmonium resonances such as J/ψ and $\psi(2S)$ peak in q^2 . The choice of q^2 bin-
2067 ning described in Sec. 5.4 constitutes a natural veto for these decays. Simulated
2068 events were used to check if resonant candidates leak inside the q^2 intervals cho-
2069 sen for the rare channel analysis. For the muonic channels the leakage is negli-
2070 gible as the peaks are sharper due to a better resolution and muons emit fewer
2071 bremsstrahlung photons, resulting in shorter radiative tails. The electronic chan-
2072 nels are instead characterised by a worse resolution and at the same time electrons
2073 can radiate several bremsstrahlung photons, yielding long tails at low q^2 . Analysing
2074 Monte Carlo events it was found that 1.3–2% (depending on the trigger category)
2075 of $B^0 \rightarrow K^*(J/\psi \rightarrow e^+e^-)$ candidates leak into the $1.1 < q^2 < 6$ GeV $^2/c^4$ interval

2076 and 1.8% of $\psi(2S)$ events leak above $15 \text{ GeV}^2/c^4$. The contribution from these
 2077 candidates is modelled in the fit.

2078 5.6.3.2 ϕ veto

2079 It can happen that a kaon from the decay $B_s \rightarrow \phi\ell^+\ell^-$, where the ϕ decays in two
 2080 kaons, is mis-identified as a pion and therefore causes the ϕ to be reconstructed as a
 2081 K^{*0} . This results in a candidate with a value of $m(K\pi)$ that is less than the nominal
 2082 K^{*0} mass but still high enough to pass the selection requirements. Figure 5.9 shows
 2083 the plot of $m(K\pi)$ versus $m(K\pi\ell\ell)$, where the kaon mass hypothesis is assigned to
 2084 the pion. A peak can clearly be seen around the ϕ mass ($1020 \text{ MeV}/c^2$). To remove
 2085 this background only candidates with $m_{K(\pi \rightarrow K)} > 1040 \text{ MeV}/c^2$) are selected. This
 2086 results in a 98% background rejection while keeping a 99% signal efficiency. The ϕ
 2087 could also constitute a background when it decays into two leptons but the branching
 2088 ratio of this decay is small compared to the one into kaons and this contribution is
 2089 taken into account by the choice of the q^2 intervals (see Sec. 5.4).

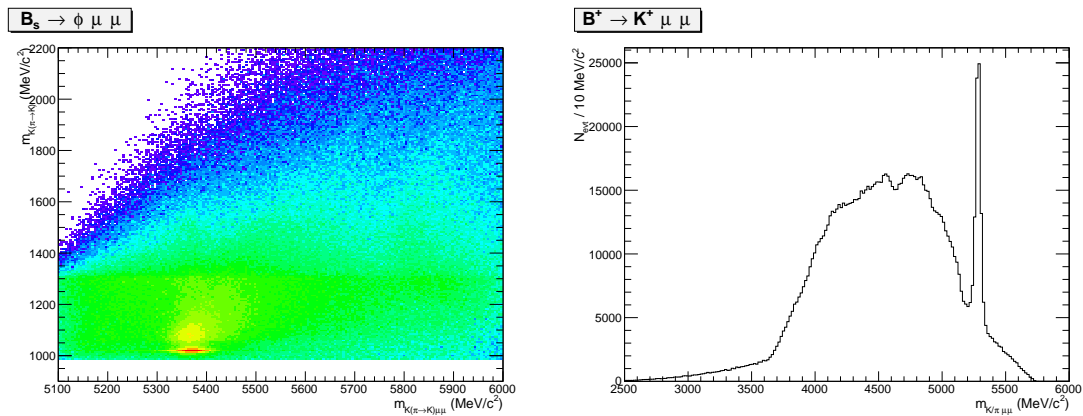


Figure 5.9: (left) Distribution of 2011 data events as a function of the variables $(m_{K(\pi \rightarrow K)})$ and $(m_{K(\pi \rightarrow K)\mu\mu})$, where $\pi \rightarrow K$ means that the kaon mass is given to the pions too. (right) The invariant mass distribution of the three-body system $(K\mu\mu)$, where the peak due to the $B^+ \rightarrow K^+\mu^+\mu^-$ decay is visible.

2091 5.6.3.3 $B^+ \rightarrow K^+ \ell^+ \ell^-$ plus a random pion

2092 $B^+ \rightarrow K^+ \ell^+ \ell^-$ decays can contaminate the upper B^0 mass sideband if they are com-
2093 bined with a soft pion from somewhere else in the event and therefore reconstructed
2094 as a B^0 decay. Similarly a kaon can be mis-identified as a pion and combined with
2095 an other kaon in the event. Figure 5.9 shows the invariant mass distribution of the
2096 three-body $K\mu^+\mu^-$ system, $m(K\mu\mu)$. This is characterised by a narrow peak at
2097 the B^+ mass. Since these candidates have $m(K\pi\ell\ell) > 5380$ MeV/ c^2 there is no
2098 contribution under the B^0 peak, but they can cause problems when using sidebands
2099 events to train the neural network. An effective veto for this decay was found to
2100 be $\max(m_{K\ell\ell}, m_{(K \rightarrow \pi)\ell\ell}) < 5100$ MeV/ c^2 , which results in 95% background rejection
2101 while keeping 99% signal efficiency.

2102 5.6.3.4 Λ_b decays

2103 $\Lambda_b^0 \rightarrow J/\psi \Lambda$ decays are unlikely to be reconstructed as $B^0 \rightarrow K^{*0} \ell^+ \ell^-$ because the
2104 Λ is long-lived and decays further in the detector with a separate vertex. How-
2105 ever, simulated events were used to check how many candidates fall into the B^0
2106 samples, which results to be negligible. The $\Lambda_b^0 \rightarrow J/\psi pK$ decay, when the pro-
2107 ton is mis-identified, can instead contribute more easily since the $m(pK)$ is above
2108 the Λ threshold and therefore they must come from Λ^* resonances, which are not
2109 long-lived. This background is already reduced by the PID requirements but a
2110 non-negligible contribution is still expected, which is modelled in the fit.

2111 5.6.3.5 $B^0 \rightarrow (D^- \rightarrow Ke^-\bar{\nu})e^+\nu$

2112 The $B^0 \rightarrow D^- e^+ \nu$ decay, where the D^- in turn decays semileptonically to $K^{*0} e^- \nu$
2113 has the same final particles as the $B^0 \rightarrow K^{*0} e^+ e^-$ decay plus two neutrinos which
2114 are not reconstructed. This decay has a branching ratio four orders of magnitude
2115 larger than $B^0 \rightarrow K^{*0} e^+ e^-$ in the low- q^2 region and it may pass the selection

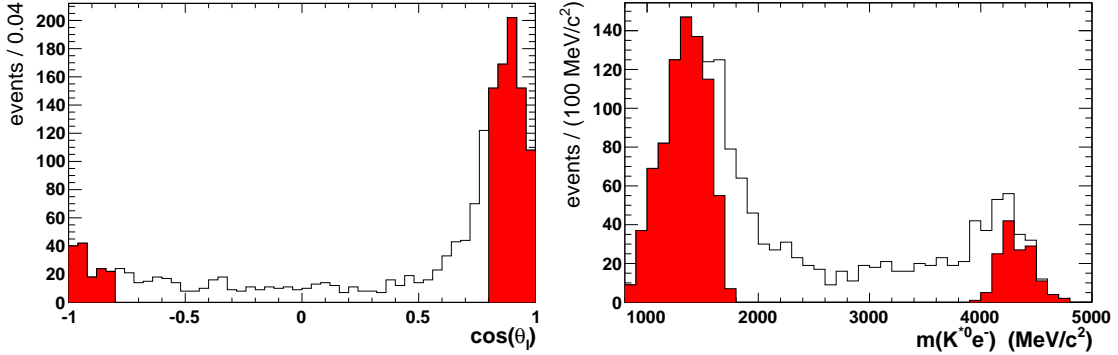


Figure 5.10: Distribution of (left) $\cos(\theta_\ell)$ and of (right) the $m(K^{*0}e^-)$ invariant mass, where the $B^0 \rightarrow (D^- \rightarrow K e^- \bar{\nu}) e^+ \nu$ background is selected by requiring $m(K^{*0}e^+e^-) < 4800 \text{ MeV}/c^2$. The red distribution corresponds to events with $|\cos(\theta_\ell)| > 0.8$.

requirements when the two neutrinos carry a low momentum. To lower the level of this background the angle θ_ℓ is used, which is defined as the angle between the direction of the e^+ (e^-) in the di-electron rest frame and the direction of the di-electron in the B^0 (\bar{B}^0) rest frame. Low momentum neutrinos demand the D^- and the e^+ to be almost back-to-back in the B^0 rest frame giving the e^+ a relatively large energy compared to the e^- . As a consequence, the direction of the e^+ is close to the direction of the di-electron pair, thus the θ_ℓ angle is close to 0. This explains why the distribution of background selected in data with an invariant mass cut of $m(K^{*0}ee) < 4800 \text{ MeV}/c^2$ is asymmetric towards higher $\cos(\theta_\ell)$ values as it can be seen in Fig. 5.10(left). The cut is chosen to be $|\cos(\theta_\ell)| < 0.8$, and is not applied in the high- q^2 bin as the variable loses its discriminating power.

In the muon channels the background from $B^0 \rightarrow (D^- \rightarrow K \mu^- \bar{\nu}) \mu^+ \nu$ decays is suppressed by the choice of the fitting range.

5.6.3.6 $B^0 \rightarrow K^{*0}(\gamma \rightarrow e^+e^-)$

For the low- q^2 region, a potentially dangerous peaking background is due to the $B^0 \rightarrow K^{*0}(\gamma \rightarrow e^+e^-)$ decay followed by a conversion of the photon in the detector. The branching fraction of $B^0 \rightarrow K^{*0}(\gamma \rightarrow e^+e^-)$ has been measured to be $\mathcal{B} = (4.33 \pm$

2133 $0.15) \times 10^{-5}$ and when the photon converts to an electron and a positron has similar
2134 characteristics to $B^0 \rightarrow K^{*0}e^+e^-$. In LHCb around 40% of the photons convert
2135 before the calorimeter. Although only a small fraction of these, $\sim 10\%$, converts in
2136 the VELO and are reconstructed as long tracks, the resulting B^0 mass should peak
2137 under that of the signal, making it a dangerous background. To veto this signal-
2138 like background an effective veto is in the reconstructed invariant mass window for
2139 the e^+e^- -pair that was chosen above $20 \text{ MeV}/c^2$. Furthermore, the e^+e^- -pair from
2140 $B^0 \rightarrow K^{*0}(\gamma \rightarrow e^+e^-)$ has a vertex at the point of conversion of the photon, but it
2141 may still be reconstructed as originating from the B^0 decay when the e^+e^- -vertex is
2142 determined with a large error. Therefore a requirement is applied on the uncertainty
2143 of the reconstructed z -coordinate of the e^+e^- -pair: $\sigma_z(e^+e^-) < 30\text{mm}$. iSimulation
2144 is used to predict the contamination from $B^0 \rightarrow K^{*0}(\gamma \rightarrow e^+e^-)$ events in the signal
2145 region which is found to be $(3.2 \pm 1.6)\%$.

2146 5.6.3.7 Other peaking backgrounds

2147 Contamination from $B^0 \rightarrow K^{*0}\eta$ and $B^0 \rightarrow K^{*0}\pi^0$ where η and the pion decay
2148 into two photons was considered and found to be small. Furthermore, a potentially
2149 dangerous background could come from events where the identity of the kaon and
2150 the pion are swapped as these candidates peak under the signal. Their contribution
2151 is found to be small, 0.5%, however the effect of their modelling into the fit is
2152 taken into account in the systematic uncertainties. Finally, charmonium decays
2153 where the identity of the kaon, or the pion, and one of the muons are swapped is
2154 a potentially dangerous background. These decays are rejected by requiring that
2155 the hadron- μ invariant mass $m((h \rightarrow \mu)\mu)$, where the muon mass hypothesis is
2156 assigned to the hadron, is not compatible with a J/ψ ($\psi(2S)$) resonance: $|m((h \rightarrow$
2157 $\mu)\mu) - m_{J/\psi,(\psi(2S))}| > 60 \text{ MeV}/c^2$.

²¹⁵⁸ 5.6.4 Mis-reconstructed background

²¹⁵⁹ Mis-reconstructed candidates are defined as decays where one or more particles
²¹⁶⁰ in the final state are not reconstructed, resulting in $m(K\pi\ell\ell)$ values smaller than
²¹⁶¹ m_{B^0} , but with tails that can still contaminate the signal peak. Sources of mis-
²¹⁶² reconstructed background are decays involving higher hadronic states such as $B^0 \rightarrow$
²¹⁶³ $(Y \rightarrow K\pi X)(J/\psi \rightarrow e^+e^-)$, where X represents one or more not reconstructed
²¹⁶⁴ particles. The Y state can be a K^* resonance as well as D mesons that decay
²¹⁶⁵ semileptonically (*e.g.* $B^0 \rightarrow D^-\ell^+\bar{\nu}_\ell$ followed by $D^- \rightarrow K^{*0}\ell^-\nu_\ell$). In case of the
²¹⁶⁶ $J/\psi(ee)$ channel, an additional source of mis-reconstructed background are decays
²¹⁶⁷ of higher $c\bar{c}$ resonances, $B^0 \rightarrow (K^{*0} \rightarrow K\pi)(Y \rightarrow (J/\psi \rightarrow e^+e^-)X)$. To reject this
²¹⁶⁸ backgrounds in the mm channels the 4-body invariant mass $m(K\pi\mu\mu)$ is recalcul-
²¹⁶⁹ ated using `DecayTreeFitter` with a vertex constraint. For the resonant case this
²¹⁷⁰ also includes a J/ψ mass constraint to the dilepton pair. By using this procedure
²¹⁷¹ mis-reconstructed events are pushed towards low masses, resulting in no contami-
²¹⁷² nation above 5150 MeV/ c^2 . To correctly model the long radiative tail of the ee and
²¹⁷³ $J/\psi(ee)$ mass shapes, a fit region that extends down to 4500 MeV/ c^2 is used. As a
²¹⁷⁴ consequence, no mass constraint to the dilepton pair is applied, as this could bias
²¹⁷⁵ the 4-body mass distribution, and the mis-reconstructed background is modelled in
²¹⁷⁶ the fit (for details see Sec. 5.8.2.2).

²¹⁷⁷ 5.6.5 Bremsstrahlung corrected mass

²¹⁷⁸ An additional handle against backgrounds that contaminate the ee channels is pro-
²¹⁷⁹ vided the analysis of the kinematics of the decay. In fact for the B^0 daughters the
²¹⁸⁰ momentum component orthogonal to the flight direction of the B^0 meson should
²¹⁸¹ cancel out. The flight direction is defined using the primary and the decay vertices
²¹⁸² and sketch is shown in Fig. 5.11.

The ratio between the p_T of the K^{*0} and the di-electron pair can be used to check

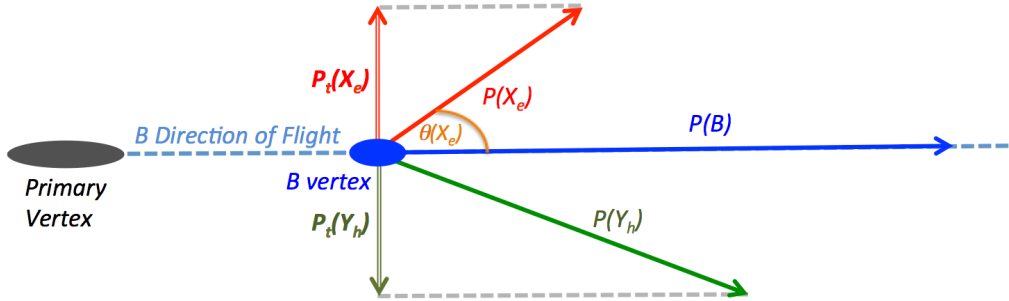


Figure 5.11: Schema of the kinematic of a $B \rightarrow Y_h X_e$ decay, highlighting the quantities relevant for the definition of the bremsstrahlung correction factor, α .

this hypothesis

$$\alpha = \frac{p_T(K^*)}{p_T(e^+e^-)}.$$

When α deviates from one, some energy is missing in the final state. For signal events, the missing energy is most likely carried away by bremsstrahlung photons emitted by the electrons. Therefore we can use α to correct the electron momentum as

$$p_{\text{corr}}(e^+e^-) = \alpha \times p(e^+e^-).$$

Since bremsstrahlung photons are emitted in the same direction of the electron, the same α correction can be applied to the longitudinal component of the di-electron momentum. In contrast, the missing particles in partially-reconstructed background candidates are not necessarily emitted in the direction of the electrons, and therefore the α correction does not work properly. A similar argument applies to the combinatorial background.

The corrected momenta can be used to re-calculate the invariant mass of the B^0 candidate, which in the following will be called Bremsstrahlung Corrected Mass (m_{BCM}). The resolution of m_{BCM} depends on the quality of the vertex reconstruction and on the B^0 lifetime, and degrades as a function of q^2 . Figure 5.12 shows the dependence of the $B^0 \chi^2_{\text{FD}}$ (flight distance χ^2) as a function of m_{BCM} in the considered q^2 regions.

As the correction does not work properly for backgrounds this leads the candidates to

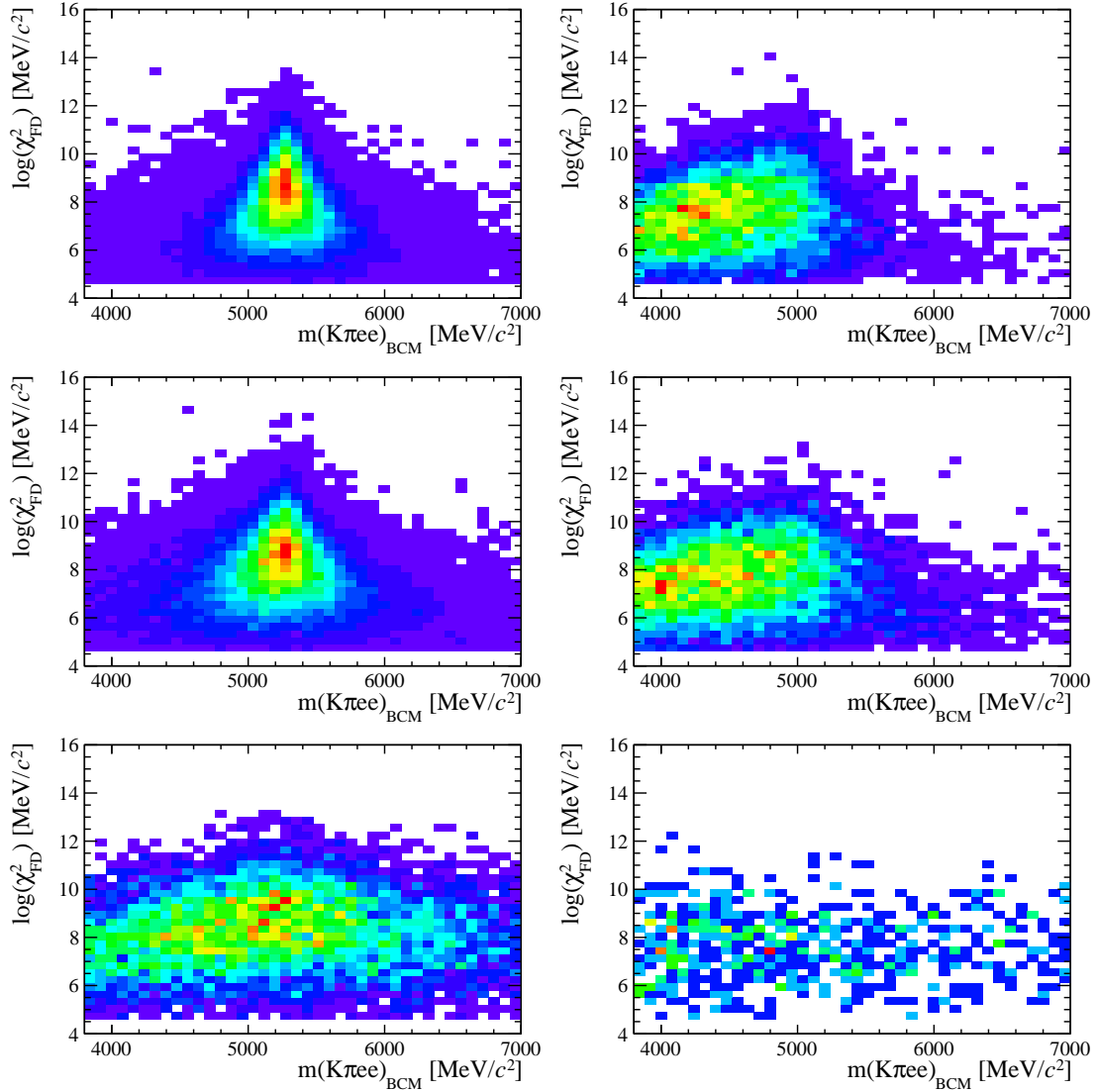


Figure 5.12: Two-dimensional distribution of χ^2_{FD} vs. m_{BCM} for (left) $B^0 \rightarrow K^{*0} e^+ e^-$ signal and (right) partially-reconstructed background. From top to bottom the low-, central- and high- q^2 intervals.

spread out making m_{BCM} a discriminating variable between signal and background shapes. A two-dimensional cut is adopted

$$m_{\text{BCM}} > a_{\text{BCM}} + b_{\text{BCM}} \cdot \log(\chi^2_{\text{FD}})$$

²¹⁹⁵ where the a_{BCM} and b_{BCM} coefficients are optimised as described in Sec. 5.6.7.

²¹⁹⁶ No cut is applied at high- q^2 nor on the muon channels for which the bremsstrahlung

²¹⁹⁷ radiation is negligible.

2198 5.6.6 Multivariate analysis

2199 The final selection is performed using a Neural Network classifier (NN) based on
 2200 the NEUROBAYES package [73, 74]. The multivariate analysis is intended to remove
 2201 some combinatorial background and obtain a clearer signal peak. In order to avoid
 2202 biases, a k -fold approach is adopted to train and optimise the classifier, using $k =$
 2203 10. This method consists in dividing the samples in k equally sized subsamples; k
 2204 classifiers are then trained and optimised each on $(k - 1)$ samples and applied to
 2205 the k th one. This approach ensures that a classifier is never applied to the events
 2206 used for its training. Each classifier is trained on half of the events included in the
 2207 $(k - 1)$ samples and optimised using the other half, which ensures that events used
 2208 for training are not used for optimisation.

2209 Samples:

2210 Representative samples of the signal and background are needed to train the clas-
 2211 sifier. For the signal, fully reconstructed $B^0 \rightarrow K^{*0}\mu^+\mu^-$ and $B^0 \rightarrow K^{*0}e^+e^-$ sim-
 2212 ulated events can be used. Instead a sample representative of the background can
 2213 be obtained using real data candidates in the upper B^0 sideband: $m(K\pi\mu\mu) >$
 2214 $5400 \text{ MeV}/c^2$ and $m(K\pi ee) > 5600 \text{ MeV}/c^2$. The lower sideband is not used in
 2215 the training as it contains a significant fraction of mis-reconstructed background.
 2216 All pre-selection cuts are applied to the background samples used for the training.
 2217 As L0 and PID variables are not well described in simulation these cuts are not
 2218 applied to the simulation but their effect is taken into account by the event weight.
 2219 An approximately equal number of signal and background events is used for the
 2220 training which corresponds to about 1000 events for the electron case and 10,000 for
 2221 the muon one.

2222 Training:

2223 The the neural-network input consists of 24 variables containing information about
 2224 the kinematic of the decays and the quality of tracks and vertices. All the vari-
 2225 ables used are listed in Tab. 5.5. In these figures the variable with ID = 1 is the

Table 5.5: List of variables used as inputs for the neural-network training.

Particle	Variables
B^0	p_T , χ_{IP}^2 , χ_{FD}^2 , χ_{vtx}^2/ndf , DIRA, χ_{DTF}^2/ndf
K^{*0}	p_T , χ_{IP}^2 , χ_{FD}^2 , χ_{vtx}^2/ndf , DIRA
h	$\min, \max(p_{T,K}, p_{T,\pi})$, $\min, \max(\chi_{IP,K}^2, \chi_{IP,\pi}^2)$
$\ell\ell$	p_T , χ_{IP}^2 , χ_{FD}^2 , χ_{vtx}^2/ndf , DIRA
ℓ	$\min, \max(p_{T,\ell+}, p_{T,\ell-})$, $\min, \max(\chi_{IP,\ell+}^2, \chi_{IP,\ell-}^2)$

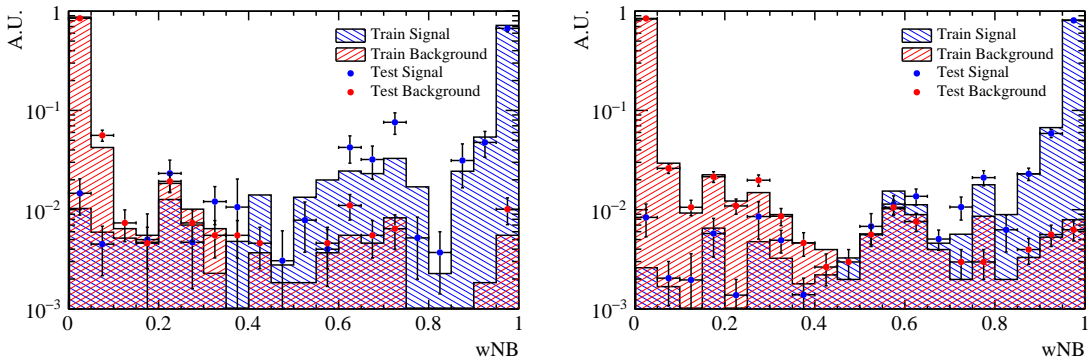


Figure 5.13: NN output distributions for training (solid) and test (stripes) samples, for simulated signal and data sideband events. For the electron (left) and muon (right) training.

2226 neural-network output and the other IDs are reported in Tab. 5.5. The single most
 2227 discriminating variable used is the χ^2 of a kinematic fit that constrains the decay
 2228 product of the B^0 , the K^{*0} and the dimuon, to originate from their respective ver-
 2229 tices. Other variables that contribute significantly are the χ_{IP}^2 of J/ψ and K^{*0} , the
 2230 transverse momentum of the B^0 and the pointing direction (DIRA) of the recon-
 2231 structed B^0 to the primary vertex.

2232 Figure 5.13 shows neural network output distributions for signal and background.
 2233 On this plot the distributions from the test samples are also overlaid in order to
 2234 check for overtraining. The distributions follow the same shape but with different
 2235 fluctuations indicating no significant overtraining. In general it can be concluded
 2236 that the neural network is able to separate signal from background and that the
 2237 training converged properly.

2238 It can happen that too much information is given to the classifier, which becomes
 2239 able to calculate the invariant mass of the candidates from its inputs. This could

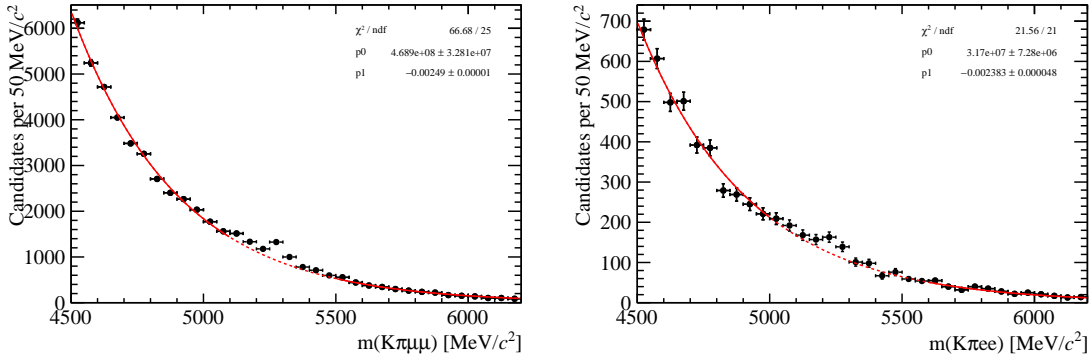


Figure 5.14: Fit to the data sidebands performed to estimate the amount of residual background in the signal mass window for (left) muons and (right) electrons. The region corresponding to the dashed line is excluded from the fit.

2240 generate fake peaks and it is therefore important to check for correlations between
 2241 the B^0 mass and the neural-network output. Figure 5.15 reports plots of the average
 2242 neural-network output as a function of the B^0 mass on sideband data and simulated
 2243 signal events. The distributions are flat showing that no significant correlation is
 2244 present.

2245 5.6.7 Optimisation

2246 In order to optimise the requirements on the m_{BCM} and the neural network output
 2247 the expected signal significance, $N_S/\sqrt{N_S + N_B}$, is maximised, where N_S (N_B) is
 2248 number of rare signal (background) candidates. When the BCM requirement is
 2249 applied, the optimisation is performed in a three-dimensional space (t_{MVA} , a_{BCM} ,
 2250 b_{BCM}) where t_{MVA} is the neural-network output threshold below which a candidate
 2251 is considered background, and a_{BCM} and b_{BCM} are the parameters of the BCM cut
 2252 described in Sec. 5.6.5. Otherwise, only the MVA cut is optimised (for all muons
 2253 samples and the high- q^2 electron sample).

The number of signal events accepted by a given requirement is determined using a data-driven method. Firstly, $B^0 \rightarrow K^{*0}(J/\psi \rightarrow \ell^+\ell^-)$ candidates selected with all the requirements except for the MVA, and BCM when applicable, cut are fitted to determine the total yield. This number is then scaled by the ratio of the signal to

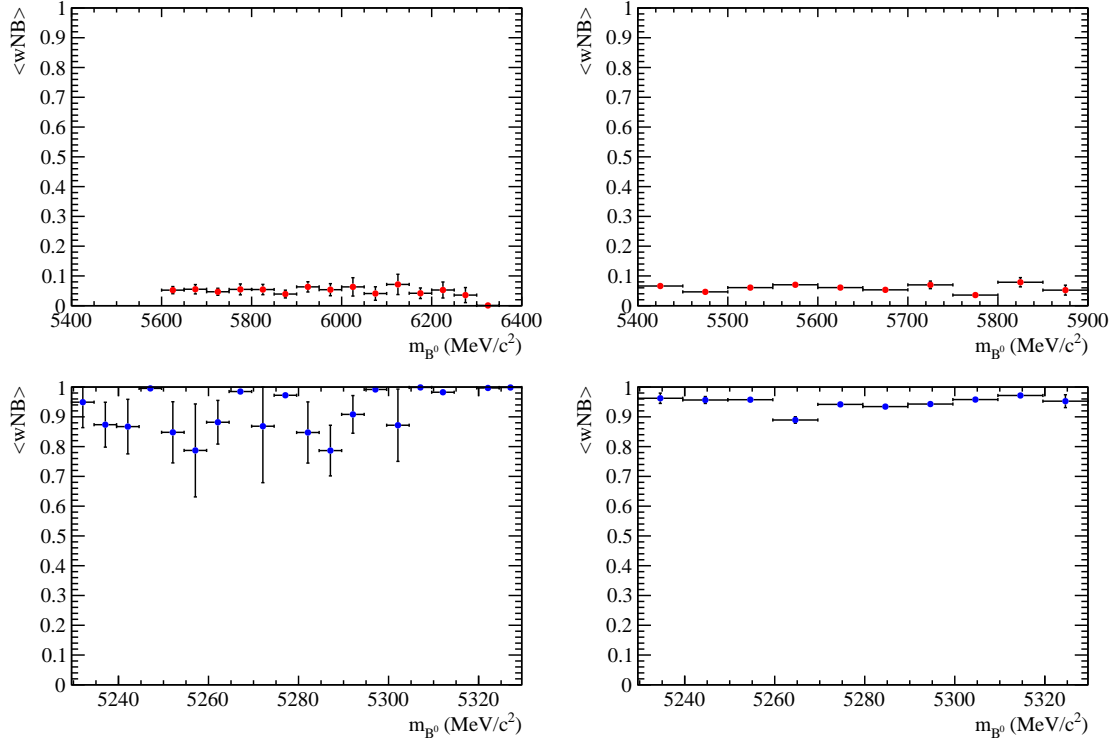


Figure 5.15: Average value of neural-network output as a function of B^0 mass for data sideband (top) and simulated signal (bottom) events for the electron (left) and muon (right) training.

$B^0 \rightarrow K^{*0}(J/\psi \rightarrow \ell^+\ell^-)$ branching fractions and the efficiency ratio as a function of the cut

$$N_S = N_{J/\psi(\ell\ell)} \cdot \frac{\mathcal{B}(S)}{\mathcal{B}(B^0 \rightarrow K^{*0}(J/\psi \rightarrow \ell^+\ell^-))} \cdot \frac{\varepsilon_S}{\varepsilon_{J/\psi(\ell\ell)}}.$$

2254 The number of background events is also derived from data by fitting the back-
 2255 ground in the lower- and upper-mass sidebands with an exponential function, and
 2256 extrapolating the residual yield in the signal region (Fig. 5.14). Because the back-
 2257 ground shape changes as a function of the requirement that is being optimised, the
 2258 sidebands are refitted for each considered cut value.

2259 The cut optimisation is performed in a signal mass window of ± 100 MeV/c² around
 2260 the nominal B^0 mass for muons, and between 5000 and 5400 MeV/c² for electrons.
 2261 The average result of the k-fold optimisations is taken as the nominal requirement.
 2262 The variation of the signal and background efficiency, signal purity and figure-of-
 2263 merit as a function of the neural-network output requirement for the central- q^2 is

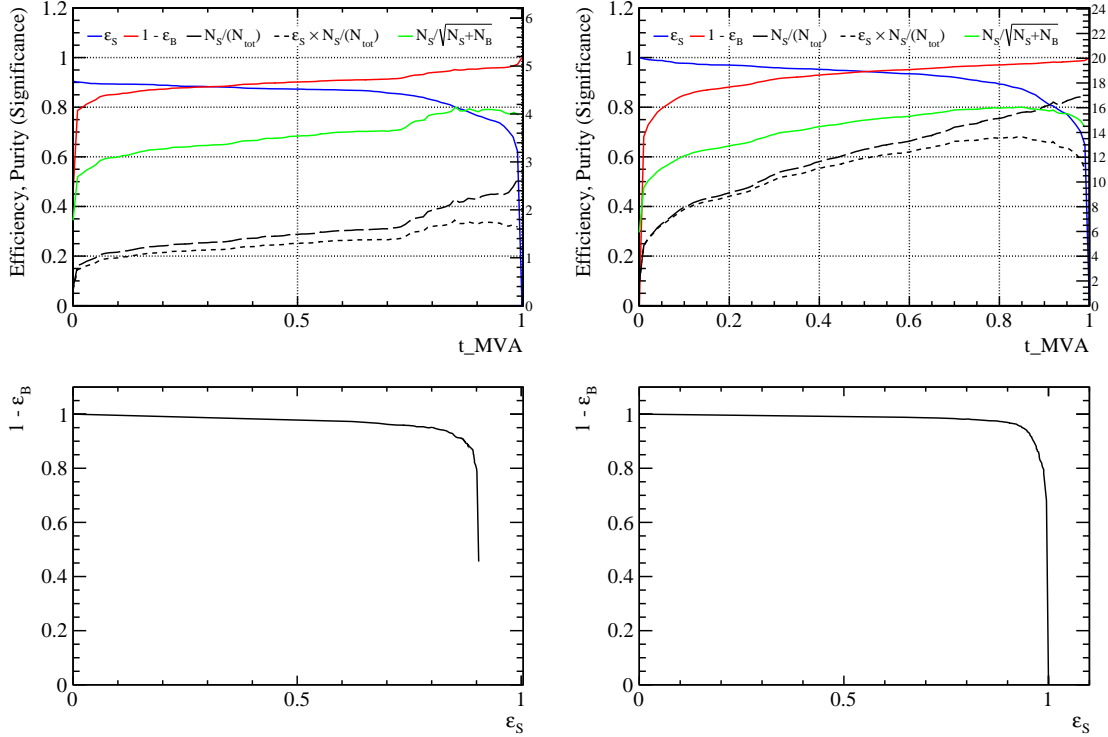


Figure 5.16: (top) Dependence of figure-of-merit on the requirement on neural network output. (bottom) Signal efficiency versus background rejection. Plots correspond to the electron (left) and muons (right) samples.

2264 shown in Fig. 5.16 together with curves of the background rejection as a function of
 2265 the signal efficiency. After full selection about $\sim 3\%$ of events still contain multiple
 2266 candidates which are removed at random keeping only a single candidate per event.

2267 5.7 Selection summary

2268 Table 5.6 summarises the requirements applied for each cut after stripping.

2269 5.8 Mass fits

2270 The signal yields are extracted using a simultaneous unbinned maximum likelihood
 2271 fit to the 4-body invariant mass, $m(K\pi\ell\ell)$, of the rare and normalisation

Table 5.6: Summary of the selection requirements. The last column indicates to which q^2 intervals the requirement is applied.

Type		Requirement	q^2
Quality	All tracks	$\chi^2/\text{ndf} < 3$	all
		$\text{GhostProb} < 0.4$	all
ID	K^{*0}	$ m(K\pi) - m_{K^{*0}}^{\text{PDG}} < 100 \text{ MeV}/c^2$	all
PID	K	$\text{ProbNNk} \cdot (1 - \text{ProbNNp}) > 0.05$	all
	π	$\text{ProbNNpi} \cdot (1 - \text{ProbNNk}) \cdot (1 - \text{ProbNNp}) > 0.1$	all
	μ	$\text{ProbNNmu} > 0.2$	all mm
	e	$\text{ProbNNe} > 0.2$	all e^+e^-
BKG	Swap	$ m((h \rightarrow \mu)\mu) - m_{J/\psi,(\psi(2S))}^{\text{PDG}} > 60 \text{ MeV}/c^2$	all
	$B^+ \rightarrow K^+\ell^+\ell^-$	$\max(m(K\ell\ell), m((\pi \rightarrow K)\ell\ell)) < 5.1 \text{ GeV}/c^2$	all
	$B_s^0 \rightarrow \phi\ell^+\ell^-$	$m(K(\pi \rightarrow K)) > 1040 \text{ MeV}/c^2$	all
	$B^0 \rightarrow D^-e^+\nu$	$ \cos \theta_\ell < 0.8$	except ee high-
	$B^0 \rightarrow K^{*0}\gamma$	$\sigma_z(e^+e^-) < 30 \text{ mm}$	except $\gamma(ee)$
	Comb	$\text{NNout} > 0.68$	$\mu\mu$ low-
		$\text{NNout} > 0.64$	ee low-
		$\text{NNout} > 0.85$	$\mu\mu$ central-
		$\text{NNout} > 0.97$	ee central-
		$\text{NNout} > 0.40$	$\mu\mu$ high-
		$\text{NNout} > 0.93$	ee high-
		$\text{NNout} > 0.06$	$J/\psi(\mu\mu)$
		$\text{NNout} > 0.20$	$J/\psi(ee)$
		$\text{NNout} > 0.16$	$\gamma(ee)$
		$\text{NNout} > 0.68$	$\psi(2S)(ee)$
	Comb, part-reco	$m_{\text{BCM}} > 4680 + 31 \cdot \log(\chi_{\text{FD}}^2)$	ee low-
		$m_{\text{BCM}} > 4437 + 64 \cdot \log(\chi_{\text{FD}}^2)$	ee central-
		$m_{\text{BCM}} > 3380 + 140 \cdot \log(\chi_{\text{FD}}^2)$	$\gamma(ee)$

samples. The simultaneous fit allows to share parameters e.g. those describing data-simulation differences. The yields of the rare channels are parameterised as a function of the corresponding J/ψ yields as

$$N_{\ell\ell}(r_{\ell\ell}, N_{J/\psi}) = N_{J/\psi} \cdot \varepsilon^{\text{rel}} \cdot r_{\ell\ell}, \quad (5.10)$$

where ε^{rel} is the relative efficiency between the rare and resonant channels (given in Tab. 5.10). Consequently, $r_{\ell\ell}$ corresponds to the efficiency corrected ratio of the

2277 raw rare and resonant yields:

$$R_{\ell\ell} = \frac{N_{\ell\ell}/\varepsilon^{\ell\ell}}{N_{J/\psi}/\varepsilon^{J/\psi(\ell\ell)}}. \quad (5.11)$$

2278 The two ratios, R_{ee} and $R_{\mu\mu}$, are then used to determine the $R_{K^{*0}}$ quantity, as
2279 described in Sec. 5.11. The following subsections contain a description of the line
2280 shapes used to model the signal and background components in each sample.

2281 5.8.1 Muon channels

2282 For the rare and resonant $\mu\mu$ channels the fitted variable is the $m(K\pi\mu\mu)$ invariant
2283 mass coming from a kinematic fit where all vertices are required to point to
2284 their mother particle. In the resonant case it is beneficial to also constrain the the
2285 dimuon mass to the known J/ψ mass. The effect of the kinematical constraint is
2286 to improve the mass resolution by roughly a factor of 2, which results in a more
2287 stable fit. Furthermore, mis-reconstructed background candidates are pushed away
2288 from the B^0 peak, which allows to use a wider mass window to better constrain the
2289 combinatorial background slope. The mass spectrum is fitted in the range 5150–
2290 5800 MeV/ c^2 with the lower limit chosen to totally exclude partially reconstructed
2291 background. As it is not needed to model partially reconstructed backgrounds in the
2292 fit this also eliminates the systematic uncertainties associated with the knowledge
2293 of their shape.

2294 5.8.1.1 $B^0 \rightarrow K^{*0}(J/\psi \rightarrow \mu^+\mu^-)$ PDF

The signal PDF adopted to describe the reconstructed $m(K\pi\mu\mu)$ invariant mass of $B^0 \rightarrow K^{*0}(J/\psi \rightarrow \mu^+\mu^-)$ candidates is the sum of a Double Crystal Ball [98] (DCB) function with opposite-side tails and a Gaussian function with a common mean, μ :

$$\begin{aligned} \mathcal{P}_{\text{sig}}(m|\vec{\lambda}) = & f_{\text{CB1}} \cdot \mathcal{P}_{\text{CB}}(m|\mu, \sigma_1, \alpha_1, n_1) + \\ & f_{\text{CB2}} \cdot \mathcal{P}_{\text{CB}}(m|\mu, \sigma_2, \alpha_2, n_2) + (1 - f_{\text{CB1}} - f_{\text{CB2}}) \cdot \mathcal{P}_{\text{Gauss}}(m|\mu, \sigma_3), \end{aligned}$$

where f_{CBi} is the relative fraction of candidates falling in the i^{th} Crystal Ball function, σ_i is the width, α_i and n_i are the parameters controlling the power law tail of each CB, and σ_3 is the width of the Gaussian function.

As a first step, the parameters of the signal PDF are extracted by fitting the $m(K\pi\mu\mu)$ distribution on $B^0 \rightarrow K^{*0}(J/\psi \rightarrow \mu^+\mu^-)$ simulation and fixed for the fit to the data. Figure E.1 shows the fitted simulated distribution for the normalisation channel, while fits for the rare channel in the three q^2 bins are reported in Appendix E. In order to account for possible discrepancies in the invariant mass distribution between data and simulation, the mass is allowed to shift, $\mu \rightarrow \mu + m'$, and the widths are allowed to scale, $\sigma_i \rightarrow c \cdot \sigma_i$, where the scale factor c is common between the three σ s.

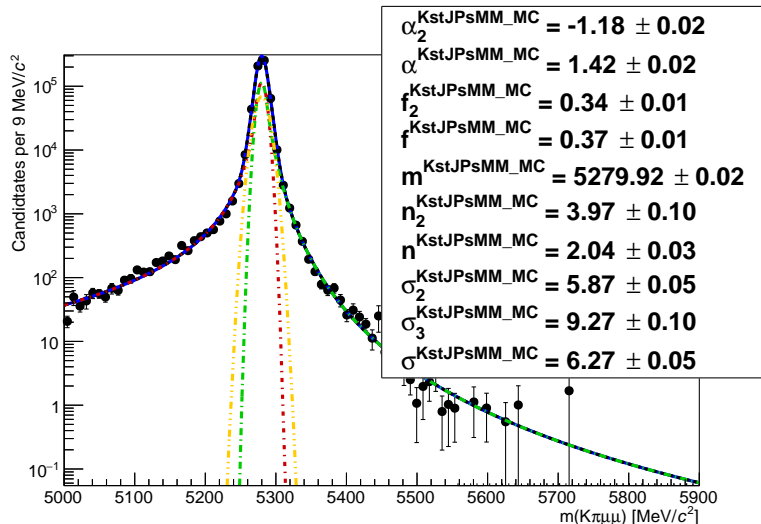


Figure 5.17: Fitted $m(K\pi\mu\mu)$ mass spectrum for $K^{*0}J/\psi$ simulated events.

2305

In summary, the signal PDF for the $J/\psi(\mu\mu)$ channel fit on data is defined as

$$\mathcal{P}_{J/\psi(\mu\mu)}(m|m', c) = f_{CB1} \cdot \mathcal{P}_{CB}(m|m', c) + f_{CB2} \cdot \mathcal{P}_{CB}(m|m', c) + (1 - f_{CB1} - f_{CB2}) \cdot \mathcal{P}_{\text{Gauss}}(m|m', c).$$

2306 where the only free parameters are the mass shift, m' and the width scale factor, c .

2307 The following backgrounds are considered:

- 2308 • *Combinatorial*: modelled with an exponential function;
- 2309 • $\Lambda_b^0 \rightarrow pK(J/\psi \rightarrow \mu^+\mu^-)$: described using simulated events to which the
2310 full selection selection and weights for the pK Dalitz plot are applied; this
2311 distribution has a broad shape under the signal peak and is smoothed using
2312 the `RooKeysPdf` class of the `ROOFIT` [114] package;
- 2313 • $B_s^0 \rightarrow K^{*0}(J/\psi \rightarrow \mu^+\mu^-)$: described using the same PDF adopted for the
2314 signal, but a different central value, μ , which is set at the B_s^0 nominal mass.
2315 The same shift m' is used as for the signal.

2316 5.8.1.2 $B^0 \rightarrow K^{*0}\mu^+\mu^-$ PDF

The signal PDF adopted to describe the reconstructed 4-body invariant mass of the $B^0 \rightarrow K^{*0}\mu^+\mu^-$ candidates is a DCB function with opposite-side tails with a common mean, μ . The parameters of the PDF are fixed to values obtained by fitting simulated candidates, separately in each q^2 interval. As for the charmonium channel, the mass is allowed to shift and the widths are allowed to scale with a common factor:

$$\mathcal{P}_{\text{mm},q^2}(m|m'_{q^2}, c_{q^2}) = f_{\text{core},q^2} \cdot \mathcal{P}_{\text{CB}}(m|m'_{q^2}, c_{q^2}) + (1 - f_{\text{core},q^2}) \cdot \mathcal{P}_{\text{CB}}(m|m'_{q^2}, c_{q^2}).$$

2317 where f_{core,q^2} is the relative fraction of candidates falling in the first Crystal Ball
2318 function, m'_{q^2} is the mass shift and c_{q^2} is the width scale. The subscript “ q^2 ” indicates
2319 that independent parameters are used for each q^2 interval.

2320 The background is described by an exponential function in all the three q^2 bins.

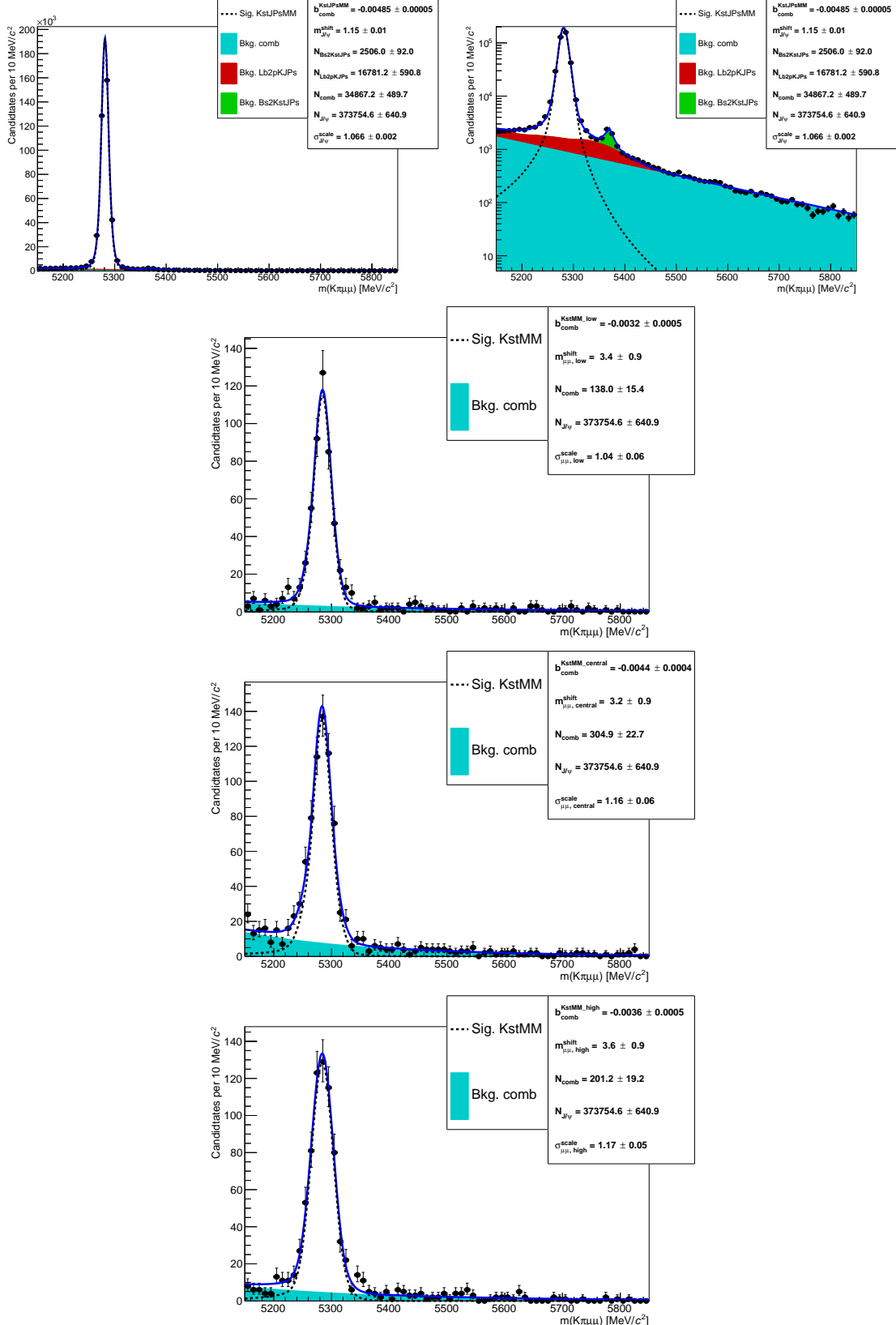


Figure 5.18: From top to bottom fitted $m(K\pi\mu\mu)$ invariant mass distributions for $K^{*0}J/\psi$ candidates and for rare candidates in the low-, central- and high- q^2 intervals. Dashed black lines represent the signal PDFs and filled shapes the background components.

2321 5.8.1.3 Summary

2322 In summary, the free parameters of the simultaneous fit to the $J/\psi(\mu\mu)$ and mm can-
2323 didates are the signal and background yields, the combinatorial background slopes,
2324 the mass shifts and the width scales. Figure 5.18 shows the results of the fit to the
2325 rare and resonant $\mu\mu$ candidates. Values of the fitted parameters are reported on
2326 the plots.

2327 5.8.2 Electron channels

2328 The reconstructed invariant mass of the B^0 depends on which L0 line triggered
2329 the event. For this reason, a simultaneous fit to the 4-body invariant mass of the
2330 $B^0 \rightarrow K^{*0}(J/\psi \rightarrow e^+e^-)$ and $B^0 \rightarrow K^{*0}e^+e^-$ channels in the three trigger categories
2331 is performed. In each trigger category, the $J/\psi(ee)$ and ee yields are extracted from
2332 the following signal channel categories:

- 2333 • $B^0 \rightarrow K^{*0}(J/\psi \rightarrow e^+e^-)$ (with a J/ψ mass constraint);
- 2334 • $B^0 \rightarrow K^{*0}e^+e^-$.

2335 Extra control channels are fit simultaneously:

- 2336 • $B^0 \rightarrow K^{*0}(\gamma \rightarrow e^+e^-)$ to constrain the yield of partially-reconstructed back-
2337 ground in the low- q^2 and the leakage of $B^0 \rightarrow K^{*0}\gamma$ into the low- q^2 ;
- 2338 • $B^0 \rightarrow K^{*0}(J/\psi \rightarrow e^+e^-)$ (without the J/ψ mass constraint) to constrain the
2339 leakage to $B^0 \rightarrow K^{*0}e^+e^-$ in the central- q^2 and the parameters that model
2340 residual data-simulation discrepancies;
- 2341 • $B^0 \rightarrow K^{*0}(\psi(2S) \rightarrow e^+e^-)$ (with a $\psi(2S)$ mass constraint) to constrain the
2342 leakage to lower and higher q^2 values.

When fitting the variable without a J/ψ mass constraint it is important to fit a wider mass range to better constrain the parameters modelling the radiative tail and the backgrounds; a mass window [4500,6200] MeV/ c^2 is used. The lower limit is given by the point in which the q^2 cut (at 6 GeV $^2/c^4$ to separate the rare and resonant channels) starts to affect the 4-body invariant mass distribution.

The invariant mass distributions are different depending on the trigger category and also on the number of bremsstrahlung photons recovered. Therefore, our samples are divided in three trigger categories, as described in Sec. 5.6.1, and three bremsstrahlung categories defined as:

- 0γ : candidates with no photon emitted
- 1γ : candidates with one photon by either of the electrons
- 2γ : candidates with one photon emitted by each electron

All samples are fitted simultaneously, which allows a better use of the available statistics as the simultaneous fit gathers information from the three categories at the same time. Furthermore, using this method the results for the three categories are naturally combined in a single r_{ee} ratio. The PDFs used to fit the invariant mass distributions are described in the next subsections.

5.8.2.1 Signal PDFs for the electron channels

As for the muon channels, simulated candidates are fitted first to constrain the shape parameters for the subsequent fit to data. The signal PDFs are built using the following method:

- Simulated $B^0 \rightarrow K^{*0}J/\psi(ee)$ and $B^0 \rightarrow K^{*0}ee$ events are divided in each trigger and bremsstrahlung category and an independent fit is performed to each sample. A different fit is also performed for the central, J/ψ and high q^2

Table 5.7: Percentages of events with 0, 1 and 2 emitted photons in the three trigger categories, obtained from simulated events.

Trigger	0γ (%)	1γ (%)	2γ (%)
$B^0 \rightarrow K^{*0} e^+ e^-$ low- q^2			
L0E	34.2	56.0	9.8
L0H	27.8	58.1	14.2
L0I	31.7	56.9	11.4
$B^0 \rightarrow K^{*0} e^+ e^-$ central- q^2			
L0E	29.2	50.0	20.8
L0H	23.6	50.5	26.0
L0I	28.5	49.9	21.6
$B^0 \rightarrow K^{*0} e^+ e^-$ high- q^2			
L0E	20.6	51.2	28.2
L0I	10.0	53.8	36.2
$B^0 \rightarrow K^{*0}(\gamma \rightarrow e^+ e^-)$			
L0E	40.4	59.6	–
L0H	32.2	67.8	–
L0I	39.3	60.7	–
$B^0 \rightarrow K^{*0}(J/\psi \rightarrow e^+ e^-)$			
L0E	29.0	50.1	20.8
L0H	18.9	51.3	29.8
L0I	26.9	51.7	21.4
$B^0 \rightarrow K^{*0}(\psi(2S) \rightarrow e^+ e^-)$			
L0E	27.2	51.3	21.5
L0H	17.4	51.5	31.2
L0I	22.0	55.0	23.0

intervals. In the case of the high- q^2 interval it is particularly important to keep signal tail parameters independent from J/ψ channel ones because, as can be seen in Fig. 5.19, the invariant mass distributions are significantly different for the two intervals.

- For each trigger category a PDF is built as the sum of the three PDFs of the bremsstrahlung categories:

$$\mathcal{P}^{\text{L0}}(m) = f_{0\gamma}^{\text{L0}} \mathcal{P}_{0\gamma}^{\text{L0}}(m) + f_{1\gamma}^{\text{L0}} \mathcal{P}_{1\gamma}^{\text{L0}}(m) + (1 - f_{0\gamma}^{\text{L0}} - f_{1\gamma}^{\text{L0}}) \mathcal{P}_{2\gamma}^{\text{L0}}(m), \quad (5.12)$$

where the $\mathcal{P}(m)_{n\gamma}^{\text{L0}}$ functions are the chosen PDFs for the trigger and bremsstrahlung categories and the $f_{n\gamma}^{\text{L0}}$ parameters are the relative fractions of events falling in each category.

- 2376 • Most parameters are fixed (details later) and the combined PDF, $P(m)$, is
 2377 used to fit real data divided only in trigger categories.

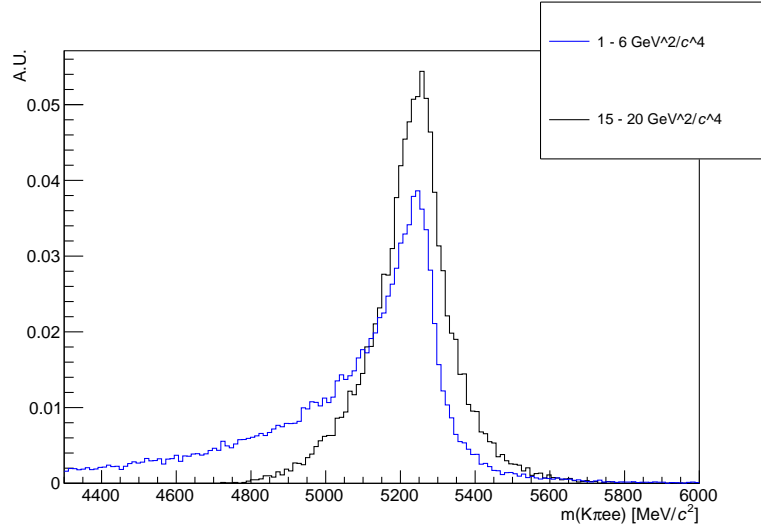


Figure 5.19: Simulated invariant mass of the $K\pi ee$ system in the $1.1 < q^2 < 6$ and $q^2 > 15$ GeV^2/c^4 intervals.

2378 The distribution of the $m(K\pi ee)$ mass in the 0γ category is characterised by a
 2379 sharp tail on the righthand side and is described with a Crystal Ball function (CB),
 2380 while the 1γ and 2γ categories are modelled using the sum of a Crystal Ball and a
 2381 Gaussian function (CBG) with independent parameters. In all the bremsstrahlung
 2382 categories the distribution of the 4-body invariant mass with a mass with the J/ψ
 2383 mass constraint is modelled using the sum of a DCB and a Gaussian functions as
 2384 done in the muon fit. To account for possible data-simulation discrepancies, the
 2385 mass (widths) of each trigger PDF is allowed to shift (scale), similarly to the muon
 2386 channels. However, due to the larger background contamination these parameters
 2387 are shared between the rare and the $B^0 \rightarrow K^{*0}(J/\psi \rightarrow e^+e^-)$ control sample (no
 2388 J/ψ mass constraint). The tail parameters are similar between the $J/\psi(ee)$ and the
 2389 central- q^2 but this is not the case at high- q^2 , as can be seen in Fig. 5.19, due to the
 2390 migration of candidates in the tail to lower reconstructed q^2 . For this reason the
 2391 initial parameters for each candidate type are obtained fitting a simulated sample
 2392 of the same candidate type.

2393 The $f_{n\gamma}^{L0}$ fractions have been shown to be in good agreement between resonant data

2394 and simulation and therefore they are fixed to the simulated values, separately for
2395 the normalisation channel and each q^2 interval. Table 5.7 lists the percentages of
2396 candidates with 0, 1 and 2 recovered photons for each trigger category.

2397 In summary the signal PDF for the fit on data is defined as:

$$\begin{aligned} \mathcal{P}_{sig}(m; c, m')^{trg} &= f_{0\gamma}^{L0} \mathcal{P}_{0\gamma}^{L0}(m; c, m') \\ &+ f_{1\gamma}^{L0} \mathcal{P}_{1\gamma}^{L0}(m; c, m') + (1 - f_{0\gamma}^{L0} - f_{1\gamma}^{L0}) \mathcal{P}_{2\gamma}^{L0}(m; c, m') \end{aligned} \quad (5.13)$$

2398 where the free parameters are: c , the scaling factor for the widths, and m' , the mass
2399 shift.

2400 5.8.2.2 Background PDFs for the electron channels

2401 This section reports the background components considered for each fitted sample.

2402 $B^0 \rightarrow K^{*0} e^+ e^-$ low- q^2

- 2403 • *Combinatorial*: described using an exponential function; the yield and slope
2404 parameters are free to vary in the fit;
- 2405 • *Partially-reconstructed* (hadronic): the shape is obtained from a $K_1^+(1270)$
2406 simulated samples as in the $B^0 \rightarrow K^{*0}(\gamma \rightarrow e^+ e^-)$ case; the fraction of
2407 partially-reconstructed candidates with respect to signal ones is expected to be
2408 very similar to that in $B^0 \rightarrow K^{*0}(\gamma \rightarrow e^+ e^-)$ and therefore the normalisation
2409 is fixed as:

$$N_{e^+ e^-, \text{low}}^{\text{part-reco}} = N_{e^+ e^-} \cdot \frac{N_{\gamma(ee)}^{\text{part-reco}}}{N_{\gamma(ee)}},$$

2405 where $N_{\gamma(ee)}^{\text{part-reco(hadronic)}}/N_{\gamma(ee)}$ is the fraction of the hadronic partially-reconstructed
2406 background relative to the signal yield in the $B^0 \rightarrow K^{*0}(\gamma \rightarrow e^+ e^-)$ channel;

- $B^0 \rightarrow K^{*0}\gamma$ leakage: the leakage from the $B^0 \rightarrow K^{*0}(\gamma \rightarrow e^+ e^-)$ decay
2407 in the low- q^2 region is modelled using a simulated candidates that pass the

low- q^2 requirements: the distribution is smoothed using a `RooKeysPdf`; the normalisation is fixed to the $B^0 \rightarrow K^{*0}(\gamma \rightarrow e^+e^-)$ yield, $N_{\gamma(ee)}$ as:

$$N_{e^+e^-, \text{low}}^{\text{leak}} = N_{\gamma(ee)} \cdot f_{\gamma(ee)}^{\text{leak, MC}},$$

where $f_{\gamma(ee)}^{\text{leak, MC}}$ is the fraction of $\gamma(ee)$ simulated candidates which leaks in the low- q^2 region.

$B^0 \rightarrow K^{*0}e^+e^-$ central- q^2

- *Combinatorial*: described using an exponential function; the yield and slope parameters are free to vary in the fit.
- *Partially-reconstructed* (hadronic): modelled in the same way as described for the low- q^2 but in this case the normalisation is left free to vary.
- $B^0 \rightarrow K^{*0}J/\psi$ leakage: the leakage from the J/ψ radiative tail into the central- q^2 interval is modelled by selecting simulated $B^0 \rightarrow K^{*0}(J/\psi \rightarrow e^+e^-)$ candidates which pass the central- q^2 requirements and smoothing the distributions with kernel estimation method. The normalisation is fixed to the $B_s^0 \rightarrow K^{*0}(J/\psi \rightarrow e^+e^-)$ yield, $N_{J/\psi ee}$, as:

$$N_{e^+e^-, \text{central}}^{\text{leak}} = N_{J/\psi ee} \cdot f_{J/\psi ee}^{\text{leak, MC}},$$

where $f_{J/\psi ee}^{\text{leak, MC}}$ is the fraction of $B^0 \rightarrow K^{*0}(J/\psi \rightarrow e^+e^-)$ simulated events reconstructed in the central- q^2 interval.

$B^0 \rightarrow K^{*0}e^+e^-$ high- q^2

- *Combinatorial*: modelled using a shape obtained by reversing the NN output cut on data, which has the effect of selecting background candidates instead of signal ones. Figure 5.21 shows the invariant mass distributions for different anti-cuts on the electron and muon samples at high- q^2 . The shapes are very

2421 similar between the two samples and as a function of the cut value. In order
2422 to have a larger statistics, the shape is taken from the muon sample with a
2423 tight NN output anti-cut at 0.1 and smoothed with a `RooKeysPdf`;

- 2424 • *Partially-reconstructed* (hadronic): the hadronic mis-reconstructed background
2425 is modelled in the same way as in the central- q^2 interval. The normalisation
2426 is left free to vary in the fit;
- $B^0 \rightarrow K^{*0}\psi(2S)$ leakage: the leakage from the $\psi(2S)$ radiative tail is modelled
 using simulated $B^0 \rightarrow K^{*0}(\psi(2S) \rightarrow e^+e^-)$ events in the high- q^2 region. The
 normalisation is fixed to the $B^0 \rightarrow K^{*0}(\psi(2S) \rightarrow e^+e^-)$ yield, $N_{\psi(2S)(ee)}$ as:

$$N_{e^+e^-, \text{high}}^{\text{leak}} = N_{\psi(2S)(ee)} \cdot f_{\psi(2S)(ee)}^{\text{leak, MC}},$$

2427 where $f_{\psi(2S)(ee)}^{\text{leak, MC}}$ is the fraction of $B^0 \rightarrow K^{*0}(\psi(2S) \rightarrow e^+e^-)$ simulated candi-
2428 dates leaking in the high- q^2 interval.

2429 $B^0 \rightarrow K^{*0}\gamma$

- *Combinatorial*: described using an exponential function; the yield and slope
 parameters are free to vary in the fit;
- *Partially-reconstructed* (hadronic): the shape is obtained from simulation sim-
 ilarly to the $J/\psi(ee)$ mode. However, as there are no inclusive samples for the
 rare channel, a sample including higher K^{*0} resonances, such as $K_1^+(1270)$,
 which is the dominant component, is used.; the yield is left free to vary;
- $B^0 \rightarrow K^{*0}e^+e^-$ leakage: as the $K^{*0}\gamma$ was added to the low- q^2 also the low- q^2
 leakage is added to $K^*\gamma$. The yield is constrained to the N_{ee}^{low} yield.

2438 $B^0 \rightarrow K^{*0}J/\psi$ and $B^0 \rightarrow K^{*0}\psi(2S)$

2439 The following backgrounds are considered for the fits to the invariant mass of $B^0 \rightarrow$
2440 $K^{*0}(J/\psi \rightarrow e^+e^-)$ candidates (with the J/ψ mass constraint):

- *Combinatorial*: described using an exponential function. The yield and slope parameters are free to vary in the fit;
- $\Lambda_b^0 \rightarrow pK(J/\psi \rightarrow e^+e^-)$: described using simulated events to which the full selection is applied. This distribution has a broad shape under the signal peak and is smoothed using a `RooKeysPdf`. The normalisation is constrained to the $\Lambda_b^0 \rightarrow pK(J/\psi \rightarrow \mu^+\mu^-)$ yield returned by the $\mu\mu$ fit after correcting for efficiency differences between final states with muons and electrons.
- $B_s^0 \rightarrow K^{*0}(J/\psi \rightarrow e^+e^-)$: described using the same PDF adopted for the signal, but a different central value, m_0 , which is set at the B_s^0 nominal mass. The normalisation is constrained to the $B^0 \rightarrow K^{*0}(J/\psi \rightarrow \mu^+\mu^-)$ yield returned by the $\mu\mu$ fit after correcting for efficiency differences between final states with muons and electrons;

The J/ψ mass constraint has the effect of pushing the partially-reconstructed background away from the peak outside the fit window. Therefore it does not need to be modelled. Instead the fit model for the variable without J/ψ mass constraint, used as control sample, includes further components:

- *Partially-reconstructed*: the partially-reconstructed background from both higher hadronic and $c\bar{c}$ resonances is modelled using inclusive $B^0 \rightarrow J/\psi X$ simulated events to which the full selection is applied. The invariant mass distributions of these candidates, shown in Fig. 5.20, is smoothed using a kernel estimation method and the yield is left free to vary;
- $B^0 \rightarrow K^{*0}\psi(2S)$ *leakage*: the leakage from the $\psi(2S)$ radiative tail into the J/ψ interval is modelled by selecting simulated $\psi(2S) \rightarrow e^+e^-$ which pass the requirements for J/ψ candidates. The normalisation is fixed to the $B^0 \rightarrow K^{*0}(\psi(2S) \rightarrow e^+e^-)$ yield, $N_{\psi(2S)(ee)}$, as:

$$N_{J/\psi(ee)}^{\text{leak}} = N_{\psi(2S)(ee)} \cdot f_{\psi(2S)(ee)}^{\text{leak, MC}},$$

²⁴⁶² where $f_{\psi(2S)(ee)}^{\text{leak, MC}}$ is the fraction of $B^0 \rightarrow K^{*0}(\psi(2S) \rightarrow e^+e^-)$ simulated events
²⁴⁶³ reconstructed in the J/ψ interval.

²⁴⁶⁴ For the fit to $B^0 \rightarrow K^{*0}(\psi(2S) \rightarrow e^+e^-)$, which includes a $\psi(2S)$ mass constraint,
²⁴⁶⁵ only the combinatorial background is considered and described using an exponential
²⁴⁶⁶ function.

²⁴⁶⁷ 5.8.2.3 Summary of the fit to the electron samples

²⁴⁶⁸ In summary, the free parameters in the fit to data are:

- ²⁴⁶⁹ • the $B^0 \rightarrow K^{*0}(J/\psi \rightarrow e^+e^-)$, $B^0 \rightarrow K^{*0}(\psi(2S) \rightarrow e^+e^-)$ and $B^0 \rightarrow K^{*0}(\gamma \rightarrow$
²⁴⁷⁰ $e^+e^-)$ yields in each trigger category;
- ²⁴⁷¹ • the r_{ee} ratio common to all trigger categories; one for the low, one for the
²⁴⁷² central- and one for the high- q^2 region;
- ²⁴⁷³ • one mass shift, m' , and one width scale factor, c , for the signal PDF common
²⁴⁷⁴ between $B^0 \rightarrow K^{*0}(J/\psi \rightarrow e^+e^-)$ and $B^0 \rightarrow K^{*0}e^+e^-$, but different for the
²⁴⁷⁵ three trigger categories and for $B^0 \rightarrow K^{*0}(\psi(2S) \rightarrow e^+e^-)$ and $B^0 \rightarrow K^{*0}(\gamma \rightarrow$
²⁴⁷⁶ $e^+e^-)$;
- ²⁴⁷⁷ • the yield and slope, when applicable (e.g. no slope at high- q^2), of the combi-
²⁴⁷⁸ natorial background in each trigger category and for each channel;
- ²⁴⁷⁹ • the yield of the backgrounds when not fixed as described in the previous sec-
²⁴⁸⁰ tion.

²⁴⁸¹ Fits to simulated $B^0 \rightarrow K^{*0}(J/\psi \rightarrow e^+e^-)$ candidates are shown in Appendix E,
²⁴⁸² while fits to real candidates are shown in Fig. 5.22 for the normalisation channel, in
²⁴⁸³ Fig. 5.23 for the rare channel and in Fig. 5.24 for the control channels. For simplicity
²⁴⁸⁴ the latter two figures show the sub of the three trigger categories, while the separate
²⁴⁸⁵ plots are reported in Appendix F, where fitted parameters are also reported on the

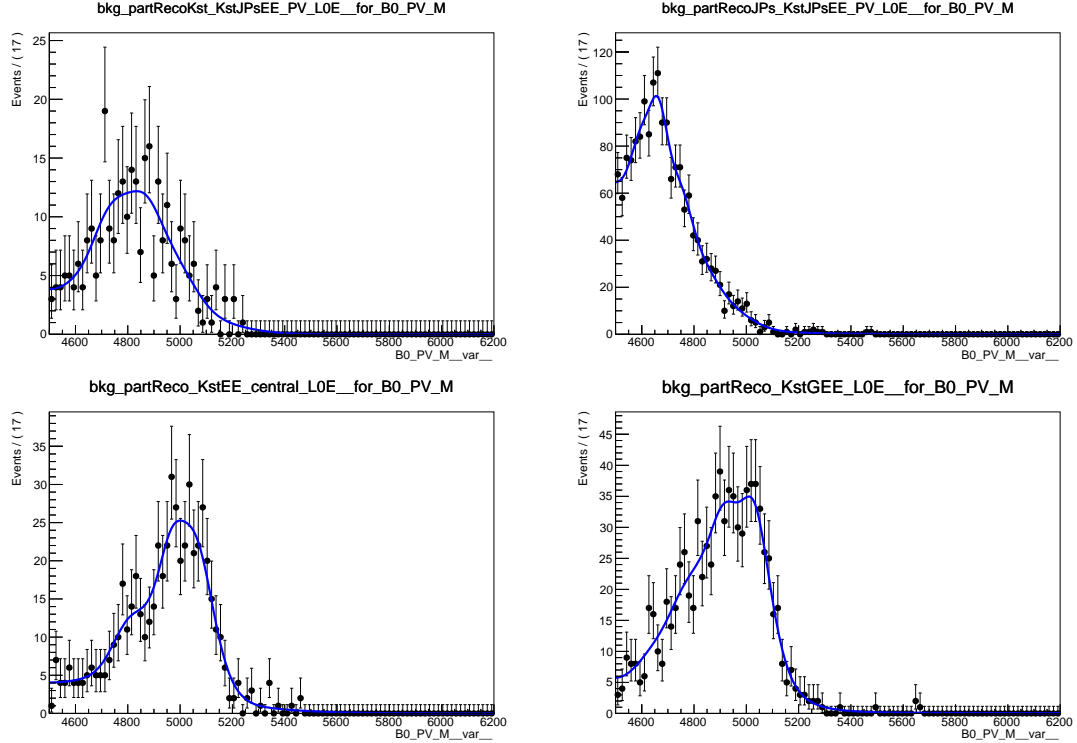


Figure 5.20: Distributions of the $m(K\pi ee)$ invariant mass for the (top left) hadronic and (top right) leptonic mis-reconstructed background to $B^0 \rightarrow K^{*0}(J/\psi \rightarrow e^+e^-)$. Distributions of the $m(K\pi ee)$ invariant mass for decays involving higher K^{*0} resonances in the (bottom left) central- q^2 interval and (bottom right) the $B^0 \rightarrow K^{*0}(\gamma \rightarrow e^+e^-)$ interval.

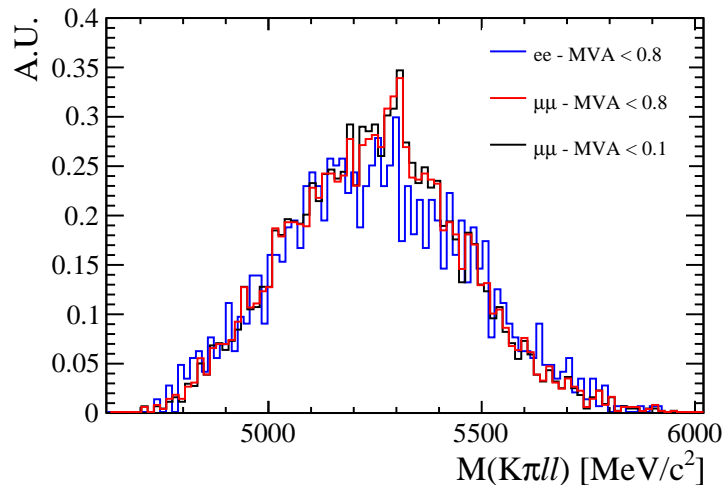


Figure 5.21: Distributions of the $m(K\pi\ell\ell)$ invariant mass for $B^0 \rightarrow K^{*0}\ell^+\ell^-$ candidates selected with a reversed cuts on the NN output.

Table 5.8: Raw yields of events found fitting invariant mass distributions of the rare and resonant events.

Sample	1.1–6 GeV^2/c^4	15–20 GeV^2/c^4	J/ψ
$\mu\mu$	626 ± 30	605 ± 27	333113 ± 604
ee L0E	132 ± 17	137 ± 27	48601 ± 326
ee L0H	31.7 ± 4.2	—	4324 ± 94
ee L0I	49.6 ± 6.5	—	12791 ± 172

plots. In the high- q^2 interval, above $15 \text{ GeV}^2/c^4$, the efficiency for the L0Hadron trigger becomes very low as the K^* has very low momentum. In this region only 9 candidates are found spread in the interval $4500 < m(K\pi ee) < 6000 \text{ MeV}/c^2$. Therefore only L0E and L0I triggered events are fitted in this region.

5.8.3 Event yields

Table 5.8 reports raw yields obtained from the fits described in the previous subsections. The values for the rare channels are not directly floating in the fits but, as described in Sec. 5.8, they are parameterised as a function of the number of resonant events found and the ratios R_{ee} and $R_{\mu\mu}$ between the resonant and rare branching fractions.

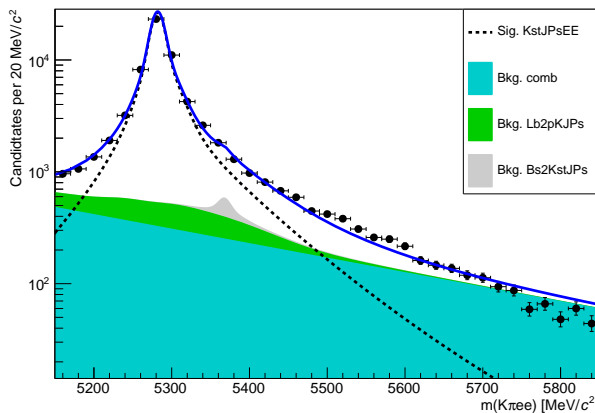


Figure 5.22: Fit to the mass constrained $m(K\pi ee)$ invariant mass of $B^0 \rightarrow K^{*0}(J/\psi \rightarrow e^+e^-)$ candidates. The dashed black line (shaded shapes) represents the signal (background) PDF.

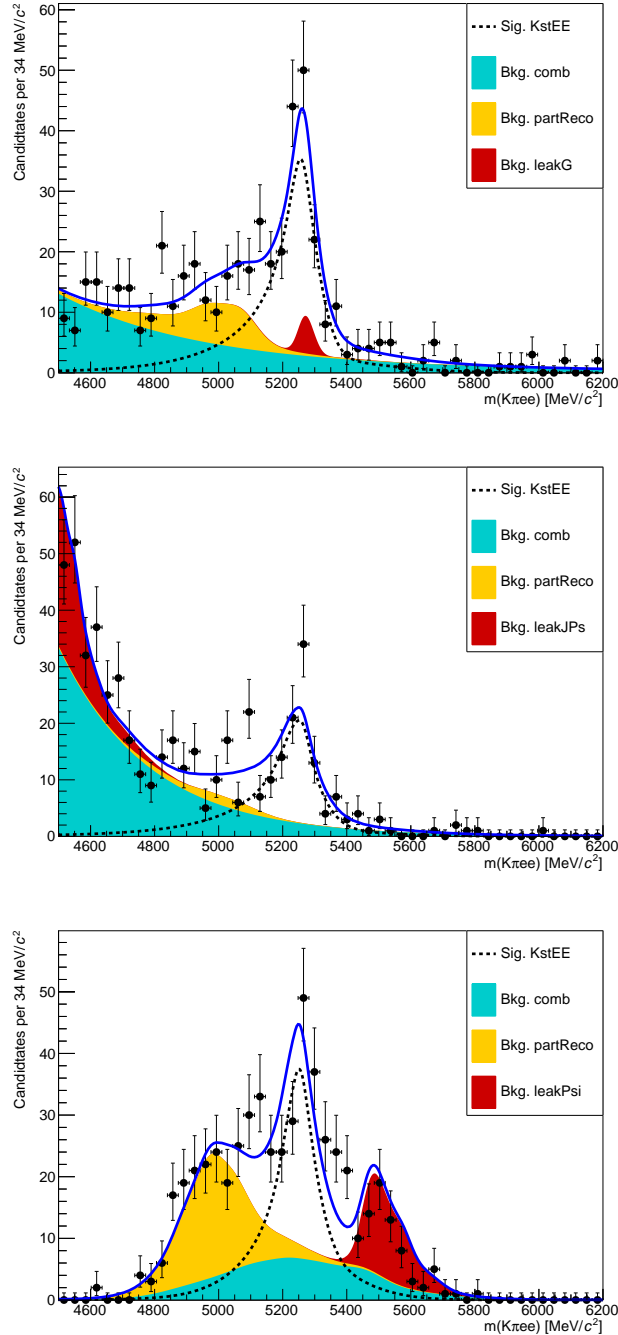


Figure 5.23: Fit to the $m(K\pi ee)$ invariant mass of $B^0 \rightarrow K^{*0} e^+ e^-$ candidates. From top to bottom for the low-, central- and high- q^2 intervals. The dashed black line (shaded shapes) represents the signal (background) PDF.

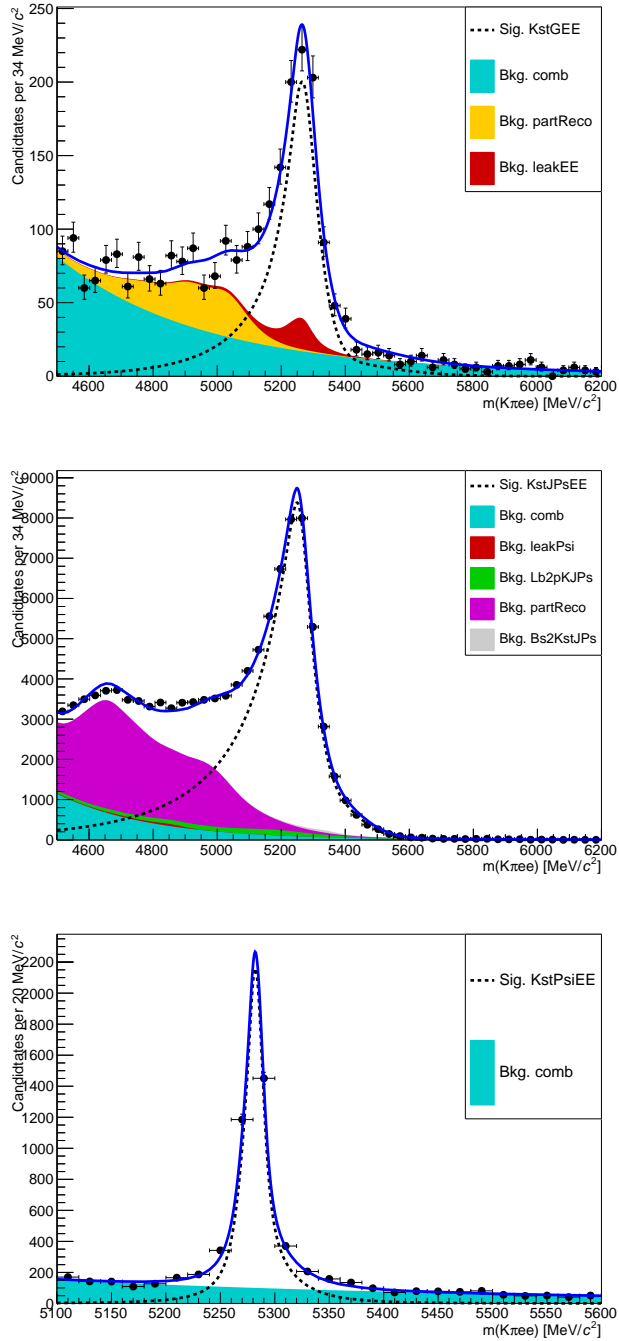


Figure 5.24: Fit to the $m(K\pi ee)$ invariant mass of control channel candidates. From top to bottom: invariant mass distribution without mass constraint of $B^0 \rightarrow K^{*0}(\gamma \rightarrow e^+e^-)$ and $B^0 \rightarrow K^{*0}(J/\psi \rightarrow e^+e^-)$ candidates and mass constrained mass of $B^0 \rightarrow K^{*0}(\psi(2S) \rightarrow e^+e^-)$ candidates. The dashed black line (shaded shapes) represents the signal (background) PDF.

²⁴⁹⁶ **5.9 Efficiency**

The efficiency for each of the decay channels is calculated according to the formula

$$\varepsilon^{tot} = \varepsilon^{\text{geom}} \cdot \varepsilon^{\text{reco|geom}} \cdot \varepsilon^{\text{PID|reco}} \cdot \varepsilon^{\text{trig|PID}} \cdot \varepsilon^{\text{MVA|trig}} \cdot \varepsilon^{\text{BCM|MVA}}$$

²⁴⁹⁷, where the first term is the efficiency to have final state particles in the LHCb
²⁴⁹⁸ detector acceptance; the second term ($\varepsilon^{\text{reco|geom}}$) carries information on reconstruc-
²⁴⁹⁹ tion and stripping efficiency; the third ($\varepsilon^{\text{PID|reco}}$) corresponds to the efficiency of
²⁵⁰⁰ the PID requirements; the fourth ($\varepsilon^{\text{trig|PID}}$) handles the trigger efficiency for those
²⁵⁰¹ events which are selected by the pre-selection process; and, finally, the latter term
²⁵⁰² deals with the efficiency of the neural network classifier. Reconstruction, trigger,
²⁵⁰³ MVA and BCM efficiencies are evaluated using simulated data samples with the
²⁵⁰⁴ trigger efficiency for $B^0 \rightarrow K^* J/\psi$ being cross-checked using the data-driven TIS-
²⁵⁰⁵ TOS method as described in Sec. 3.6.3. The PID efficiency is calculated with a
²⁵⁰⁶ data-driven method as described in Sec. 5.9.3.

²⁵⁰⁷ Absolute efficiencies for the muon and electron normalisation channel are reported in
²⁵⁰⁸ Tab. 5.9 and relative efficiencies between the rare and resonant channel, $\varepsilon(\ell\ell)/\varepsilon(J/\psi(\ell\ell))$,
²⁵⁰⁹ are listed in Tab. 5.10; these are the efficiencies which are used in the fit.

Table 5.9: Absolute efficiencies for the resonant ee and $\mu\mu$ channels.

ε	$\mu\mu$	ee		
		L0E	L0H	L0I
$\varepsilon^{\text{geom}}$	0.1598 ± 0.0005		0.1589 ± 0.0005	
$\varepsilon^{\text{reco geom}}$	0.0947 ± 0.0001		0.0603 ± 0.0001	
$\varepsilon^{\text{PID reco}}$	0.8148 ± 0.0000		0.8222 ± 0.0000	
$\varepsilon^{\text{trig PID}}$	0.7511 ± 0.0005	0.1939 ± 0.0005	0.0163 ± 0.0002	0.0707 ± 0.0003
$\varepsilon^{\text{MVA trig}}$	0.8944 ± 0.0004	0.8597 ± 0.0007	0.8983 ± 0.0006	0.8276 ± 0.0017
$\varepsilon^{\text{Total}}$	0.0083 ± 0.0000	0.0013 ± 0.0000	0.0001 ± 0.0000	0.0005 ± 0.0000

Table 5.10: Relative efficiencies, $\varepsilon^{rel} = \varepsilon^{\ell\ell}/\varepsilon^{J/\psi}$, for the ee and $\mu\mu$ channels in the central and high q^2 intervals.

ε	$\mu\mu$	ee		
		L0E	L0H	L0I
low-q^2				
ε^{geom}	1.0200 ± 0.0091		1.0429 ± 0.0084	
$\varepsilon^{reco geom}$	0.1309 ± 0.0010		0.1961 ± 0.0007	
$\varepsilon^{PID reco}$	0.9861 ± 0.0003		0.9718 ± 0.0001	
$\varepsilon^{trig PID}$	0.8103 ± 0.0048	0.6478 ± 0.0058	2.5556 ± 0.0455	1.2748 ± 0.0139
$\varepsilon^{MVA trig}$	0.9528 ± 0.0024	0.9568 ± 0.0014	0.9570 ± 0.0013	0.9463 ± 0.0030
$\varepsilon^{BCM MVA}$	–	0.9394 ± 0.0014	0.9492 ± 0.0013	0.9590 ± 0.0023
ε^{tot}	0.7810 ± 0.0168	0.5809 ± 0.0097	2.2685 ± 0.0514	1.1073 ± 0.0200
central-q^2				
ε^{geom}	1.0200 ± 0.0091		1.0429 ± 0.0084	
$\varepsilon^{reco geom}$	0.1891 ± 0.0012		0.1580 ± 0.0006	
$\varepsilon^{PID reco}$	0.9784 ± 0.0002		0.9672 ± 0.0001	
$\varepsilon^{trig PID}$	0.8925 ± 0.0038	0.7909 ± 0.0069	2.1344 ± 0.0439	1.1208 ± 0.0141
$\varepsilon^{MVA trig}$	0.9068 ± 0.0024	0.8397 ± 0.0024	0.8512 ± 0.0022	0.7946 ± 0.0054
$\varepsilon^{BCM MVA}$	–	0.8960 ± 0.0020	0.8978 ± 0.0020	0.9283 ± 0.0037
ε^{tot}	0.7171 ± 0.0124	0.8145 ± 0.0157	2.2235 ± 0.0595	1.0542 ± 0.0236
high-q^2				
ε^{geom}	1.0200 ± 0.0091		1.0429 ± 0.0084	
$\varepsilon^{reco geom}$	0.1172 ± 0.0009		0.0530 ± 0.0003	
$\varepsilon^{PID reco}$	1.0286 ± 0.0001		1.0113 ± 0.0002	
$\varepsilon^{trig PID}$	1.1122 ± 0.0038	1.5639 ± 0.0148	–	0.8090 ± 0.0195
$\varepsilon^{MVA trig}$	0.8986 ± 0.0027	0.8228 ± 0.0036	–	0.7201 ± 0.0115
ε^{tot}	0.7843 ± 0.0155	0.6063 ± 0.0131	–	0.2745 ± 0.0095

2510 5.9.1 Geometric efficiency

2511 In order to save disk space, simulated samples only contain decays with final daugh-
2512 ters in the LHCb detector acceptance, which can therefore be reconstructed. This
2513 corresponds to the requirement for each of the final particles to have polar angle θ
2514 between 10 and 400 mrad. The efficiency of this cuts is obtained using a generator
2515 level simulated sample.

2516 5.9.2 Reconstruction efficiency and bin migration

2517 The reconstruction efficiency is here defined as the efficiency to reconstruct each
2518 decay channel given that its daughters are into the geometrical acceptance of the
2519 detector. This includes both the probability that the final particles generate ob-
2520 servable signatures and the efficiency of all the pre-selection requirements described
2521 in Sec. 5.6, including those done to remove peaking backgrounds. The efficiency of
2522 the PID cuts is kept separate as it is known to be not well simulated and there are
2523 reliable data-driven methods which can be used to extract it (see Sec. 5.9.3).

2524 5.9.2.1 Bin migration

2525 It can happen that events generated in a q^2 interval are reconstructed in a different
2526 one, this is referred to as “bin migration” and can be due to two different effects.
2527 First of all, as the resolution of real detectors is not perfect, events close to the edges
2528 of the considered intervals can fall on the wrong side of the edge. This effect is only
2529 important in case of non-flat true distributions, as the amount of bin migration in the
2530 two directions is different. The second possible source of bin migration are systematic
2531 effects due, for example, to the presence of bremsstrahlung photons that cannot be
2532 recovered. It is particularly important to take into account the bin migration in the
2533 electron channels case because more photons are radiated from the final state and
2534 the mass resolution is worse. Figure 5.25 shows the response matrix for simulated

*B*⁰ → $K^{*0}e^+e^-$ events, which represents the correlation between reconstructed and generated q^2 . In the ideal case of perfect resolution this plot would look like a diagonal line and in case no bias is present its slope would be 1. Table 5.11 lists the net amounts of bin migration, M_{net} , in the considered q^2 intervals defined as:

$$M_{net} = N(\text{in} \rightarrow \text{in}) + N(\text{out} \rightarrow \text{in}) - N(\text{in} \rightarrow \text{out}) \quad (5.14)$$

where $N(\text{in} \rightarrow \text{in})$ is the number of candidates that are generated and reconstructed inside the considered interval, $N(\text{out} \rightarrow \text{in})$ the number of candidates that are generated outside the interval but reconstructed inside and $N(\text{in} \rightarrow \text{out})$ the number of candidates generated inside that fall outside. The reconstruction efficiency is calculated comparing generated to reconstructed samples and therefore already includes bin migration effects. Nevertheless, it is useful to single out this component to better assess the corresponding systematic uncertainty.

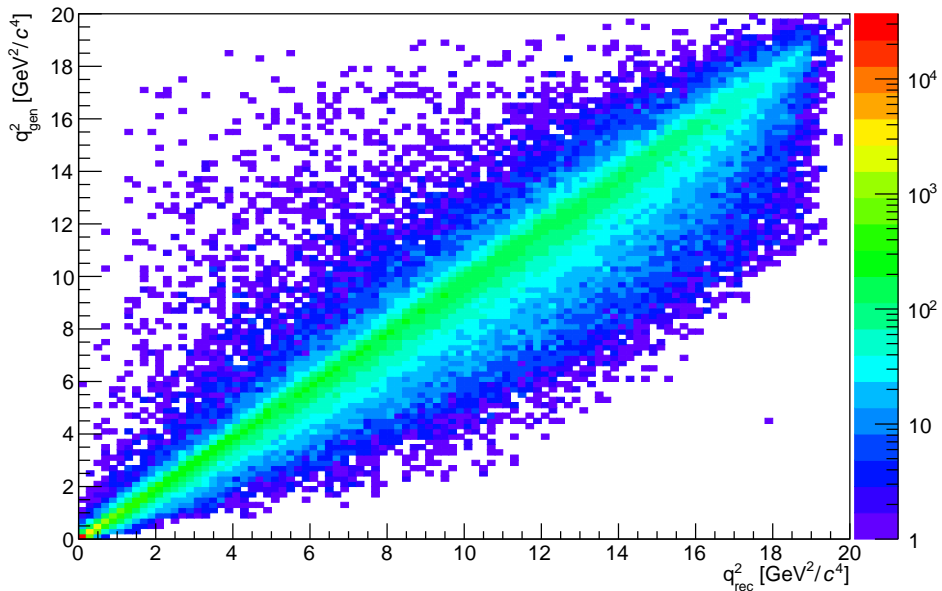


Figure 5.25: Generated versus reconstructed q^2 in simulated $B^0 \rightarrow K^* e^+ e^-$ events.

2546 5.9.3 PID efficiency

2547 The simulation is known not to reliably describe particle ID variables and therefore
2548 a data-driven method is used to obtain this efficiency component. This is done using
2549 the `PIDCalib` package described in Sec. 2.8.1. Furthermore, the same method is used
2550 to weight the simulation in order to calculate the MVA and trigger efficiencies. The
2551 package `PIDCalib` allows to divide the phase-space in intervals of quantities relevant
2552 for the determination of the PID efficiency and obtain a data-driven efficiency for
2553 each interval. For this analysis the phase-space is divided in equi-populated bins
2554 of momentum and pseudorapidity of the particle under study. Figure 5.26 shows
2555 performance tables for pions, kaons, muons and electrons. Once the efficiency tables
2556 are obtained for each particle, the total efficiency is calculated for each candidate
2557 as the product of the four final particles efficiencies. $\varepsilon^{ev} = \varepsilon_K \cdot \varepsilon_\pi \cdot \varepsilon_{\ell_1} \cdot \varepsilon_{\ell_2}$. Finally,
2558 as the decay channel under study generally has different kinematical distributions
2559 than the calibration sample, the total efficiency is found by averaging over simulated
2560 events.

$$\varepsilon_{PID} = \frac{1}{N} \sum_i^N \varepsilon_K(p_K^i, \eta_K^i) \cdot \varepsilon_\pi(p_\pi^i, \eta_\pi^i) \cdot \varepsilon_\ell(p_{\ell_1}^i, \eta_{\ell_1}^i) \cdot \varepsilon_K(p_{\ell_2}^i, \eta_{\ell_2}^i) \quad (5.15)$$

2561

2562 5.9.4 Trigger efficiency

2563 While the trigger efficiency for the muon channels is calculated using simulated
2564 events, for the electron channels a combination of simulation and data-driven meth-
2565 ods is used. The efficiency of the software stage, HLT, is always obtained from

Table 5.11: Net bin migration amounts (M_{net}) in the considered q^2 intervals. Positive values indicate “net in”, negative values “net out”.

Sample	low- q^2	central- q^2	J/ψ	high- q^2
$\mu\mu$	0.0002 ± 0.0001	-0.0021 ± 0.0003	0.0032 ± 0.0004	-0.0012 ± 0.0000
ee	0.0268 ± 0.0005	0.0663 ± 0.0009	-0.4277 ± 0.0048	-0.0445 ± 0.0003

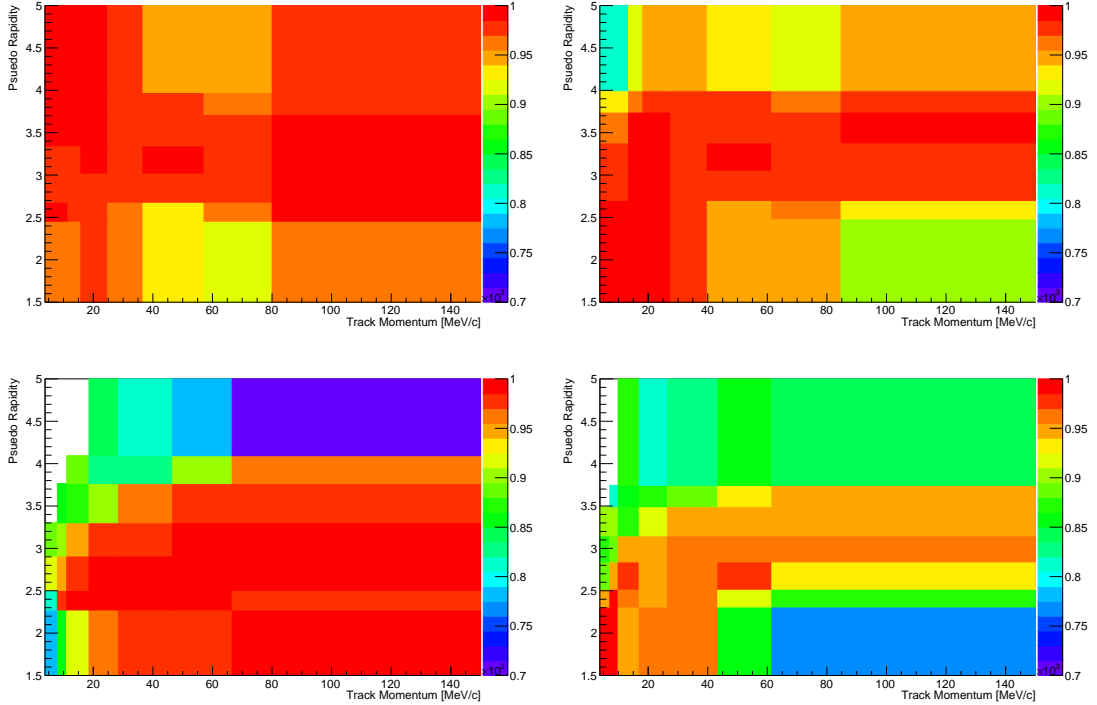


Figure 5.26: Performance tables obtained with data-driven methods for pions (top left), kaons (top right), muons (bottom left) and electrons (bottom right).

simulation, while the efficiency of the hardware stage, L0, is obtained using a data-driven method as described in the next subsection. For both muon and electron channels it is possible to use the resonant sample to cross-check the efficiency obtained using the simulation, as explained in Sec. 5.9.4.2.

5.9.4.1 Electron triggers

For the electron channels data is fitted separately in three trigger categories: L0E, L0H and L0I. Therefore the efficiency is calculated separately for each category. While the HLT (1 and 2) efficiency is always derived using simulated events, the L0Electron and L0Hadron efficiencies cannot be reliably modelled in simulation. In fact data-simulation discrepancies are caused by the ageing of the calorimeters, which is not simulated in the Monte Carlo. The ageing modifies the response of the calorimeters with time, which affects the L0 trigger efficiency. Therefore this must be calibrated using data driven-methods.

Tables of efficiencies are obtained applying the TISTOS method to a calibration sample. For each trigger category these tables contain the efficiency as a function of p_T of the considered particle and are given for different calorimeter regions as these have different properties (e.g. cell size) due to the different position with respect to the beam line. The considered regions are the inner and outer HCAL, and the inner, middle and outer ECAL. Figure 5.27 shows data-driven efficiencies for the L0Electron trigger in the three ECAL regions.

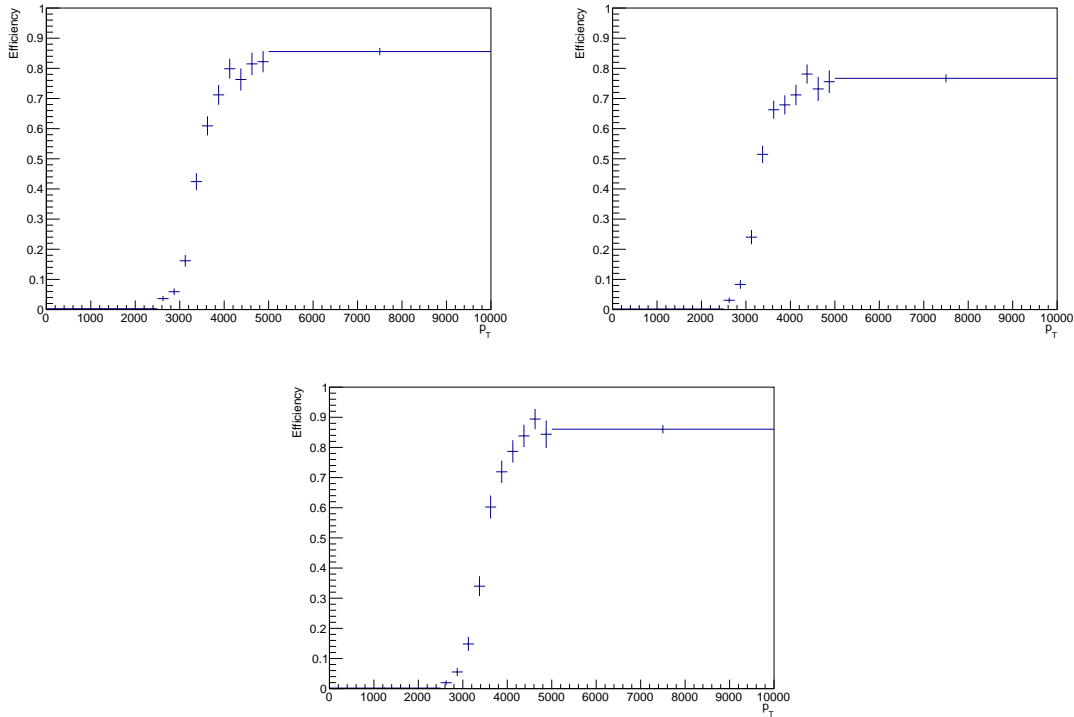


Figure 5.27: Data-driven L0Electron trigger efficiencies as a function of the transverse momentum of the electrons for the three ECAL regions.

2585

The probabilities of an event being triggered by L0Electron or L0Hadron are calculated for each candidate as:

$$P_{L0E} = \varepsilon(e^+) + \varepsilon(e^-) - \varepsilon(e^+)\varepsilon(e^-) \text{ and } P_{L0H} = \varepsilon(\pi) + \varepsilon(K) - \varepsilon(\pi)\varepsilon(K).$$

2586 The probability of TIS trigger is defined to be independent of the signal and therefore
2587 must be the same in the rare and resonant channels and cancel in their ratio.

2588 Then event by event efficiencies for the three trigger categories are defined to be
2589 exclusive in the following way:

- 2590 • L0E: $\varepsilon^{L0E} = P_{L0E}$, namely the probability that at least one electron triggered;
- 2591 • L0H: $\varepsilon^{L0H} = P_{L0H} \cdot (1 - P_{L0E})$, namely the probability that at least one hadron
2592 triggered but none of the electrons;
- 2593 • L0I: $\varepsilon^{L0I} = (1 - P_{L0H}) \cdot (1 - P_{L0E})$, namely the probability that neither the
2594 hadrons or the electrons in the candidate triggered. Note that in this case ε^{L0I}
2595 does not correspond to the efficiency of TIS trigger but to the probability that
2596 the event does not fall into the L0E or L0H categories.

2597 Finally, as in the PID case, the total efficiency is found averaging over all events of
2598 a simulated sample:

$$\varepsilon^{\text{trg}} = \frac{1}{N} \sum_i^N \varepsilon^{\text{trg}}(p_T^i) \quad (5.16)$$

2599 where “trg” is a label indicating the trigger category under consideration.

2600 5.9.4.2 TISTOS cross-check

2601 The efficiency obtained using the simulation is cross-checked applying the TISTOS
2602 method, already described in Sec. 3.6.3, to resonant data. For this purpose a sample
2603 of $B^0 \rightarrow K^{*0}(J/\psi \rightarrow e^+e^-)$ candidates triggered independent-of-signal (TIS) is used
2604 as control sample. As data also contains non negligible amounts of background
2605 a narrow interval around the peak, dominated by the signal, is selected and the
2606 $s\mathcal{P}\text{lot}$ method is used to remove residual background in the data sample. Results
2607 are shown in Tab. 5.12, where the efficiency obtained using the TISTOS method is
2608 compared between data and simulation. These are found to be in agreement for the
2609 muon channel, while they show deviations in the electron channels. In particular
2610 a significant discrepancy is found, for the L0I category, for which the procedure
2611 explained in Sec. 5.9.4.1 does not ensure a correct calibration. The table also reports

Table 5.12: Trigger efficiencies obtained using the TISTOS method on simulated and real $B^0 \rightarrow K^{*0} J/\psi (\rightarrow \ell^+ \ell^-)$ decays.

Sample	MC	Data	Correction factor
$J/\psi \rightarrow \mu\mu$	0.797 ± 0.002	0.803 ± 0.004	1.0073
$J/\psi \rightarrow ee$ L0E	0.268 ± 0.002	0.255 ± 0.004	0.9536
$J/\psi \rightarrow ee$ L0H	0.028 ± 0.001	0.026 ± 0.002	0.9269
$J/\psi \rightarrow ee$ L0I	0.017 ± 0.001	0.011 ± 0.001	0.6760

2612 a correction factor obtained according to the formula

$$f = 1 + \frac{\varepsilon_{data}^{\text{TISTOS}} - \varepsilon_{MC}^{\text{TISTOS}}}{\varepsilon_{MC}^{\text{TISTOS}}}, \quad (5.17)$$

2613 which can be used to correct the absolute resonant yields. On the other hand, even
2614 though discrepancies are present, they should cancel out in the ratio between the
2615 rare and J/ψ channels; only the residual discrepancy on this ratio is relevant for
2616 the measurement of $R_{K^{*0}}$. In order to check if discrepancies cancel out we need to
2617 obtain a data-driven efficiency also for the rare channels. To do this the TISTOS
2618 efficiency obtained on $B^0 \rightarrow K^{*0}(J/\psi \rightarrow \ell^+ \ell^-)$ candidates must be reweighted for
2619 the difference in the kinematics between the rare and resonant channels. This is
2620 done by determining the TISTOS efficiency as function of the maximum p_T of the
2621 particles that fired L0 (the leptons for LOElectron and LOMuon, the kaon and the
2622 pion for LOHadron, and all final state particles for LOGlobal). Results are shown
2623 in Fig. 5.28 and used to re-weight the distribution of rare simulated candidates.
2624 The ratios $\varepsilon_{\ell\ell}^{\text{tistos}} / \varepsilon_{J/\psi}^{\text{tistos}}$ obtained using the data-driven method and simulation are
2625 compared and found to be fully compatible. This means that, even though the
2626 TISTOS correction has an effect on the absolute efficiency of each channel, this
2627 becomes negligible on their ratio. Therefore, no correction due to this effect is
2628 applied for the calculation of the $R_{K^{*0}}$ ratio.

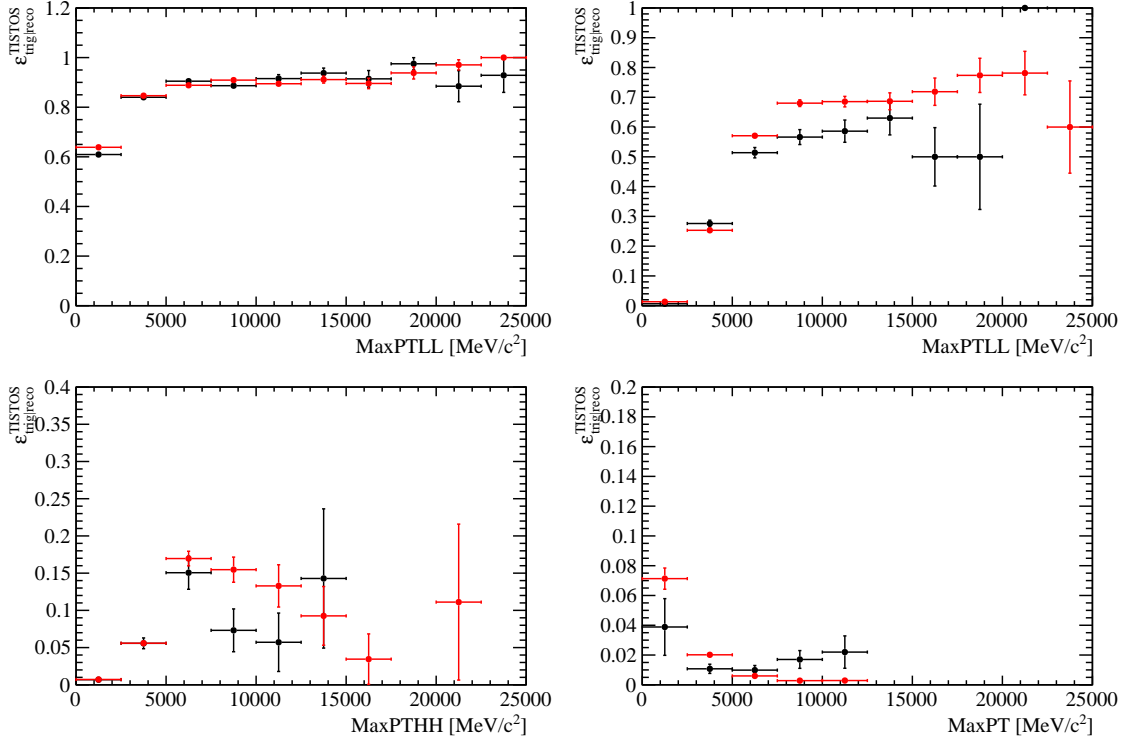


Figure 5.28: Trigger efficiency obtained applying the TISTOS method on $B^0 \rightarrow J/\psi K^*$ candidates as a function of the maximum p_T of the two muons (top left) of the two electrons for the L0E category (top right), the maximum p_T of p and π for L0H (bottom left) and the maximum p_T of all the final particles for L0I (bottom right).

2629 5.9.5 Neural networks and BCM efficiencies

2630 The neural network and BCM efficiencies are evaluated from fully weighted
 2631 simulated samples, and separately for each trigger category for the electron channels.
 2632 In order to check for biases one can compare the efficiency obtained using $B^0 \rightarrow$
 2633 $K^{*0}(J/\psi \rightarrow \ell^+\ell^-)$ events and rare $B^0 \rightarrow K^{*0}\ell^+\ell^-$ events in the same q^2 region
 2634 selected for the resonant case. The ratio between the two should be close to unity
 2635 with small deviations due the fact that the q^2 interval width is finite and the events
 2636 are distributed differently inside the interval. This ratio is found to be 0.997 ± 0.004
 2637 for the $\mu\mu$ channels and on average 0.981 ± 0.005 for the ee channels. Values for the
 2638 electron channels show a small deviation from one due to the very large q^2 interval
 2639 used to select the resonant channel ($6\text{--}11$ GeV $^2/c^4$).

Table 5.13: Summary of the relative percent systematic uncertainties on $R_{K^{*0}}$.

Source	low- q^2 (%)	central- q^2 (%)	high- q^2 (%)
Signal shape	1.65	1.10	2.92
Bremsstrahlung categories	0.04	0.06	0.37
Swap	0.30	0.12	0.13
$\Lambda_b^0 \rightarrow p K \ell^+ \ell^-$	0.25	0.28	0.77
Partially-reconstructed	0.11	4.13	0.10
Combinatorial	0.00	0.02	8.02
J/ψ leakage	0.06	0.01	0.10
$\psi(2S)$ leakage	0.03	0.01	2.00
RooKeysPdf ($\rho = 1.1$)	0.11	0.28	0.14
RooKeysPdf ($\rho = 1.3$)	0.10	0.24	0.49
Efficiency	0.65	0.74	0.83
TISTOS	2.47	2.30	2.80
Bin migration	0.69	1.43	1.19

2640 5.10 Systematic uncertainties

2641 This section describes the main sources of systematic uncertainties considered. Other
 2642 sources, which would matter in measurements of absolute quantities, cancel in the
 2643 ratio between the rare and resonant channels. A list of the systematic uncertainties
 2644 that are considered and their effect on the $R_{K^{*0}}$ ratio is summarised in Tab. 5.13.
 2645 The total uncertainty is evaluated by summing in quadrature the single components.

2646 5.10.1 Choice of signal and background PDFs

2647 There is a certain arbitrariness in the choice of PDFs to model signal and background
 2648 contributions in the invariant mass fits, which could translate in a bias on the final
 2649 result. The systematic uncertainty due to the parameterisation of line shapes is
 2650 studied in the following ways.

2652 For the signal PDF:

- 2653 • *Shape*: in the electron channels the PDF is changed from a Crystal Ball and
2654 Gaussian to a Double Crystal Ball. Modifying the PDF has a negligible effect
2655 in the muon modes, while it affects the electron ones. Furthermore the data-
2656 simulation discrepancy parameters (m' and c) are constrained using the $B^0 \rightarrow$
2657 $K^{*0}(\gamma \rightarrow e^+e^-)$ sample instead of $B^0 \rightarrow K^{*0}(J/\psi \rightarrow e^+e^-)$.
- 2658 • *Bremsstrahlung categories*: gaussian constraints are applied to the relative
2659 fractions of the bremsstrahlung categories, instead of fixing them to the values
2660 observed on simulation. This yields a $\sim \%$ systematic on $R_{K^{*0}}$ in the central-
2661 and high- q^2 region.

2662 For the background PDFs:

- 2663 • *Swaps*: a component that describes candidates where the particle identities are
2664 swapped is added both to the muon and electron resonant fits, and constrained
2665 to the number of candidates expected from simulation. This amounts to a $\sim \%$
2666 variation on $R_{K^{*0}}$ in the central- and high- q^2 region.
- 2667 • $\Lambda_b^0 \rightarrow pK J/\psi (\rightarrow e^+e^-)$: the normalisation is left free to vary. This results in
2668 a $\sim \%$ variation on $R_{K^{*0}}$ in the central- and high- q^2 region.
- 2669 • *Partially-reconstructed*: the yield of the mis-reconstructed background to $B^0 \rightarrow$
2670 $K^{*0}e^+e^-$ is left free to vary in the fit. This only applies to the central- q^2
2671 interval as this contribution is already free to vary in the high- q^2 range. This
2672 yields a $\sim \%$ systematic on $R_{K^{*0}}$.
- 2673 • *Combinatorial*: the PDF at high- q^2 is changed from an exponential (anti-MVA
2674 cut) to an anti-MVA cut (exponential) for the $\mu\mu$ (ee) mode. This amounts
2675 to a $\sim \%$ variation on $R_{K^{*0}}$ in the central- and high- q^2 region.
- 2676 • $\Lambda_b^0 \rightarrow pK\ell^+\ell^-$: this background is added to the fit to the rare channel and
2677 returns zero yield for both the muon and the electron samples. Therefore this
2678 yields no systematic uncertainty.

- 2679 • *Leakage*: gaussian constraints are applied to the amounts of $B^0 \rightarrow K^{*0}(J/\psi \rightarrow$
2680 $e^+e^-)$ leakage in the central- q^2 region and to the $B^0 \rightarrow K^{*0}(\psi(2S) \rightarrow e^+e^-)$
2681 leakage in the high- q^2 region, which are fixed in the default fit. This results in
2682 a $\sim \%$ variation on $R_{K^{*0}}$ in the central- and high- q^2 region.

2683 Furthermore in all case where a simulated sample is used and smoothed to obtain a
2684 PDF the kernel of the density estimation is varied by ± 0.1 from the value used in
2685 the nominal fit.

2686 5.10.2 Efficiency determinations

2687 The statistical uncertainty on the efficiency determinations is taken as the corre-
2688 sponding systematic uncertainty. The correlation among the electron trigger cate-
2689 gories is taken into account (e.g. L0E and L0H are anti-correlated). A further source
2690 of systematic uncertainty associated to the trigger efficiency is estimated using the
2691 data-simulation differences observed in Sec. 5.9.4.2. Ratios of efficiencies for the
2692 rare to resonant decays are found to be compatible between the electron and muon
2693 modes, indicating that the effect on $R_{K^{*0}}$ is negligible, but the statistical precision
2694 on the determinations is taken as an extra systematic uncertainty.

2695 5.10.3 Bin migration

2696 The determination of the reconstruction efficiency is affected by the knowledge of
2697 the amount of bin migration as explained in Sec. 5.9.2. This amount depends on
2698 the shape of the q^2 distribution, which in turn depends on the simulated $B^0 \rightarrow$
2699 $K^{*0}e^+e^-$ decay model. In order to asses this systematic, simulated samples are
2700 generated using different models corresponding to different form factors [115, 116].
2701 The q^2 distributions obtained using each model are compared with the ones obtained
2702 using the default one [117]. Figure 5.29 shows normalised ratios between these
2703 q^2 distributions and the default one, which are used to re-weight the simulation.

²⁷⁰⁴ The amount of bin migration is recalculated using the simulation reweighted to
²⁷⁰⁵ reproduce each model; Table 5.14 lists the percent variations obtained. The largest
²⁷⁰⁶ difference between two values is taken as systematic uncertainty. This results in a
²⁷⁰⁷ $\sim 5\%$ uncertainty for the central- q^2 interval and $\sim 11\%$ for the high- q^2 one, which
represent in both channel the biggest systematic uncertainty.

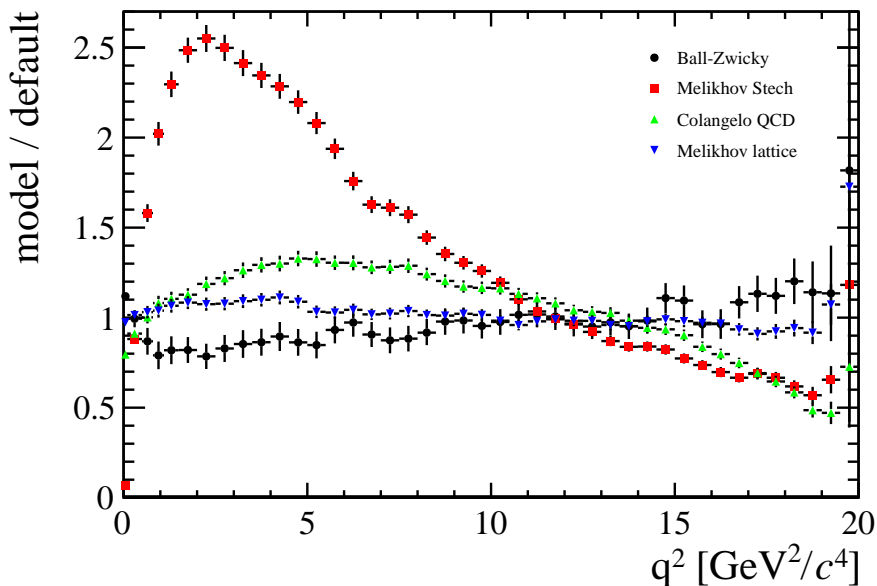


Figure 5.29: Ratios between the q^2 distributions obtained using different form factors models with respect to the default model.

Table 5.14: Percent variation on the bin migration amount obtained using different form factors models.

Model	low- q^2	central- q^2	central- q^2
Ball-Zwicky (6)	-0.3	1.0	0.2
Colangelo 2pt QCD (3)	0.4	0.4	0.8
Melikhov lattice (4)	0.1	-0.4	-0.4

²⁷⁰⁸

²⁷⁰⁹ 5.11 Result extraction

²⁷¹⁰ This section presents the procedure to obtain the $R_{K^{*0}}$ ratio together with methods
²⁷¹¹ to check robustness of the analysis.

²⁷¹² 5.11.1 $R_{J/\psi}$ sanity check

²⁷¹³ In order to cross-check the analysis procedure, the ratio between the measured
²⁷¹⁴ branching ratio of the electron and muon resonant channels is calculated:

$$r_{J/\psi} = \frac{\mathcal{B}(B^0 \rightarrow K^{*0} J/\psi (\rightarrow \mu^+ \mu^-))}{\mathcal{B}(B^0 \rightarrow K^{*0} J/\psi (\rightarrow e^+ e^-))} = \frac{\varepsilon_{J/\psi(\mu\mu)} \cdot N_{B^0 \rightarrow K^{*0} J/\psi (\rightarrow e^+ e^-)}}{\varepsilon_{J/\psi(ee)} \cdot N_{B^0 \rightarrow K^{*0} J/\psi (\rightarrow \mu^+ \mu^-)}}. \quad (5.18)$$

²⁷¹⁵ Unlike absolute branching fractions calculations, the determination of $R_{J/\psi}$ repre-
²⁷¹⁶ sents a better sanity test as it is not affected by uncertainties due to the knowledge
²⁷¹⁷ of the amount of collected luminosity, \mathcal{L} , or the fragmentation fraction, f_d , the
²⁷¹⁸ probability for a b quark to produce a B^0 meson. These quantities come with large
²⁷¹⁹ uncertainties but they cancel in the $r_{J/\psi}$ ratio.

²⁷²⁰ 5.11.2 $R_{K^{*0}}$

²⁷²¹ The ratio $R_{K^{*0}}$ is extracted by dividing the r_{ee} and $r_{\mu\mu}$ parameters described in
²⁷²² Sec. 5.8. These ratios are direct parameters of the fit but they can also be built from
²⁷²³ the yields in Tab. 5.8 and the efficiencies in Tab. 5.10. In summary the definition of
²⁷²⁴ the $R_{K^{*0}}$ ratio is the following:

$$R_{K^{*0}} = \frac{r_{ee}}{r_{\mu\mu}} = \frac{N_{ee}}{N_{J/\psi(ee)}} \cdot \frac{N_{J/\psi(\mu\mu)}}{N_{\mu\mu}} \cdot \frac{\varepsilon_{J/\psi(ee)}}{\varepsilon_{ee}} \cdot \frac{\varepsilon_{\mu\mu}}{\varepsilon_{J/\psi(\mu\mu)}}. \quad (5.19)$$

²⁷²⁵ As the electron ratio R_{ee} is a shared parameter in the simultaneous fit to the three
²⁷²⁶ electron categories its value is already a combination of the three samples.

2727

CHAPTER 6

2728

2729

Conclusions

2730

2731 In this work rare decays were analysed in order to look for hints of new physics using
2732 data recorded by the LHCb detector at centre-of-mass energies of 7 and 8 TeV and
2733 corresponding to a total integrated luminosity of 3.0 fb^{-1} .

2734 First, a measurement of the differential branching fraction of the rare $\Lambda_b^0 \rightarrow \Lambda\mu^+\mu^-$
2735 decay was performed together with the first measurement of angular observables
2736 for this decay. Evidence for the signal was found for the first time in the q^2 region
2737 below the square of the J/ψ mass in in the $0.1 < q^2 < 2.0 \text{ GeV}^2/c^4$ interval, where
2738 an enhanced yield is expected due to the vicinity of the photon pole. Due to a larger
2739 data sample and a better control of systematic, the uncertainty of the measurement
2740 in the $15 < q^2 < 20 \text{ GeV}^2/c^4$ interval are reduced by approximately a factor of three
2741 with respect to the previous LHCb measurements. The branching fraction measure-
2742 ments are compatible with SM predictions in the high- q^2 region, above the square
2743 of the J/ψ mass, and lie below the predictions in the low- q^2 region. In the angular
2744 analysis of $\Lambda_b^0 \rightarrow \Lambda\mu^+\mu^-$ decays two forward-backward asymmetries, in the dimuon

and $p\pi$ systems, were measured. The measurements of the A_{FB}^h observable are in good agreement with the SM predictions while for the A_{FB}^ℓ observable measurements are consistently above the SM predictions.

Secondly, an analysis is set up to test flavour universality between electrons and muons exploiting rare decays. A set of requirements is defined to select the rare and normalisation, $B^0 \rightarrow K^{*0}\ell^+\ell^-$ and $B^0 \rightarrow K^{*0}(J/\psi \rightarrow \ell^+\ell^-)$ modes in both electron and muons channels, which includes the definition of a multivariate classifier. Efficiencies are obtained for this selection for all channels. A study of the possible backgrounds to these channels is performed, which results in a set of requirements to lower their yield in the selected samples and a set of PDFs to model the remaining contributions in the invariant mass fits. Preliminary fits to the 4-body invariant mass distributions of all channels are performed. Finally, a preliminary study of the systematic uncertainties is presented and a set a procedure to obtain the result and check its robustness are defined. The results are currently blinded.

2759

2760

REFERENCES

2761

- [1] **LHCb** Collaboration, R. Aaij et al., *Differential branching fraction and angular analysis of $\Lambda_b^0 \rightarrow \Lambda\mu^+\mu^-$ decays*, *JHEP* **1506** (2015) 115, [[arXiv:1503.07138](https://arxiv.org/abs/1503.07138)].
- [2] **Particle Data Group** Collaboration, K. Olive et al., *Review of Particle Physics*, *Chin.Phys.* **C38** (2014) 090001.
- [3] **ATLAS** Collaboration, G. Aad et al., *Observation of a new particle in the search for the Standard Model Higgs boson with the ATLAS detector at the LHC*, *Phys. Lett.* **B716** (2012) 1–29, [[arXiv:1207.7214](https://arxiv.org/abs/1207.7214)].
- [4] **CMS** Collaboration, S. Chatrchyan et al., *Observation of a new boson at a mass of 125 GeV with the CMS experiment at the LHC*, *Phys. Lett.* **B716** (2012) 30–61, [[arXiv:1207.7235](https://arxiv.org/abs/1207.7235)].
- [5] L. Susskind, *Dynamics of Spontaneous Symmetry Breaking in the Weinberg-Salam Theory*, *Phys.Rev.* **D20** (1979) 2619–2625.
- [6] S. Glashow, *Partial Symmetries of Weak Interactions*, *Nucl.Phys.* **22** (1961) 579–588.
- [7] “Wikipedia.” https://en.wikipedia.org/wiki/Standard_Model. Accessed: 2016-02-26.
- [8] D. J. Gross and F. Wilczek, *Ultraviolet Behavior of Nonabelian Gauge Theories*, *Phys. Rev. Lett.* **30** (1973) 1343–1346.
- [9] **LHCb** Collaboration, R. Aaij et al., *Observation of the resonant character of the $Z(4430)^-$ state*, *Phys. Rev. Lett.* **112** (2014), no. 22 222002, [[arXiv:1404.1903](https://arxiv.org/abs/1404.1903)].

- [10] **LHCb** Collaboration, R. Aaij et al., *Observation of $J/\psi p$ resonances consistent with pentaquark states in $\Lambda_b^0 \rightarrow J/\psi K^- p$ decays*, [arXiv:1507.03414](#).
- [11] C. Wu, E. Ambler, R. Hayward, D. Hoppes, and R. Hudson, *Experimental Test of Parity Conservation in Beta Decay*, *Phys. Rev.* **105** (1957) 1413–1414.
- [12] F. Strocchi, *Spontaneous Symmetry Breaking in Local Gauge Quantum Field Theory: The Higgs Mechanism*, *Commun. Math. Phys.* **56** (1977) 57.
- [13] N. Cabibbo, *Unitary Symmetry and Leptonic Decays*, *Phys. Rev. Lett.* **10** (1963) 531–533. [,648(1963)].
- [14] M. Kobayashi and T. Maskawa, *CP Violation in the Renormalizable Theory of Weak Interaction*, *Prog. Theor. Phys.* **49** (1973) 652–657.
- [15] J. Charles, O. Deschamps, S. Descotes-Genon, H. Lacker, A. Menzel, et al., *Current status of the Standard Model CKM fit and constraints on $\Delta F = 2$ New Physics*, *Phys. Rev.* **D91** (2015), no. 7 073007, [[arXiv:1501.05013](#)].
- [16] F. Zwicky, *Spectral displacement of extra galactic nebulae*, *Helv. Phys. Acta* **6** (1933) 110–127.
- [17] M. Gavela and Hernandez, *Standard model CP violation and baryon asymmetry*, *Mod. Phys. Lett.* **A9** (1994) 795–810, [[hep-ph/9312215](#)].
- [18] M. Maltoni, *Status of three-neutrino oscillations*, *PoS EPS-HEP2011* (2011) 090.
- [19] B. T. Cleveland, T. Daily, R. Davis, Jr., J. R. Distel, K. Lande, C. K. Lee, P. S. Wildenhain, and J. Ullman, *Measurement of the solar electron neutrino flux with the Homestake chlorine detector*, *Astrophys. J.* **496** (1998) 505–526.
- [20] **Super-Kamiokande** Collaboration, Y. Fukuda et al., *Evidence for oscillation of atmospheric neutrinos*, *Phys. Rev. Lett.* **81** (1998) 1562–1567, [[hep-ex/9807003](#)].
- [21] **KamLAND** Collaboration, K. Eguchi et al., *First results from KamLAND: Evidence for reactor anti-neutrino disappearance*, *Phys. Rev. Lett.* **90** (2003) 021802, [[hep-ex/0212021](#)].
- [22] J. L. Feng, *Naturalness and the Status of Supersymmetry*, *Ann. Rev. Nucl. Part. Sci.* **63** (2013) 351–382, [[arXiv:1302.6587](#)].
- [23] B. Pontecorvo, *Neutrino Experiments and the Problem of Conservation of Leptonic Charge*, *Sov. Phys. JETP* **26** (1968) 984–988. [Zh. Eksp. Teor. Fiz. 53, 1717 (1967)].
- [24] Z. Maki, M. Nakagawa, and S. Sakata, *Remarks on the unified model of elementary particles*, *Prog. Theor. Phys.* **28** (1962) 870–880.

- [25] P. Fayet and S. Ferrara, *Supersymmetry*, *Phys.Rept.* **32** (1977) 249–334.
- [26] L. Randall and R. Sundrum, *A Large mass hierarchy from a small extra dimension*, *Phys.Rev.Lett.* **83** (1999) 3370–3373, [[hep-ph/9905221](#)].
- [27] J. R. Ellis, G. Gelmini, C. Jarlskog, G. G. Ross, and J. W. F. Valle, *Phenomenology of Supersymmetry with Broken R-Parity*, *Phys. Lett.* **B150** (1985) 142.
- [28] G. Isidori and D. M. Straub, *Minimal Flavour Violation and Beyond*, *Eur.Phys.J.* **C72** (2012) 2103, [[arXiv:1202.0464](#)].
- [29] A. J. Buras, *Minimal flavor violation*, *Acta Phys.Polon.* **B34** (2003) 5615–5668, [[hep-ph/0310208](#)].
- [30] T. Blake, T. Gershon, and G. Hiller, *Rare b hadron decays at the LHC*, *Ann.Rev.Nucl.Part.Sci.* **65** (2015) 8007, [[arXiv:1501.03309](#)].
- [31] A. J. Buras, D. Buttazzo, J. Giribach-Noe, and R. Knegjens, *Can we reach the Zeptouniverse with rare K and B_{s,d} decays?*, *JHEP* **1411** (2014) 121, [[arXiv:1408.0728](#)].
- [32] G. Hiller and M. Schmaltz, *R_K and future b → sℓℓ physics beyond the standard model opportunities*, *Phys.Rev.* **D90** (2014) 054014, [[arXiv:1408.1627](#)].
- [33] K. G. Chetyrkin, M. Misiak, and M. Munz, *Weak radiative B meson decay beyond leading logarithms*, *Phys.Lett.* **B400** (1997) 206–219, [[hep-ph/9612313](#)].
- [34] G. Buchalla, A. J. Buras, and M. E. Lautenbacher, *Weak decays beyond leading logarithms*, *Rev.Mod.Phys.* **68** (1996) 1125–1144, [[hep-ph/9512380](#)].
- [35] A. J. Buras, *Weak Hamiltonian, CP violation and rare decays*, [hep-ph/9806471](#).
- [36] M. Della Morte, J. Heitger, H. Simma, and R. Sommer, *Non-perturbative Heavy Quark Effective Theory: An application to semi-leptonic B-decays*, *Nucl.Part.Phys.Proc.* **261-262** (2015) 368–377, [[arXiv:1501.03328](#)].
- [37] C. W. Bauer, S. Fleming, D. Pirjol, and I. W. Stewart, *An Effective field theory for collinear and soft gluons: Heavy to light decays*, *Phys.Rev.* **D63** (2001) 114020, [[hep-ph/0011336](#)].
- [38] A. Khodjamirian, T. Mannel, A. Pivovarov, and Y.-M. Wang, *Charm-loop effect in B → K^(*)ℓ⁺ℓ⁻ and B → K^{*}γ*, *JHEP* **1009** (2010) 089, [[arXiv:1006.4945](#)].
- [39] **LHCb** Collaboration, R. Aaij et al., *Observation of a resonance in B⁺ → K⁺μ⁺μ⁻ decays at low recoil*, *Phys. Rev. Lett.* **111** (2013) 112003, [[arXiv:1307.7595](#)].

- [40] C. Bobeth, M. Gorbahn, T. Hermann, M. Misiak, E. Stamou, et al., $B_{s,d} \rightarrow l + l-$ in the Standard Model with Reduced Theoretical Uncertainty, *Phys. Rev. Lett.* **112** (2014) 101801, [[arXiv:1311.0903](#)].
- [41] CMS, LHCb Collaboration, V. Khachatryan et al., Observation of the rare $B_s^0 \rightarrow \mu^+ \mu^-$ decay from the combined analysis of CMS and LHCb data, *Nature* **522** (2015) 68–72, [[arXiv:1411.4413](#)].
- [42] LHCb Collaboration, R. Aaij et al., Differential branching fractions and isospin asymmetry of $B \rightarrow K^{(*)} \mu^+ \mu^+$ decays, *JHEP* **06** (2014) 133, [[arXiv:1403.8044](#)].
- [43] LHCb Collaboration, R. Aaij et al., Differential branching fraction and angular analysis of the decay $B_s^0 \rightarrow \phi \mu^+ \mu^-$, *JHEP* **07** (2013) 084, [[arXiv:1305.2168](#)].
- [44] LHCb Collaboration, R. Aaij et al., Differential branching fraction and angular analysis of the decay $B^0 \rightarrow K^{*0} \mu^+ \mu^-$, *JHEP* **08** (2013) 131, [[arXiv:1304.6325](#)].
- [45] LHCb Collaboration, R. Aaij et al., Measurement of form-factor-independent observables in the decay $B^0 \rightarrow K^{*0} \mu^+ \mu^-$, *Phys. Rev. Lett.* **111** (2013) 191801, [[arXiv:1308.1707](#)].
- [46] S. Descotes-Genon, J. Matias, and J. Virto, Understanding the $B \rightarrow K^* \mu^+ \mu^-$ Anomaly, *Phys. Rev.* **D88** (2013), no. 7 074002, [[arXiv:1307.5683](#)].
- [47] LHCb Collaboration, R. Aaij et al., Angular analysis of charged and neutral $B \rightarrow K \mu^+ \mu^-$ decays, *JHEP* **05** (2014) 082, [[arXiv:1403.8045](#)].
- [48] LHCb Collaboration, R. Aaij et al., Measurement of CP asymmetries in the decays $B^0 \rightarrow K^{*0} \mu^+ \mu^-$ and $B^+ \rightarrow K^+ \mu^+ \mu^-$, *JHEP* **1409** (2014) 177, [[arXiv:1408.0978](#)].
- [49] LHCb Collaboration, R. Aaij et al., Measurement of the $B^0 \rightarrow K^{*0} e^+ e^-$ branching fraction at low dilepton mass, *JHEP* **05** (2013) 159, [[arXiv:1304.3035](#)].
- [50] LHCb Collaboration, R. Aaij et al., Angular analysis of the $B^0 \rightarrow K^{*0} e^+ e^-$ decay in the low- q^2 region, *JHEP* **04** (Jan, 2015) 064. 18 p.
- [51] MEGA Collaboration, M. Ahmed et al., Search for the lepton family number nonconserving decay $\mu u^+ \rightarrow e^+ \gamma$, *Phys. Rev.* **D65** (2002) 112002, [[hep-ex/0111030](#)].
- [52] SINDRUM Collaboration, U. Bellgardt et al., Search for the Decay $\mu u^+ \rightarrow e^+ e^+ e^-$, *Nucl. Phys.* **B299** (1988) 1.
- [53] LHCb Collaboration, R. Aaij et al., Search for the lepton-flavour-violating decays $B_s^0 \rightarrow e^\pm \mu^\mp$ and $B^0 \rightarrow e^\pm \mu^\mp$, *Phys. Rev. Lett.* **111** (2013) 141801, [[arXiv:1307.4889](#)].

- [54] **LHCb** Collaboration, R. Aaij et al., *Searches for violation of lepton flavour and baryon number in tau lepton decays at LHCb*, *Phys. Lett.* **B724** (2013) 36, [[arXiv:1304.4518](#)].
- [55] W. J. Marciano, T. Mori, and J. M. Roney, *Charged Lepton Flavor Violation Experiments*, *Ann.Rev.Nucl.Part.Sci.* **58** (2008) 315–341.
- [56] L. Evans, *The LHC machine*, *PoS EPS-HEP2009* (2009) 004.
- [57] **LHCb** Collaboration, A. A. Alves Jr. et al., *The LHCb detector at the LHC*, *JINST* **3** (2008) S08005.
- [58] **LHCb** Collaboration, R. Aaij et al., *Measurement of $\sigma(pp \rightarrow b\bar{b}X)$ at $\sqrt{s} = 7$ TeV in the forward region*, *Phys.Lett.* **B694** (2010) 209–216, [[arXiv:1009.2731](#)].
- [59] M. Adinolfi et al., *Performance of the LHCb RICH detector at the LHC*, *Eur. Phys. J.* **C73** (2013) 2431, [[arXiv:1211.6759](#)].
- [60] A. A. Alves Jr. et al., *Performance of the LHCb muon system*, *JINST* **8** (2013) P02022, [[arXiv:1211.1346](#)].
- [61] **LHCb** Collaboration, R. e. a. Aaij, *LHCb technical design report: Reoptimized detector design and performance*, CERN-LHCC-2003-030.
- [62] **LHCb** Collaboration, R. e. a. Aaij, *LHCb Detector Performance*, *Int. J. Mod. Phys. A* **30** (Dec, 2014) 1530022. 82 p.
- [63] M. Pivk and F. R. Le Diberder, *SPlot: A Statistical tool to unfold data distributions*, *Nucl.Instrum.Meth.* **A555** (2005) 356–369, [[physics/0402083](#)].
- [64] R. Aaij et al., *The LHCb trigger and its performance in 2011*, *JINST* **8** (2013) P04022, [[arXiv:1211.3055](#)].
- [65] T. Sjöstrand, S. Mrenna, and P. Skands, *PYTHIA 6.4 physics and manual*, *JHEP* **05** (2006) 026, [[hep-ph/0603175](#)].
- [66] T. Sjostrand, S. Mrenna, and P. Z. Skands, *A Brief Introduction to PYTHIA 8.1*, *Comput. Phys. Commun.* **178** (2008) 852–867, [[arXiv:0710.3820](#)].
- [67] I. Belyaev et al., *Handling of the generation of primary events in GAUSS, the LHCb simulation framework*, *Nuclear Science Symposium Conference Record (NSS/MIC) IEEE* (2010) 1155.
- [68] D. J. Lange, *The EvtGen particle decay simulation package*, *Nucl. Instrum. Meth.* **A462** (2001) 152–155.
- [69] P. Golonka and Z. Was, *PHOTOS Monte Carlo: a precision tool for QED corrections in Z and W decays*, *Eur.Phys.J.* **C45** (2006) 97–107, [[hep-ph/0506026](#)].

- [70] **Geant4 collaboration** Collaboration, J. Allison, K. Amako, J. Apostolakis, H. Araujo, P. Dubois, et al., *Geant4 developments and applications, IEEE Trans.Nucl.Sci.* **53** (2006) 270.
- [71] M. Clemencic et al., *The LHCb simulation application, GAUSS: design, evolution and experience, J. Phys. Conf. Ser.* **331** (2011) 032023.
- [72] R. Brun, F. Rademakers, and S. Panacek, *ROOT, an object oriented data analysis framework, Conf.Proc. C000917* (2000) 11–42.
- [73] M. Feindt and U. Kerzel, *The NeuroBayes neural network package, Nucl.Instrum.Meth.* **A559** (2006) 190–194.
- [74] M. Feindt, *A Neural Bayesian Estimator for Conditional Probability Densities, physics/0402093*.
- [75] W. D. Hulsbergen, *Decay chain fitting with a Kalman filter, Nucl.Instrum.Meth.* **A552** (2005) 566–575, [physics/0503191].
- [76] H. W. Bertini, *Low-Energy Intranuclear Cascade Calculation, Phys. Rev.* **131** (1963) 1801–1821.
- [77] B. Andersson, G. Gustafson, and H. Pi, *The FRITIOF model for very high-energy hadronic collisions, Z. Phys.* **C57** (1993) 485–494.
- [78] **COMPASS** Collaboration, P. Abbon et al., *The COMPASS experiment at CERN, Nucl. Instrum. Meth.* **A577** (2007) 455–518, [hep-ex/0703049].
- [79] G. Hiller, M. Knecht, F. Legger, and T. Schietinger, *Photon polarization from helicity suppression in radiative decays of polarized Lambda(b) to spin-3/2 baryons, Phys.Lett.* **B649** (2007) 152–158, [hep-ph/0702191].
- [80] T. Mannel and S. Recksiegel, *Flavor changing neutral current decays of heavy baryons: The Case $\Lambda_b^0 \rightarrow \Lambda \gamma$, J.Phys.* **G24** (1998) 979–990, [hep-ph/9701399].
- [81] M. J. Aslam, Y.-M. Wang, and C.-D. Lu, *Exclusive semileptonic decays of $\Lambda_b^0 \rightarrow \Lambda l^+l^-$ in supersymmetric theories, Phys.Rev.* **D78** (2008) 114032, [arXiv:0808.2113].
- [82] Y.-m. Wang, Y. Li, and C.-D. Lu, *Rare Decays of $\Lambda_b^0 \rightarrow \Lambda \gamma$ and $\Lambda_b^0 \rightarrow \Lambda l^+l^-$ in the Light-cone Sum Rules, Eur.Phys.J.* **C59** (2009) 861–882, [arXiv:0804.0648].
- [83] C.-S. Huang and H.-G. Yan, *Exclusive rare decays of heavy baryons to light baryons: $\Lambda_b^0 \rightarrow \Lambda \gamma$ and $\Lambda_b^0 \rightarrow \Lambda l^+l^-$, Phys.Rev.* **D59** (1999) 114022, [hep-ph/9811303].
- [84] C.-H. Chen and C. Geng, *Rare $\Lambda_b^0 \rightarrow \Lambda l^+l^-$ decays with polarized lambda, Phys.Rev.* **D63** (2001) 114024, [hep-ph/0101171].

- [85] C.-H. Chen and C. Geng, *Baryonic rare decays of $\Lambda_b^0 \rightarrow \Lambda l^+l^-$* , *Phys.Rev.* **D64** (2001) 074001, [[hep-ph/0106193](#)].
- [86] C.-H. Chen and C. Geng, *Lepton asymmetries in heavy baryon decays of $\Lambda_b^0 \rightarrow \Lambda l^+l^-$* , *Phys.Lett.* **B516** (2001) 327–336, [[hep-ph/0101201](#)].
- [87] F. Zolfagharpour and V. Bashiry, *Double Lepton Polarization in $\Lambda_b^0 \rightarrow \Lambda l^+l^-$ Decay in the Standard Model with Fourth Generations Scenario*, *Nucl.Phys.* **B796** (2008) 294–319, [[arXiv:0707.4337](#)].
- [88] L. Mott and W. Roberts, *Rare dileptonic decays of Λ_b^0 in a quark model*, *Int.J.Mod.Phys.* **A27** (2012) 1250016, [[arXiv:1108.6129](#)].
- [89] T. Aliev, K. Azizi, and M. Savci, *Analysis of the $\Lambda_b^0 \rightarrow \Lambda l^+l^-$ decay in QCD*, *Phys.Rev.* **D81** (2010) 056006, [[arXiv:1001.0227](#)].
- [90] R. Mohanta and A. Giri, *Fourth generation effect on Λ_b decays*, *Phys.Rev.* **D82** (2010) 094022, [[arXiv:1010.1152](#)].
- [91] S. Sahoo, C. Das, and L. Maharana, *Effect of both Z and Z' -mediated flavor-changing neutral currents on the baryonic rare decay $\Lambda_b^0 \rightarrow \Lambda l^+l^-$* , *Int.J.Mod.Phys.* **A24** (2009) 6223–6235, [[arXiv:1112.4563](#)].
- [92] **CDF Collaboration** Collaboration, T. Aaltonen et al., *Observation of the Baryonic Flavor-Changing Neutral Current Decay $\Lambda_b \rightarrow \Lambda \mu^+ \mu^-$* , *Phys.Rev.Lett.* **107** (2011) 201802, [[arXiv:1107.3753](#)].
- [93] **CDF** Collaboration, S. Behari, *CDF results on $b \rightarrow s \mu \mu$ decays*, [arXiv:1301.2244](#).
- [94] **LHCb** Collaboration, R. Aaij et al., *Measurement of the differential branching fraction of the decay $\Lambda_b^0 \rightarrow \Lambda \mu^+ \mu^-$* , *Phys. Lett.* **B725** (2013) 25, [[arXiv:1306.2577](#)].
- [95] T. Gutsche, M. A. Ivanov, J. G. Korner, V. E. Lyubovitskij, and P. Santorelli, *Rare baryon decays $\Lambda_b \rightarrow \Lambda l^+l^- (l = e, \mu, \tau)$ and $\Lambda_b \rightarrow \Lambda \gamma$: differential and total rates, lepton- and hadron-side forward-backward asymmetries*, *Phys.Rev.* **D87** (2013) 074031, [[arXiv:1301.3737](#)].
- [96] **LHCb** Collaboration, R. Aaij et al., *Measurements of the $\Lambda_b^0 \rightarrow J/\psi \Lambda$ decay amplitudes and the Λ_b^0 polarisation in pp collisions at $\sqrt{s} = 7$ TeV*, *Phys.Lett.* **B724** (2013) 27, [[arXiv:1302.5578](#)].
- [97] G. Punzi, *Sensitivity of searches for new signals and its optimization*, in *Statistical Problems in Particle Physics, Astrophysics, and Cosmology* (L. Lyons, R. Mount, and R. Reitmeyer, eds.), p. 79, 2003. [physics/0308063](#).
- [98] T. Skwarnicki, *A study of the radiative cascade transitions between the Upsilon-prime and Upsilon resonances*. PhD thesis, Institute of Nuclear Physics, Krakow, 1986. DESY-F31-86-02.

- 3004 [99] W. Detmold, C.-J. D. Lin, S. Meinel, and M. Wingate, $\Lambda_b^0 \rightarrow \Lambda \mu^+ \mu^-$ form
 3005 factors and differential branching fraction from lattice QCD, *Phys. Rev.* **D87**
 3006 (2013), no. 7 074502, [[arXiv:1212.4827](https://arxiv.org/abs/1212.4827)].
- 3007 [100] **LHCb** Collaboration, R. Aaij et al., Precision measurement of the Λ_b^0 baryon
 3008 lifetime, *Phys.Rev.Lett.* **111** (2013) 102003, [[arXiv:1307.2476](https://arxiv.org/abs/1307.2476)].
- 3009 [101] T. Blake, S. Coquereau, M. Chrzaszcz, S. Cunliffe, C. Parkinson, K. Petridis,
 3010 and M. Tresch, The $B_0 \rightarrow K_0^* \mu \mu$ selection using $3fb^{-1}$ of LHCb data, Tech.
 3011 Rep. LHCb-INT-2013-058. CERN-LHCb-INT-2013-058, CERN, Geneva,
 3012 Nov, 2013.
- 3013 [102] F. James and M. Roos, *Minuit: A System for Function Minimization and*
 3014 *Analysis of the Parameter Errors and Correlations*, *Comput. Phys.*
 3015 *Commun.* **10** (1975) 343–367.
- 3016 [103] **LHCb** Collaboration, R. Aaij et al., Measurements of the $\Lambda_b^0 \rightarrow J/\psi \Lambda$ decay
 3017 amplitudes and the Λ_b^0 polarisation in pp collisions at $\sqrt{s} = 7$ TeV, *Phys.*
 3018 *Lett.* **B724** (2013) 27, [[arXiv:1302.5578](https://arxiv.org/abs/1302.5578)].
- 3019 [104] G. J. Feldman and R. D. Cousins, A Unified approach to the classical
 3020 statistical analysis of small signals, *Phys.Rev.* **D57** (1998) 3873–3889,
 3021 [[physics/9711021](https://arxiv.org/abs/physics/9711021)].
- 3022 [105] T. M. Karbach, *Feldman-Cousins Confidence Levels - Toy MC Method*,
 3023 [[arXiv:1109.0714](https://arxiv.org/abs/1109.0714)].
- 3024 [106] S. Meinel, Flavor physics with Λ_b baryons, *PoS LATTICE2013* (2014) 024,
 3025 [[arXiv:1401.2685](https://arxiv.org/abs/1401.2685)].
- 3026 [107] G. Hiller and F. Kruger, More model independent analysis of $b \rightarrow s$
 3027 processes, *Phys.Rev.* **D69** (2004) 074020, [[hep-ph/0310219](https://arxiv.org/abs/hep-ph/0310219)].
- 3028 [108] G. Hiller and M. Schmaltz, Diagnosing lepton-nonuniversality in $b \rightarrow s \ell \ell$,
 3029 *JHEP* **1502** (2015) 055, [[arXiv:1411.4773](https://arxiv.org/abs/1411.4773)].
- 3030 [109] **BaBar** Collaboration, J. Lees et al., Measurement of
 3031 Branching Fractions and Rate Asymmetries in the Rare Decays
 3032 $B \rightarrow K^{(*)} l^+ l^-$, *Phys.Rev.* **D86** (2012) 032012, [[arXiv:1204.3933](https://arxiv.org/abs/1204.3933)].
- 3033 [110] **BELLE** Collaboration, J.-T. Wei et al., Measurement of the
 3034 Differential Branching Fraction and Forward-Backward Asymmetry for
 3035 $B \rightarrow K^{(*)} l^+ l^-$, *Phys.Rev.Lett.* **103** (2009) 171801, [[arXiv:0904.0770](https://arxiv.org/abs/0904.0770)].
- 3036 [111] **LHCb** Collaboration, R. Aaij et al., Test of lepton universality using
 3037 $B^+ \rightarrow K^+ \ell^+ \ell^-$ decays, *Phys. Rev. Lett.* **113** (2014) 151601,
 3038 [[arXiv:1406.6482](https://arxiv.org/abs/1406.6482)].
- 3039 [112] “Lhcbl Loki twiki.”
 3040 <https://twiki.cern.ch/twiki/bin/view/LHCb/LoKiHybridFilters>.
 3041 Accessed: 2015-09-30.

- 3042 [113] “Probnn presentation at ppt meeting.” <https://indico.cern.ch/event/226062/contribution/1/material/slides/0.pdf>. Accessed: 2015-09-30.
- 3043
- 3044 [114] W. Verkerke and D. P. Kirkby, *The RooFit toolkit for data modeling*, *eConf C0303241* (2003) MOLT007, [[physics/0306116](#)].
- 3045
- 3046 [115] P. Ball and R. Zwicky, *New results on $B \rightarrow \pi, K, \eta$ decay form factors from light-cone sum rules*, *Phys. Rev. D* **71** (2005) 014015, [[hep-ph/0406232](#)].
- 3047
- 3048 [116] D. Melikhov and B. Stech, *Weak form-factors for heavy meson decays: An Update*, *Phys. Rev. D* **62** (2000) 014006, [[hep-ph/0001113](#)].
- 3049
- 3050 [117] A. Ali, P. Ball, L. T. Handoko, and G. Hiller, *A Comparative study of the decays $B \rightarrow (K, K^*)\ell^+\ell^-$ in standard model and supersymmetric theories*, *Phys. Rev. D* **61** (2000) 074024, [[hep-ph/9910221](#)].
- 3051
- 3052
- 3053 [118] J. Hrivnac, R. Lednický, and M. Smizanska, *Feasibility of beauty baryon polarization measurement in $\Lambda^0 J/\psi$ decay channel by ATLAS LHC*, *J.Phys.G* **G21** (1995) 629–638, [[hep-ph/9405231](#)].
- 3054
- 3055
- 3056 [119] W. Detmold and S. Meinel, *$\Lambda_b \rightarrow \Lambda \ell^+ \ell^-$ form factors, differential branching fraction, and angular observables from lattice QCD with relativistic b quarks*, [arXiv:1602.01399](#).
- 3057
- 3058

3059

APPENDIX A

3060

3061

Decay models

3062

A.1 $\Lambda_b^0 \rightarrow \Lambda \mu^+ \mu^-$ distribution

3064 The q^2 and angular dependancies of the $\Lambda_b^0 \rightarrow \Lambda \mu^+ \mu^-$ decays are modelled based on
 3065 Ref. [95], where the angular distribution for unpolarised Λ_b^0 production is defined as

$$\begin{aligned} W(\theta_\ell, \theta_B, \chi) &\propto \sum_{\lambda_1, \lambda_2, \lambda_j, \lambda'_j, J, J', m, m', \lambda_\Lambda, \lambda'_\Lambda, \lambda_p} h_{\lambda_1 \lambda_2}^m(J) h_{\lambda_1 \lambda_2}^{m'}(J') e^{i(\lambda_j - \lambda'_j)\chi} \\ &\times \delta_{\lambda_j - \lambda_\Lambda, \lambda'_j - \lambda'_\Lambda} \delta_{J, J'} d_{\lambda_j, \lambda_1 - \lambda_2}^J(\theta_\ell) d_{\lambda'_j, \lambda_1 - \lambda_2}^{J'}(\theta_\ell) H_{\lambda_\Lambda \lambda_j}^m(J) H_{\lambda'_\Lambda \lambda'_j}^{m'\dagger}(J') \\ &\times d_{\lambda_\Lambda \lambda_p}^{1/2}(\theta_B) d_{\lambda'_\Lambda \lambda_p}^{1/2}(\theta_B) h_{\lambda_p 0}^B h_{\lambda_p 0}^{B\dagger}. \end{aligned} \quad (\text{A.1})$$

3066 In this formula θ_ℓ and θ_B correspond to the lepton and proton helicity angles, χ
 3067 is angle between dimuon and Λ decay planes (for unpolarised production we are
 3068 sensitive only to difference in azimuthal angles), $d_{i,j}^J$ are Wigner d-functions and h ,
 3069 h^B and H are helicity amplitudes for virtual dimuon, Λ and Λ_b^0 decays. The sum
 3070 runs over all possible helicities with the dimuon being allowed in spin 0 and 1 states
 3071 (J and J'). The m and m' indices run over the vector and axial-vector current
 3072 contributions.

3073 The production polarisation is introduced by removing $e^{i(\lambda_j - \lambda'_j)\chi}$ from the expression,
 3074 swapping small Wigner d-functions $d_{i,j}^J$ to the corresponding capital ones $D_{i,j}^J$ which
 3075 are related as

$$D_{i,j}^J(\theta, \phi) = d_{i,j}^J(\theta) e^{i\phi(i-j)} \quad (\text{A.2})$$

and substitute spin density matrix for $\delta_{\lambda_j - \lambda_\Lambda, \lambda'_j - \lambda'_\Lambda} \delta_{JJ'}$. The spin density matrix itself is given by

$$\rho_{\lambda_j - \lambda_\Lambda, \lambda'_j - \lambda'_\Lambda} = \frac{1}{2} \begin{pmatrix} 1 + P_b \cos \theta & P_b \sin \theta \\ P_b \sin \theta & 1 - P_b \cos \theta \end{pmatrix}. \quad (\text{A.3})$$

Those changes lead to the formula

$$\begin{aligned} W(\theta\ell, \theta_B, \chi) &\propto \sum_{\lambda_1, \lambda_2, \lambda_j, \lambda'_j, J, J', m, m', \lambda_\Lambda, \lambda'_\Lambda, \lambda_p} h_{\lambda_1 \lambda_2}^m(J) h_{\lambda_1 \lambda_2}^{m'}(J') \\ &\times \rho_{\lambda_j - \lambda_\Lambda, \lambda'_j - \lambda'_\Lambda} D_{\lambda_j, \lambda_1 - \lambda_2}^J(\theta\ell, \phi_L) D_{\lambda'_j, \lambda_1 - \lambda_2}^{J'}(\theta\ell, \phi_L) H_{\lambda_\Lambda \lambda_j}^m(J) H_{\lambda'_\Lambda \lambda'_j}^{m'\dagger}(J') \\ &\times D_{\lambda_\Lambda \lambda_p}^{1/2}(\theta_B, \phi_B) D_{\lambda'_\Lambda \lambda_p}^{1/2}(\theta_B, \phi_B) h_{\lambda_p 0}^B h_{\lambda_p 0}^{B\dagger}. \end{aligned} \quad (\text{A.4})$$

The lepton amplitudes come directly from Ref. [95], eq. 3. The Λ decay amplitudes are related to the Λ decay asymmetry parameter as

$$\alpha_\Lambda = \frac{|h_{\frac{1}{2}0}^B|^2 - |h_{-\frac{1}{2}0}^B|^2}{|h_{\frac{1}{2}0}^B|^2 + |h_{-\frac{1}{2}0}^B|^2}. \quad (\text{A.5})$$

Finally, the Λ_b^0 decay amplitudes receive contributions from vector and axial-vector currents and can be written as

$$H_{\lambda_2, \lambda_j}^m = H_{\lambda_2, \lambda_j}^{Vm} - H_{\lambda_2, \lambda_j}^{Am}. \quad (\text{A.6})$$

Finally, the remaining amplitudes are expressed in terms of form factors (Ref. [95], eq. C6) as

$$\begin{aligned} H_{\frac{1}{2}t}^{Vm} &= \sqrt{\frac{Q_+}{q^2}} \left(M_- F_1^{Vm} + \frac{q^2}{M_1} F_3^{Vm} \right), \\ H_{\frac{1}{2}1}^{Vm} &= \sqrt{2Q_-} \left(F_1^{Vm} + \frac{M_+}{M_1} F_2^{Vm} \right), \\ H_{\frac{1}{2}0}^{Vm} &= \sqrt{\frac{Q_-}{q^2}} \left(M_+ F_1^{Vm} + \frac{q^2}{M_1} F_2^{Vm} \right), \\ H_{\frac{1}{2}t}^{Am} &= \sqrt{\frac{Q_-}{q^2}} \left(M_+ F_1^{Am} - \frac{q^2}{M_1} F_3^{Am} \right), \\ H_{\frac{1}{2}1}^{Am} &= \sqrt{2Q_+} \left(F_1^{Am} - \frac{M_-}{M_1} F_2^{Am} \right), \\ H_{\frac{1}{2}0}^{Am} &= \sqrt{\frac{Q_+}{q^2}} \left(M_- F_1^{Am} - \frac{q^2}{M_1} F_2^{Am} \right), \end{aligned} \quad (\text{A.7})$$

where $M_\pm = M_1 \pm M_2$, $Q_\pm = M_\pm^2 - q^2$. The form factors F are expressed in

3084 terms of dimensionless quantities in eqs. C8 and C9 in Ref. [95]. In our actual
3085 implementation form factors calculated in the covariant quark model [95] are used
3086 and for the numerical values of the Wilson coefficients Ref. [95] is used.

To assess effect of different form factors on efficiency calculations, an alternative set of form factors is implemented, based on the LQCD calculation from Ref. [99]. The form factors relations are found by comparing eqs. 66 and 68 in Ref. [95] to eq. 51 in Ref. [99]. Denoting LQCD form factors by F_i^L and dimensionless covariant quark model ones by f_i^{XX} we have

$$\begin{aligned} f_1^V &= c_\gamma(F_1^L + F_2^L), \\ f_2^V &= -2c_\gamma F_2^L, \\ f_3^V &= c_v(F_1^L + F_2^L), \\ f_1^A &= c_\gamma(F_1^L - F_2^L), \\ f_2^A &= -2c_\gamma F_2^L, \\ f_3^A &= -c_v(F_1^L - F_2^L), \\ f_1^{TV} &= c_\sigma F_2^L, \\ f_2^{TV} &= -c_\sigma F_1^L, \\ f_1^{TA} &= c_\sigma F_2^L, \\ f_2^{TA} &= -c_\sigma F_1^L, \end{aligned}$$

where

$$\begin{aligned} c_\gamma &= 1 - \frac{\alpha_s(\mu^2)}{\pi} \left[\frac{4}{3} + \ln\left(\frac{\mu}{m_b}\right) \right], \\ c_v &= \frac{2}{3} \frac{\alpha_s(\mu^2)}{\pi}, \\ c_\sigma &= 1 - \frac{\alpha_s(\mu^2)}{\pi} \left[\frac{4}{3} + \frac{5}{3} \ln\left(\frac{\mu}{m_b}\right) \right]. \end{aligned} \quad (\text{A.8})$$

3087 In the calculations $\mu = m_b$ is used. For the strong coupling constant, we start
3088 from the world average value at the Z mass, $\alpha_s(m_Z^2) = 0.1185 \pm 0.0006$ [2], and we
3089 translate it to the scale m_b^2 by

$$\alpha_s(\mu^2) = \frac{\alpha_s(m_Z^2)}{1 + \frac{\alpha_s(m_Z^2)}{12\pi} (33 - 2n_f) \ln\left(\frac{\mu^2}{m_Z^2}\right)}, \quad (\text{A.9})$$

3090 where $n_f = 5$. The LQCD form factors F_1^L and F_2^L can be then taken directly from
3091 Ref. [99] and plugged into the code implementing the calculation from Ref. [95].

3092 A.2 Bi-dimensional distribution parameters

3093 Expectations values for parameters in the bi-dimensional angular distribution for
 3094 the $\Lambda_b^0 \rightarrow \Lambda \mu^+ \mu^-$ decay calculated using form factors and numerical inputs from
 3095 Ref. [95].

$q^2 [GeV^2/c^2]$	A_{FB}^ℓ	P_z^Λ	f_L	O_P	O_{Lp}	O_{UVA}
0.1 – 2.0	0.082	-0.9998	0.537	-0.463	-0.537	0.055
2.0 – 4.0	-0.032	-0.9996	0.858	-0.142	-0.857	-0.021
4.0 – 6.0	-0.153	-0.9991	0.752	-0.247	-0.752	-0.102
V.0 – VA.5	-0.348	-0.9834	0.508	-0.478	-0.505	-0.239
15.0 – 16.0	-0.384	-0.9374	0.428	-0.524	-0.413	-0.280
16.0 – 18.0	-0.377	-0.8807	0.399	-0.513	-0.368	-0.294
18.0 – 20.0	-0.297	-0.6640	0.361	-0.404	-0.260	-0.314
1.0 – 6.0	-0.040	-0.9994	0.830	-0.170	-0.830	-0.027
15.0 – 20.0	-0.339	-0.7830	0.385	-0.461	-0.3A	-0.302

Table A.1: Prediction for angular observables entering two-dimensional angular distributions. Prediction is based on covariant quark model form factors from Ref. [95].

3096 A.3 $\Lambda_b^0 \rightarrow J/\psi \Lambda$ distribution

3097 The angular distribution of the $\Lambda_b^0 \rightarrow J/\psi \Lambda$ decay is modelled using Ref. [118]. The
 3098 differential rate is written as

$$w(\Omega, \Omega_1, \Omega_2) = \frac{1}{(4\pi)} \sum_{i=0}^{3} \sum_{i=1}^{19} f_{1i} f_{2i}(P_b, \alpha_\Lambda) F_i(\theta, \theta_1, \theta_2, \phi_1, \phi_2), \quad (\text{A.10})$$

3099 The expression uses four observables (angles) and depends on four complex amplitudes
 3100 a_+, a_-, b_+, b_- and two real valued parameters for the production polarisation,
 3101 P_b , and the Λ decay asymmetry, α_Λ . The angle θ is the angle of the Λ momentum
 3102 in Λ_b^0 rest frame with respect to the vector $\vec{n} = \frac{\vec{p}_{inc} \times \vec{p}_{\Lambda_b^0}}{|\vec{p}_{inc} \times \vec{p}_{\Lambda_b^0}|}$, where \vec{p}_{inc} and $\vec{p}_{\Lambda_b^0}$ are the
 3103 momenta of incident proton and Λ_b^0 in the center of mass system. The angles θ_1 and
 3104 ϕ_1 are polar and azimuthal angle of the proton coming from the Λ decay in the Λ
 3105 rest frame with axis defined as $z_1 \uparrow\uparrow \vec{p}_\Lambda$, $y_1 \uparrow\uparrow \vec{n} \times \vec{p}_\Lambda$. Finally, the angles θ_2 and ϕ_2
 3106 are the angles of the momenta of the muons in J/ψ rest frame with axes defined as
 3107 $z_2 \uparrow\uparrow \vec{p}_{J/\psi}$, $y_2 \uparrow\uparrow \vec{n} \times \vec{p}_{J/\psi}$.

3108 The distribution depends on the Λ decay asymmetry parameter, α_Λ , the production
 3109 polarisation P_b and four complex amplitudes. The α_Λ is measured to be 0.642 ± 0.013
 3110 for Λ . The production polarisation P_b and magnitudes of a_+, a_-, b_+ and b_- are

₃₁₁₁ measured in Ref. [103]. Phases are not measured therefore, as default all phases are
₃₁₁₂ set to zero and then they are randomly varied to calculate the systematic uncertainty.

3113

APPENDIX B

3114

3115

Data-simulation comparison

3116

This appendix reports a comparison between distributions in data and simulated $\Lambda_b^0 \rightarrow J/\psi \Lambda$ events. In the plots what is labeled as “Data” is real data in a 20 MeV interval around the Λ_b^0 mass, where a sideband subtraction technique to remove background. “Side” is real data for masses above 6 GeV containing mostly combinatorial background. These can be compared to the previous sample to see which variables differ the most. “MC” corresponds to Pythia8 $\Lambda_b^0 \rightarrow J/\psi \Lambda$ simulated events. Finally, the label “MC fully W” refers to the same simulated sample but weighted for the Λ_b^0 and Λ kinematics (Sec. 3.3.2) and the decay model (Sec. 3.3.1). Distributions are shown separately for long and downstream events.

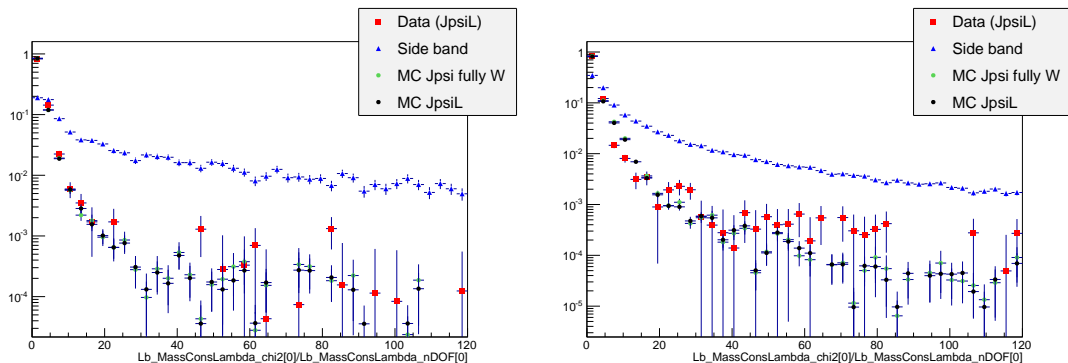


Figure B.1: Distributions of χ^2/N_{DOF} of the kinematic fit in data and simulation for LL (left) and DD (right) events.

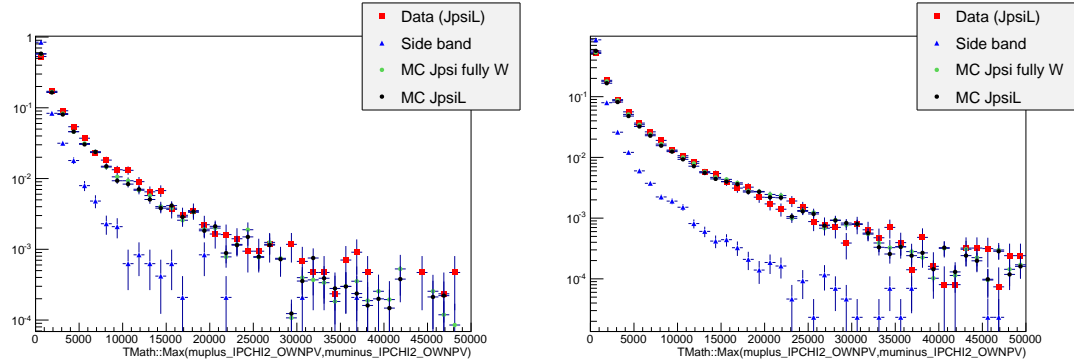


Figure B.2: Distributions of maximum muon $IP\chi^2$ variable in data and simulation for LL (left) and DD (right) events.

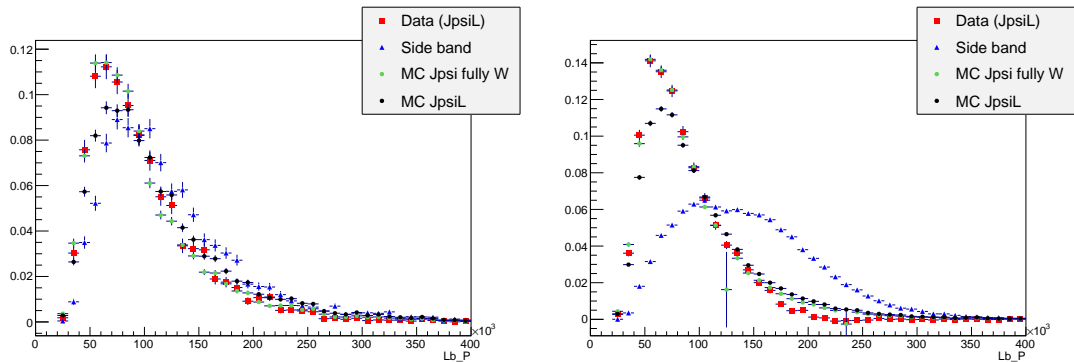


Figure B.3: Distributions of Λ_b^0 momentum variable in data and simulation for LL (left) and DD (right) events.

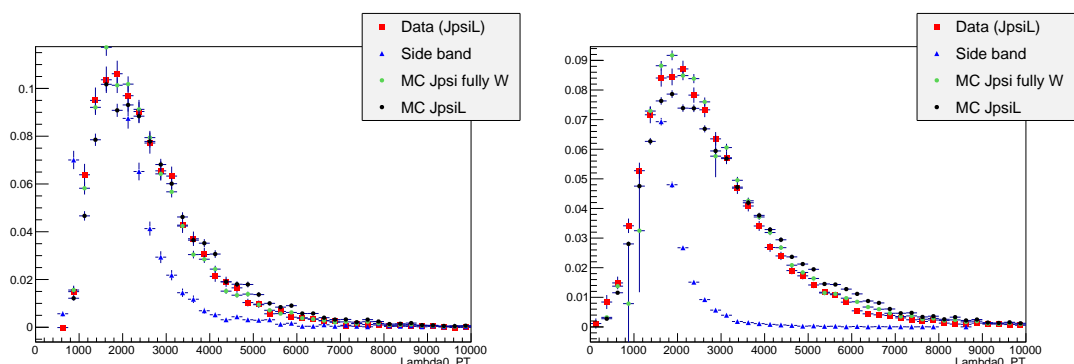


Figure B.4: Distributions of Λ transverse momentum variable in MC, data signal and data background for LL (left) and DD (right) events.

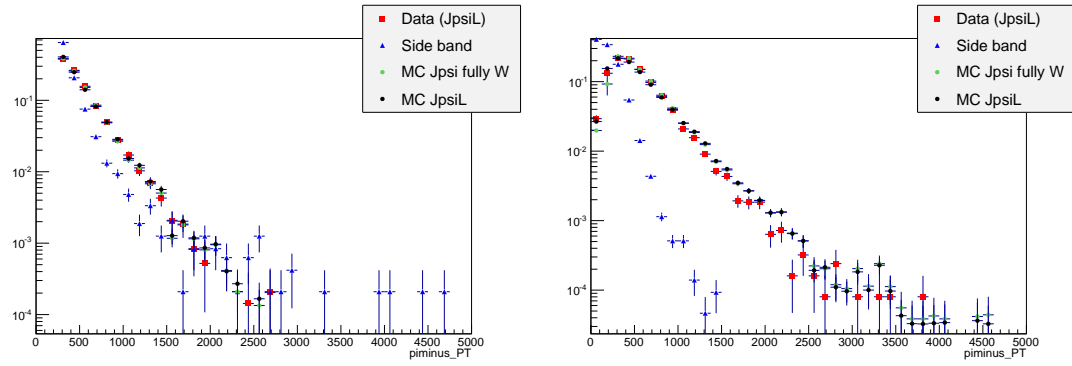


Figure B.5: Distributions of pion transverse momentum variable in data and simulation for LL (left) and DD (right) events.

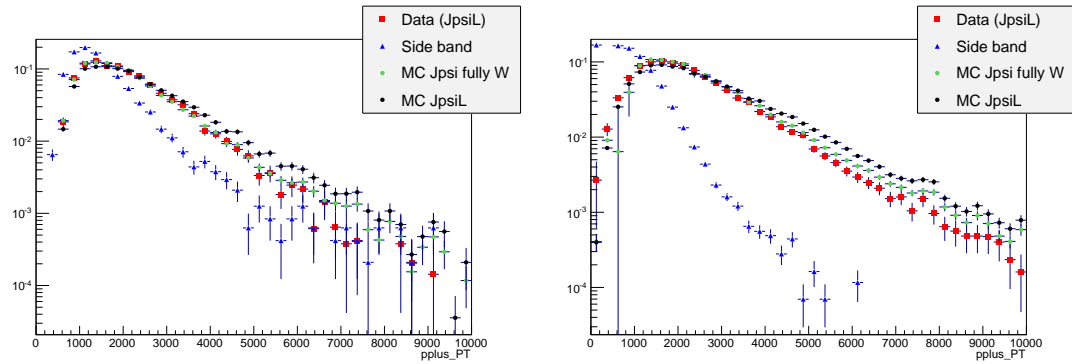


Figure B.6: Distributions of proton transverse momentum variable in data and simulation for LL (left) and DD (right) events.

³¹²⁶

APPENDIX C

³¹²⁷

³¹²⁸ Systematic uncertainties on the efficiency calculation for the ³¹²⁹ $\Lambda_b^0 \rightarrow \Lambda \mu^+ \mu^-$ branching fraction analysis.

³¹³⁰

³¹³¹ This appendix reports systematic uncertainties on absolute and relative efficiencies
³¹³² for the $\Lambda_b^0 \rightarrow \Lambda \mu^+ \mu^-$ branching fraction analysis.

q^2 [GeV $^2/c^4$]	Lifetime	Decay Model	Polarisation
0.1-2.0	0.003%	0.059%	0.145%
2.0-4.0	0.007%	0.156%	0.145%
4.0-6.0	0.002%	0.156%	0.144%
6.0-8.0	0.003%	0.080%	0.144%
11.0-12.5	0.012%	0.101%	0.144%
15.0-16.0	0.007%	0.050%	0.144%
16.0-18.0	0.002%	0.059%	0.145%
18.0-20.0	0.009%	0.016%	0.145%
1.1-6.0	0.005%	0.651%	0.144%
15.0-20.0	0.007%	0.088%	0.144%

Table C.1: Absolute values of systematic uncertainties on relative geometric efficiency.

q^2 [GeV $^2/c^4$]	Lifetime	Decay Model	Polarisation
0.1-2.0	0.007%	0.004%	0.008%
2.0-4.0	0.006%	0.001%	0.009%
4.0-6.0	0.009%	0.003%	0.008%
6.0-8.0	0.008%	0.005%	0.008%
11.0-12.5	0.010%	0.005%	0.009%
15.0-16.0	0.004%	0.006%	0.008%
16.0-18.0	0.003%	0.010%	0.010%
18.0-20.0	0.004%	0.011%	0.008%
1.1-6.0	0.009%	0.043%	0.010%
15.0-20.0	0.005%	0.072%	0.009%

Table C.2: Absolute values of systematic uncertainties on relative detection efficiency.

q^2 [GeV $^2/c^4$]	Downstream			Long		
	Lifetime	Model	Polarisation	Lifetime	Model	Polarisation
0.1-2.0	0.350%	0.234%	0.463%	0.066%	0.264%	1.081%
2.0-4.0	0.170%	0.640%	0.488%	0.005%	0.953%	1.088%
4.0-6.0	0.073%	0.514%	0.465%	0.052%	1.607%	1.087%
6.0-8.0	0.054%	0.298%	0.458%	0.011%	1.517%	1.075%
11.0-12.5	0.043%	0.030%	0.469%	0.025%	0.187%	1.080%
15.0-16.0	0.078%	0.499%	0.462%	0.030%	0.110%	1.082%
16.0-18.0	0.100%	0.215%	0.477%	0.021%	0.412%	1.078%
18.0-20.0	0.130%	0.044%	0.471%	0.034%	0.216%	1.079%
1.1-6.0	0.137%	0.279%	0.460%	0.025%	0.656%	1.078%
15.0-20.0	0.107%	0.511%	0.460%	0.016%	0.742%	1.077%

Table C.3: Absolute values of systematic uncertainties on relative reconstruction efficiency for long and downstream candidates.

q^2 [GeV $^2/c^4$]	Downstream			Long		
	Lifetime	Model	Polarisation	Lifetime	Model	Polarisation
0.1-2.0	0.038%	0.226%	0.070%	0.003%	0.061%	0.117%
2.0-4.0	0.009%	0.091%	0.034%	0.020%	0.072%	0.076%
4.0-6.0	0.028%	0.162%	0.058%	0.018%	0.165%	0.040%
6.0-8.0	0.005%	0.080%	0.075%	0.041%	0.035%	0.053%
11.0-12.5	0.002%	0.207%	0.079%	0.002%	0.148%	0.076%
15.0-16.0	0.036%	0.094%	0.035%	0.022%	0.021%	0.089%
16.0-18.0	0.023%	0.027%	0.029%	0.023%	0.003%	0.031%
18.0-20.0	0.017%	0.145%	0.034%	0.008%	0.199%	0.063%
1.1-6.0	0.024%	0.215%	0.029%	0.012%	0.733%	0.051%
15.0-20.0	0.025%	0.220%	0.031%	0.004%	0.108%	0.029%

Table C.4: Absolute values of systematic uncertainties on relative trigger efficiency for long and downstream candidates.

q^2 [GeV $^2/c^4$]	Downstream			Long		
	Lifetime	Model	Polarisation	Lifetime	Model	Polarisation
0.1-2.0	0.022%	0.019%	0.025%	0.060%	0.106%	0.072%
2.0-4.0	0.127%	0.267%	0.017%	0.095%	0.002%	0.031%
4.0-6.0	0.116%	0.106%	0.045%	0.081%	0.139%	0.119%
6.0-8.0	0.111%	0.186%	0.020%	0.085%	0.387%	0.047%
11.0-12.5	0.008%	0.056%	0.017%	0.057%	0.030%	0.027%
15.0-16.0	0.002%	0.004%	0.066%	0.070%	0.124%	0.023%
16.0-18.0	0.024%	0.088%	0.027%	0.068%	0.105%	0.023%
18.0-20.0	0.031%	0.050%	0.027%	0.180%	0.506%	0.077%
1.1-6.0	0.118%	0.164%	0.037%	0.080%	0.183%	0.058%
15.0-20.0	0.001%	0.125%	0.037%	0.102%	0.541%	0.034%

Table C.5: Absolute values of systematic uncertainties on relative MVA efficiency for long and downstream candidates.

q^2 [GeV $^2/c^4$]	Reconstruction	Trigger	MVA
0.1-2.0	0.612%	0.250%	0.173%
2.0-4.0	0.515%	0.246%	0.223%
4.0-6.0	0.408%	0.180%	0.272%
6.0-8.0	0.412%	0.090%	0.218%
11.0-12.5	0.175%	0.047%	0.103%
15.0-16.0	0.962%	0.010%	0.141%
16.0-18.0	1.173%	0.037%	0.103%
18.0-20.0	1.557%	0.050%	0.122%
1.1-6.0	0.475%	0.220%	0.246%
15.0-20.0	1.254%	0.040%	0.083%

Table C.6: Values of DD vertexing systematic uncertainties on relative reconstruction, trigger and MVA efficiencies for downstream candidates.

APPENDIX D

3133

3134

3135

Improved predictions for $\Lambda_b^0 \rightarrow \Lambda \mu^+ \mu^-$ observables.

3136

3137 The publication of the results included in this thesis triggered interest in the theory community, which produced improved lattice calculations and predictions [119].
 3138 This section reports the measured quantities with the new predictions overlaid as
 3139 reported in Ref. [119].

	Prediction	Measurement
$\langle d\mathcal{B}/dq^2 \rangle_{[15, 20]}$	0.756 ± 0.070	1.20 ± 0.27
$\langle F_L \rangle_{[15, 20]}$	0.409 ± 0.013	$0.61^{+0.11}_{-0.14}$
$\langle A_{FB}^\ell \rangle_{[15, 20]}$	-0.350 ± 0.013	-0.05 ± 0.09
$\langle A_{FB}^\Lambda \rangle_{[15, 20]}$	-0.2710 ± 0.0092	-0.29 ± 0.08

Table D.1: Comparison of predictions for the $\Lambda_b^0 \rightarrow \Lambda \mu^+ \mu^-$ observables with the LHCb data presented in this thesis in the interval $[15, 20]$ GeV^2/c^4 , where the measurement is most precise.

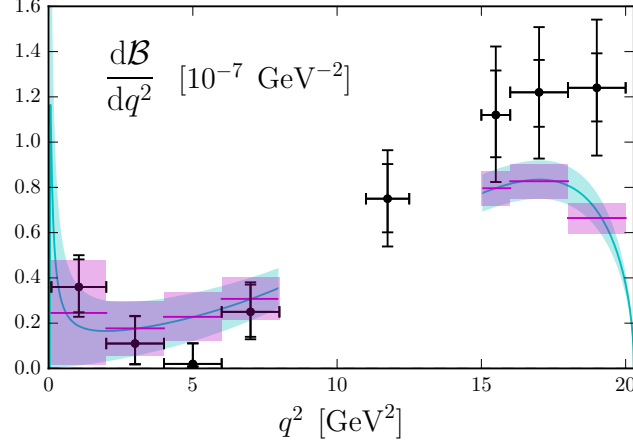


Figure D.1: Measurement of the differential branching fraction of the $\Lambda_b^0 \rightarrow \Lambda \mu^+ \mu^-$ decay as a function of q^2 already presented in Ch. 3 with improved Standard Model predictions from Ref. [119] overlaid.

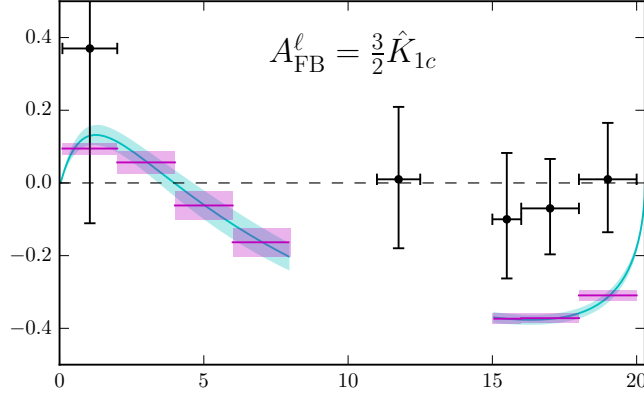


Figure D.2: Measurement of the lepton side forward-backward asymmetry, A_{FB}^ℓ , as a function of q^2 already presented in Ch. 4 with improved Standard Model predictions from Ref. [119] overlaid.

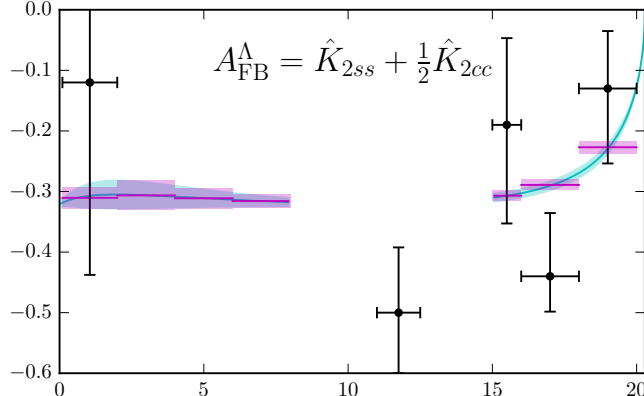


Figure D.3: Measurement of the hadron side forward-backward asymmetry, A_{FB}^h , as a function of q^2 already presented in Ch. 4 with improved Standard Model predictions from Ref. [119] overlaid.

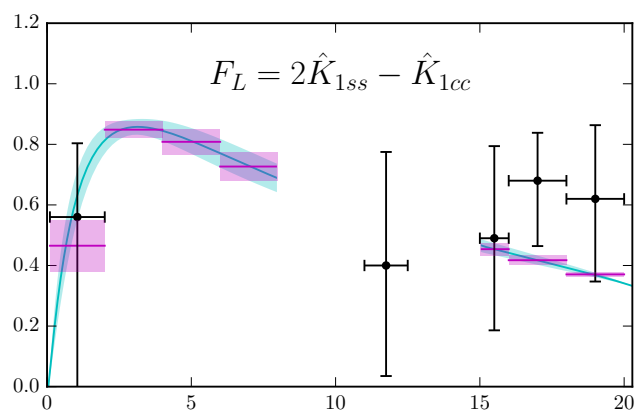


Figure D.4: Measurement of the fraction of longitudinally polarised dimuons, f_L , as a function of q^2 already presented in Ch. 4 with improved Standard Model predictions from Ref. [119] overlaid.

3141

APPENDIX E

3142

3143 **Invariant mass fits to $B^0 \rightarrow K^{*0}\ell^+\ell^-$ simulated candidates**

3144

3145 This appendix contains fits to the $m(K\pi\mu\mu)$ and $m(K\pi ee)$ invariant mass of $B^0 \rightarrow$
3146 $K^{*0}\ell^+\ell^-$ simulated candidates used to constrain parameters in the fit to data.

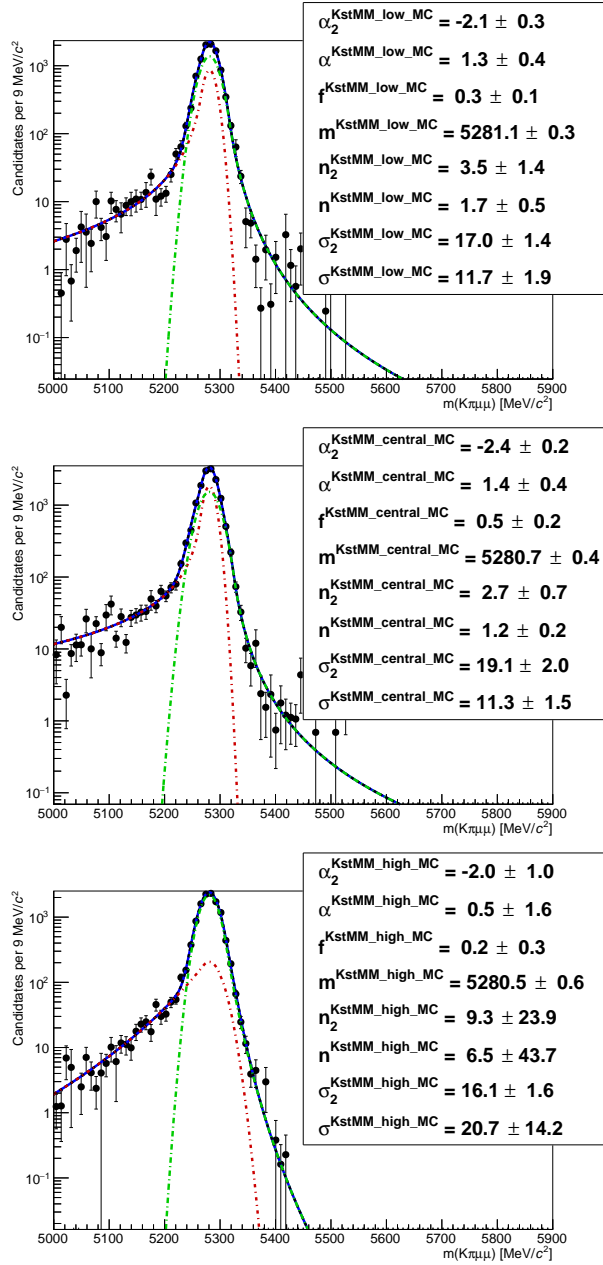


Figure E.1: Fitted $m(K\pi\mu\mu)$ mass spectrum for simulated events in the low (top), central (medium) and high (bottom) q^2 intervals.

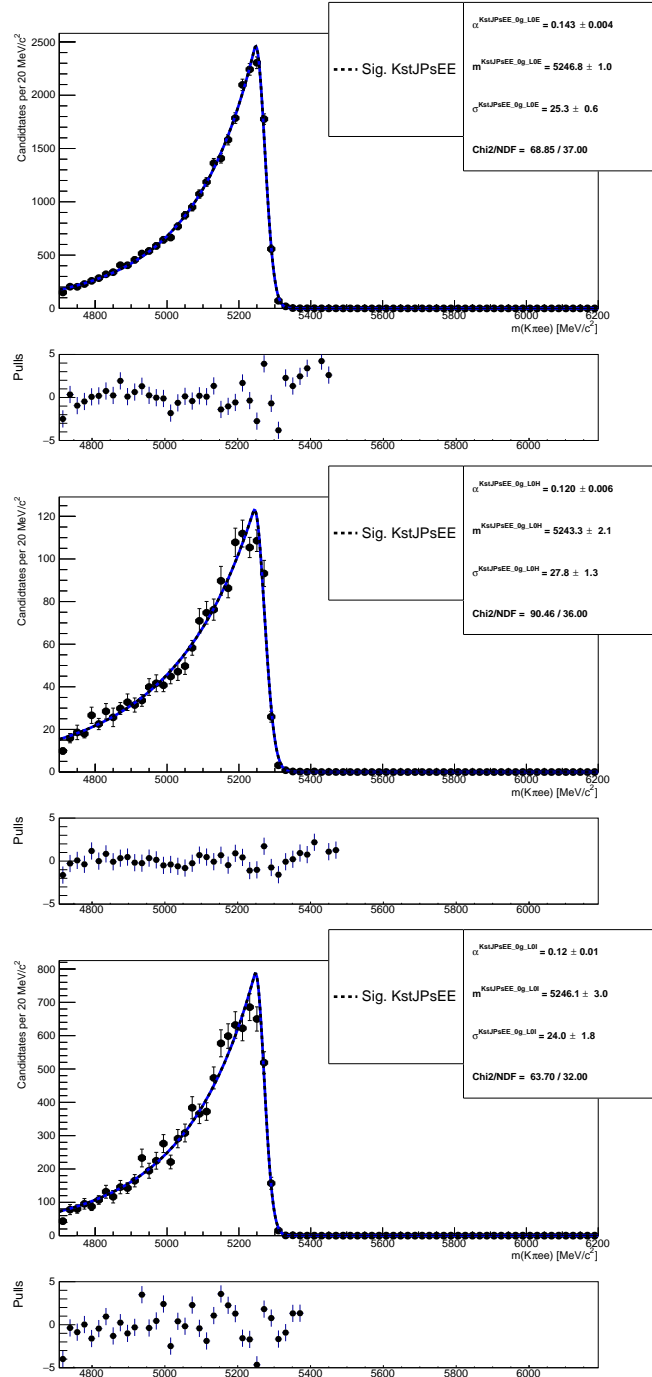


Figure E.2: Fitted $m(K\pi ee)$ mass spectrum of $B^0 \rightarrow K^{*0} J/\psi (J/\psi \rightarrow ee)$ simulated events in the three trigger categories and no photon emitted.

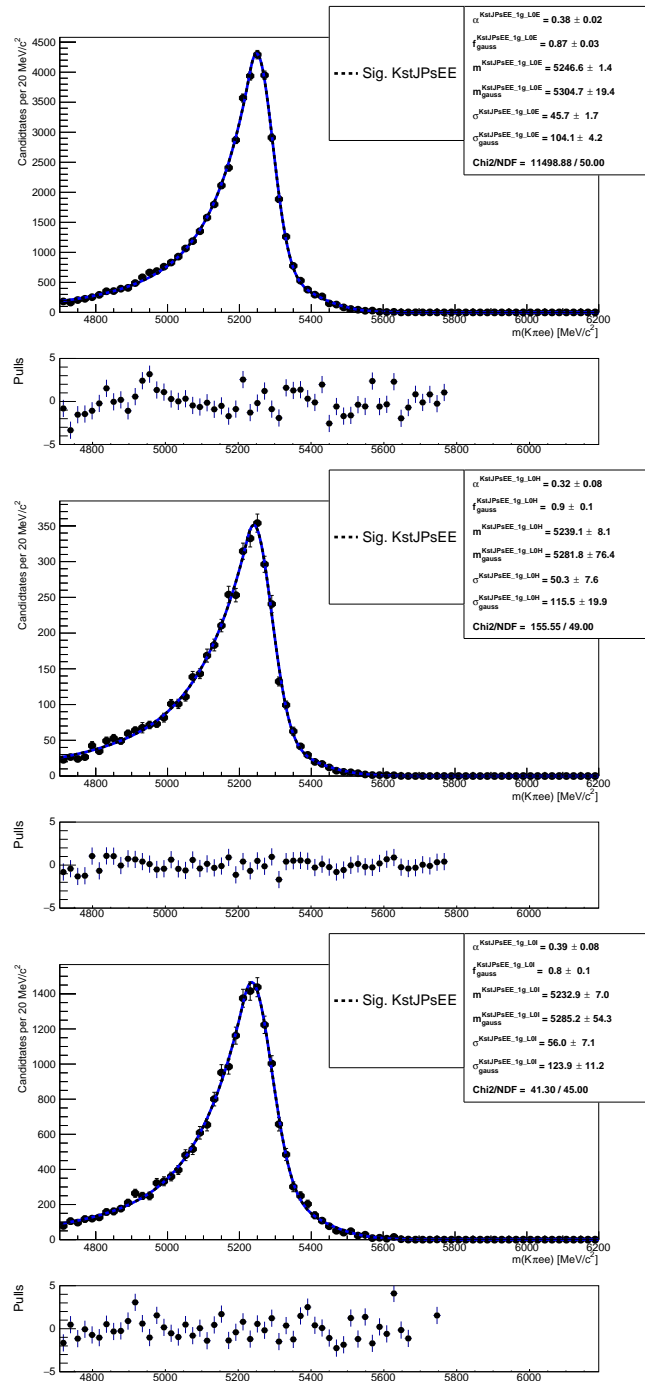


Figure E.3: Fitted $m(K\pi ee)$ mass spectrum of $B^0 \rightarrow K^{*0} J/\psi(J/\psi \rightarrow ee)$ simulated events in the three trigger categories and one photon emitted.

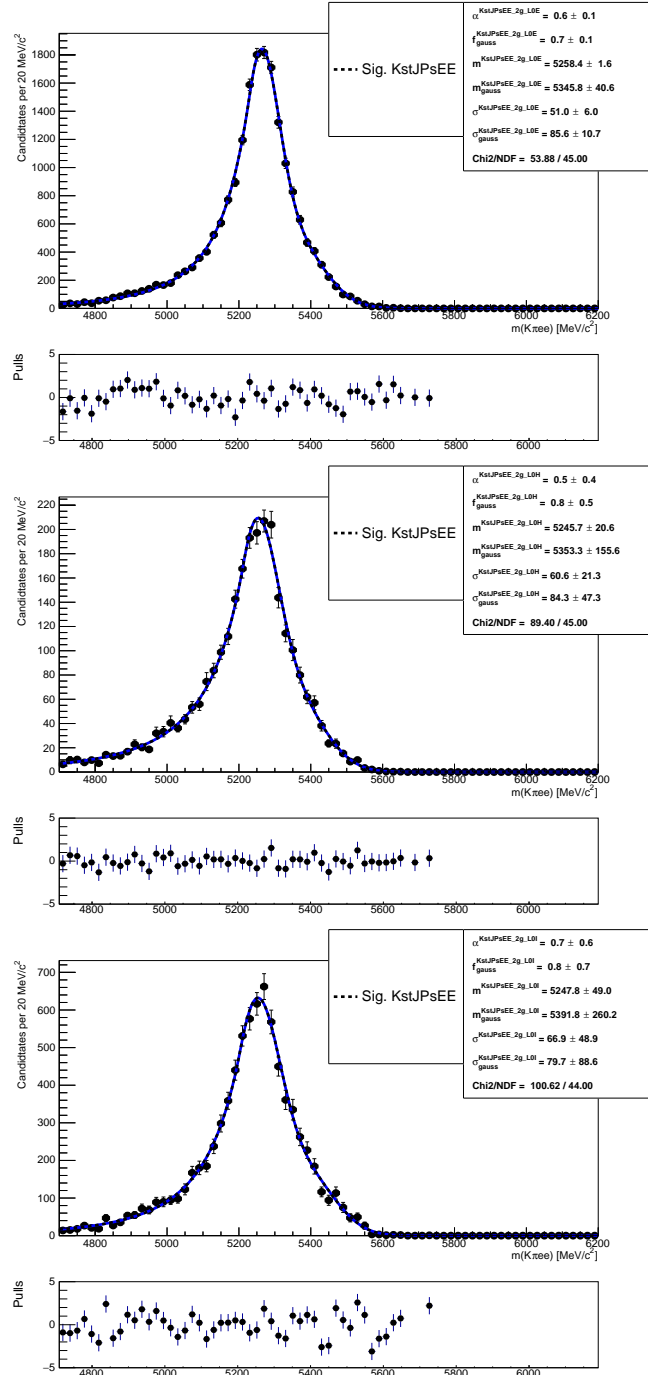


Figure E.4: Fitted $m(K\pi ee)$ mass spectrum of $B^0 \rightarrow K^{*0} J/\psi (J/\psi \rightarrow ee)$ simulated events in the three trigger categories and two photons emitted.

APPENDIX F

3148

Invariant mass fits to $B^0 \rightarrow K^{*0} e^+ e^-$ candidates divided in trigger categories

3151

This appendix contains fits to the $m(K\pi ee)$ invariant mass of rare and control channel candidates separately in the tree trigger categories. Each trigger category is always fit with its own PDF but in the main text only their sum is shown for simplicity.

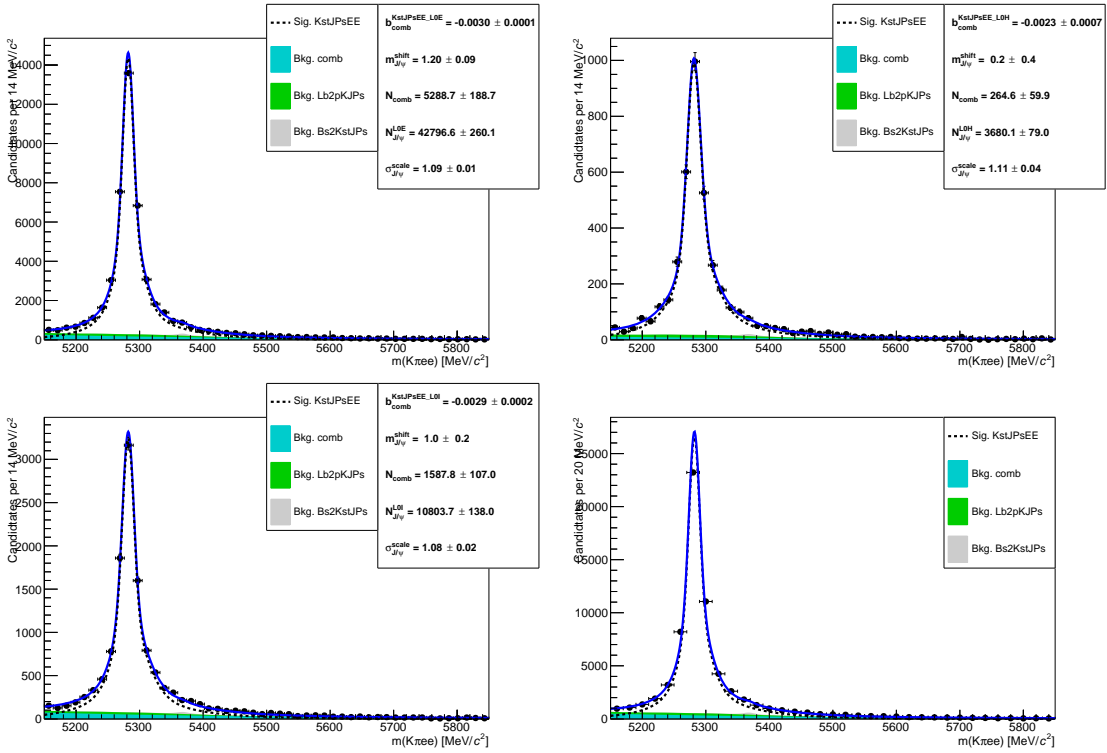


Figure F.1: Fit to the $m(K\pi ee)$ invariant mass of $B^0 \rightarrow K^{*0}(J/\psi \rightarrow e^+ e^-)$ candidates in the three trigger categories (L0E, L0H and L0I) separately, and (bottom right) combined. The dashed black line (shaded shapes) represents the signal (background) PDF.

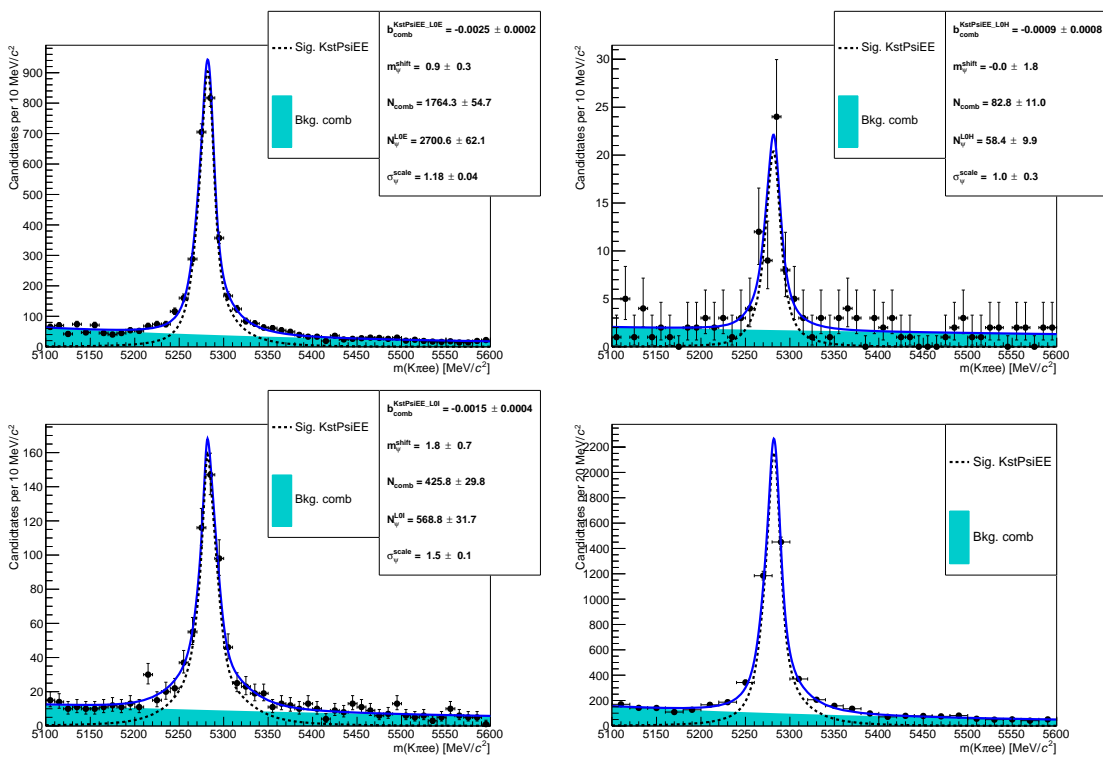


Figure F.2: Fit to the $m(K\pi ee)$ invariant mass of $B^0 \rightarrow K^{*0}(\psi(2S) \rightarrow e^+e^-)$ candidates in the three trigger categories (L0E, L0H and L0I) separately, and (bottom right) combined. The dashed black line (shaded shapes) represents the signal (background) PDF.

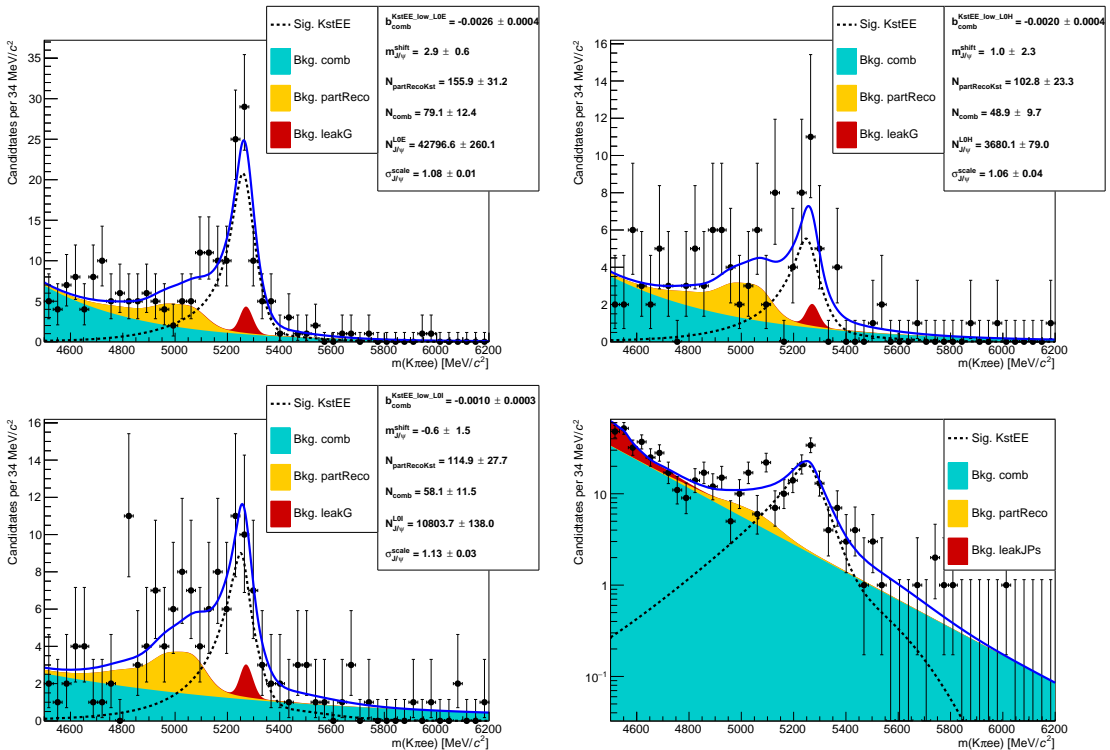


Figure F.3: Fit to the $m(K\pi ee)$ invariant mass of $B^0 \rightarrow K^{*0} e^+ e^-$ candidates at low- q^2 in the three trigger categories (L0E, L0H and L0I) separately, and (bottom right) combined. The dashed black line (shaded shapes) represents the signal (background) PDF.

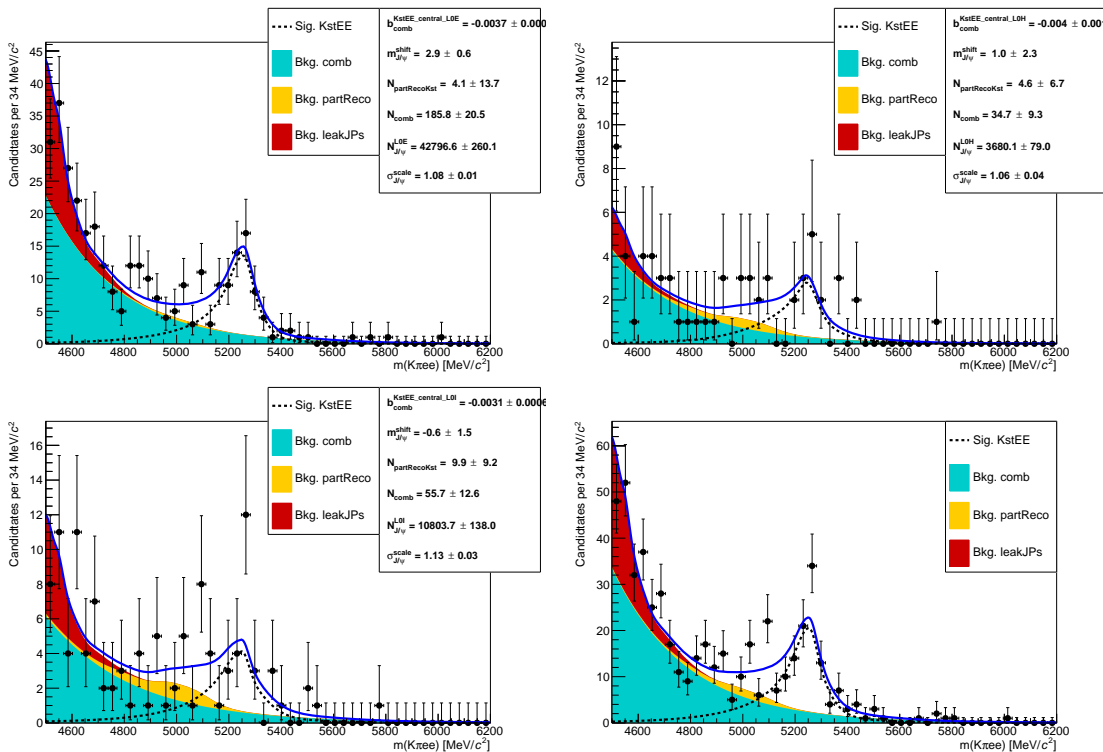


Figure F.4: Fit to the $m(K\pi ee)$ invariant mass of $B^0 \rightarrow K^{*0} e^+ e^-$ candidates at central- q^2 in the three trigger categories (L0E, L0H and L0I) separately, and (bottom right) combined. The dashed black line (shaded shapes) represents the signal (background) PDF.

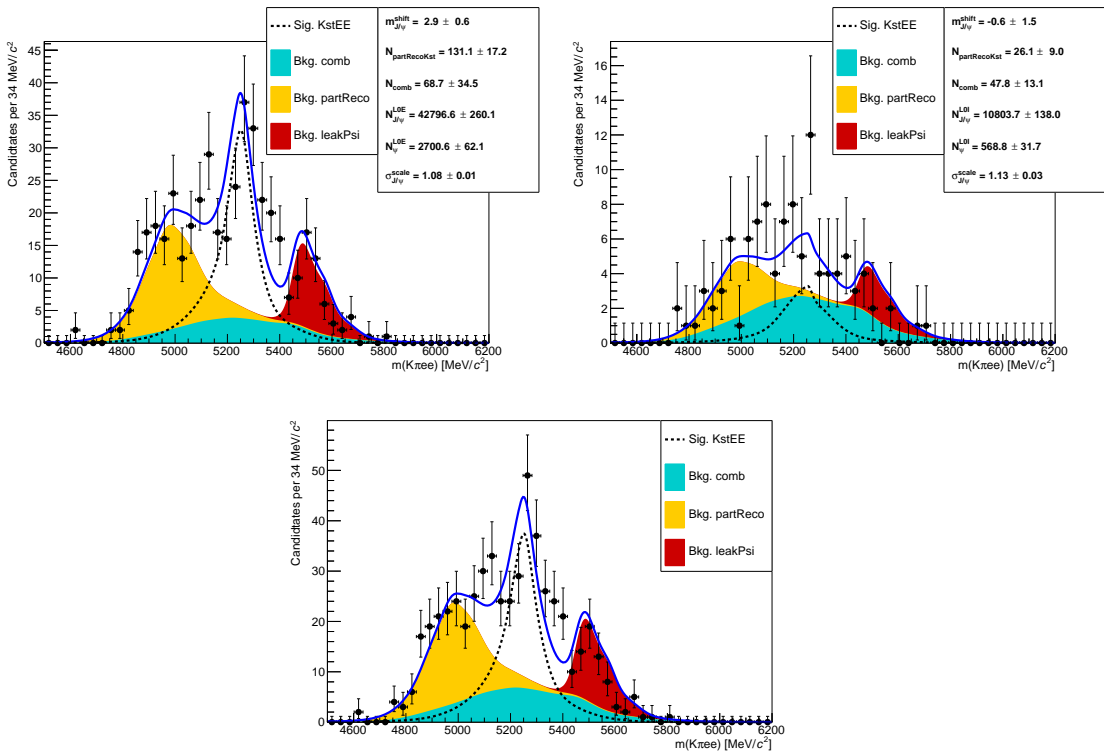


Figure F.5: Fit to the $m(K\pi ee)$ invariant mass of $B^0 \rightarrow K^{*0} e^+ e^-$ candidates at high- q^2 in the L0E and L0I trigger categories (top) separately, and (bottom) combined. The dashed black line (shaded shapes) represents the signal (background) PDF.